# DEVELOPMENT OF ELECTROCATALYSTS FOR GLYCEROL OXIDATION

---

**A thesis submitted in partial fulfilment of the requirements for the Degree of Doctor of Philosophy in Chemical and Process Engineering at the University of Canterbury**

**by Diandree Padayachee**

**University of Canterbury**

**2013**

---

# TABLE OF CONTENTS

# ACKNOWLEDGEMENTS

There are a number of people whose guidance, assistance and support have helped make this a smoother journey. I would like to thank the following people:

- My supervisor, Dr Aaron Marshall, for his invaluable assistance and guidance throughout my study. I am deeply appreciative of his supervisory style; for always allowing me the independence to run with ideas, while at the same time guiding me along with his incredible ability to ask the most pertinent questions, which often kept me thinking for days
- My co-supervisor, Dr Vladimir Golovko, for his enthusiasm and willingness to assist wherever he could, and for his insightful ideas and comments. Thanks also to Vladimir and his students for analysing some of my samples at the Australian Synchrotron
- The Department of Chemical and Process Engineering for my PhD scholarship
- Departmental technicians in the Mechanical Workshop (Leigh Richardson, Stephen Hood, Frank Weerts) and Electrical Workshop (Stephen Beuzenberg, Tim Moore) for their technical assistance. Thanks also go to Tony Allen for helping with computer issues, Michael Sandridge for analytical support and Glenn Wilson for purchasing lab supplies
- Technicians in other departments for all their assistance – Stephen Brown in Geological Sciences for XRD analysis, Alistair Duff from Chemistry for AA analysis, Rob McGregor from the Glassblowing Workshop in Chemistry for making up reactors, and Mike Flaws from Mechanical Engineering for TEM and SEM training and support
- Dr Colin Doyle (University of Auckland) for XPS analysis
- The Australian Synchrotron for providing beamtime and assistance and the NZ Synchrotron Group Ltd for providing travel funding
- My parents, Sothie and Indranie, for their love, faith and support throughout my life. I am also grateful to them for my spiritual upbringing, which has provided the foundation for the faith and certainty that has guided all my endeavours, and kept me going during difficult times
- To other family members – my sister, gran, uncles, aunts, cousins and parents-in-law, who have shown their love and support. In loving remembrance of my late grandfather, “Dadda”, who lit the spark for this dream
- Finally, to my *liefie*, Rainer, for his unwavering love and support throughout the years. Thank you for being such an amazing husband. May the force be with you, always.

# ABSTRACT

Glycerol is a very promising alternative fuel to hydrogen in fuel cells. However, the utilisation of glycerol as a fuel requires a good catalyst, due to the slow kinetics of glycerol electrooxidation. Gold has been identified as a promising catalyst due to its high activity and stability for glycerol electrooxidation – although the overpotentials are higher than on platinum and palladium. Modification of a nano-Au/C catalyst by the addition of $MnO_2$, in an attempt to further improve the activity and lower the overpotential for glycerol oxidation, was therefore first explored. This was followed by investigations into the effects of gold particle size and loading. Finally, the effect of gold particle size on oxidation of gold-catalysed glycerol oxidation intermediates was also briefly explored.

Studies into $MnO_2$ addition showed that the pre-deposition of $MnO_2$ yielded catalysts with smaller, more uniform gold particles, and catalysts with $MnO_2$ contents of 5 and 9 wt % had higher mass activities and lower onset- and peak- potentials than Au/C. All the Au/*x*$MnO_2$/C catalysts were more active than the palladium- and platinum-based catalysts reported in literature, which effectively demonstrated the advantage of using a gold-based catalyst for glycerol oxidation – especially when supported by $MnO_2$ which lowered the overpotential for glycerol oxidation over gold.

For the study into gold particle size, small gold particles of average diameter ≤ 4.7 nm had higher gold mass-based activities than medium-sized (14.7 nm) particles and were at least twice as active as catalysts containing large (≥ 43 nm) gold particles. The small gold particles also gave lower glycerol oxidation onset potentials, which was attributed to the predominance of Au(110) planes on those particles. Glycerol oxidation also appeared to proceed further along the oxidation pathway over small gold particles, which was confirmed in preliminary studies into the oxidation of glycerol oxidation intermediates. However, specific activity increased with increasing gold particle size, due mainly to the higher intrinsic activity of the Au(111) plane, which increased relative to Au(110) with increasing gold particle size. The important requirements for fuel cell applications are factors such as high mass activity, low overpotentials and high stability – all of which were met by the catalysts containing small gold particles defined by predominantly Au(110) facets.

Investigations into the gold loading effect showed similar mass- and specific- activities for catalysts with 5-20 % gold loading. However, only the catalysts with higher gold loadings (15-20 %) did not deactivate early during CV, indicating that a larger gold surface area is necessary to resist poisoning at high potentials. On the basis of low onset potentials, high mass activity, and stability at low overpotentials, a minimum gold loading of 12.5 % appears to be necessary for a supported gold catalyst with small gold nanoparticles; although even higher loadings may be preferable for a higher power output in a fuel cell.

Importantly, the insights gleaned from this study on the fundamental properties required for early activation, activity and stability of the gold catalysts could lead to a more intelligent design of gold-based catalysts in future.

# GLOSSARY

| | |
|---|---|
| AFC | alkaline fuel cell |
| AAS | atomic absorption spectroscopy |
| ATR | attenuated total reflectance |
| $d_{ave}$ | average diameter |
| CA | chronoamperometry |
| CP | chronopotentiometry |
| CV | cyclic voltammetry/voltammogram |
| DEMS | differential electrochemical mass spectrometry |
| DAFC | direct alcohol fuel cell |
| DEFC | direct ethanol fuel cell |
| DGFC | direct glycerol fuel cell |
| DMFC | direct methanol fuel cell |
| EIS | electrochemical impedance spectroscopy |
| EASA | electrochemically active surface area |
| EMIRS | electromodulated infrared reflectance spectroscopy |
| EDS | energy-dispersive X-ray spectroscopy |
| FTIR | Fourier transform infrared spectroscopy |
| GCP | glassy carbon plate electrode |
| GCE | glassy carbon rod electrode |
| GlOH | glycerol |
| HPLC | high performance liquid chromatography |
| IC | ion chromatography |
| IPA | isopropanol |

| | |
|---|---|
| MCFC | molten carbonate fuel cell |
| MWCNT | multi-walled carbon nanotube |
| NMR | nuclear magnetic resonance |
| OPD | overpotential deposition |
| PSD | particle size distribution |
| PAFC | phosphoric acid fuel cell |
| PGM | platinum group metal |
| PF comp. | positive feedback compensation |
| PEM | proton exchange membrane |
| PEMFC | proton exchange membrane fuel cell |
| SCE | saturated calomel electrode |
| SEM | scanning electron microscopy |
| SAMFC | solid alkaline membrane fuel cell |
| SOFC | solid oxide fuel cell |
| S.A. | surface area |
| TEM | transmission electron microscopy |
| $R_{ct}$ | charge transfer resistance |
| $R_u$ | uncompensated resistance |
| UPD | underpotential deposition |
| XRD | X-ray diffraction |
| XPS | X-ray photoelectron spectroscopy |

# 1 INTRODUCTION

Dwindling energy resources (such as oil and coal) and the need to cut down on emissions worldwide, have intensified efforts to identify new sources of clean, renewable energy. This naturally requires the development and/or improvement of technologies which could utilise such resources. One of the most promising solutions is fuel cell technology [1].

In a typical fuel cell, the oxidant is oxygen and the fuel is hydrogen. However, organic alternatives to hydrogen are preferred as they are less dangerous to store and transport [2]. They are also advantageous in that they can be used in small, low-power fuel cells for electronic devices [3, 4].

A number of alcohols have been studied with the purpose of replacing hydrogen in fuel cell applications. Of these, glycerol ($C_3H_8O_3$), a by-product of biodiesel production, is one very promising alternative. Since biodiesel is currently the only viable alternative fuel to petroleum, its production has increased considerably in recent years [5]. This has resulted in an excess of glycerol by-product in the market, leading to a significant decrease in the price of crude glycerol.

Glycerol is also a renewable fuel. This means that any $CO_2$ produced as a waste product gets used up in photosynthesis, helping to generate more plant material to continue the cycle (Figure 1 [6]). Other factors which make glycerol a very attractive fuel option are its low flammability, low volatility and high boiling point [7-9]. The drawback is that glycerol oxidation is slow, and its utilisation as a fuel therefore requires the development of efficient catalysts [10].

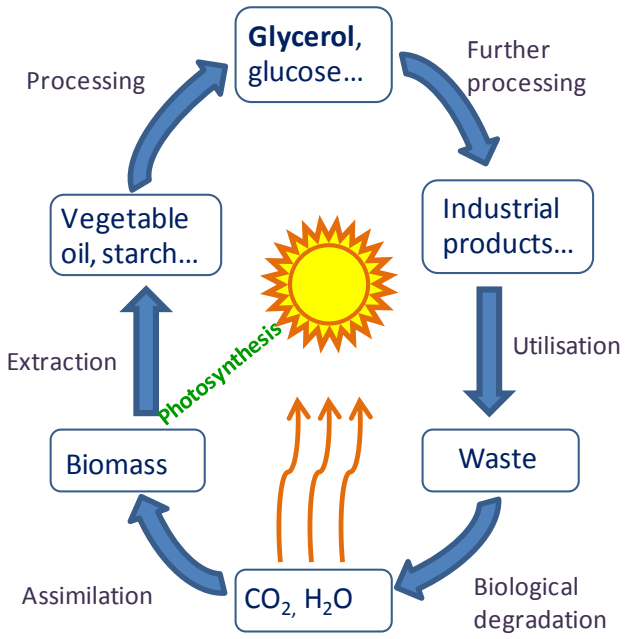


***Figure 1. Biomass cycle (redrawn from [6])***

Of the catalyst systems investigated for glycerol, most of the focus has been on platinum- or palladium- based electrocatalysts – possibly because platinum and palladium are reported to be the best catalysts for the electrooxidation of methanol and ethanol, respectively [11]. However, for glycerol electrooxidation, it has been shown that gold outperforms both platinum and palladium in an alkaline medium, with 6.5 and 8.8 times higher peak current densities, respectively – although at much higher peak potentials [8].

Since gold nanoparticles are more active than bulk gold for alcohol electrooxidation [12, 13], the focus in this project was on the development of effective nano-gold catalysts for the electrooxidation of glycerol, with the aim of attempting to lower the high overpotential for glycerol oxidation over gold and, if possible, to improve on the already-superior activity and stability of gold. In addition, it was attempted to obtain an understanding of the intrinsic factors which contribute to catalytic activity.

The thesis has been structured as follows:

A review of the literature is covered in Chapter 2, with brief descriptions of the various types of fuel cells, and an overview of the alcohols which have been most investigated as alternative fuels to hydrogen. The types of alcohol-oxidation catalysts (metals and support) which have been investigated are then discussed, along with methods to identify oxidation products and the subsequent glycerol oxidation pathways which have been derived using these methods.

Before activities of the synthesised gold catalysts could be compared, it was essential to optimise the electrochemical cell design and testing methodology. These investigations are reported on, in Chapter 3.

Chapter 4 deals with investigations into the addition of $MnO_2$ as a potential co-catalyst and support for gold nanoparticles. This chapter was published as a paper [14] in the journal Electrochimica Acta, and is reproduced here, along with additional information. The catalyst preparation, characterisation and electrochemical techniques are covered in depth in the Experimental section of this chapter. Therefore, in order to prevent repetition, only the experimental techniques which were not covered in Chapter 4 are detailed in the chapters thereafter.

In Chapter 5, the influence of gold particle size on glycerol oxidation is dealt with. This study was recently published in Electrochimica Acta [15].

An off-shoot of the investigation into gold particle size was the effect of gold loading on glycerol oxidation. This is covered in Chapter 6 and is currently a work-in-progress for submission to a journal.

It was speculated in Chapter 5, that glycerol oxidation proceeded further over the more active catalysts. So finally, investigations into the effect of gold particle size on the oxidation of potential gold-catalysed glycerol oxidation products are reported in Chapter 7.

One of the issues of concern throughout this PhD was the accuracy of the methods traditionally used by researchers to determine the electrochemically active surface area (EASA) of gold, particularly

when these methods were originally used in studies on bulk (polycrystalline) gold. It was initially intended to have this as a separate chapter in the thesis. However, since further insights into the EASA conundrum were revealed as investigations progressed, it was decided that it would make more sense to discuss this in context of the subject under investigation, rather than as a disjointed chapter. Methods to determine EASA are therefore covered in Chapters 2 and 3, and attempts to understand the discrepancies between exposed gold surface (determined using microscopy techniques) and electrochemically measured surface (EASA) are discussed in Chapters 5 and 6.

For ease of correlating appendices to the relevant chapters, numbering for each appendix has been done according to the corresponding chapter. For this reason, the numbering starts at “Appendix 3”, since there were no appendices to Chapters 1 and 2.

# 2 LITERATURE REVIEW

## 2.1 Fuel cells

Fuel cells are used to convert the chemical energy of the reactants (fuel and oxidant) directly into electrical energy. This circumvents limitations imposed by the Carnot cycle, making fuel cells more efficient than heat engines [16, 17], with predicted energy efficiencies of 40-50 % in electrical energy and 80-85 % in total energy [18]. An additional advantage of fuel cells is that undesirable gaseous and particulate product formation is minimal [19].

The fuel cell is composed of an anode (at which the fuel is oxidised), a cathode (at which the oxidant is reduced) and an electrolyte, which is sandwiched between the two electrodes. The faster the electrochemical reactions can occur at the electrodes, the higher the current output of the fuel cell [19], which makes the selection of catalysts a very important criterion for fuel cell design.

Various types of fuel cells have been developed, to meet specific needs. The main types of fuel cells are discussed below.

### 2.1.1 Proton exchange membrane fuel cell (PEMFC)

In a PEMFC, hydrogen is oxidised at the anode to form protons and electrons. The protons then migrate through the membrane and react with oxygen at the cathode to produce water, while the electrons travel through an external circuit to the cathode (Figure 2).The PEMFC utilises a proton exchange membrane (PEM) – typically a perfluoro-sulphonic acid membrane, e.g. Nafion – which acts as a solid electrolyte [16, 20, 21], to conduct protons to the cathode.

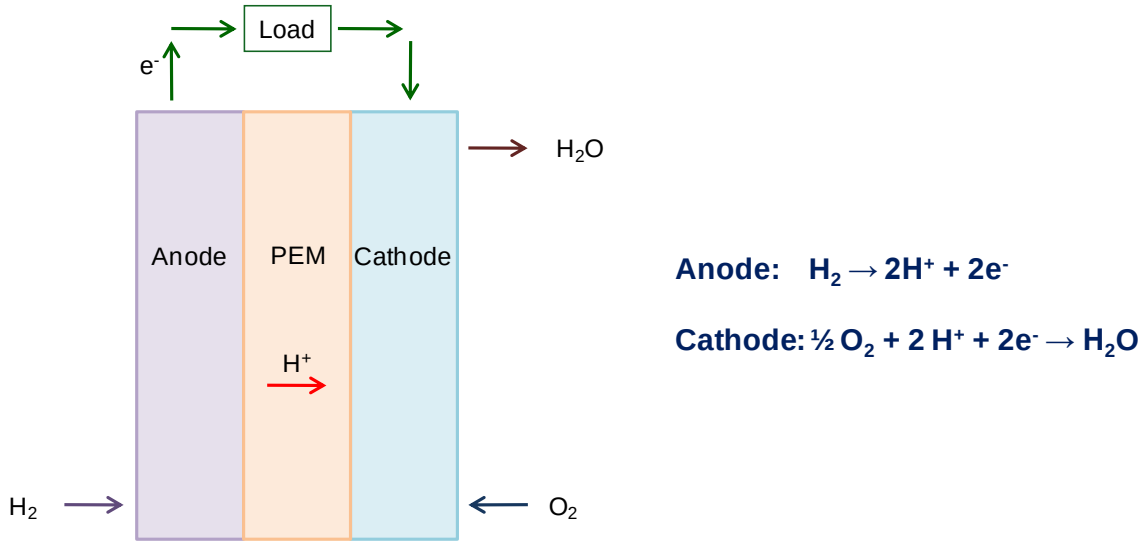


***Figure 2. Diagram of $H_2$-$O_2$ PEMFC***

The PEM needs to be hydrated in order to efficiently conduct protons and is therefore usually operated between 60-100$^{o}$C [20]. Above 100$^{o}$C, the membrane's water content decreases and its

resistance increases drastically [3]. However, the low operating temperatures pose problems with respect to conductivity, water management, slow oxygen reduction kinetics and low tolerance for impurities (e.g. CO and sulphur), cooling and heat recovery [20].

PEMFCs which can operate at higher temperatures than Nafion have therefore been investigated. Of these, the polybenzimidazole (PBI) membrane doped with phosphoric acid is a very promising alternative for medium temperature (150-200$^{o}$C) PEMFC applications [16, 22].

The direct methanol fuel cell (DMFC) differs from PEMFCs in that methanol and oxygen are the reactants. Methanol is introduced either in the vapour form or in a 2-5 M aqueous solution, although aqueous methanol is preferred so that preliminary vaporisation is not required [3]. However, these fuel cells suffer from problems of cathode flooding (due to electro-osmosis of water from the anode to the cathode), slow kinetics and methanol crossover (through the PEM) to the cathode [23].

### 2.1.2 Alkaline fuel cell (AFC)

AFCs were the first fuel cells to have practical applications [24]. As with PEMFCs, AFCs also use hydrogen and oxygen as reactants and operate at low temperatures (~ 100$^{o}$C) [25]. The difference is that an alkaline electrolyte, typically KOH, is used [3, 16, 24].

The mechanism of an AFC involves $OH^-$ ions produced at the cathode, migrating to the anode where they react with hydrogen to form water and electrons. The electrons then move along an outside circuit to the cathode while some of the water reacts with oxygen at the cathode, generating $OH^-$ to maintain the process [24] (Figure 3).

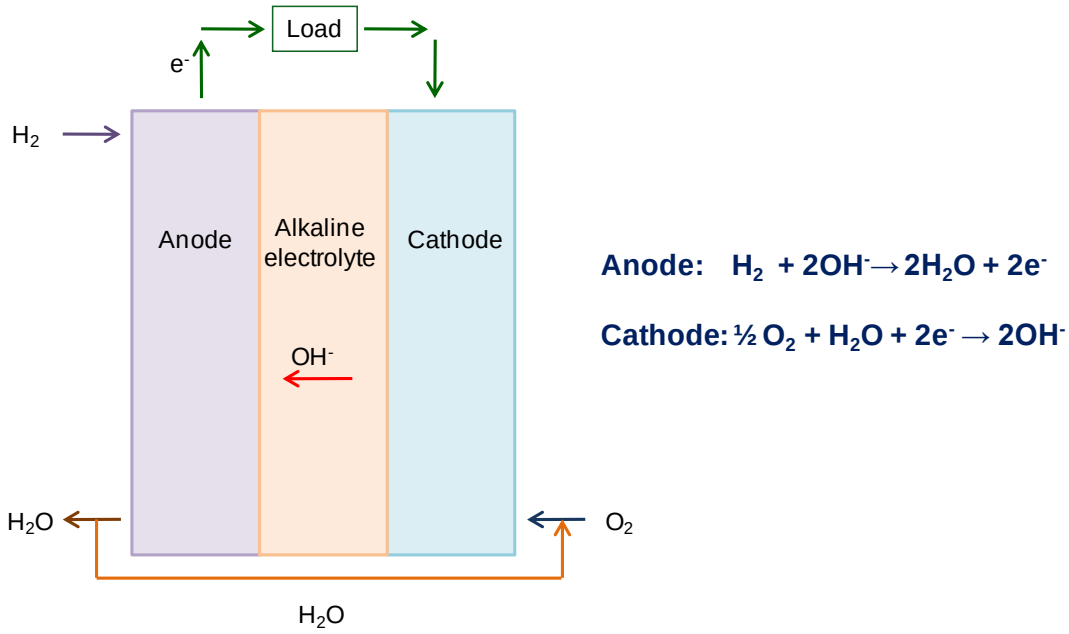


***Figure 3. Diagram of alkaline fuel cell***

AFCs have several advantages over PEMFCs, such as faster kinetics at both the anode and cathode, being able to use a diverse range of catalyst materials, instead of being limited to platinum group

metals (PGMs) [11, 16, 23, 24] and it can be switched off and on by stopping or starting electrolyte circulation [3].

In DMFCs which operate in an alkaline medium, the consumption of water at the cathode reduces the problem of cathode flooding which is experienced in acid electrolytes [23]. For these and other direct alcohol fuel cells (DAFCs), an alkaline environment is preferred, as it also favours lower overpotentials for alcohol oxidation, reduction of alcohol cross-over to the cathode and reduced risk of catalyst corrosion [2, 11].

The disadvantage with AFCs is that the electrolyte could become carbonated by $CO_2$ impurities in the oxygen source – which is why methanol oxidation studies have been carried out mainly in $H_2SO_4$ [4, 16]. Carbonation decreases electrolyte conductivity, oxygen solubility and electrode activity and can also block the pores of the electrode [24]. For these reasons, KOH is preferred to NaOH, due to its higher ionic conductivity and higher solubility product of $K_2CO_3$ [26].

However, modifications to AFCs can make it possible, in principle, to use less pure reactants and carbon-based fuels. In a solid alkaline membrane fuel cell (SAMFC), where the KOH electrolyte is replaced by a polymer, carbonation of the electrolyte is curbed [27]. This is because SAMFCs utilise $OH^-$ conducting anion exchange membranes and as such, there are no cations (e.g. $K^+$) in solution to cause precipitation of solid carbonate salts [23]. This promising membrane technology is attracting industrial interest due to recent successful developments [2] and is associated with the current increase in AFC research [11].

### 2.1.3 Phosphoric acid fuel cell (PAFC)

The PAFC has been very successful commercially for stationary power applications [16, 28], due to its efficiency and reliability [29]. PAFCs are regarded as medium temperature fuel cells, with operating temperatures of 150-200$^oC$ [28]. The higher operating temperatures of PAFCs make them more resistant to CO poisoning than PEMFCs [28]. The temperature range is chosen so as to ensure good electrolyte conductivity without seriously affecting cell life [29].

The electrolyte consists of 85-95 % (by volume) phosphoric acid [3]. At such high concentrations, $H_3PO_4$ has special properties which makes it a good electrolyte, capable of being immobilised in a porous matrix [16]. The matrix typically contains PTFE and SiC along with $H_3PO_4$ [16, 28]. It has recently been reported that replacing the typical SiC-containing matrix with a $BPO_4$-$H_3PO_4$-PTFE matrix increases the operating temperature window of stability from 150-200$^oC$ to room temperature-250$^oC$ [28].

The reactions occurring in PAFCs are the same as in PEMFCs (Figure 2).

### 2.1.4 Molten carbonate fuel cell (MCFC)

MCFCs are high temperature fuel cells, operating at temperatures at which the carbonate electrolyte is in a molten state (600-700$^{o}$C) [30]. The electrolyte is impregnated into a porous solid matrix, such as $LiAlO_2$ [30].

In MCFCs, $CO_2$ and oxygen are reduced at the cathode to form $CO_3^{2-}$ ions. These ions migrate to the anode where they react with hydrogen to generate electrons, $CO_2$ and $H_2O$. The electrons move to the cathode via an external circuit and the $CO_2$ is recycled at the cathode for further reaction (Figure 4).

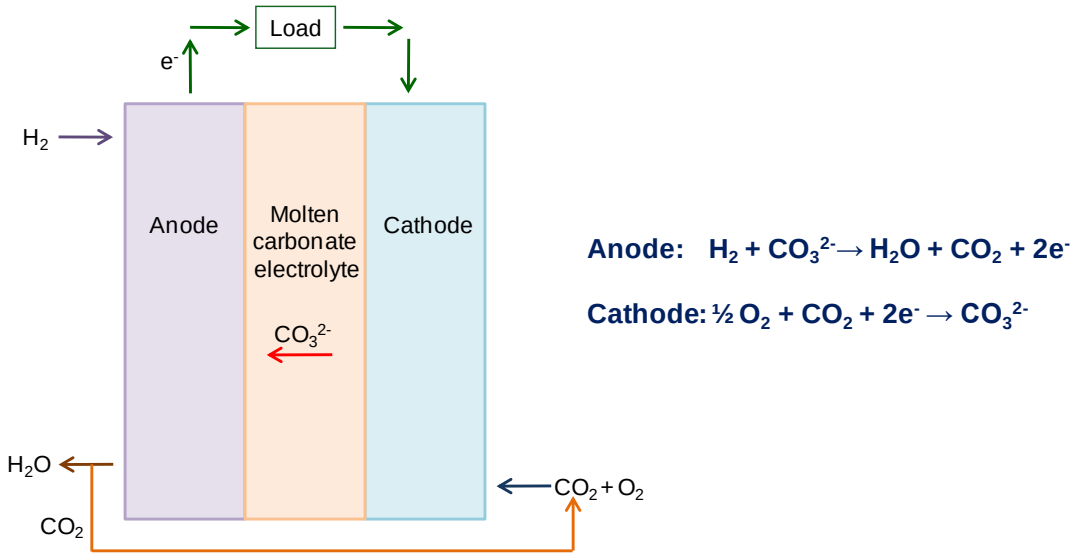


***Figure 4. Diagram of molten carbonate fuel cell***

Unlike the low and intermediate temperature fuel cells discussed above, MCFCs do not require external reforming and/or CO removal to obtain hydrogen from hydrocarbon fuels. Instead, the fuels are reformed to hydrogen and CO within the fuel cell [25]. Another advantage of the conditions under which MCFCs operate, is that platinum electrodes/catalysts are not required; instead, nickel-based anodes and cathodes are used [16, 30].

However, the extreme conditions also result in these fuel cells suffering from short lifetimes. Ongoing research into MCFCs is focussed on finding solutions to problems such as cathode degradation, anode creep and corrosion of fuel cell components [16, 30], in order to improve the lifetime of these fuel cells.

### 2.1.5 Solid oxide fuel cell (SOFC)

SOFCs contain a solid, oxide-conducting ceramic material which acts as the electrolyte [17, 31]. Oxidation of a fuel in a SOFC occurs by the following means (depicted in Figure 5):

Oxygen introduced to the cathode gets reduced to $O^{2-}$ ions. The $O^{2-}$ ions travel through the solid electrolyte to the anode where they oxidise hydrogen and CO in the fuel, forming $H_2O$ and $CO_2$. Electrons released at the anode travel through an external circuit to the cathode, where further reduction of oxygen takes place.

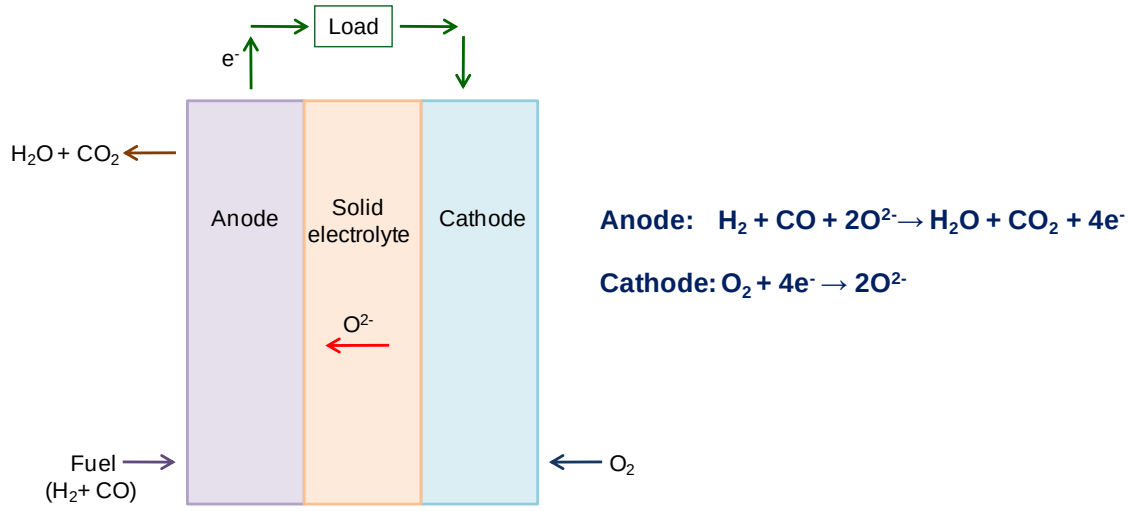


***Figure 5. Diagram of solid oxide fuel cell***

SOFCs are conventionally high temperature fuel cells, with a working temperature of 900-1000$^{o}$C [3, 17]. The most popular SOFC electrolyte is $Y_2O_3$-doped $ZrO_2$, due to its ionic conductivity, chemical stability and mechanical strength [31].

Due to the high temperatures of operation, SOFCs have the advantages of not requiring noble-metal catalysts [32] and of being able to oxidise natural fuels and biofuels, in addition to hydrogen and CO [17, 32]. However, treatment of natural fuels can result in poisoning of the anode catalyst by carbon and sulphur compounds, prompting investigations into alternate process conditions or electrode materials to limit such poisoning [16]. The high working temperatures limit the materials of construction which can be used and much of the ongoing research is also on the development of SOFCs which would work at lower temperatures [3, 16, 31].

## 2.2 Alcohol fuel alternatives to hydrogen

The most studied alcohols to date have been the simpler alcohols, methanol and ethanol [18], but there is also a fair amount of interest in ethylene glycol and glycerol. As already discussed, an alkaline medium is preferred for alcohol fuel cells. For this reason, the oxidation reactions for the alcohols discussed below have been given for an alkaline medium.

Methanol, the simplest alcohol, has a comparable energy density (6 kWh $kg^{-1}$) to petrol (10-11 KWh $kg^{-1}$) [33] and is electrochemically quite active, making it a promising fuel for future electric cars [3]. The methanol oxidation reaction in an alkaline medium is:

$$CH_3OH + 8OH^- \rightarrow CO_3^{2-} + 6H_2O + 6e^- \quad (\mathbf{1})$$

Methanol has several advantages over hydrogen as a fuel. Being a liquid, it is more easily handled, cheaper and more available than hydrogen [34]. Compared to the higher alcohols, methanol achieves complete oxidation to $CO_2$ relatively easily, as no C-C bond-breaking is required. However, some of the drawbacks of methanol are that it is highly volatile, toxic, inflammable and is not normally a renewable fuel [4, 33].

Ethanol is less toxic than methanol and has the advantage that it can be readily produced from biomass [35-38]. Total oxidation of ethanol generates 12 electrons, as shown below.

$$C_2H_5OH + 16OH^- \rightarrow 2\ CO_3^{2-} + 11\ H_2O + 12\ e^- \quad (\mathbf{2})$$

However, ethanol C-C bond breakage for total oxidation to $CO_2$ is difficult [37], resulting in the formation of mainly acetaldehyde, acetic acid and acetate [35]. This is problematic as it produces less electricity [37] and undesirable products with little- to no- added value [39]. As with methanol, ethanol cross-over to the cathode in a direct ethanol fuel cell (DEFC) is also possible and electrolyte swelling is worse with ethanol than with methanol [40].

Ethylene glycol is less toxic than methanol [10] and has the advantage over ethanol, of having an alcohol group on both carbons. This means that partial oxidation of ethylene glycol can generate 8 electrons, as opposed to 10 electrons from full oxidation [39]. The full oxidation reaction is:

$$C_2H_4(OH)_2 + 14\ OH^- \rightarrow 2CO_3^{2-} + 10H_2O + 10\ e^- \quad (\mathbf{3})$$

However, ethylene glycol has the disadvantage of not being produced from biomass [39] but is instead mainly produced from ethylene oxidation [8].

Glycerol, as with ethanol and ethylene glycol, has low toxicity in comparison with methanol [10]. The theoretical energy density of glycerol (5.0 KWh $kg^{-1}$) is comparable with that of methanol (6.1 kWh $kg^{-1}$), ethanol (8.0 kWh $kg^{-1}$) [35] and ethylene glycol (5.2 KWh $kg^{-1}$) [39]. Furthermore, since each carbon on glycerol has an alcohol group, the partial oxidation of glycerol (i.e. without C-C bond-breaking) to a substance such as mesoxalate, generates 10 electrons while full oxidation generates 14 electrons, according to the reactions below [35].

$$C_3H_5(OH)_3 + 12\ OH^- \rightarrow C_3O_5^{2-} + 10\ H_2O + 10\ e^- \quad (\mathbf{4})$$

$$C_3H_5(OH)_3 + 20\ OH^- \rightarrow 3\ CO_3^{2-} + 14\ H_2O + 14\ e^- \quad (\mathbf{5})$$

This implies that *theoretically*, glycerol partial oxidation could generate as much as 71.5 % of its total energy, whereas partial oxidation of ethanol would only utilise 17-33 % of its total energy [35]. Another advantage of glycerol partial oxidation is the reported formation of the costly chemical, hydroxypyruvate [35, 41], which could enable direct glycerol fuel cells to produce both electrical work and valuable chemicals. It has recently been shown that by regulating the anode potential, selective oxidation of glycerol to more valuable chemicals can be achieved [42].

The summarised properties of the above alcohols (Table 1) clearly indicate the potential advantages of utilising glycerol as a fuel.

***Table 1. Properties of common fuel cell alcohols***

| Property | Methanol | Ethanol | Ethylene Glycol | Glycerol |
|---|---|---|---|---|
| **Theoretical energy density / kWh.kg$^{-1}$** | 6.1 | 8.0 | 5.2 | 5.0 |
| **Toxicity** | High | Moderate | Moderate | Very low |
| **Flammability** | High | High | Low | Low |
| **Renewable?** | No | Yes | No | Yes |
| **Full oxidation** | Easy | Difficult | Difficult | Difficult |
| **Partial oxidation value-add products** | No | No | No | Yes |
| **Partial oxidation - % of total energy** | | 17-33 | 80 | 71.5 |

## 2.3 Catalysts for alcohol electrooxidation

On a thermodynamic basis, alcohols can easily undergo full oxidation to $CO_2$ but in reality, a number of partial oxidation products are formed; which can be attributed to kinetic factors [43]. Even the simplest alcohol, methanol, yields intermediates such as formic acid and formaldehyde [3, 33]. A good catalyst is therefore a very important consideration in the electrooxidation of alcohols. Since water is an essential requirement for this, it is important that the catalyst is able to activate both water and alcohol adsorption [33].

The use of bulk noble metal catalysts is expensive and impractical, so the catalyst is usually dispersed on a support such as carbon black, to make a cheaper and more active catalyst [3]. A number of methods have been utilised to prepare catalysts for alcohol electrooxidation. These have been covered in the literature [2, 44, 45] and include techniques such as electrodeposition, impregnation, colloidal, sol-gel and micro-emulsion.

### 2.3.1 Platinum-group catalysts

Platinum has the advantage over other metals in the PGM grouping, in that it is the only metal which is electroactive in an acidic medium [46]. For methanol electrooxidation, the best catalysts are reportedly based on platinum [34]. However, platinum is easily poisoned by alcohol electrooxidation

intermediates such as CO and effective oxidation is only possible at high potentials, where the poisonous intermediates can also be oxidised [47]. As this is uneconomical (the fuel cell output voltage is reduced), the more feasible solution is to modify platinum catalysts by the addition of one or more metals, in order to minimise the poisoning effect [33]. Even so, all platinum-based catalysts have been reported to deactivate with time and require high metal loadings to achieve acceptable stabilities [48].

The mixed Pt-Ru catalyst is claimed to be the most promising catalyst for methanol electrooxidation [49, 50] and is both more active and resistant to poisoning, than platinum alone [3]. While these catalysts are often referred to as Pt-Ru alloys, some researchers believe that ruthenium in these catalysts is actually mostly present as hydrous ruthenium oxides, and have furthermore shown that the fully reduced $Pt^0$-$Ru^0$ alloy is orders of magnitude less active for methanol oxidation than hydrous ruthenium oxides [51, 52]. There is also often no consensus on the optimum Pt:Ru ratio, but this has been attributed to insufficient knowledge of the surface composition of the catalysts reported [18]. It has been speculated that ruthenium improves catalyst durability by either altering the electronic state of platinum [3, 50], or that OH species (from water) generated on ruthenium oxidise CO adsorbed on platinum at lower potentials, which then leaves the platinum surface free for further oxidation [10, 18]. In order to maximise the efficiency of the catalyst by providing a larger catalytic surface area, the diameter of the Pt-Ru nanoparticles is required to be small (typically 2-5 nm) [53]. However, in terms of fuel cell operation, the catalyst is not durable enough and its activity decreases quickly, probably as a result of agglomeration or dissolution of nanoparticles or degradation of the support [54].

Methods of protecting the nanoparticles have been devised for methanol catalysts, such as the addition of $TiO_2$ nanosheets to Pt-Ru catalysts, which improved catalyst durability by retarding ruthenium loss from the catalyst [49]. Other examples are $MnO_2$ deposition over a Pt-Ru/C-nanotube catalyst, which stabilised the catalyst and gave good electrocatalytic activity [54], molybdenum impregnated over Pt-Ru/C improved catalyst activity [55], and the deposition of protective silica layers improved the durability of platinum catalysts [53, 56].

One novel approach to reduce the amount of platinum while increasing the catalyst activity and stability for methanol electrooxidation, has been to synthesise core-shell catalysts with a platinum shell. Examples are core-shell catalysts with a gold [57] or Pd-Co [58] core. It is noteworthy that the catalyst with a gold core was reported to have a high CO tolerance.

For ethanol electrooxidation, the challenge of platinum poisoning has been mainly dealt with by the addition of ruthenium or tin to platinum [37] and the Pt-Sn based catalysts are reportedly the most active [18, 33, 36]. However, in alkaline media, palladium-based catalysts have been more favourably reported for ethanol – such as Pd/carbon microspheres [59], Pd/MWCNTs (multi-walled carbon nanotubes) [48], Pd-Ag/C [60], Pd-Tb/C [61], Pd/TiN [62] and Pd-Ni/C [63]. The synergistic effect of metal oxides deserves mention here, in that nanocrystalline metal oxide ($CeO_2$, $Co_3O_4$, $Mn_3O_4$, NiO)-promoted Pd/C was seen to be more active than Pd/C, Pt/C or Pt-Ru/C [64], and Pd/$TiO_2$-C was more active than Pd/C [65] for ethanol electrooxidation.

Promising results for glycerol electrooxidation using palladium-based catalysts have been reported over Pd-Au/C [35, 66], Pd-Ni/C [35], Pd-Pt-Bi/C [67] and $Pd/TiO_2$ nanofibres [68]. It is worth noting that a comparison of methanol, ethylene glycol, 1,2-propanediol and glycerol electrooxidation over $Pd/TiO_2$ nanofibres showed that although glycerol had a higher onset potential than the other alcohols, it also yielded the highest current density overall. The same observation was made for Pd/MWCNT catalysts [48] and Pd on carbonised porous anodic alumina [69] – except in the last instance, the glycerol onset potential was second lowest after ethanol.

Platinum-based binary systems have also shown positive synergistic effects for glycerol electrooxidation. For example, the addition of $CeO_2$ to Pt/C catalysts improved the electrooxidation of glycerol and also methanol, ethanol and ethylene glycol [70], Pt-Ni/C catalysts were more active and had higher poisoning resistance than Pt/C [71] and Pt-Pd alloys improved glycerol electrooxidation currents significantly over those obtained with the pure metals [46]. The higher glycerol oxidation activities of bimetallic Pt-Pd nanoparticles have been attributed to palladium reducing CO build-up on platinum sites; and the addition of ruthenium nanoparticles to the Pt-Pd system further improved glycerol oxidation, due to its affinity for water [10].

In terms of fuel cell applications, one example is the addition of bismuth to platinum ($Pt_{0.9}Bi_{0.1}/C$), which improved the performance of a direct glycerol (1 M in 4 M KOH) SAMFC, with maximum power densities of 11 mW $cm^{-2}$ and 25 mW $cm^{-2}$ at 25°C and 60°C, respectively [39]. This was a better performance than that obtained over Pt/C, Pd/C, $Pt_{0.5}Pd_{0.5}/C$ or $Pd_{0.9}Bi_{0.1}/C$ catalysts. Then for palladium catalysts, promising results were obtained in a glycerol (5 wt % in 2 M KOH) SAMFC over Pd/MWCNT (multi-walled carbon nanotubes), achieving 13 and 55 mW $cm^{-2}$ at 25°C and 60°C [48]. Notably, these were comparable power densities to using methanol as a fuel at those temperatures. Methanol only showed superiority as a fuel at the highest temperature tested (80°C), with power densities of 95, 73 and 70 mW $cm^{-2}$ being achieved for methanol, ethanol and glycerol (note – all power densities quoted from Ref. [48] were measured off the graphs in Figure 13 of that paper).

### 2.3.2 Gold catalysts

Unlike platinum, gold is only active in alkaline solutions [72], but has still found use as a catalyst stabiliser in an acidic medium. Gold deposited onto a commercial Pt-Ru/C catalyst was shown to prevent catalyst poisoning by oxidising CO faster and to also increase the oxidation state of ruthenium, reducing ruthenium dissolution from the catalyst [73]. Platinum nanoparticles deposited on gold were more active for glycerol electrooxidation than platinum nanoparticles deposited on glassy carbon [74].

In an alkaline medium, gold has been reported to yield a peak current density eight times higher than platinum for glycerol electrooxidation [72]. The significant difference in activity has also been verified in more recent studies [8], where it was shown that gold was at least 6.5 times more active than palladium and platinum for glycerol oxidation - although (as stated in the Introduction) oxidation over gold occurred at much higher potentials. They also showed for gold-catalysed alcohol oxidation, that the peak current density for glycerol was at least 3.8 times higher than the other alcohols and the

activity decreased in the order glycerol > ethylene glycol > n-propanol > iso-propanol > ethanol > methanol. Gold is also not as easily poisoned as platinum or palladium – adsorption of glycerolic residues was far less on gold than on platinum [75], chronoamperometry (CA) and chronopotentiometry (CP) studies showed far less poisoning on gold than on palladium or platinum [8] and a comparison of glycerol electrooxidation products obtained over carbon-supported nano- gold, palladium and platinum catalysts showed that only the gold catalyst had no trace of CO adsorption [35]. In addition, the latter authors found that increasing the amount of gold in Au-Pd/C catalysts resulted in the disappearance of the adsorbed CO peak.

Gold-palladium synergistic effects have been noted for the electrooxidation of a number of alcohols, such as ethanol [76], isopropanol [77] and glycerol [35], where both the activities and stabilities of the catalysts were improved. In the case of glycerol, an interesting result was that both Au/C and Pd/C had the same onset potential, indicating that unlike bulk gold, nano-gold was activated at similar potentials to nano-palladium. Promisingly for the gold-palladium system, the Au-Pd/C catalysts had even lower onset potentials (almost 0.1 V lower) than Au/C or Pd/C. Gold-platinum synergies have also been reported, where Au-Pt alloys yielded much higher glycerol oxidation currents than the individual metals in alkaline solution [72].

Recently, Au/C was compared with Pt/C and Pd/C in a direct glycerol (1 M in 2 M KOH) SAMFC, and was shown to yield much lower peak power densities (18 and 60 mW $cm^{-2}$) than Pd/C (38 and 72 mW $cm^{-2}$) and especially Pt/C (59 and 125 mW $cm^{-2}$) at 50$^{o}$C and 80$^{o}$C, respectively [78]. However, it should be noted that the reported internal resistances of the fuel cells were highest for the Au/C fuel cell (244 mΩ $cm^{-2}$) and lowest for the Pt/C (151 mΩ $cm^{-2}$) fuel cell. Since the authors indicated that internal resistance arises mainly from the membrane and cathode, the performance of the SAMFC using the Au/C anode may actually be limited by the cathode and membrane behaviour rather than the specific performance of the anode. Accurate comparison of anode catalysts in fuel cell setups requires identical membrane and cathode performance or the use of a reference electrode – which is problematic to implement. In this case however, the authors also compared the anode catalysts using standard half-cell tests in glycerol-KOH solutions, which confirmed that the Au/C anode was less active than Pt/C at potentials below ~ 0 V (*vs*. Hg/HgO), but exhibited far higher activity than both Pt/C and Pd/C at potentials above ~ 0.15 V (*vs*. HgHgO). This suggests that Au/C is less easily deactivated compared with Pt/C and Pd/C – and provided the onset potential for Au/C can be lowered, Au/C catalysts may deliver better performance.

### 2.3.3 Non-noble/base metal catalysts

Research into noble metal alcohol electrooxidation catalysts far outweighs that into non-noble catalysts. Of the latter grouping, however, nickel tends to feature most. In fact, alcohol oxidation has been reported as one of the significant uses of nickel as a catalyst [79].

Even with the non-noble catalysts, the synergistic effects of combining different metals has been seen, e.g. Ni-Cu alloy gave significantly higher methanol electrooxidation currents than nickel alone [79].

While it is clear from the lack of papers on base metal catalysts for alcohol electrooxidation, that base metals cannot compete with noble metals, it cannot be denied that base metals – or as is more often the case, base metal oxides – have a vital role to play as a co-catalyst for noble metals.

$MnO_2$ is one base metal oxide which has featured favourably as a co-catalyst for PGM catalysts in a number of publications (discussed in Chapter 4). The wide range of oxidation states available to manganese makes it a very strong oxidant in its own right [80] and $MnO_2$ has been reported as being an attractive support option because of its electrochemical properties [81]. This makes manganese a potentially very useful co-catalyst/support in precious metal systems.

### 2.3.4 Catalyst support

A good fuel cell catalyst support requires a high surface area, good electrical and thermal conductivity and needs to be sufficiently porous and stable [2]. Carbon black, specifically Vulcan® XC72R, is the most common support, used in 80 % of electrocatalyst applications [82]. It is cheap, easily available, has a high surface area and is conductive [83]. The drawback is that agglomeration or dissolution of metal nanoparticles or corrosion of these carbon supports is often a problem [54]. However, carbon corrosion is actually more of a problem on the cathode side (i.e. at high potentials) of a fuel cell operating at > 90$^{o}$C in an acidic medium and furthermore, it is possible to activate carbon black, so as to anchor and stabilise the metal nanoparticles on the support [2].

A number of new carbon materials have been investigated as supports for alcohol electrooxidation catalysts, such as carbon nanotubes [84], nanocoils [85], hollow carbon hemispheres [86], graphene nanosheets [87], etc. Despite the promising results, there are still a number of issues (e.g. cost, large-scale production) which need to be addressed with these supports [44, 82].

Alternatives to carbon-based supports have also been successfully investigated, such as $TiO_2$ nanofibres [68], $TiO_2$ nanotubes [88], Ti nitride [62], Ru-Ir oxide [7], β-$MnO_2$ nanotubes [81], etc. Oxide supports have the capability to be both stable and conductive, and can influence the activity of a catalyst [89]. The support used can also determine the resistance of the catalyst to poisoning; e.g. for gold catalysts, the rate of CO electrooxidation was seen to increase with increasing potential over $Au/TiO_2$ but no oxidation occurred over Au/C (or polycrystalline gold) over the same potential range [90].

## 2.4 Reaction pathways for the electrocatalytic oxidation of alcohols

As discussed in Section 2.3.1, platinum catalysts are usually modified by the addition of one or more metals, in order to solve the problem of catalyst poisoning by the CO intermediate. Some catalyst modifiers are able to achieve this by changing the reaction pathway to favour the formation of an alternative intermediate species on the path to $CO_2$ formation; e.g. formyl ($^{\bullet}$CHO) from methanol [33, 55] and formic acid from glycerol [10]. An example of such a catalyst is $H_2$ heat-treated Pt-Mo-Ru/C for methanol [55].

Since full oxidation to $CO_2$ is more difficult for the higher alcohols, the type of catalyst used can change the selectivity towards certain oxidation end-products. For example, the popular ethanol electrooxidation catalyst, Pt-Sn/C was shown to decrease the $CO_2$ yield to half of that obtained with a Pt/C catalyst and to favour acetic acid formation over acetaldehyde [18], while Pd/MWCNT selectively converted ethanol to acetate in a basic medium [48]. Interestingly, while the latter catalyst was not able to effect cleavage of the C-C bond in ethanol, it was able to do so with glycerol, forming (amongst others) products such as $CO_3^{2-}$, glycolate ($CH_2OH\text{-}COO^-$) and oxalate ($COO^-\text{-}COO^-$).

Glycerol electrooxidation products have been analysed by various techniques, such as in-situ electromodulated infrared reflectance spectroscopy (EMIRS) [91], ion chromatography (IC) and nuclear magnetic resonance (NMR) spectroscopy [92], Fourier transform infrared spectroscopy (FTIR) [46], in-situ FTIR [9, 35, 93], high performance liquid chromatography (HPLC) [42, 94, 95] and differential electrochemical mass spectrometry (DEMS) [9]. Two of the more interesting methods reported recently are firstly, that of Kwon, *et al*. [94], who combined HPLC with voltammetry by means of a sampling tip placed in close proximity to the working electrode. This allowed for a direct comparison of reaction products with voltammetry measurements. Secondly, Schnaidt, *et al*. [9] used in-situ attenuated total reflectance (ATR)-FTIR in conjunction with DEMS. In-situ ATR-FTIR was used to correlate reaction products with oxidation potential, while online DEMS was used to identify any volatile products formed.

Analysis of the reaction products of glycerol is complicated because of the numerous possible glycerol electrooxidation products that can be formed. The reported reaction products and pathways are sometimes conflicting, even on the same system being studied – although this could be due to a number of reasons, such as limitations of the analytical techniques used, differences in concentration of reactants, type of catalyst, etc. For example, Simões, *et al*. [35] reported the formation of the value-add chemical, hydroxypyruvate, over a Au/C catalyst (Scheme 1), while Zhang, *et al*. [42] did not report its formation over Au/C. On the other hand, Kwon, *et al*. [41] showed hydroxypyruvate formation over platinum, but not over gold (Scheme 2).

Furthermore, Simões, *et al*. [35] did not find a CO adsorption band (using in-situ FTIR), and believed this was either due to glycerol adsorption not occurring on gold at low potentials or that gold was not able to induce breaking of carbon bonds – which is why, unlike Scheme 2, their reaction sequence (Scheme 1) does not show any products of C-C splitting. However, this was also refuted by Jeffery, *et al*. [96], who detected glycerol (0.1 M in 0.1 M KOH) dissociation products such as $CO_2$, $CO_3^{2-}$, formate ($HCOO^-$), and glycolate during glycerol electrooxidation over a polycrystalline gold catalyst – although Kwon, *et al*. [41] have dismissed the possibility of $CO_2$ formation.

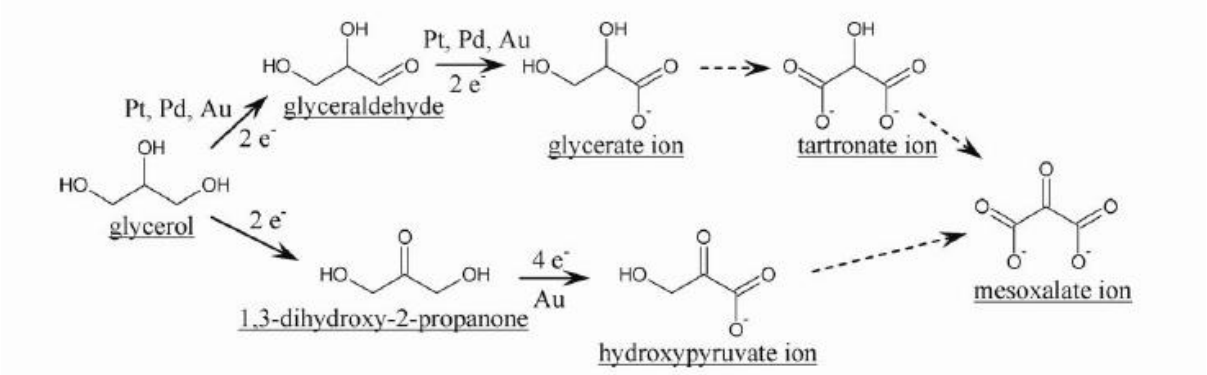


***Scheme 1. Reaction mechanism for glycerol (0.1 M in 1 M NaOH) electrooxidation over Au/C, Pd/C and Pt/C, elucidated using in-situ FTIR. [35]***

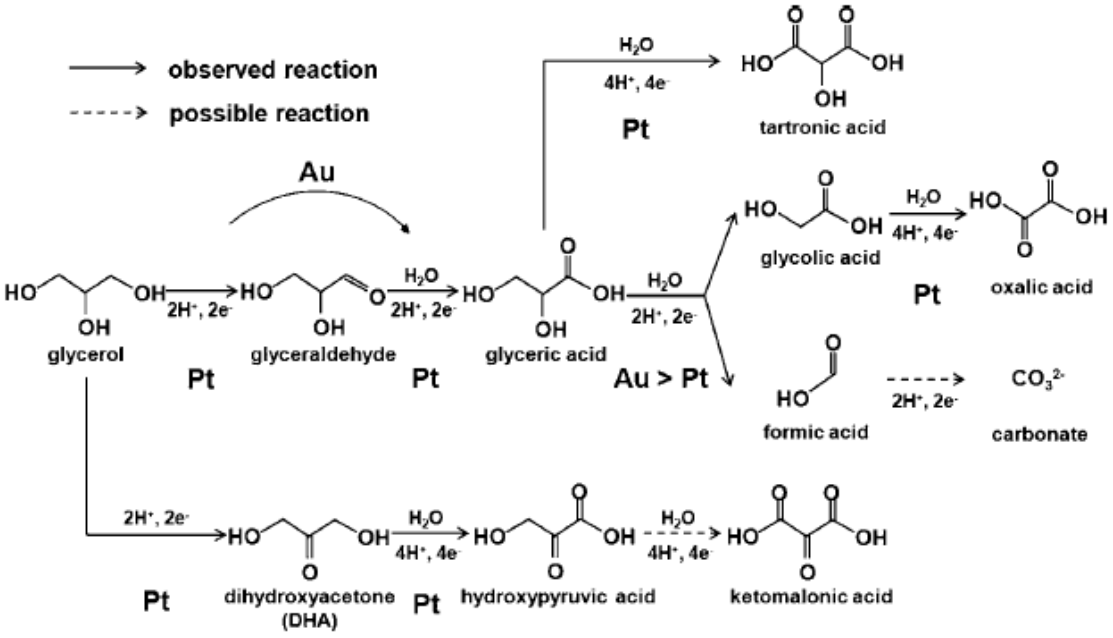


***Scheme 2. Reaction mechanism for glycerol (0.1 M in 0.1 M NaOH) electrooxidation over polycrystalline gold and platinum, determined using online HPLC and OLEMS (Online Electrochemical Mass Spectrometry) [41]***

## 2.5 Determination of electrochemically active surface area (EASA)

Polycrystalline metal electrode surfaces often contain defects which can be significant on the atomic or molecular scale [97]. This means that the EASA can be orders of magnitude greater than the geometric surface area ($A_{geom}$) of the electrode - which is especially significant when dealing with surface reactions such as adsorption and catalysis [98]. Techniques such as electropolishing are commonly used to activate metal electrodes by removing surface impurities – but to also produce a

smooth surface and provide a reproducible condition [98]. The evenness of a smooth metal surface can be determined by the roughness factor, which is defined by the equation

$$R_f = \frac{EASA}{A_{geom}} \quad (\mathbf{6})$$

Metal nanoparticles on the other hand, have significantly higher surface areas than the bulk metal, which is what makes them such active catalysts. The surface area of a nanoparticle catalyst can vary significantly depending on the size and shape of the particles.

In order to accurately express intrinsic electrocatalytic activity (analogous to turnover frequency in heterogeneous catalysis) – whether for smooth bulk metal surfaces or for nanoparticles – it needs to be reported in terms of the electrochemically active surface area.

EASA is calculated from

$$EASA = \frac{Q_{measured}}{Q_{theoretical}} \quad (\mathbf{7})$$

where $Q_{measured}$ is the charge (μC) measured by integration of a voltammetric peak associated with an adsorption process, while $Q_{theoretical}$ (μC $cm^{-2}$) is the charge required for monolayer coverage of 1 $cm^2$ of electrode surface by the adsorbed species [98]. If $Q_{theoretical}$ is known for a certain system, this then allows for EASA ($cm^2$) determination. For nano-catalysts, EASA is often reported in terms of its specific surface area ($m^2\ g^{-1}$), in order to account for the metal loading on the catalyst support.

A number of techniques have been reported for EASA determination of catalysts, with some techniques being better suited to certain metals. The relative advantages and disadvantages of the techniques most relevant to the study of fuel cell catalysts are described below.

#### *2.5.1.1 Hydrogen adsorption*

This method is commonly used for EASA determination of metals which can adsorb hydrogen, e.g. platinum, rhodium, iridium, nickel. It cannot be used with gold, which has no hydrogen adsorption region or with palladium, which *absorbs* hydrogen [97, 98].

The method is well established for platinum but not so much for the other metals. In the case of rhodium and iridium, it has been reported that monolayer completion does not occur, requiring additional determinations to confirm the results [97].

It has also been reported that on supported catalysts, hydrogen spillover onto the support may occur [97] – which would provide exaggerated values for the catalyst EASA.

### 2.5.1.2 *Oxide reduction*

Unlike the hydrogen adsorption method, the oxide reduction method can be used for both gold and palladium [97, 98]. $Q_{measured}$ (Equation 7) is obtained by integration of the oxide reduction peak (Figure 6).

This method is reportedly less accurate than the hydrogen adsorption method and could potentially modify the electrode surface [97]. Despite the impreciseness of the oxide reduction method, it appears to be the most widely used for gold EASA determination.

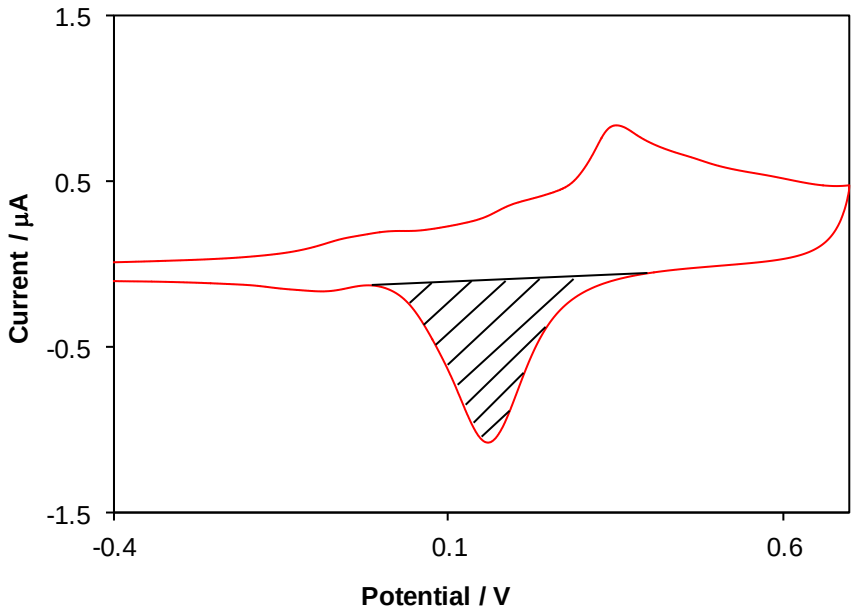


***Figure 6. Voltammogram of polycrystalline gold in 1 M KOH, showing gold oxide reduction peak. The area under the peak (shaded region) represents $Q_{measured}$, which is used to calculate EASA. Potentials are shown vs. Hg/HgO reference.***

### 2.5.1.3 *Underpotential deposition (UPD)*

UPD is the deposition of a metal monolayer onto another metal at potentials more positive of the Nernst potential for bulk deposition [99].

UPD has traditionally been used for electrodes which cannot be characterised by the above methods, e.g. silver and copper [97] and has also been used to determine the EASA of polycrystalline- and nano- gold catalysts. The use of copper [100, 101], lead [102, 103] and thallium [99] UPD have been reported for gold catalysts.

The advantage of this method is that it has good reproducibility. However, it also has the potential disadvantage of some of the UPD atoms being retained on, or changing, the surface of the metal [97].

#### *2.5.1.4 CO stripping*

This involves CO adsorption onto- and subsequent stripping from- the electrode surface. The charge under the stripping peak is used to determine the EASA of the catalyst.

CO stripping has been used for EASA determination on platinum and Pt-Ru/C catalysts [104], as well as on palladium – although with palladium, this method was reported to not be as accurate as oxide reduction or copper UPD [105]. No information could be found in the literature on CO stripping for gold EASA determination.

## 2.6 Glycerol electrooxidation over gold

For alcohol electrooxidation half-cell studies (explained in Chapter 3), techniques such as cyclic voltammetry (CV) are typically used to assess catalysts' activities, since the current generated is proportional to the rate of the reaction:

$$\textit{Rate of reaction} = I/nF \qquad (8)$$

Glycerol oxidation over gold begins when the metal surface starts to oxidise [43, 75], with the active form of gold being hydrous gold oxides [106]. Then at higher potentials, the formation of the gold oxide monolayer (discussed in more detail in Chapter 3) renders the gold surface inactive [107], resulting in a drop-off in glycerol oxidation (Figure 7). On the reverse sweep, reduction of the oxide then allows the surface to reactivate for further oxidation of adsorbed glycerol and its reaction intermediates [108], resulting in a second oxidation peak.

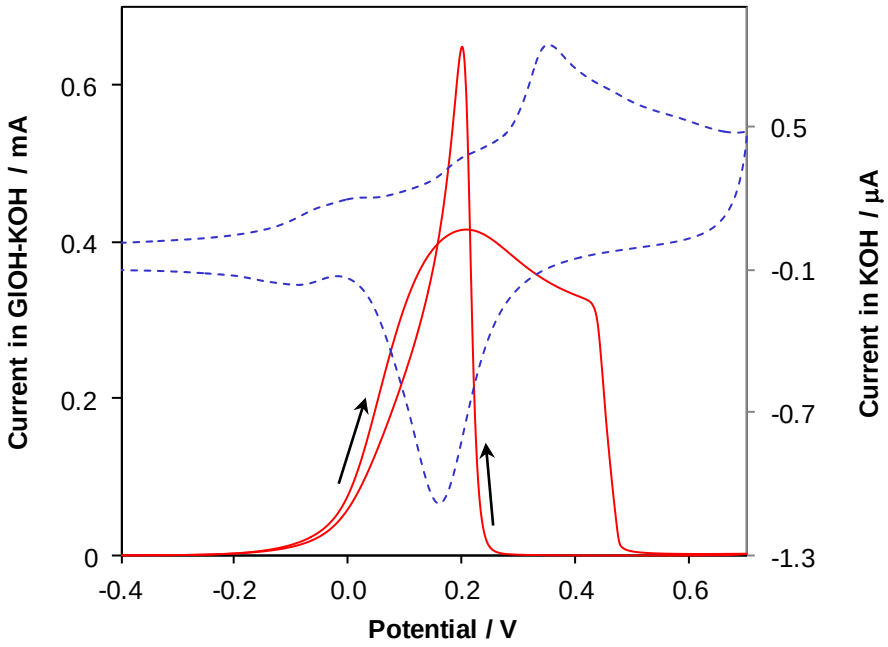


***Figure 7. CVs of polycrystalline gold in 0.5 M glycerol/1 M KOH at 10 mV $s^{-1}$ (solid curve) and 1 M KOH at 50 mV $s^{-1}$ (dashed curve)***

For investigations into the oxidation of glycerol as well as other alcohols, catalyst activity is typically reported using the peak current from the forward sweep of the CV [48, 64, 109, 110], while the catalyst's resistance to poisoning from alcohol oxidation intermediates is determined by the forward/reverse peak current ratio ($I_f/I_r$) [111-113]. For bulk gold, the reverse peak current is larger than the forward peak current (Figure 7), giving an $I_f/I_r$ ratio of < 1; which indicates poor oxidation of the alcohol in the forward sweep, as well as poor resistance to poisoning residues on the electrode surface [111, 113].

# 3 OPTIMISATION OF ELECTROCHEMICAL TESTING METHODOLOGY

## 3.1 Introduction

Prospective fuel cell catalysts are initially tested by investigating only the half-cell reaction for which the catalyst is being developed – in this instance, the electrooxidation of glycerol. A 3-electrode cell is usually set up so that the potential of the working electrode (incorporating the catalyst) is controlled relative to the potential of a reference electrode and the current is measured between the counter and working electrode.

There was quite a large amount of optimisation work that had to go into ensuring that accurate, repeatable and reproducible electrochemical measurements were obtained using such a set-up, and the more pertinent aspects of this are covered here.

Since this section deals with the optimisation of the electrochemical testing parameters and not the activity of the catalysts, the catalyst synthesis methods are only covered in the following chapters. Furthermore, results given here were often generated in partially optimised testing conditions and may therefore differ from results shown in the following chapters – the latter being obtained only after the testing procedure had been finalised.

## 3.2 Experimental

In order to test the supported nano-gold catalysts, the catalyst powders had to be deposited as thin layers onto an electrode. Titanium disc, glassy carbon rod (GCE) and glassy carbon plate (GCP) electrodes were used as substrates for the catalyst powders. In addition to the nano-gold catalysts, tests were also carried out on a 0.5 mm polycrystalline gold electrode.

Before first use, the treatment for the polycrystalline gold electrode and substrate electrodes (i.e. titanium disc, GCE and GCP electrodes) was as follows:

The electrode was mechanically polished using $Al_2O_3$ suspensions in the order of decreasing $Al_2O_3$ particle size (1, 0.3 and 0.05 μm), to remove any surface impurities and create a clean, flat surface for testing. The electrode was ultrasonicated in a fresh 1:1 isopropanol (IPA):$H_2O$ solution after each mechanical polish, so as to remove any residual $Al_2O_3$ particles. For the polycrystalline gold electrode, a final electropolishing treatment was carried out in 1 M KOH by cycling the electrode between -1 and 1 V (*vs*. Hg/HgO) for 20 cycles at a scan rate of 200 mV $s^{-1}$. For the titanium and glassy carbon electrodes, it was sufficient to use only 0.05 μm $Al_2O_3$ thereafter, to maintain the surface of those electrodes between experiments.

For electrochemical testing of the catalysts (gold nanoparticles synthesised by reduction with borohydride [114], followed by deposition onto Vulcan XC-72R carbon), the catalyst powder was dispersed in a solution of Nafion (LIQUion solutions – Ion Power, Inc.) which had been pre-diluted in 4:1 IPA:$H_2O$ (except for drop-coating onto GCEs, where the Nafion solution was diluted only in $H_2O$ – discussed later). The amount of Nafion added into the dispersion was 10 wt % of the catalyst mass. The mixture was then diluted with enough 4:1 IPA:$H_2O$ solution (only $H_2O$ for GCEs) to yield a final catalyst concentration of 1 mg $ml^{-1}$ for drop-deposition onto GCEs and GCPs. The dispersion was ultrasonicated for 30 min to ensure good mixing before spray- or drop-coating of the electrode (except for GCEs – discussed later). For spray-coating onto titanium discs and GCPs, a final catalyst loading of 1 mg $cm^{-2}$ was aimed for, while for drop-coating onto GCEs and GCPs, a 10 µl drop was pipetted onto the electrode, giving a catalyst loading of 10 µg on the substrate electrode. A generalised schematic of the procedure for preparing a catalyst-coated electrode (applicable mainly to GCP and titanium disc electrodes) is shown in Figure 8.

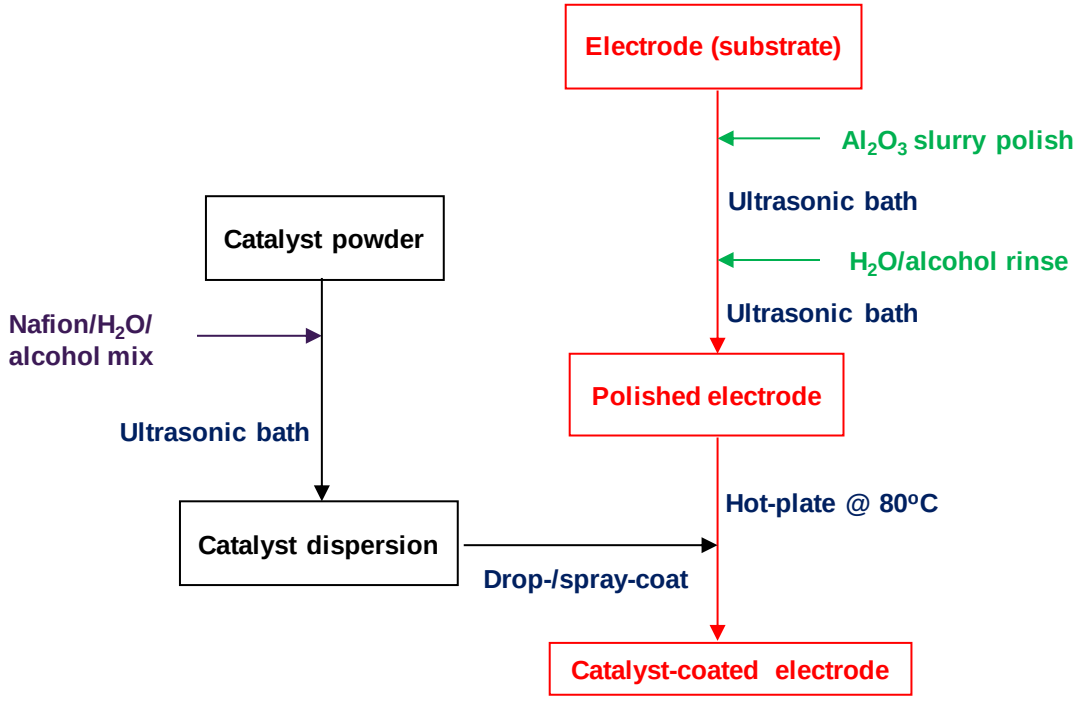


***Figure 8. Generalised flow-diagram for preparation of catalyst-coated electrode for electrochemical testing.***

Electrochemical measurements were run in a standard 3-electrode PTFE cell with a Hg/HgO, 1 M KOH reference electrode (or saturated calomel electrode (SCE) in acid) and a ~ 6 $cm^2$ platinum counter electrode, using a Gamry Reference 600 potentiostat. Gamry Echem Analyst Version 5.63 software was used for analysis of the electrochemical data.

Most of the electrochemical testing optimisation was carried out on a 19 wt % Au/C catalyst with average gold diameter ($d_{ave}$) of 5.0 nm (fully characterised in Chapter 4). A few of the tests reported in

this section were also carried out on 20 % Au/C ($d_{ave}$ 4.0 nm) and 7.5 % Au/C ($d_{ave}$ 3.9 nm) catalysts (fully characterised in Chapters 5 and 6, respectively).

## 3.3 Results and discussion

### 3.3.1 Electrochemical cell design

A number of cell designs were tested during the attempt to obtain accurate, repeatable and reproducible measurements. These are described briefly below. All cells were made of PTFE since glass can be corroded by strong basic solutions.

In the first cell (EC1), the working electrode was created by spray-coating 12.7 mm diameter titanium discs with the catalyst dispersion over a hot-plate at 80$^{o}$C. A catalyst-coated disc was then fitted into the bottom of a PTFE cell over a silicon o-ring which was used to create a seal and to expose only a small section (7 mm diameter) of the working electrode to the solution. Electrical contact was made with a stainless steel plate placed over the electrode and screwed into the cell. The counter and reference electrodes were inserted from the top, though the lid (Figure 9). However, numerous problems were experienced with this set-up, which included very high overpotentials for glycerol oxidation, which increased with each subsequent scan (indicating increasing resistance during cycling), and the catalyst layer often peeling off the titanium surface during electrochemical scanning or between KOH- and glycerol- solution changes.

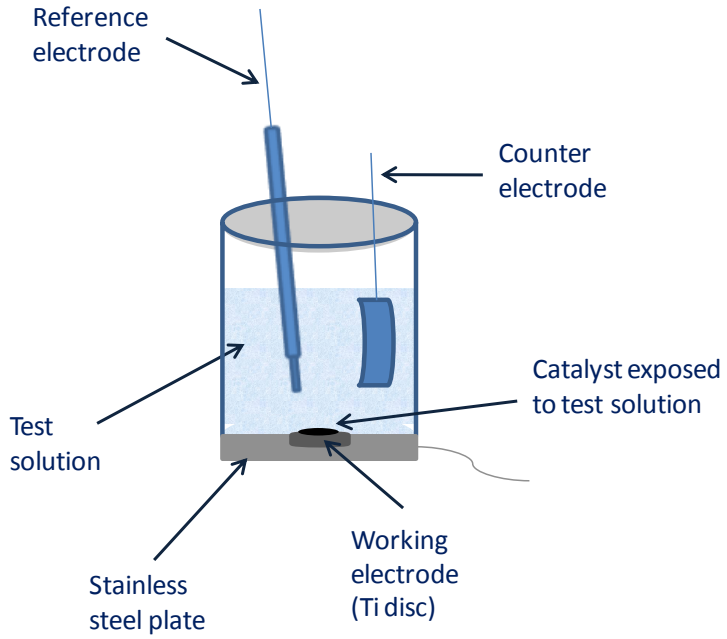


***Figure 9. Diagram of first electrochemical cell (EC1).***

The second electrochemical cell (EC2) is one commonly encountered in literature, and used a working electrode which consisted of a glassy carbon rod (3 mm diameter) embedded into a PTFE cylinder (Figure 10). In order to ensure a tight, leak-proof seal without the possibility of solution contamination from any glue or binder, the glassy carbon rods were pushed into PTFE cylinders

which had been drilled out to an inner diameter of 15 % less than the diameter of the rods. A stainless steel wire inserted into the PTFE cylinder from the top was bonded to the glassy carbon rod using silver epoxy for electrical contact and non-conductive epoxy was used at the top of the cylinder to hold the stainless steel wire in place. A commercial 3 mm electrode (BASi MF-2012) was also tested to compare with the ones made in-house. Initial attempts to drop-coat the catalyst/Nafion/IPA/$H_2O$ dispersion onto the exposed glassy carbon surface of the GCEs were unsuccessful, as the droplet spread out and most of the catalyst ended up on the surrounding PTFE. This was discovered to be caused by the IPA reducing the surface tension of the droplet, resulting in spreading of the dispersion across the whole surface of the electrode. In order to avoid this, the catalyst and Nafion were then dispersed only in $H_2O$ before deposition. While this method worked in keeping the droplet only on the glassy carbon surface, it had several disadvantages. Because of the hydrophobic nature of the Vulcan XC-72R carbon, wetting of the catalyst took much longer without the IPA. The catalyst only dispersed properly in solution after a treatment which consisted of ultrasonication for 20-30 min, then being left to soak overnight, followed by further ultrasonication the next day. Then, once the GCEs had been drop-coated, they had to be left to dry – which took longer because of the lack of IPA in the dispersion. The entire process was therefore time-consuming, taking at least a day, and often the dried catalyst dispersion on the electrode did not form an even layer. In addition, the catalyst layer was not always stable on the electrode and sections of the layer would sometimes fall off the electrode during electrochemical scanning. These problems were encountered with both the commercial electrode and those made in-house, which caused huge errors in repeatability measurements.

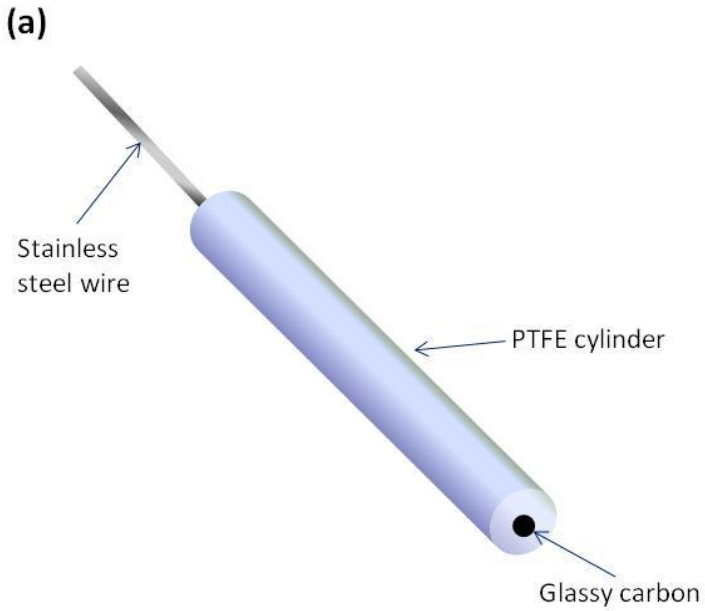

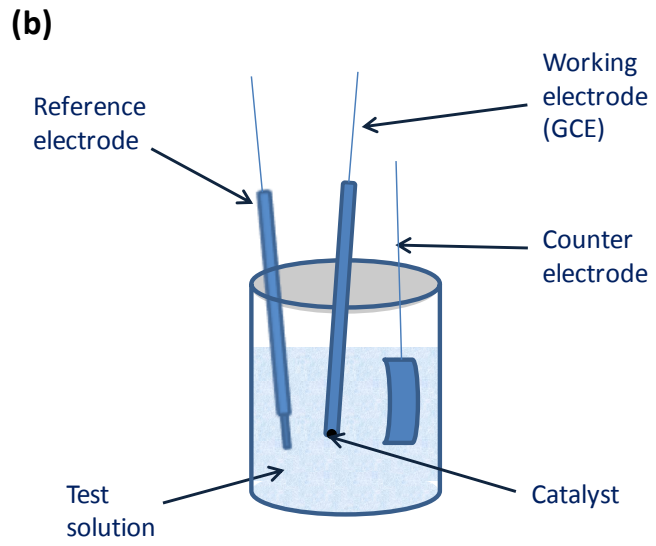


***Figure 10. (a) Diagram of glassy carbon rod electrode (GCE) – the catalyst of interest is drop-coated onto the surface of the glassy carbon; (b) Cell design EC2 with GCE working electrode.***

For the third cell design (EC3), it was decided to revert to the spray-coating technique, but using glassy carbon plates (Grade 11; 25 x 25 x 1 mm - SPI® Supplies) instead of titanium discs. Since this could be done over a hot-plate at 80$^{o}$C and the catalyst could again be dispersed in a solution containing IPA, the procedure was far less time-consuming and the catalyst layer was found to adhere more firmly to the glassy carbon plate than to the titanium disc. A new electrochemical cell was then designed, similar in all respects to the first cell, but with the working electrode fitted into the side of the PTFE cell, instead of at the bottom (Figure 11). An o-ring defined an electrode diameter of 4.3 mm to be exposed to the solution. However, there appeared to be significant mass transport problems with this cell and the lowest catalyst activities were obtained with this set-up. In addition, the uncompensated resistance ($R_u$) was much higher than for any of the other cell designs (57 Ω), which made electrochemical measurements very difficult (refer to section 3.3.5).

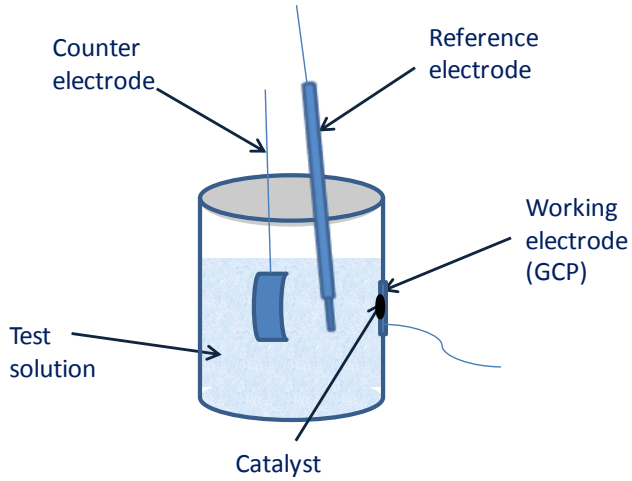


***Figure 11. Diagram of third electrochemical cell (EC3).***

For the final cell design (EC4), it was then decided to combine the positive aspects of the different techniques and cell designs which had thus far been attempted, while trying to address the problems of poor mass transport, high $R_u$ and unstable catalyst layers. This was achieved by drop-deposition of the catalysts onto the GCPs which had been used in the third cell design. A catalyst dispersion consisting of 1 mg $ml^{-1}$ catalyst and 10 % Nafion:catalyst loading in 4:1 $H_2O$ was ultrasonicated for 30 min, followed by the casting of 10 µl drops of catalyst dispersion onto several GCPs over a hot-plate at 80$^{o}$C. Unlike the 3 mm GCEs, the catalyst was not limited by the area of the GCP surface and was able to spread out on the electrode (typically to a diameter of 1-1.5 cm) for optimum exposure of the catalyst surface. Drop-casting over a hot-plate enabled the Nafion to set and fix the catalyst securely to the glassy carbon surface. With this method, the problems experienced with the GCEs where the catalyst layer often dropped off the electrode, was resolved. For electrochemical testing, the GCP was submerged approximately two-thirds of the way into the solution, so that the catalyst layer was fully submerged in the solution. An alligator clip which had been modified by filing the ends of the clip and soldering flat copper strips onto the ends, was then inserted through the lid and clipped onto the GCP for electrical contact. The reference and counter electrodes were inserted in close proximity (< 2 cm) to the GCP. The lowest $R_u$ values were obtained with this cell design, generally ranging from 1.0 – 2.2 Ω. A schematic of the final, optimised cell design is shown in Figure 12.

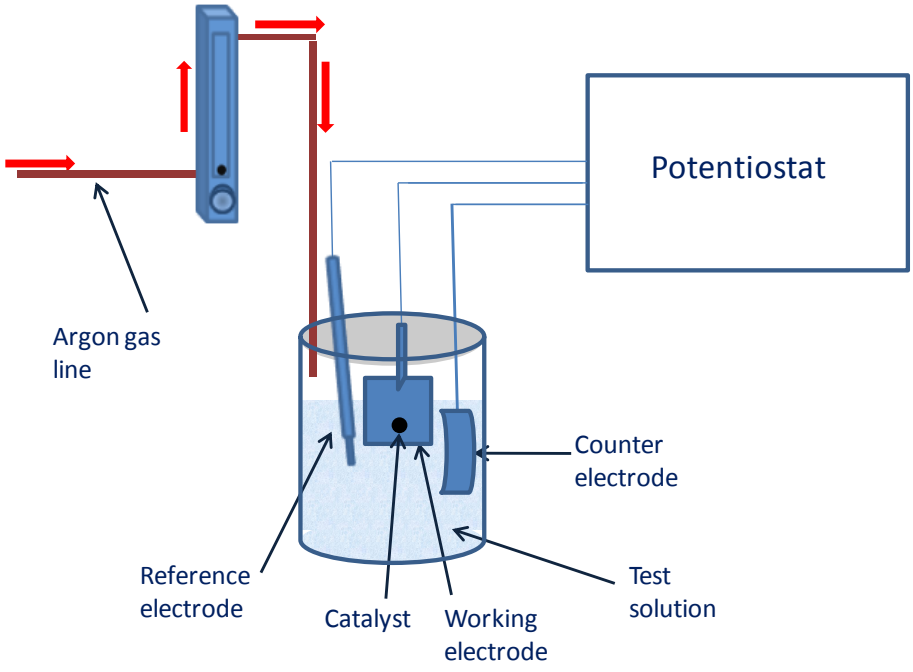


***Figure 12. Electrochemical set-up including optimised cell design (EC4)***

Importantly, the currents obtained with the optimised cell design were much higher for the same catalyst (19 % Au/C) tested in the various cells (Figure 13), indicating that the catalyst had significantly better exposure to the solution in EC4. Supporting data for Figure 13 and typical glycerol oxidation curves obtained in the various electrochemical cells are shown in Appendix 3.1.

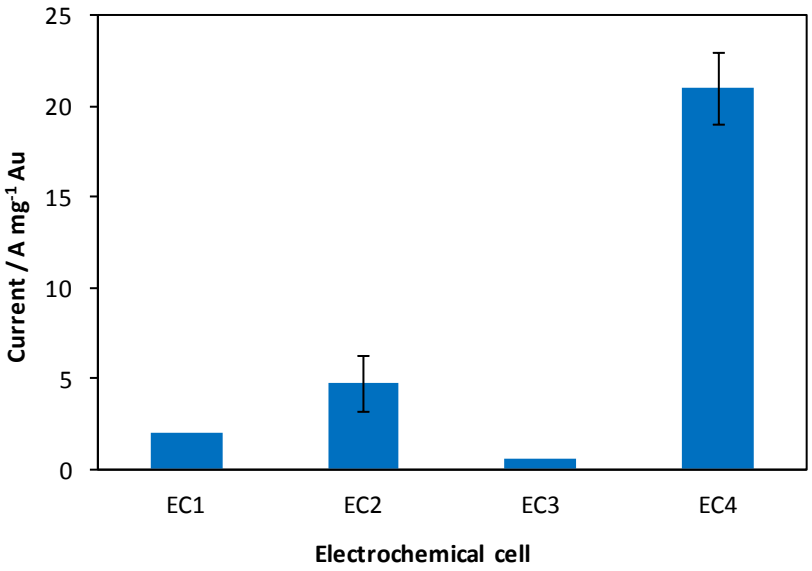


***Figure 13. Comparison of mass activity of 19 % Au/C for glycerol oxidation in different electrochemical cells. Activities are calculated from peak currents measured from forward sweep of CV in 0.5 M glycerol/1 M KOH solution at 50 mV $s^{-1}$.***

### 3.3.2 EASA determination of gold-based catalysts

In order to identify the conditions for activation of the gold surface on supported nano-gold catalysts, it first needed to be fully investigated over polycrystalline gold. Scans were therefore initially carried out on polycrystalline gold in 1 M KOH, to identify the gold oxidation/reduction regions, as well as to determine the conditions for EASA determination of the gold surface.

The onset potential for monolayer oxide formation on gold in 1 M NaOH was shown to occur at 1.25 V *vs*. RHE) [106]. This should therefore occur in 1 M KOH at approximately 0.3 V *vs*. Hg/HgO (Appendix 3.2) and the major oxidation peak was found to start at a similar potential (Figure 14). The oxidation peaks occurring at lower potentials are attributed to the premonolayer oxidation of gold, resulting in the formation of catalytically active hydrous gold oxides, while the increase in current occurring after oxide monolayer formation is attributed to early oxygen evolution catalysed by hydrous gold oxides formed at the monolayer/solution interface [106].

The reduction peak at 0.15 V is considered to be the oxide monolayer reduction peak [98, 106], which (as discussed in Chapter 2) is commonly used to determine the EASA of gold. A second reduction peak at -0.08 V is also evident, which also increased in magnitude upon scanning to a higher potential. This second peak is said to be due to the reduction of hydrous gold oxides which form at higher potentials and was not observed in an acidic medium ([106]; Appendix 3.3).

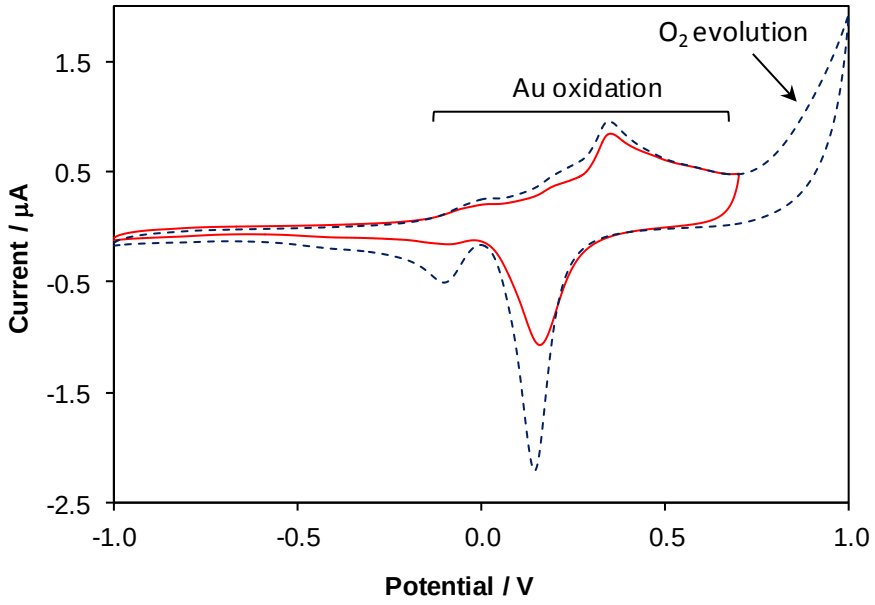


***Figure 14. CVs of polycrystalline gold in 1 M KOH scanned at 50 mV $s^{-1}$ to anodic limits of 0.7 V (red curve) and 1.0 V (blue curve). Potentials are shown vs. Hg/HgO reference.***

The EASA value is determined from integration of the oxide monolayer reduction peak, but from Figure 14 it was clear that the peak at 0.15 V cannot be regarded as a true monolayer peak, as it changes depending on the applied upper potential limit. For this reason, it has been reported that it is difficult to determine the potential at which formation of a complete monolayer of oxide occurs [97] and it was stated by Woods [98] that the real surface area of gold can only be estimated. Woods suggested that holding a gold electrode at 1.8 V (*vs*. RHE) for 100 s in 1 M $H_2SO_4$ would give an approximate monolayer of oxygen on the gold surface. This is by no means the standard used by other researchers, and gold EASA has also been determined in both acid and base, by integrating the oxide reduction peak from CV scans [35, 115-117]. The upper potential limit used by researchers has been seen to vary, but one accepted limit is the potential corresponding to the current minimum just before oxygen evolution [115] – which is approximately 0.7 V in Figure 14. To further add to the uncertainty of this technique, it was found that the $Q_{theoretical}$ value can vary significantly from one researcher to the next, with some of the reported values being 386 [98], 482 [116] and 493 [35] µC $cm^{-2}$. The value of 386 µC $cm^{-2}$ was originally calculated based on a ratio of one oxygen atom per gold site for the Au(100) plane [98]. Values of 384, 444 and 272 µC $cm^{-2}$ have been reported for the Au (100), (111) and (110) planes respectively (supporting information in [118]), so it is likely that the larger values of 482 and 493 µC $cm^{-2}$ were calculated based on the Au(111) plane. It has also sometimes been assumed that the low-index planes have equal distribution on a polycrystalline metal surface [98], for which the values in reference [118] would give an average of 367 µC $cm^{-2}$ – which is close to the value for Au(100).

Since gold nanoparticles oxidise more readily than polycrystalline gold (shown later in Chapter 5), it had to be accepted for EASA determination of gold nanoparticles, that oxide monolayer formation

might occur sooner on these particles. Further complications could also arise from the possibility of gold nanoparticles of varying sizes demonstrating oxide monolayer formation at varying potentials, and possible masking of the gold oxide peaks caused by oxidation of the glassy carbon surface at higher potentials. However, considering the already inexact nature of the EASA measurements on polycrystalline gold, it was decided to adhere to a standard range of potentials for all catalysts tested, as well as for polycrystalline gold. This consisted of cycling the electrode between -0.4 and 0.7 V (*vs*. Hg/HgO) in 1 M KOH and determining the EASA by means of integration of the oxide reduction peak using Woods' [98] value of 386 µC $cm^{-2}$. It was also confirmed by comparing the CVs of a GCP with and without a 19 % Au/C catalyst, that the capacitive charging of the glassy carbon surface was not masking the gold oxide reduction peak at 0.1 V (Figure 15).

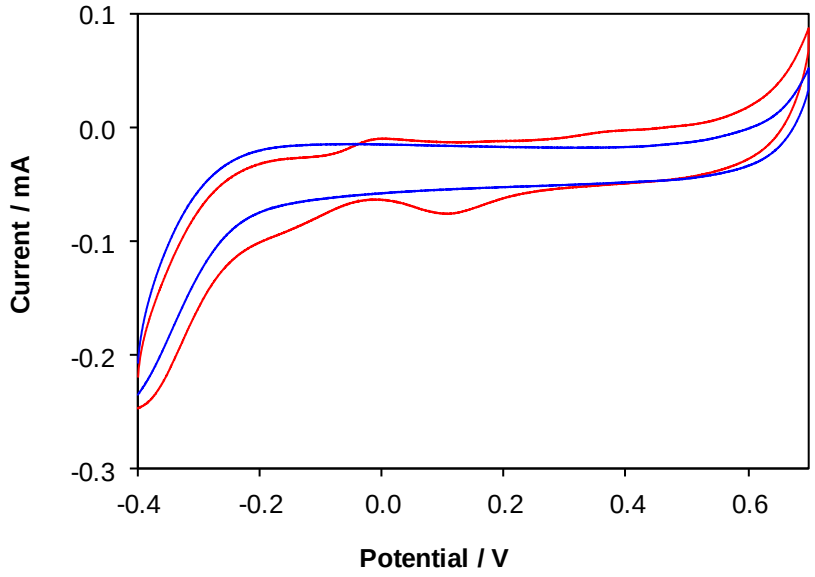


***Figure 15. CVs of clean GCP (blue curve) and 19 % Au/C deposited on GCP (red curve) in 1 M KOH at 50 mV $s^{-1}$. Potentials are shown vs. Hg/HgO reference***

The alternative methods of gold EASA determination were also considered, *viz*. the underpotential deposition (UPD) of lead, copper or thallium. However, since it has already been shown that no thallium UPD region exists for small (10 nm) gold particles [99], this method was not an option for this project.

Lead UPD is a very useful method as not only can it provide EASA determination, but it can also be used to identify low-index surface facets, and it has also been shown that lead UPD occurs on gold nanoparticles ($d_{ave}$ 3.7 - 4.8 nm) [103]. However, when applied to the carbon-supported gold catalysts, it was found that bulk lead deposition occurred on both the Vulcan carbon support and the GCP electrode, to the extent that it masked the lead UPD region. A similar finding of lead overpotential deposition (OPD) occurring on both the support (MWCNT) and electrode (basal plane pyrolitic graphite) has been reported in literature [99]. It was therefore not possible to utilise this technique for the Au/C catalysts.

Hickey and Riley [100] have shown that copper UPD can be used for EASA determination of 15 nm gold colloids, and that unlike the gold oxide reduction method, this is a true UPD process. This was confirmed by comparing polycrystalline gold scanned to cathodic limits of 0 V (just before bulk copper deposition) and -0.2 V (just after bulk copper deposition) *vs*. SCE (Figure 16). It was clear that scanning to lower potentials did not significantly impact the size of the copper UPD stripping peak, from which EASA is determined. Integrations of the copper UPD stripping peaks for both potential limits gave similar EASA values and roughness factors, but were less than half that obtained by integration of the gold oxide reduction peak scanned from an upper potential limit of 0.7 V (Table 2, Appendix 3.4). The EASA value for copper UPD was calculated using a $Q_{theoretical}$ value of 430 µC.cm$^{-2}$ [100].

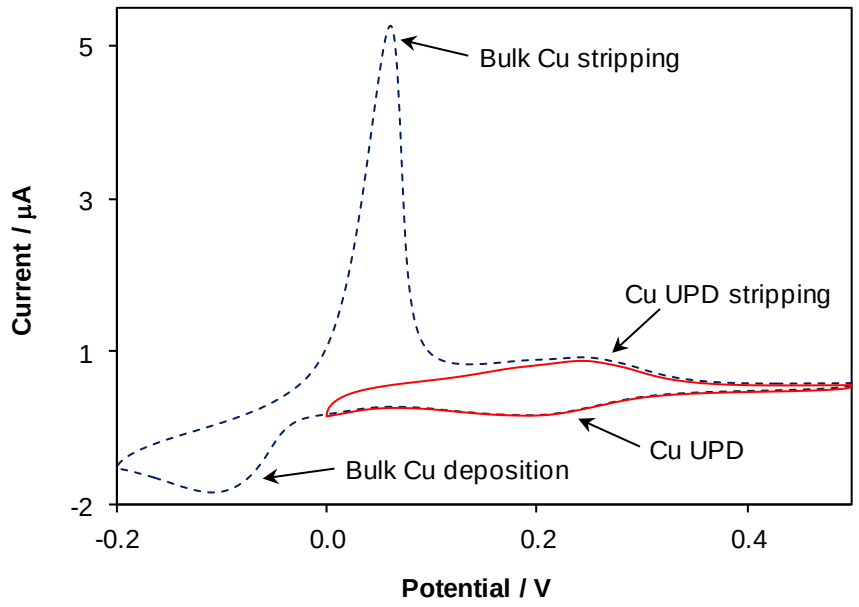


***Figure 16. CV of polycrystalline gold in 3 mM $CuSO_4$/0.1 M $H_2SO_4$ solution, scanned at 50 mV $s^{-1}$ to cathodic limits of 0 V (red curve) and -0.2 V (blue curve). Potentials are referenced vs. SCE.***

***Table 2. EASA and roughness factors for 0.5 mm polycrystalline gold electrode calculated from oxide reduction and copper UPD techniques.***

| EASA determination method | Integrated peak charge / *µC* | Monolayer charge / *µC cm $^{-2}$* | EASA / *cm$^2$* | Geometric surface area / *cm$^2$* | Roughness factor |
|---|---|---|---|---|---|
| Oxide reduction | 2.381 | 386 | 6.17E-03 | 1.96E-03 | 3.1 |
| Cu UPD – scanned to 0 V | 1.019 | 430 | 2.37E-03 | 1.96E-03 | 1.2 |
| Cu UPD – scanned to -0.2 V | 1.133 | 430 | 2.63E-03 | 1.96E-03 | 1.3 |

Based on the roughness factors obtained for polycrystalline gold, copper UPD initially appeared to be a more accurate method to use. This method was then applied to the 19 % Au/C catalyst. There was a clear copper UPD profile for this catalyst, which could be attributed to copper UPD on gold only, since this feature was not observed for the carbon support (Figure 17).

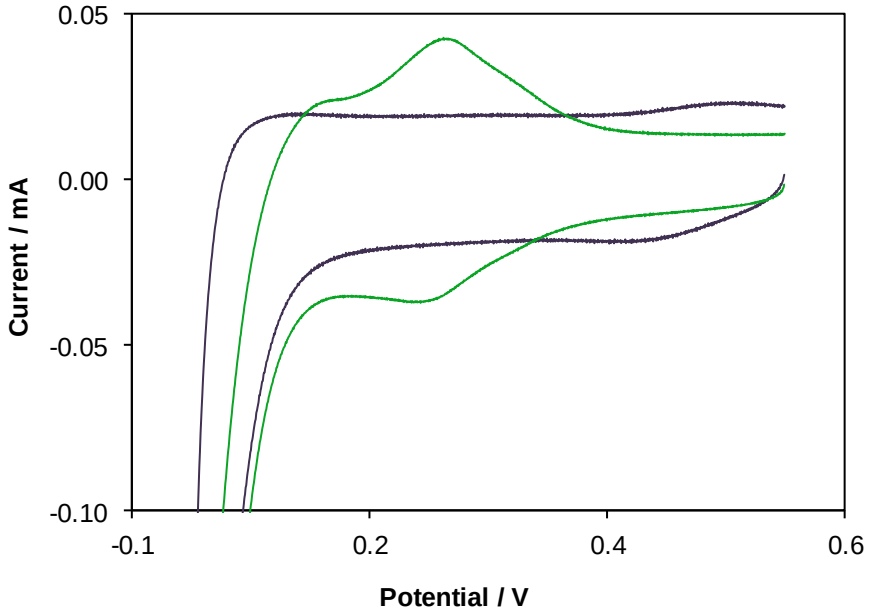


***Figure 17. CVs of 19 % Au/C catalyst (green curve) and carbon support (blue curve) in 3 mM $CuSO_4$/0.1 M $H_2SO_4$ solution, scanned at 50 mV $s^{-1}$. Potentials are referenced vs. SCE.***

It was noticed that as with lead, bulk copper deposition occurred on the glassy carbon electrode (Appendix 3.5) and possibly the Vulcan carbon support. However, in this instance the copper UPD region was distinct from the OPD region. In order to prevent the possibility of any residual deposited copper from influencing the glycerol oxidation results and also because the copper UPD determination method had to be carried out in an acidic medium, EASA determination using copper UPD was only done after the scans in 1 M KOH and 0.5 M glycerol/1 M KOH solutions. The assumption was made that the catalyst surface area had not been significantly changed by the previous scans.

Unlike the gold oxide reduction peak, there was no clear baseline from which the copper UPD region could be integrated. Attempts to use the CV generated in 0.1 M $H_2SO_4$ solution as a baseline were unsuccessful, as the curve cut into the copper UPD region (Figure 18). This gave half the charge value compared with integration using an extension of the straight section of the curve at the upper potential region as a baseline (Appendix 3.6). It was therefore decided to integrate using the latter method.

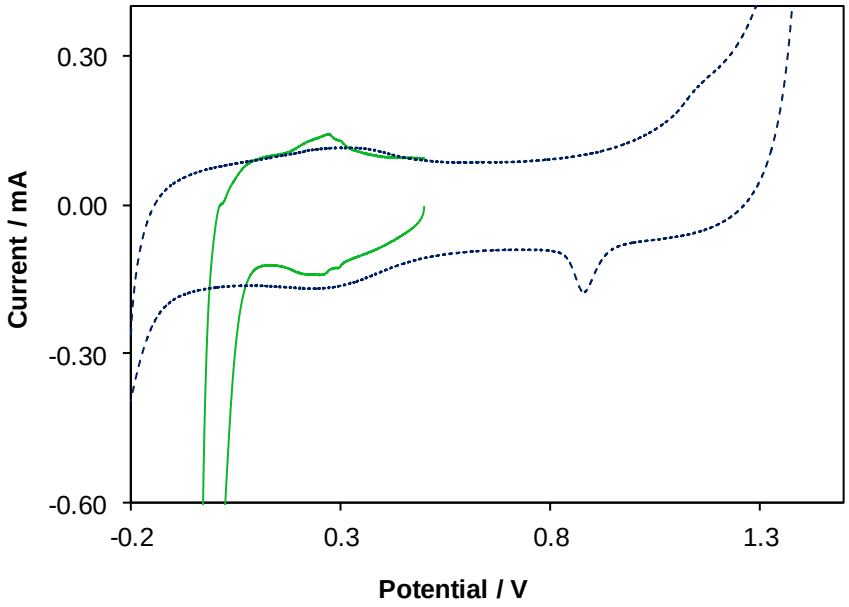


***Figure 18. CVs of 20 % Au/C in 3 mM $CuSO_4$/0.1 M $H_2SO_4$ (green curve) and 0.1 M $H_2SO_4$ (blue curve), scanned at 50 mV $s^{-1}$. Potentials are referenced vs. SCE.***

EASA was calculated for a number of catalysts using both copper UPD and oxide reduction. In some instances, good agreement was obtained between the two methods – an example of which is shown in Table 3 (with detailed information in Appendix 3.7).

***Table 3. Comparison of average EASA obtained for 20 % Au/C using gold oxide reduction and copper UPD methods.***

| EASA determination method | EASA / $m^2$ $g^{-1}$ |
|---|---|
| Oxide reduction in 1 M KOH | 16.0 ± 0.7 |
| Oxide reduction in 0.1 M $H_2SO_4$ | 12 ± 3 |
| Cu UPD in 3 mM $CuSO_4$/0.1 M $H_2SO_4$ | 14 ± 1 |

However, using copper UPD as an EASA determination method was often problematic, due to the difficulties outlined above. In addition, the lower gold surface areas on catalysts with larger supported gold particles or lower gold loadings resulted in large errors in repeatability measurements. For these reasons and also because integration of the oxide reduction peak was more straightforward, it was ultimately decided to report the catalysts' specific activities (in mA $cm^{-2}$) based on the peak charges obtained from gold oxide reduction in KOH.

Finally, an alternative option for reporting catalyst specific activities was to forgo the EASA determination method altogether and to instead normalise currents by the gold surface area determined from TEM analysis [119]. As will be seen in the following chapters, catalysts' specific

activities were calculated and compared, where possible, using gold surface area values calculated from both EASA- and TEM- measurements.

### 3.3.3 Electrochemical cleaning/stripping

Nafion, the proton-exchange membrane commonly used in PEMFCs, is also available commercially in solution form, making it a convenient binder for testing of catalysts in both fuel cells and electrochemical cells. However, for alkaline media, soluble hydroxide-conducting polymers are not readily available commercially – resulting in researchers either synthesising their own, using anionic polymers still in development or alternatively using readily available polymers such as PTFE or Nafion [120]. While it is clearly not ideal to use neutral polymers or cation-exchangers as binding agents for testing catalysts in an alkaline medium, current anionic alternatives are not necessarily better. For example, Li, *et al*. [121] demonstrated that a commercially available anion-conducting polymer blocked catalyst sites by forming a dense coating over the catalyst, while the neutral PTFE polymer formed a porous coating, resulting in improved cell performance with the latter polymer. With this in mind, it was therefore decided to use Nafion as a binder for the purposes of testing the catalysts in an electrochemical cell. The concentration of Nafion was kept low at 10 wt % of the catalyst mass, so that there was enough Nafion to act as a "glue" to fix the catalyst to the electrode, but not enough to seriously impact the exposure of the catalyst to the solution.

Since blocking of surface sites by Nafion has been reported on platinum black, Pt/Ru black and Pt/Pd [122], the effect of Nafion on the supported gold catalyst was investigated by comparing the EASA of unsupported precursor gold colloids ($d_{ave}$ 3.2 nm [114]) with the 19 % Au/C catalyst. The colloids were deposited onto the glassy carbon surface and left to dry before being tested in the electrochemical cell.

As with the PGM catalysts, it was found that Nafion blocked gold sites on the catalyst – but it was also found that introducing cycles (referred to hereafter as "cleaning" or "strip" cycles) over a wider potential range (-0.9 → 0.8 V *vs*. Hg/HgO) prior to evaluation of EASA of the catalyst, resulted in similar EASA values to the unsupported gold colloids (Figure 19, Appendix 3.8). Five strip cycles were seen to be sufficient for the supported Au/C catalyst. It was also noted that the unsupported colloids were not as stable as the Au/C catalyst, with larger variations in measured EASA and a lower EASA value after 5 strip cycles, than the Au/C catalyst. This confirms the importance of stabilising the gold colloids by some means – as in this case, on the carbon support.

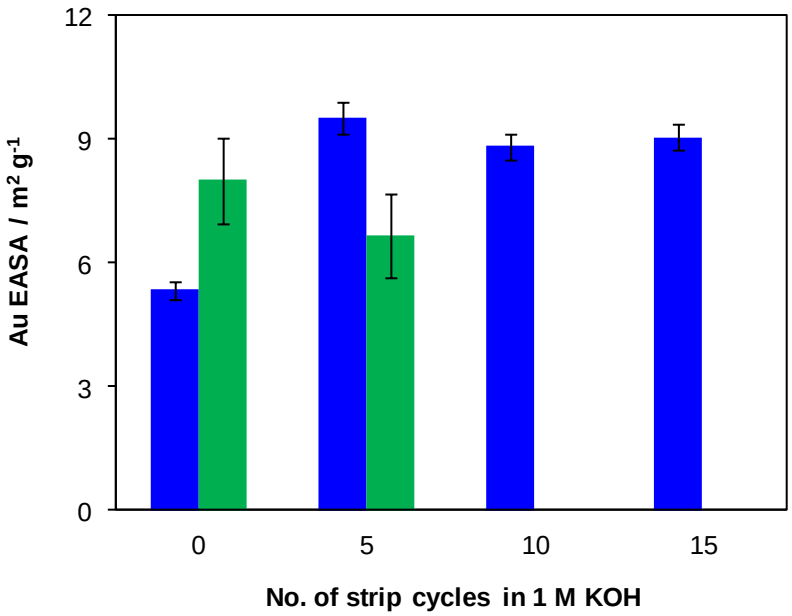


***Figure 19. Effect of electrochemical cleaning/stripping on gold EASA for 19 % Au/C catalyst dispersion with 10 % Nafion loading (blue columns) and precursor gold colloids (green columns).***

It was also considered essential to have the electrochemical stripping step as part of the testing procedure in the likelihood of there being any remaining colloid-stabilising ligands on the carbon-supported gold nanoparticles. The use of colloids to prepare catalysts is a convenient way of ensuring that the metal nanoparticles are of similar size. However, the ligands can potentially block the active sites of the catalyst and conventional techniques for removal of such ligands, such as heating and (chemical) oxidation, can be problematic in that they can change the size and shape of the nanoparticles [123]. It was therefore hoped that if there were any remaining gold colloid-stabilising ligands, these could be oxidised electrochemically without affecting the stability of the nanoparticles.

### 3.3.4 Pre-soaking of catalyst layer

Over the course of testing catalysts, large inconsistencies in repeatability measurements were sometimes apparent. These were found to be related to the varying degrees to which the catalyst layer was wetted in the electrolyte solution – likely due to the hydrophobicity of the Vulcan carbon support. Since this indicated inadequate exposure of the catalyst to the electrolyte solution, pre-soaking of the catalyst in the electrolyte was therefore investigated. This consisted of holding the electrode at a low potential (-0.2 V *vs*. Hg/HgO) for a required amount of time, before carrying out the electrochemical stripping and EASA determination scans. While pre-soaking alone did not improve on the EASA obtained using electrochemical stripping, the combination of both pre-soaking and stripping was found to double the gold EASA value (Figure 20, Appendix 3.9). A soaking period of 10 min was found to be sufficient when combined with electrochemical stripping.

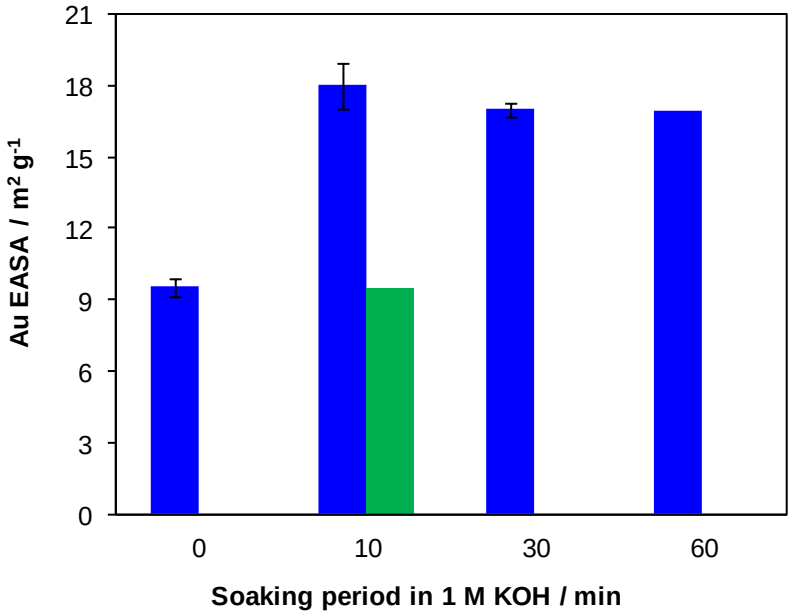


***Figure 20. Effect of soaking time on EASA of 19 % Au/C catalyst. Blue columns represent tests for which 5 strip cycles were carried out after soaking, while green column represents 10 min soak only.***

A comparison of electrochemical pre-treatment conditions in 1 M KOH on subsequent glycerol oxidation (Figure 21, Appendix 3.10) showed negligible difference in gold mass-based activities (i.e. independent of measured gold surface area) between no pre-treatment, electrochemical stripping and the combination of soaking and stripping (the last treatment also included a 10 min pre-soak in glycerol at -0.2 V *vs*. Hg/HgO). This is most likely because glycerol is an alcohol and can therefore assist in lowering the surface tension of the aqueous-based electrolyte solution, resulting in effective wetting of the catalyst surface. The increase in EASA as a result of increased exposure of the gold surface with each electrochemical pre-treatment condition is reflected in the decrease in calculated specific activities of the catalyst (green columns in Figure 21).

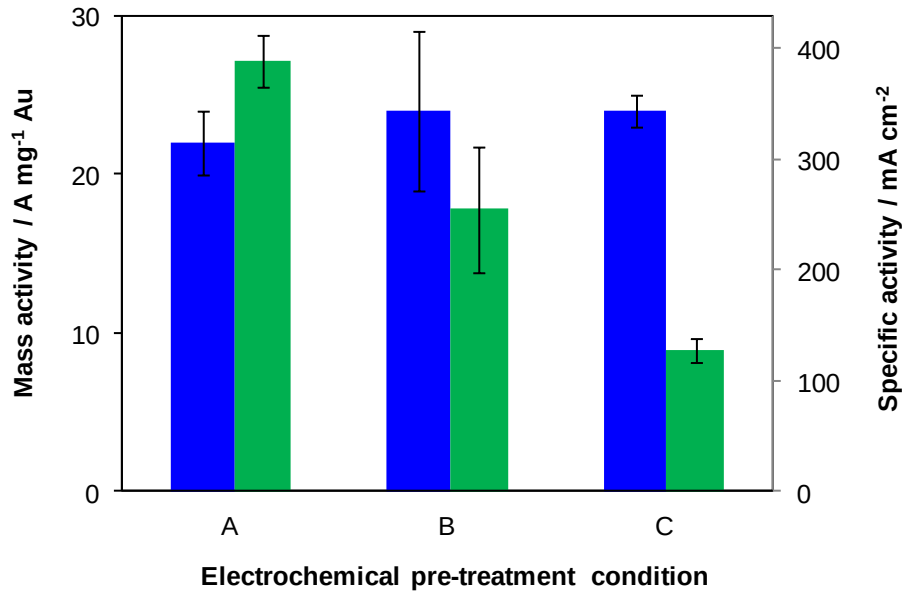


***Figure 21. Mass activities (blue columns) and specific activities (green columns) of 19 % Au/C catalyst as a function of various electrochemical pretreatment conditions, where A = no soak or strip, B = no soak + 5 strip cycles and C = 10 min soak + 5 strip cycles. Activities are calculated from peak currents measured from forward sweep of CV in 0.5 M glycerol/1 M KOH solution at 50 mV $s^{-1}$.***

### 3.3.5 Uncompensated resistance correction

In the final cell design, despite the $R_u$ values being relatively small, it was deemed necessary to carry out an ohmic correction in order to compensate for the potential drop caused by the high glycerol oxidation currents which were achieved over the gold catalysts.

$$E_{actual} = E_{applied} - I*R_u \quad (9)$$

A positive feedback (PF) compensation of 75 – 95 % of the measured $R_u$ value is recommended by the Gamry instrument suppliers. However, application of 80 % PF compensation was observed to sometimes cause the potentiostat to oscillate, so it was therefore decided to apply a standard PF correction of 0.5 Ω (maximum 50 % compensation) during the electrochemical scans. The remainder of the resistance was corrected for, using the post-run IR correction option in the Gamry software.

### 3.3.6 Overall procedure for testing of gold-based catalysts

Taking into consideration the various experimental conditions discussed in this chapter, the finalised electrochemical testing methodology for each catalyst was as follows (all potentials referenced *vs.* Hg/HgO):

a) <u>1 M KOH</u>

- A 10 min pre-soak at a constant potential of -0.2 V
- 5 strip/cleaning cycles from -0.9 → 0.8 V at 50 mV $s^{-1}$
- 5 cycles from -0.4 → 0.7 V at 50 mV $s^{-1}$ for EASA determination

b) 0.5 M glycerol/1 M KOH

- A 10 min pre-soak at a constant potential of -0.2 V
- Typically 5 cycles from -0.4 → 0.7 V at 10 mV $s^{-1}$
- Any additional electrochemical tests which may be required, e.g. potentiostatic measurements, EIS, etc (discussed in following chapters).

The optimised electrochemical cell and test procedure gave confidence not only in the accuracy and reproducibility of the results reported within this body of work, but also the assurance (since further changes to the test procedure did not result in any further increases in activity) that maximum exposure of the catalyst surface was being achieved. However, it should be noted that this could make direct comparisons with results reported in literature difficult – as there is no guarantee that if better activities are reported here, that it is due purely to the catalysts and not also the result of the optimised electrochemical testing method. In other words, there is no way of knowing if the catalyst activities reported by other researchers are the maximum possible activities that can be obtained over their catalysts. It would therefore be a good idea for a standardised test procedure to be adopted by the electrocatalyst community, in order to ensure that accurate comparisons can be carried out.

# 4 INVESTIGATIONS INTO $MnO_2$ AS A SUPPORT/CO-CATALYST FOR GOLD

## 4.1 Introduction

As discussed in Chapter 2, the addition of metal oxides to PGM-based catalysts has improved the activity and/or stability of these catalysts for alcohol electrooxidation reactions. The addition of manganese oxides as co-catalysts for the electrooxidation of a number of alcohols has been very favourably reported in the literature. For example, $MnO_2$ coated over a Pt-Ru/C catalyst improved the activity and stability of the catalyst for methanol electrooxidation [54], $Mn_3O_4$-promoted Pd/C was more stable than Pd/C catalysts promoted with other oxides for alcohol electrooxidation [64] and electrodeposited nano-MnOx improved both the activity and stability of platinum electrodes for methanol electrooxidation [124].

While manganese oxides have clearly benefited platinum- and palladium-containing catalysts, there did not appear to be any investigations into the effect of manganese oxide on a gold-based catalyst system for the electrooxidation of alcohols. Therefore, a systematic study was undertaken to investigate the effect of $MnO_2$-modification of Au/C catalysts, for the glycerol electrooxidation reaction.

## 4.2 Experimental

Ultra-pure de-ionised water (18.2 MΩ cm) was used in all preparation, synthesis, washing, electrochemistry and analysis procedures. ACS grade glycerol (≥ 99.5 %) and KOH (≥ 85 %) were sourced from Sigma-Aldrich.

### 4.2.1 $MnO_2$/C support

Because of its poor electrical conductivity [125, 126], $MnO_2$ was first deposited onto carbon black (Vulcan XC-72R) using an electroless deposition method [127], before deposition of the gold colloids. In this method, $KMnO_4$ is used to oxidise the carbon surface, while being simultaneously reduced and deposited onto the carbon as $MnO_2$.

5 g of carbon was stirred into 150 ml of water until well mixed. The appropriate amount of 0.625 M $KMnO_4$ stock solution was then added in and stirred for 1 h for 10 and 20 wt % $MnO_2$/C or 22-26 h for 30 and 40 wt % $MnO_2$/C. After the appropriate contact time, the solids were filtered, washed and dried overnight at 60$^{o}$C.

### 4.2.2 Gold deposition

Gold colloids were synthesised using a modified method of Martin, *et al*. [114]. 6.1 ml of 0.05 M gold solution (from $HAuCl_4.3H_2O$, Sigma-Aldrich) in 0.05 M HCl was stirred into 280 ml water. This was followed by the addition, with rapid stirring, of 18.3 ml of 0.05 M $NaBH_4$ in 0.05 M NaOH. The gold colloids were stirred for 5 min, after which 0.24 g of the support (which had been pre-dispersed in 50

ml water by ultrasonication) was added. The slurry was stirred for 20 h, followed by filtering and washing of the solid catalyst. It was then dried at 60$^{o}$C overnight under vacuum. The expected gold loading was 20 wt %.

### 4.2.3 Characterisation

Powder X-ray diffraction (XRD) analysis of the catalysts was carried out at the Australian Synchrotron at a X-ray wavelength of 0.588 Å. The samples were loaded into 0.3 mm diameter capillaries (Special glass, Charles Supper Company Inc.) and diffraction data was obtained in the 2θ range of 1.68-150 degrees, using a Mythen detector. The average gold particle size was determined from the XRD data using the Scherrer equation.

Wet chemical analysis was used to determine gold and manganese contents. Catalyst samples were dissolved in *aqua regia* (3:1 volume ratio of concentrated HCl:$HNO_3$) and analysed by atomic absorption spectroscopy (AAS).

The catalyst morphology was investigated by means of scanning electron microscopy (SEM) using the JEOL 7000F FE-SEM. The homogeneity of the $MnO_2$-modified catalyst supports was investigated using SEM coupled with energy-dispersive X-ray spectroscopy (EDS). The support and catalyst powders were pressed onto double-sided carbon tape for SEM analysis.

Dilute catalyst suspensions in isopropanol were deposited onto lacey carbon grids for analysis by transmission electron microscopy (TEM), using a Philips CM-200 operated at 200 kV. The gold particle size distribution and gold surface area of each catalyst were determined from TEM measurements.

Catalyst surface composition was determined by X-ray photoelectron spectroscopy (XPS), using a Kratos Axis DLD spectrometer with monochromated Al Kα source. Peak fitting was done with the XPS Peak 4.1 program.

### 4.2.4 Electrochemistry

For electrochemical testing, 5 mg of each catalyst was weighed out into a polypropylene test tube. 1 ml of 0.5 mg ml$^{-1}$ Nafion in a 4:1 isopropanol (IPA):$H_2O$ solution was added to yield a Nafion: catalyst ratio of 10 wt %. The catalyst/Nafion suspension was then diluted to 5 ml with 4:1 IPA:$H_2O$ solution, to obtain a catalyst concentration of 1 mg ml$^{-1}$. The suspension was ultrasonicated for 30 min to ensure good catalyst dispersion. A 10 µl drop of catalyst suspension was then pipetted onto a polished glassy carbon electrode plate over a hot-plate at 80 $^{o}$C, and allowed to dry at that temperature for 1 min. Prepared in this way, each electrode contained 0.8-2 µg of Au, 9.2 – 8 µg of carbon and 1 µg of Nafion. Based on the approximate diameter of the drop-cast layer (1-1.5 cm) and an assumed porosity of 50%, the thickness of the electrocatalytic layer is estimated to be in the order of ~ 0.1 µm.

For repeatability measurements, each catalyst was deposited and tested on 5 electrodes.

Electrochemical measurements were run in a standard 3-electrode PTFE cell (cell design EC4) with a Hg/HgO, 1 M KOH reference electrode and a ~ 6 $cm^2$ platinum counter electrode, using a Gamry Reference 600 potentiostat. The electrochemical testing procedure outlined in Section 3.3.6 (i.e. soak, strip, EASA and glycerol oxidation) was followed. Additional testing procedures included potentiostatic measurements at both 0 and 0.2 V and EIS measurements at the same potentials in a frequency range of 1 MHz to 10 mHz. Gamry Echem Analyst Version 5.63 software was used for analysis of the electrochemical data.

## 4.3 Results and discussion

From AAS analysis, it was found for all the $MnO_2$-containing catalysts, that the actual $MnO_2$ loading onto carbon was only about half that of the expected values (Table 4). This correlates with the limited $MnO_2$ loadings obtained by Fischer, *et al*. [126], which they attributed to the small pore size of their carbon nanofoam support, with a total pore volume of 0.62 $cm^3\ g^{-1}$. Vulcan XC-72R carbon has a comparable total pore volume (0.67 $cm^3\ g^{-1}$), as well as a significant amount of micropores [128].

The actual gold loading was very close to the expected value on the unmodified carbon support, but gold loadings were lower on the $MnO_2$-modified supports and decreased with increasing $MnO_2$ concentration (Table 4).

***Table 4. Expected and actual gold and $MnO_2$ content of Au/x$MnO_2$/C catalysts.***

| Catalyst | Au loading / % | | $MnO_2$ loading / % | |
|---|---|---|---|---|
| | Expected | Actual | Expected | Actual |
| Au/C | 20 | 19 | 0 | 0 |
| Au/5$MnO_2$/C | 20 | 14 | 10 | 5.2 |
| Au/9$MnO_2$/C | 20 | 13 | 20 | 8.6 |
| Au/16$MnO_2$/C | 20 | 13 | 30 | 16 |
| Au/23$MnO_2$/C | 20 | 7.9 | 40 | 23 |

From this result it can be implied that the surface of the deposited $MnO_2$ does not have the same affinity for the gold colloids as Vulcan XC-72R carbon. This could be due to the $MnO_2$/C support having a lower surface area than the carbon support, as shown in BET surface area measurements by Ma, *et al*. [127]. Another reason for the low gold loadings could be the lower point of zero charge (approximately pH 4) of $MnO_2$ [129, 130], as compared to that of the unmodified carbon support (pH 7.05 [83]). Since the gold nanoparticles are stabilised by adsorbed anions [114], the support would have to be positively charged, in order to effectively adsorb the negatively charged gold nanoparticle clusters. In the basic medium of the colloidal solution (measured at pH 8.9), $MnO_2$ would be more

negatively charged than the unmodified carbon support. However, as the carbon support is also negatively charged at that pH, there must be another driving force for the attraction of gold to the carbon surface, and it is possible that there is an initial physisorption step as a precursor to chemisorption.

XRD analysis showed the presence of only metallic gold on all the catalysts (Figure 22).

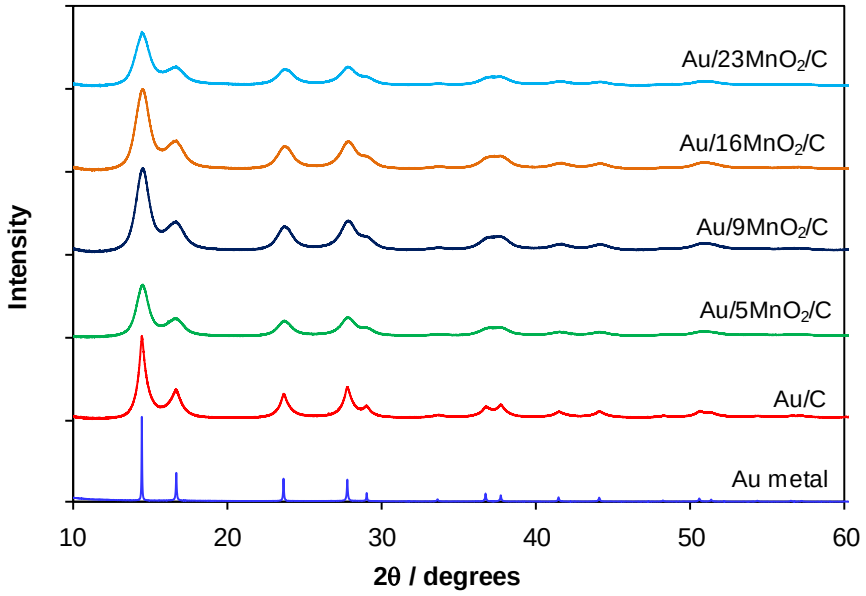


***Figure 22. XRD patterns of Au/xMnO$_2$/C catalysts at an X-ray wavelength of 0.588 Å.***

The gold peaks for the Au/C catalyst were very crystalline and the average gold crystallite size for that catalyst was calculated using the Scherrer equation, to be 17 nm. In comparison, the $MnO_2$-modified catalysts had average gold crystallites in the region of 8.4-10 nm. As will be shown later, TEM analysis showed the majority of gold particles were actually smaller than the values calculated by XRD. In agreement with other researchers [127, 131], no crystalline $MnO_x$ phases were evident in X-ray diffraction patterns of $MnO_2$/C synthesised by electroless deposition, suggesting that $MnO_2$ exists as very thin or amorphous layers on the carbon surface.

XPS studies confirmed that the gold particles were metallic in nature, with all catalysts having Au $4f_{7/2}$ peaks centred around 84.1 – 84.2 eV, consistent with $Au^0$ [132]. Gold peak full widths at half peak height (FWHM) values increased with the addition of $MnO_2$, from 0.78 eV for Au/C to 0.84-0.88 eV for the catalysts containing 5, 9 and 16 % $MnO_2$/C and 0.93 eV for Au/23$MnO_2$/C. The line broadening indicates a decrease in gold particle size [133] for the catalysts containing $MnO_2$. The presence of $MnO_2$ was also confirmed, with all Mn $2p_{3/2}$ peaks in the region of 641.9 – 642.0 eV and O 1s peaks close to 529.6 eV, indicative of oxygen in $MnO_2$ [131]. The Au 4f and Mn 2p XPS spectra of some catalysts are shown in Figure 23, while the O 1s and C 1s spectra of the Au/C and Au/23$MnO_2$/C catalysts are shown in Appendix 4.1. Deconvolution of the O 1s and C 1s spectra was more complicated and attempts to definitively assign the C-O, C=O and O=C-O species to the

deconvoluted peaks by means of correlating the peak assignments from the O 1s and C 1s spectra, were not successful. This was also complicated by the discrepancies in binding energies for the various carbon and oxygen interactions given in literature [131, 134-136] (shown in Appendix 4.2).

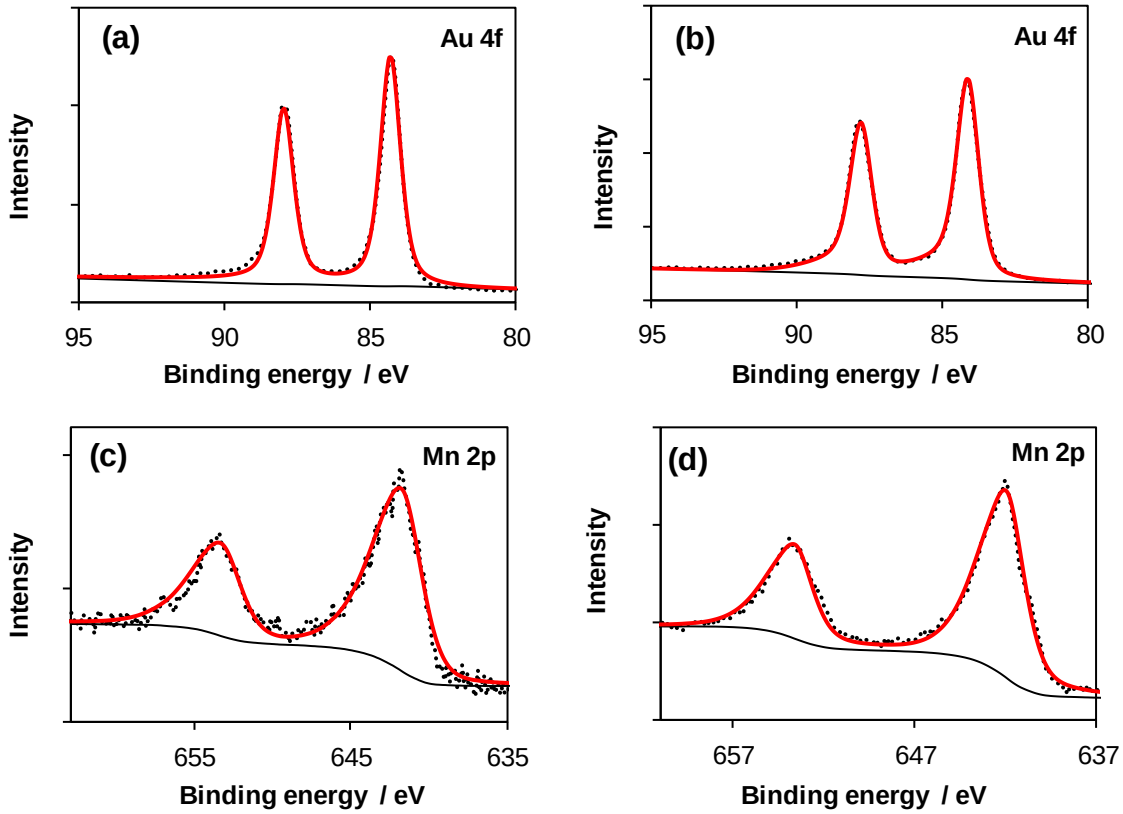


***Figure 23. Au 4f XPS spectra of (a) Au/C and (b) Au/23 $MnO_2$/C, and Mn 2p spectra of (c) Au/9$MnO_2$/C and (d) Au/23$MnO_2$/C. Dotted lines indicate raw data and solid lines indicate fitted peaks.***

TEM micrographs (Figure 24) showed very different gold nanoparticle distributions on the carbon and $MnO_2$/C supports. While gold nanoparticles were quite evenly dispersed across the carbon support, they appeared to cluster together in a thread-like formation on the $MnO_2$/C supports. This latter phenomenon was also reported by Padayachee [129] for co-precipitated Au/$Mn_xO_y$ catalysts. The gold particles also appeared to be smaller and more uniform for the Au/$MnO_2$/C catalysts.

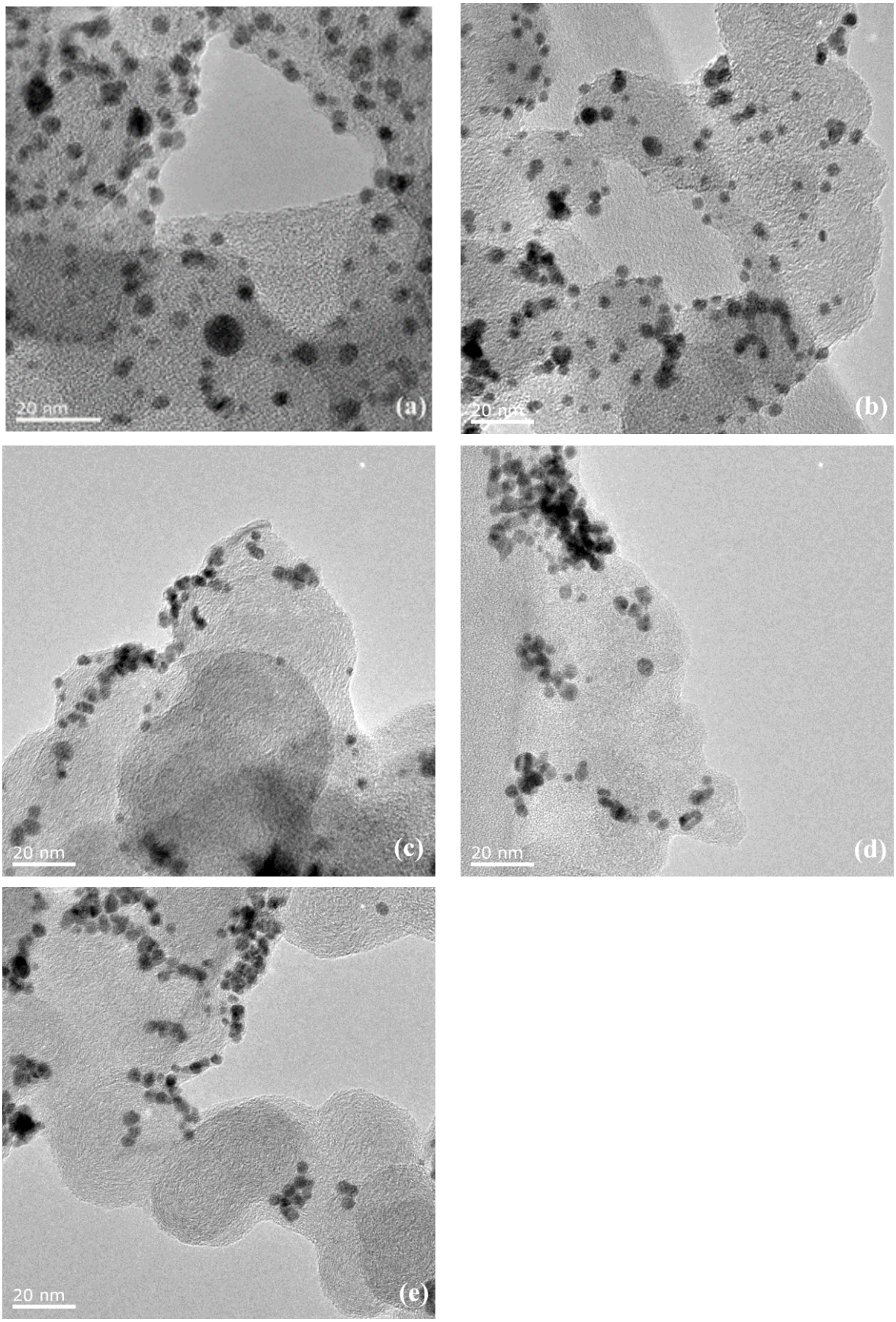


***Figure 24. TEM images of Au/$x$MnO$_2$/C catalysts, where $x$ = (a) 0 %, (b) 5 %, (c) 9 %, (d) 16 % and (e) 23%. Scale bar is 20 nm.***

It was not possible to distinguish between carbon and $MnO_2$ with microscopy techniques, implying that $MnO_2$ is uniformly deposited on the carbon support. SEM-EDS analysis of the $MnO_2$/C supports confirmed the homogeneity of all the supports (Appendix 4.3). Ma, *et al*. [127] have also reported being unable to distinguish $MnO_2$ from carbon with SEM analysis, for $MnO_2$/C synthesised in a similar manner.

The gold nanoparticles synthesis method of Martin, *et al*. [114] used in this work, is reported to yield colloids with a PSD of 1.5 – 6 nm and average size of 3.2 nm, which are stable in water for more than a year. The gold colloids synthesised here had a UV/Vis spectrum similar to one reported by Martin, *et al*., indicating a comparable average gold particle size in solution.

Size-based histograms (Figure 25) were generated by measuring at least 145 gold particles per catalyst from TEM images. The gold particle size distribution (PSD), number-weighted $d_{ave}$ and gold surface area (S.A.) of each catalyst were determined from TEM measurements. S.A. was calculated from

$$\boldsymbol{S.A.} = \sum_{i=1}^{n} \boldsymbol{4\pi r_i^2} \,/\, \sum_{i=1}^{n} \boldsymbol{\rho \frac{4}{3} \pi r_i^3} \qquad (\mathbf{10})$$

The statistical error on the gold surface area was determined by error propagation based on an initial standard error of ±0.2 nm per measured particle.

From the histograms, it was clear that $MnO_2$ stabilised the gold nanoparticles, giving a narrower PSD (2 – 6 nm) and smaller $d_{ave}$ values (< 4 nm) than the Au/C catalyst. A significant number of gold particles were above 6 nm in size for Au/C (Figure 25a).

The narrower PSD and smaller average sizes of the Au/$MnO_2$/C catalysts are not believed to be due to the lower gold loadings but rather to a support effect, since a wide distribution of gold particle sizes has also been observed for a 1 % Au/C catalyst prepared using the same method as for the catalysts reported here (see Chapter 6).

All the $d_{ave}$ values obtained from TEM analysis were much smaller than those calculated from XRD analysis, indicating that gold $d_{ave}$ values calculated from the latter technique were skewed by the presence of a small proportion of larger particles which were not distinguishable from overlapping clusters of smaller particles.

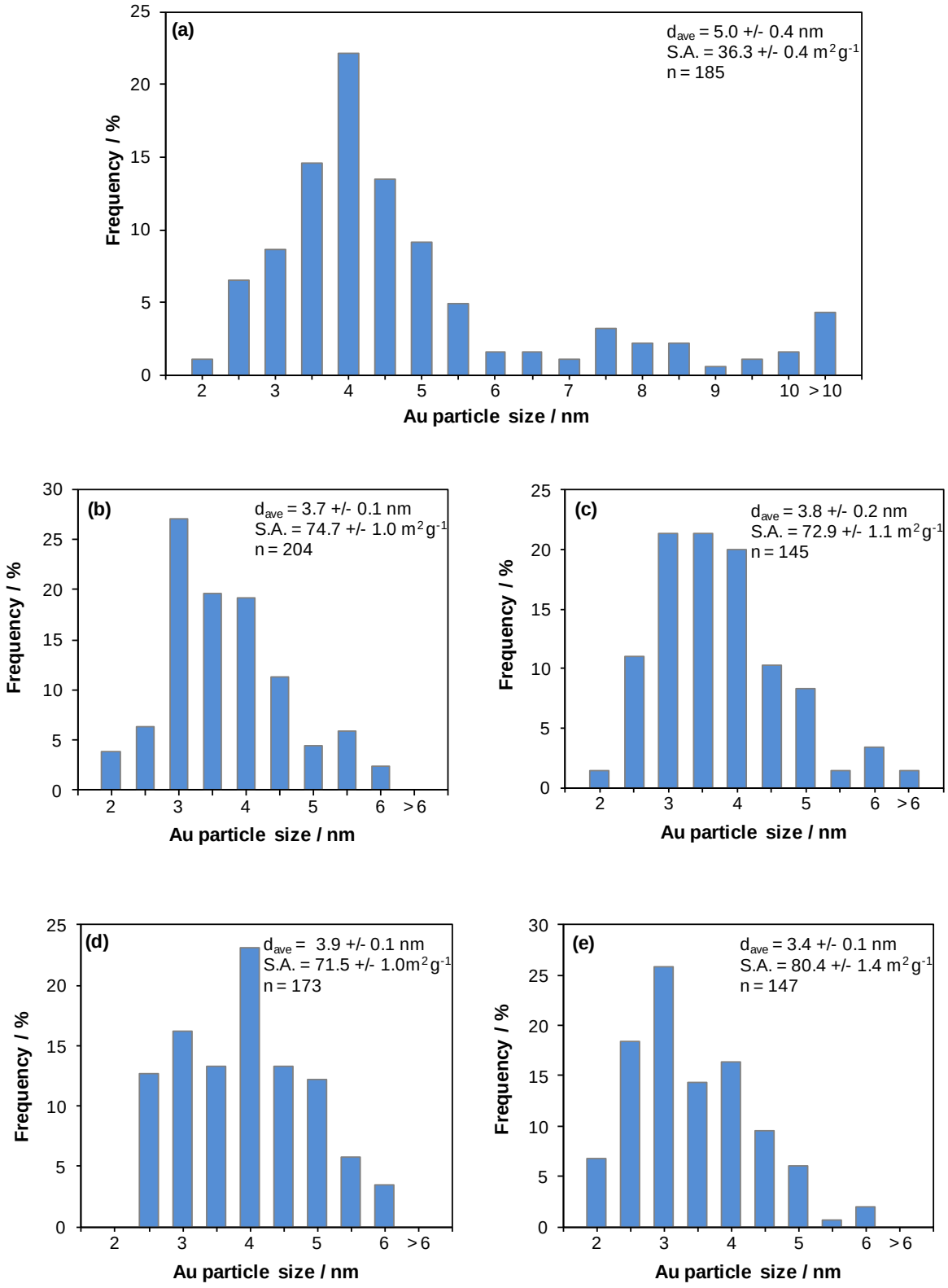


***Figure 25. Gold PSDs, $d_{ave}$ values and surface areas (S.A.) of Au/x$MnO_2$/C catalysts determined using TEM, where $x$ = (a) 0 %, (b) 5 %, (c) 9 %, (d) 16 % and (e) 23%.***

Comparisons of CVs of all the catalysts in 1 M KOH (Figure 26) showed that only Au/C (Figure 26a) had a similar voltammetric response to bulk gold [98, 106], with a prominent gold oxide reduction peak at 0.1 V. For the catalysts containing 5 and 9 wt % $MnO_2$/C, very small gold oxide reduction peaks were present, while no gold oxide reduction peaks were seen for the catalysts with higher $MnO_2$ concentrations.

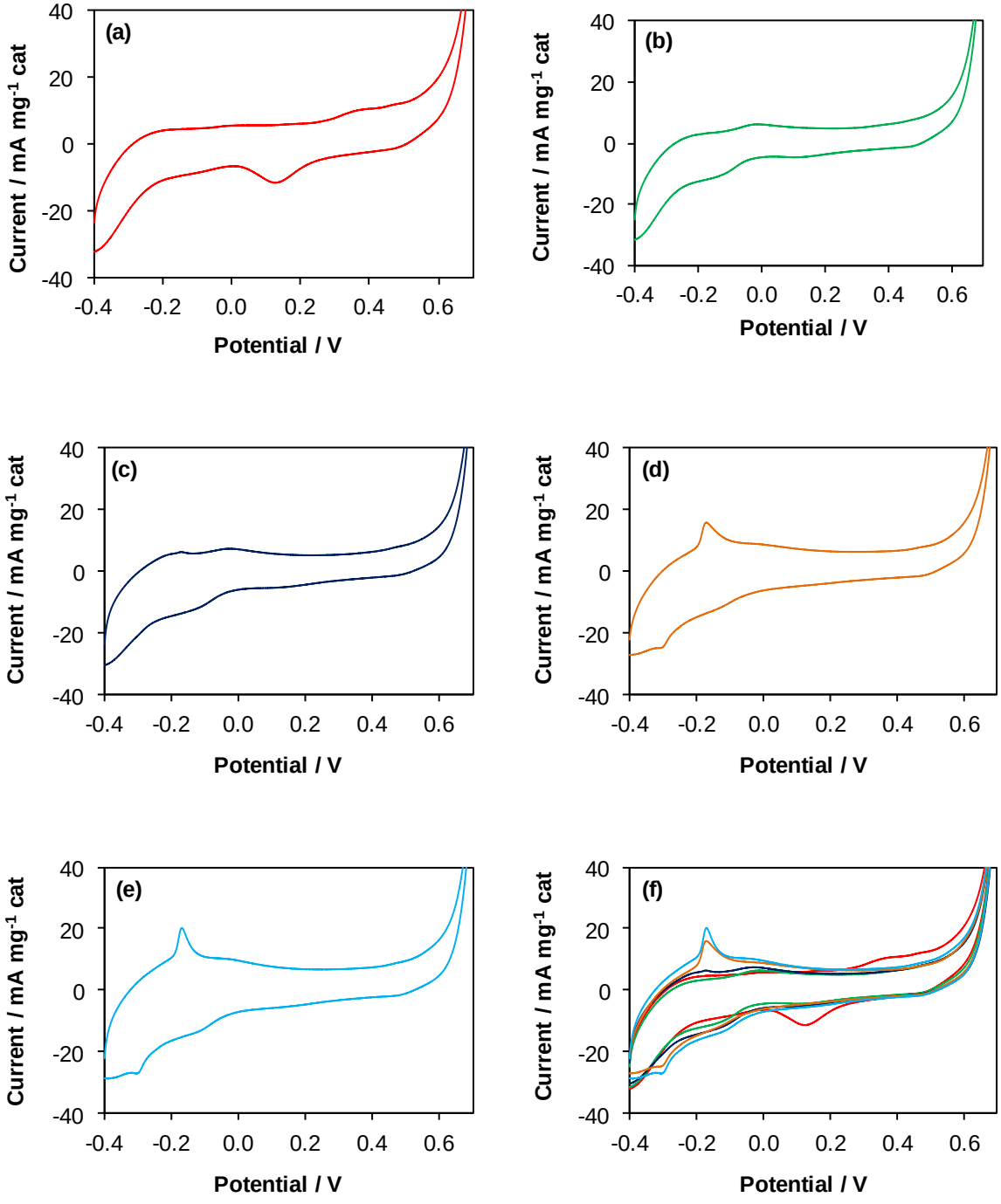


***Figure 26. CV scans of Au/x$MnO_2$/C catalysts in 1 M KOH at 50 mV $s^{-1}$, where x = (a) 0 %, (b) 5 %, (c) 9 %, (d) 16 %, (e) 23%. CVs of all the catalysts are overlaid in (f). Potentials are shown vs. Hg/HgO reference.***

For the $MnO_2$-modified catalysts, the two reduction peaks observed at approximately -0.10 and -0.35 V correspond to $MnO_2$ reduction peaks in 1 M KOH reported by Wu, *et al*. [137] and unsurprisingly, the manganese oxidation (-0.17 and -0.03 V) and reduction peaks became more intense with increasing $MnO_2$ concentration (Figure 26f).

Similar electrochemical behaviour to bulk gold was observed for Au/C in 1 M KOH and 0.5 M glycerol/1 M KOH solutions. Anodic currents corresponding to glycerol oxidation were observed to start at approximately -0.2 V (Figure 27), indicating that the catalyst became activated at this potential.

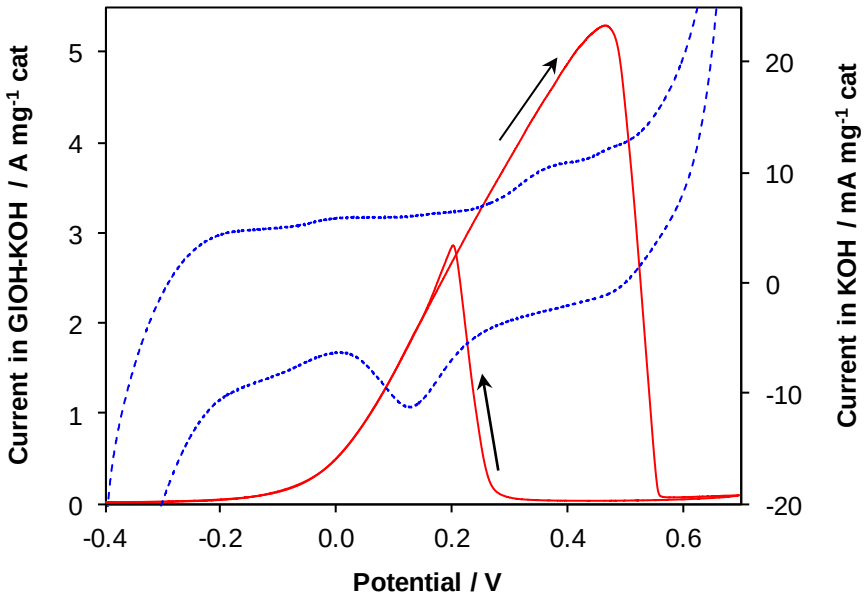


***Figure 27. CVs of Au/C catalyst in 0.5 M glycerol/1M KOH at 10 mV $s^{-1}$ (solid curve) and 1 M KOH at 50 mV $s^{-1}$ (dotted curve).***

The forward peak current obtained over the Au/C catalyst was very high (5.1 ± 0.2 A $mg^{-1}$ cat), indicating excellent glycerol oxidation activity (confirmed later in comparisons with literature). Neither the carbon, nor any of the $MnO_2$-modified carbon supports, gave any glycerol oxidation peaks, indicating that the supports on their own have no catalytic activity for glycerol oxidation (Appendix 4.4). The maximum forward peak currents of all the gold catalysts are compared in Figure 28 (comprehensive electrochemical data in Appendix 4.5).

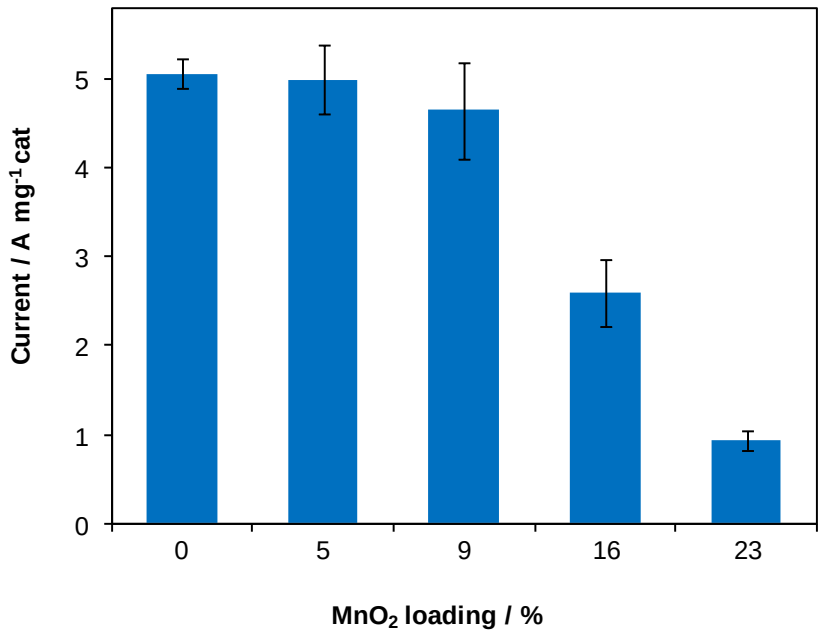


***Figure 28. Effect of $MnO_2$ concentration on catalyst-mass activities of Au/x$MnO_2$/C catalysts for glycerol oxidation. Peak currents were measured from forward sweep of CV in 0.5 M glycerol/1 M KOH.***

From a comparison of the peak currents, $MnO_2$ appears to have a detrimental effect on glycerol oxidation at 16 and 23 % $MnO_2$/C concentrations. Taking into account the standard errors from repeatability measurements, $MnO_2$/C contents of ≤ 9 % appear to have little to no effect. However, normalising currents with respect to actual gold loading (measured by AAS), showed that $MnO_2$/C contents of ≤ 9 % promoted the mass activity of the gold catalysts for glycerol oxidation (Figure 29).

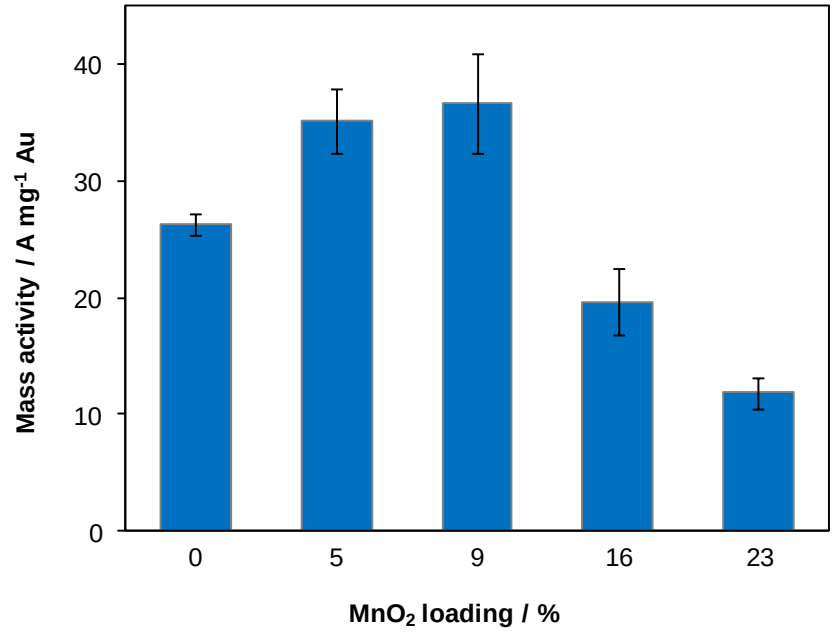


***Figure 29. Effect of $MnO_2$ concentration on gold-mass activities of Au/x$MnO_2$/C catalysts for glycerol oxidation. Peak currents were measured from forward sweep of CV in 0.5 M glycerol/1 M KOH.***

The higher gold-based mass activities resulting from the addition of $MnO_2$ in small quantities, could possibly be due to $MnO_2$ having a stabilising effect by preventing the agglomeration of gold nanoparticles, thus ensuring a larger gold surface area for reaction. Despite the 16 and 23 wt % $MnO_2$/C-supported gold catalysts also having smaller $d_{ave}$ values than Au/C (Figure 25), these catalysts were significantly less active than the catalysts containing ≤ 9 % $MnO_2$/C on a current and mass activity basis. This is probably due to the increasing concentration of poorly conductive $MnO_2$ [125] introducing an additional ohmic resistance on some particles.

$MnO_2$ was also found to assist with the oxidation of glycerol at lower potentials. Lower glycerol oxidation onset- (except for Au/23 % $MnO_2$/C) and peak- potentials were apparent for all $MnO_2$-containing catalysts (Table 5). Importantly, the catalysts with 5 and 9 % $MnO_2$ had similar forward peak currents to Au/C (Figure 28), indicating that on the former catalysts, lower anodic potentials are required to effect the same rate of glycerol oxidation as Au/C.

***Table 5. Effect of $MnO_2$ concentration on glycerol oxidation onset- and forward peak- potentials measured from CV in 0.5 M glycerol/1 M KOH***

| Catalyst | Onset potential / V | Peak potential / V |
|---|---|---|
| Au/C | -0.23 | 0.47 |
| Au/5 % $MnO_2$/C | -0.24 | 0.43 |
| Au/9 % $MnO_2$/C | -0.27 | 0.38 |
| Au/16 % $MnO_2$/C | -0.24 | 0.37 |
| Au/23 % $MnO_2$/C | -0.21 | 0.26 |

It has been speculated that oxides in contact with metal nanoparticles help to promote alcohol oxidation by the formation of adsorbed OH species at lower potentials. These adsorbed species assist in the oxidation and removal of carbonaceous residues, freeing the metal surface for further reaction [64]. It is possible that $MnO_2$ works for gold by a similar mechanism, which could explain the lower onset potentials. It has been shown that manganese oxides can lower the overpotentials of metals such as gold and platinum for the oxygen evolution reaction in KOH [138, 139]. It is therefore possible that, especially at higher potentials, there is an additional mechanism which comes into play, *viz.* oxygen "spillover" from $MnO_2$ to the gold surface, resulting in peak shifts to lower potentials and higher mass activities for the catalysts containing 5 and 9 wt % $MnO_2$.

The drop in glycerol oxidation peak current was much sharper for the catalysts containing ≤ 9 % $MnO_2$/C than for the catalysts containing 16 and (especially) 23 % $MnO_2$/C (Figure 30; all catalysts compared in Appendix 4.6). In addition, glycerol oxidation currents were higher over the latter catalysts at extremely positive potentials (0.6 – 0.7 V *vs.* Hg/HgO). The continued electrochemical

response of metal oxide-supported gold catalysts at higher potentials has also been noted by Hayden, *et al*. [119] for CO electrooxidation over Au/$TiO_2$ catalysts. Hayden, *et al*. attributed this to an increase in the overpotential for gold oxide formation (delaying the deactivation of the gold surface) and to an increase in the irreversibility of the gold-gold oxide couple. This was evidenced by the lack of gold oxide reduction peaks in KOH for the catalysts containing 16 and 23 % $MnO_2$ (Figure 26d and e).

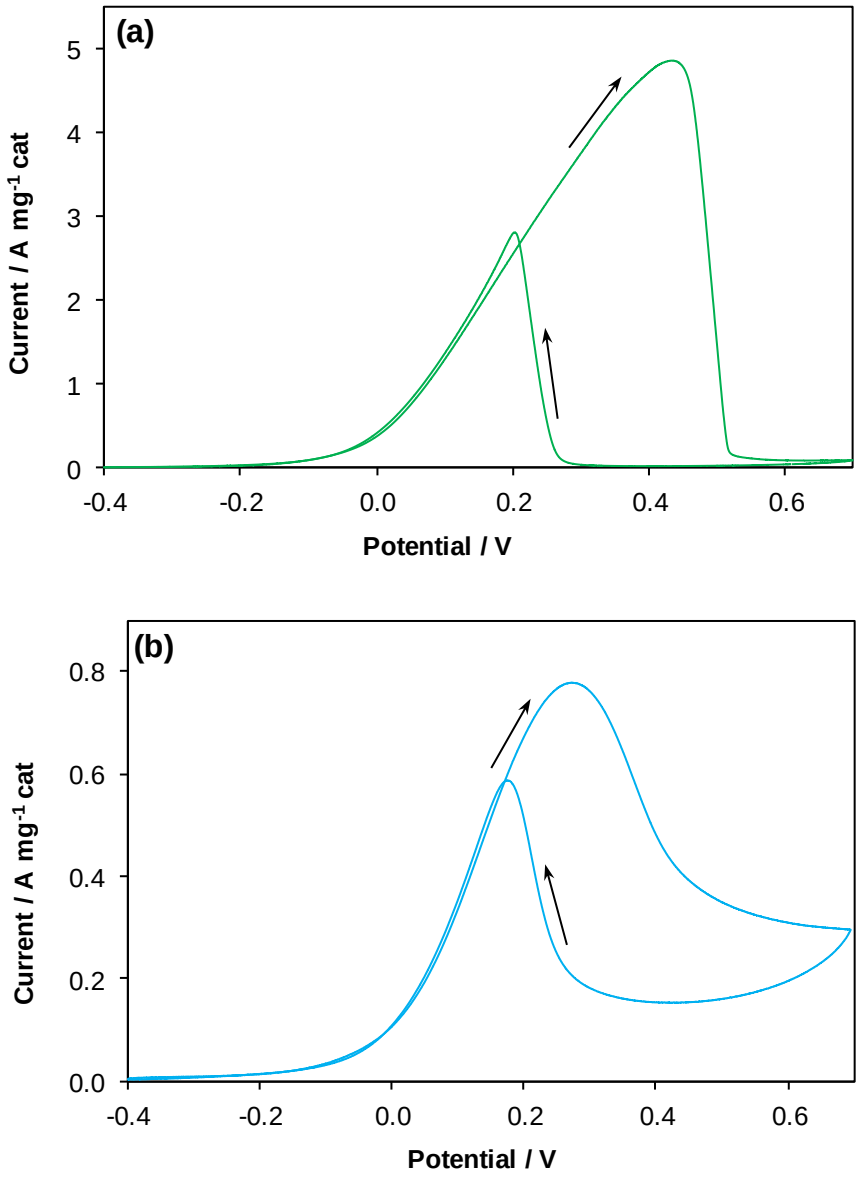


***Figure 30. CVs of (a) Au/5 % $MnO_2$/C and (b) Au/23 % $MnO_2$/C in 0.5 M glycerol/1 M KOH at 10 mV $s^{-1}$. Potentials are shown vs. Hg/HgO reference.***

It was not possible to calculate EASA-based specific activities for all the catalysts, due to the absence of gold oxide reduction peaks for the catalysts containing 16 and 23 % $MnO_2$/C. Therefore, catalyst specific activities (Figure 31) have been depicted in terms of real surface area calculated from TEM analysis [119]. These results showed that all the $MnO_2$-modified catalysts had significantly lower specific activities (≤ 50±6 mA $cm^{-2}$) than Au/C (72±3 mA $cm^{-2}$). As with the current- and mass activity-

trends (Figure 28 and Figure 29, respectively), the catalysts containing 16 and 23 % $MnO_2$/C had the lowest specific activities for glycerol oxidation. The considerably higher specific activity of Au/C is due to the contribution of a small percentage of larger gold particles (Figure 25a), causing a decrease in the total specific gold surface area to half that of the $MnO_2$-modified catalysts. This difference is only valid if it is assumed that the larger gold particles are equally or more active than the smaller gold particles for glycerol oxidation. To this end, it was decided to carry out investigations to determine whether there is a gold particle size effect on the electrocatalytic oxidation of glycerol (discussed in Chapter 5).

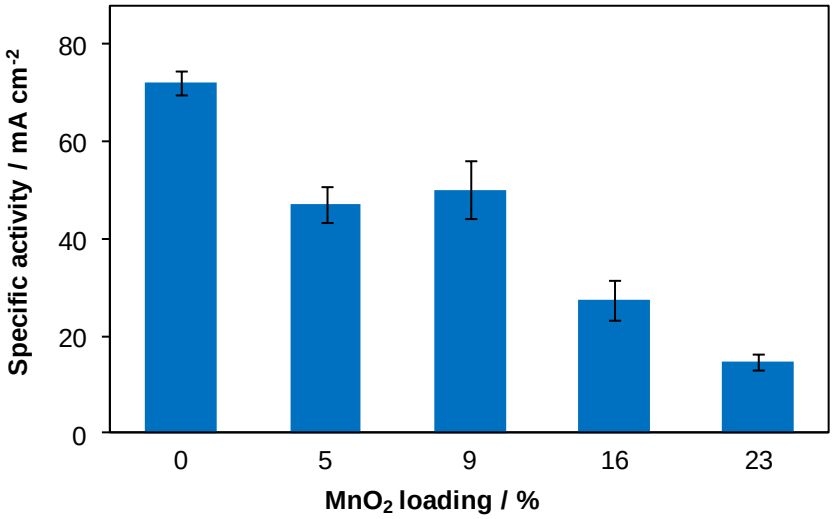


***Figure 31. Effect of $MnO_2$ concentration on specific activities of Au/x$MnO_2$/C catalysts for glycerol oxidation. Peak currents were measured from forward sweep of CV in 0.5 M glycerol/1 M KOH.***

Glycerol oxidation forward-to-reverse ($I_f/I_r$) peak ratios were calculated for all the catalysts (Figure 32), in order to determine the catalysts' resistance to poisoning from glycerol and its oxidation intermediates. The most active catalysts (with ≤ 9 % $MnO_2$/C) had the highest forward/reverse peak currents, indicating that these catalysts were also the most resistant to poisoning. Lower $I_f/I_r$ ratios for the catalysts containing 16 and 23 % $MnO_2$ show that these catalysts were more easily poisoned. This indicates an actual difference as it is not the result of any normalisation procedures, and cannot be attributed to a gold particle size effect, since all the $MnO_2$-containing catalysts had similar gold $d_{ave}$ values and specific surface areas. It is possibly due to the irreversibility of the gold-gold oxide couple [119] on these catalysts, leading to the reduced ability of gold to effectively "clean" its surface of adsorbed glycerol and glycerol oxidation products. However, even the catalysts with the lowest $I_f/I_r$ ratios were more resistant to poisoning than bulk gold, which was found to have an $I_f/I_r$ ratio of < 1 in glycerol (shown in Chapter 2).

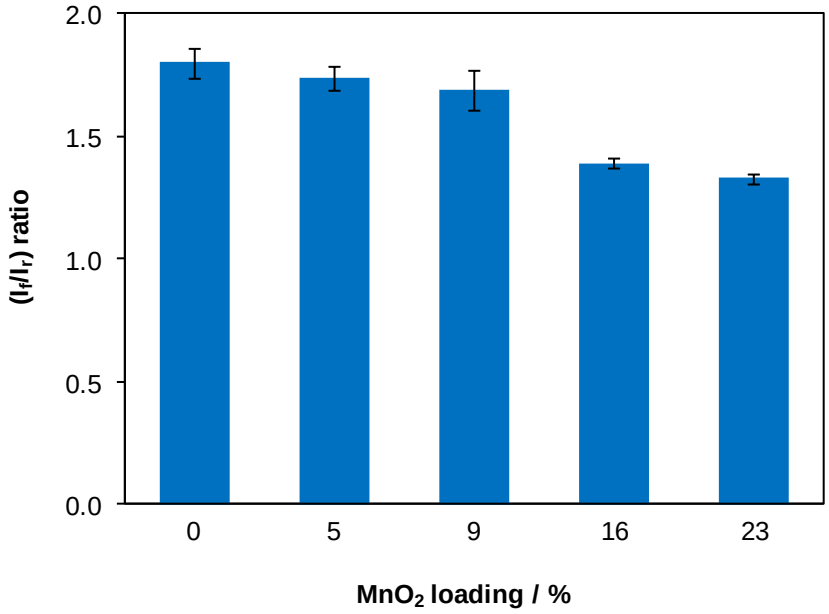


***Figure 32. Forward-to-reverse peak ($I_f/I_r$) ratios of Au/x$MnO_2$/C catalysts in glycerol measured from CV in 0.5 M glycerol/1 M KOH.***

Potentiostatic measurements were used to assess catalyst stability over time (Figure 33). At 0 V (Figure 33a), a trend of decreasing activity with increasing $MnO_2$/C content was apparent. Although Au/5$MnO_2$/C started out with the highest mass activity, it was less stable than Au/C and showed a sharper drop in current over time. That this could be due to manganese not being fully oxidised to $MnO_2$ and therefore not activated at that potential (the second manganese oxidation peak occurred very close to 0 V - Figure 26), was supported by potentiostatic measurements at 0.2 V (Figure 33b). All the catalysts had activities an order of magnitude higher at 0.2 V than at 0 V. At 0.2 V, the gold-based catalysts which had the highest mass activities for glycerol oxidation in CV scans (5 and 9 % $MnO_2$/C), were also the most active for the duration of the scan. All catalysts had slower current decay rates ($I_{30\ min}/I_{0\ min}$) at 0.2 V than at 0 V (Table 6) and the Au/5 % $MnO_2$/C catalyst was the most stable at that potential.

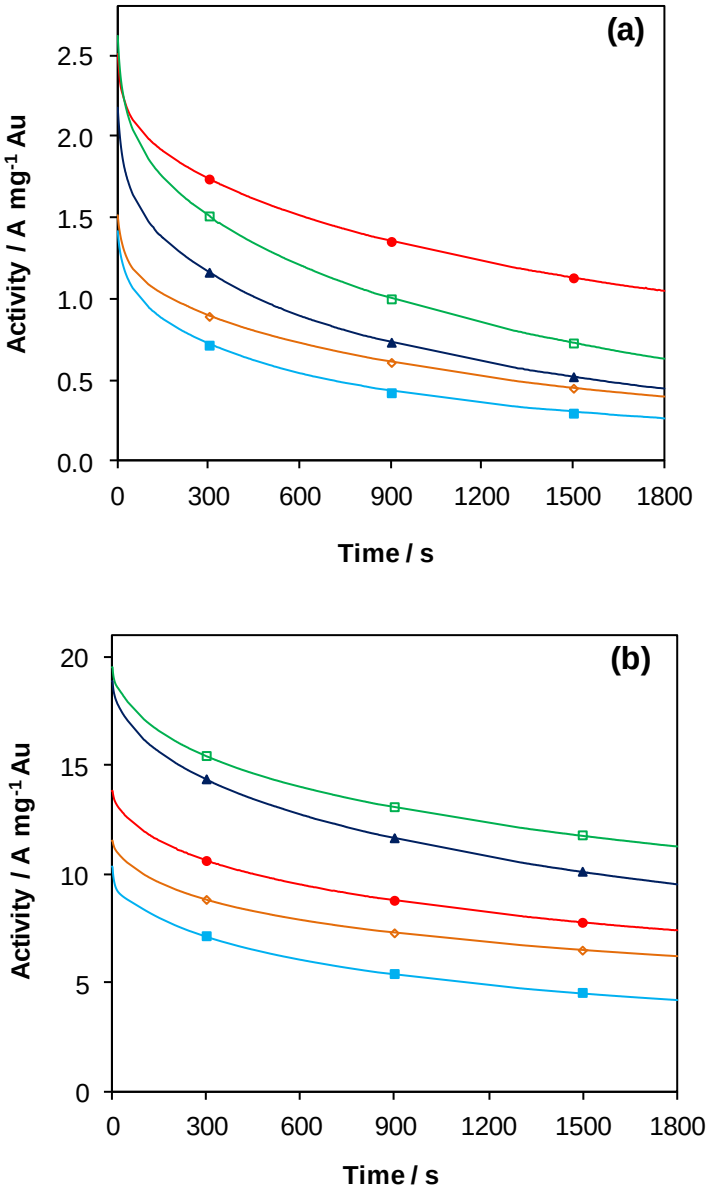


***Figure 33. Potentiostatic measurements of Au/$x$MnO$_2$/C catalysts in 0.5 M glycerol/1 M KOH solutions, where $x$ = ● 0 %, □ 5 %, ▲ 9 %, ◊ 16 %, ■ 23 %, recorded at (a) 0 V and (b) 0.2 V (vs. Hg/HgO) for 30 min.***

***Table 6. Glycerol oxidation current ratios ($I_{30\ min}/I_{0\ min}$) of Au/x$MnO_2$/C catalysts, from potentiostatic measurements at 0 V and 0.2 V (vs. Hg/HgO) in 0.5 M glycerol/1 M KOH.***

| Catalyst | Current ratio ($I_{30\ min}/I_{0\ min}$) | |
|---|---|---|
| | **0 V** | **0.2 V** |
| Au/C | 0.42 | 0.54 |
| Au/5 % $MnO_2$/C | 0.24 | 0.58 |
| Au/9 % $MnO_2$/C | 0.21 | 0.51 |
| Au/16 % $MnO_2$/C | 0.26 | 0.54 |
| Au/23 % $MnO_2$/C | 0.18 | 0.41 |

Electrochemical impedance spectroscopy (EIS) was used to carry out a qualitative evaluation of the kinetics of glycerol oxidation on the Au/x$MnO_2$/C catalysts in 0.5 M glycerol/1 M KOH solution, at 0 V and 0.2 V (Figure 34).

The charge transfer resistance ($R_{ct}$) of the reaction is indicated by the diameter of the semi-circle at high frequencies [140, 141], located within the first quadrant [142]. Increasing the potential from 0 V to 0.2 V gave decreased $R_{ct}$ for all catalysts, signifying improved glycerol oxidation kinetics at the higher potential. Au/C and Au/5 % $MnO_2$/C had the lowest $R_{ct}$ values at 0 V and 0.2 V, respectively, correlating well with the conclusions drawn from potentiostatic measurements.

At low frequencies, in most instances, the curves then stretched into another quadrant (+ve $Z_{real}$, +ve $Z_{imag}$ values). This feature has been attributed to pseudoinductance caused by the oxidation of adsorbed intermediates [142]. The absence of this characteristic for Au/23 $MnO_2$/C at 0 V implies a lack of oxidation of adsorbed intermediates, as evidenced by the lowest $I_f/I_r$ ratio (Figure 32) and the lowest ($I_{30\ min}/I_{0\ min}$) current ratio (Table 6).

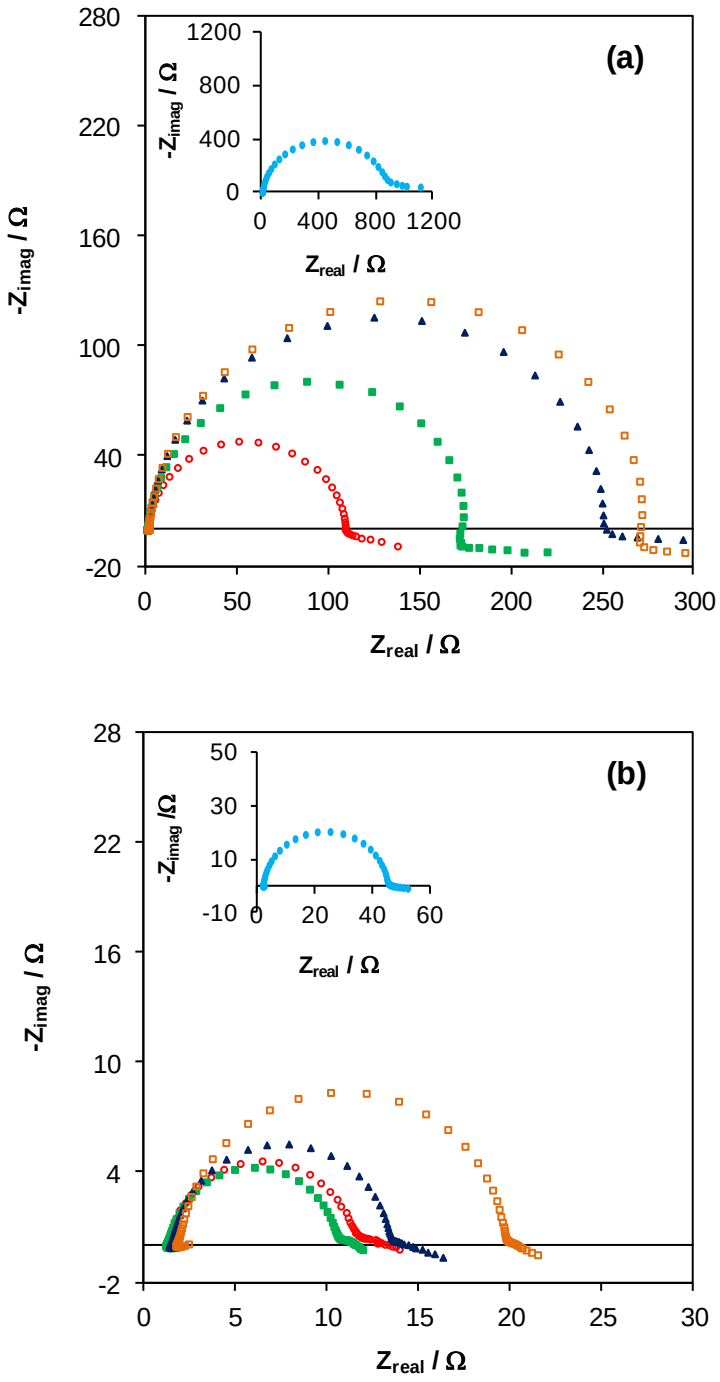


***Figure 34. Nyquist plots of 3nm Au/x$MnO_2$/C catalysts in 0.5 M glycerol/1 M KOH, where x = ○ 0 %, ■ 5 %, ▲, 9 % □ 16 %. Inset shows EIS for Au/23 % $MnO_2$/C catalyst. Plots were recorded at (a) 0V and (b) 0.2 V (vs. Hg/HgO).***

From an assessment of the electrochemical analysis, it is clear from CV that $MnO_2$ at low concentrations has the ability to be both a support and co-catalyst for Au-based catalysts for glycerol electrooxidation. However, while $MnO_2$-containing catalysts can promote the glycerol oxidation reaction, they are also more readily poisoned at lower potentials, as was evident from potentiostatic

and EIS measurements. The poisoning could be due to blocking of (likely mixed-valence) manganese oxide sites at 0 V by glycerol and its residues, resulting in a reduced ability over time, to free the gold surface. It is also possible that the smaller gold particles present on the $MnO_2$-containing catalysts are more easily poisoned at lower potentials.

Once $MnO_2$ is "activated" at a higher potential, it shows evident co-catalytic activity, with the Au/5 % $MnO_2$/C being highly active as well as stable, and also demonstrating the lowest $R_{ct}$ at 0.2 V. However, this result may not translate well into a fuel cell set-up, as any catalytic advantage obtained from using a $MnO_2$- containing catalyst may be offset by the higher anodic overpotentials which would be required to maintain the catalyst's activity and stability.

In order to get an indication of how these gold-based catalysts compared with the nano- platinum and palladium catalysts already reported in literature (assuming that the results reported in literature are the maximum possible activities that could be obtained over those catalysts – see point raised at end of Chapter 3), comparisons were done only with those papers where similar or higher concentrations of glycerol (≥ 0.5 M) and KOH (≥ 1 M) solutions were used [48, 64, 65, 69, 70, 109, 110, 143-145]. It was found that all the catalysts reported on in this chapter had higher mass activities, with the best-performing Au/9 % $MnO_2$/C catalyst giving at least a 12 times higher mass activity than activities reported in literature. Even the worst-performing Au/23 % $MnO_2$/C catalyst was at least 4 times more active on a mass basis. In order to compare the catalysts' specific activities with those of other researchers, the specific activities were calculated from those papers reporting the metal $d_{ave}$ values determined with TEM [48, 64, 70, 143-145]. The best-performing Au/C catalyst was at least 27 times more active and the worst-performing Au/23$MnO_2$/C catalyst was at least 5 times more active, on a specific activity basis. These results therefore serve as additional confirmation that gold-based catalysts give much higher glycerol oxidation peak currents than palladium- or platinum- based catalysts. As has been demonstrated, the disadvantage of glycerol oxidation peak currents occurring at higher overpotentials over both bulk gold [8] and carbon-supported nano-gold [35] than on their PGM- analogues, can be partially negated by the addition of a synergistic metal oxide, such as $MnO_2$.

# 5 INFLUENCE OF GOLD PARTICLE SIZE ON GLYCEROL ELECTROOXIDATION OVER Au/C CATALYSTS

## 5.1 Introduction

A systematic study was undertaken to investigate the effect of gold particle size on Au/C catalysts for glycerol electrooxidation. This investigation arose partly from the issue raised in the previous chapter, that the difference in specific activity between Au/C and the manganese-modified gold catalysts was only valid if the larger gold particles were considered to be at least as active as the smaller particles, and was expanded to also include catalysts with significantly larger gold $d_{ave}$ values than the catalysts studied in the previous chapter.

## 5.2 Experimental

### 5.2.1 Preparation of gold colloids

#### *5.2.1.1 Reduction with $NaBH_4$*

Gold colloids were synthesised using the modified method of Martin, *et al*. [114], following the same procedure outlined in Chapter 4.

#### *5.2.1.2 Reduction with tetrakis(hydroxymethyl)phosphonium chloride (THPC)*

The method of Duff, *et al*. [146] was used as a basis for the preparation of gold colloids with THPC. To prepare the colloids, 231 ml water was added to a beaker, followed by the appropriate amounts of 0.2 M NaOH and 0.068 M THPC (from 80 % THPC solution, Sigma-Aldrich). After 2 min, 10.2 ml of gold solution was added with rapid stirring. The gold concentration used was 0.025 M for small (< 2 nm) colloids and 0.05 M for large colloids.

#### *5.2.1.3 Reduction with citrate*

The gold : citrate molar ratios specified by Kimling, *et al*. [147] were used as a guideline for the preparation of size-controlled colloids. The colloids were prepared by adding 5.1 ml of 0.05 M gold solution in 0.05 M HCl to 249 ml water and then heating the solution to boiling. The required amount of trisodium citrate ($Na_3$-cit) solution, which had been heated separately, was added to the gold solution and stirred vigorously while maintaining the temperature, until colloid formation was complete (3-10 min). The colloidal gold solution was then removed from heat and stirred until it reached ambient temperature.

### 5.2.2 Catalyst preparation

The carbon support (Vulcan XC-72R) was stirred in a small volume of water (minimum 20 ml) until fully wetted. The carbon dispersion was then added to the colloidal solution and the slurry was stirred

for 20 h to ensure adequate time for gold deposition to occur. Thereafter, the catalyst was filtered and washed several times under filtration to remove any residual ions, and then dried at 60$^{o}$C overnight.

### 5.2.3 Characterisation

Powder X-ray diffraction (XRD) analysis of the catalysts was carried out at the Australian Synchrotron at a X-ray wavelength of 0.689 Å and diffraction data was obtained in the 2θ range of 8.2-88 degrees (other details are the same as reported in Chapter 4).

Other characterisation methods included TEM analysis of all samples and wet chemical analysis (AAS) of all filtrates and some solids (covered in Chapter 4).

### 5.2.4 Electrochemistry

In addition to the electrochemical testing procedure outlined in Chapter 4, lead UPD was also used to identify the exposed low-index surface facets of the gold nanoparticles. Gold colloids were deposited directly onto a 3 mm glassy carbon electrode and allowed to dry. Prior to carrying out the lead UPD characterisation in a 1 mM $Pb(NO_3)_2$/0.1 M NaOH solution, the electrode was cleaned using the $PbO_2$ deposition/dissolution technique [103], by cycling the electrode twice between -1 and 1 V (*vs*. SCE). Lead UPD characterisation was then carried out at 50 mV $s^{-1}$ between -0.2 and -0.75 V (*vs*. SCE).

## 5.3 Results and discussion

A number of approaches were initially trialled in an attempt to obtain gold catalysts with varying average diameters ($d_{ave}$): the utilisation of different reducing agents, altering the Au : reducing agent molar ratio and adjusting the gold loading on the catalysts. The preparation conditions, gold loadings and $d_{ave}$ of each catalyst are listed in Table 7.

***Table 7. Preparation conditions of size-controlled gold catalysts***

| **$d_{ave}$ (TEM) / nm** | **Reducing agent** | **Au : reducing agent molar ratio** | **Au : NaOH molar ratio** | **Au loading (from AAS) / %** |
|---|---|---|---|---|
| 2.1 | THPC | 1 : 2 | 1 : 9 | 15 |
| 4.0 | $NaBH_4$ | 1 : 3 | 1 : 3 | 20 |
| 4.7 | $NaBH_4$ | 1 : 3 | 1 : 3 | 15 |
| 14.7 | $Na_3$-cit | 1 : 10 | - | 20 |
| 43 | $Na_3$-cit | 1 : 2 | - | 20 |
| 88 | $Na_3$-cit | 1 : 1 | - | 20 |
| 120 | THPC | 1.5 : 1 | 1 : 3 | 33 |

It has been shown that the average gold particle size can be increased by increasing the gold loading on the catalyst [148]. This was originally attempted using $NaBH_4$ as a reducing agent and varying gold loadings from 1 to 20 wt % by simply changing the amount of carbon support added to the colloidal gold solution. However, while some variation in particle size was observed, with average gold diameters ranging from 3.9 – 5.7 nm, no trend was found relating particle size to gold loading. Since the colloids produced by this method have an average size of 3.2 nm [114], the slightly larger average diameters of the carbon-supported gold indicates that there was some agglomeration of gold on the support. However, due to the gold nanoparticles made with $NaBH_4$ being stabilised by adsorbed anions [114], it is possible that electrostatic repulsion between the nanoparticles prevented any significant growth with increased gold loadings. It can therefore only be assumed that the method of increasing particle size by increasing the gold loading is more effective for the more conventional gold catalyst preparation methods, such as deposition-precipitation. While no clear influence of loading on the final gold particle size was evident, it was found that the catalysts with lower gold loadings (< 12.5 wt %) exhibited mass-transfer limitations in glycerol (discussed in Chapter 6). Therefore, the particle size comparisons were restricted to catalysts with gold loadings ≥ 15 wt%, to minimise the possibility of mass transfer limitations masking the true particle size effect.

The use of THPC as a reducing agent for gold, to produce colloids with an average diameter of 1-2 nm, was first described by Duff, *et al*. [146]. The original method was modified by increasing the gold : THPC ratio, to produce a catalyst with very large gold particles (average diameter 120 nm). For the THPC-reduced gold catalyst with very small particles (average diameter 2.1 nm), both the THPC and NaOH ratios were increased to produce smaller gold colloids [149]. The addition of excess NaOH resulted in a high colloidal solution pH of 12.2, which was adjusted to pH 2.7 with 0.5 M $H_2SO_4$ before addition of the carbon support, in order to ensure efficient adsorption of the negatively charged gold clusters [150] at a pH well below the point of zero charge (pH 7.05 [83]) of the carbon support.

The gold : reducing agent ratio was also varied for the citrate method, to produce colloids of varying average diameter. As citrate acts as both a reducing agent and stabiliser, at low citrate concentrations there is insufficient coverage of the gold colloids, leading to the formation of larger gold colloids [147]. Catalysts with gold nanoparticles of average diameter 14.7, 43 and 88 nm were prepared in this way.

From XRD analysis, it was evident that only metallic gold was present on all the catalysts (Figure 35). As expected, the catalysts with the largest gold particles had the most crystalline peaks and the peaks became broader with decreasing gold particle size.

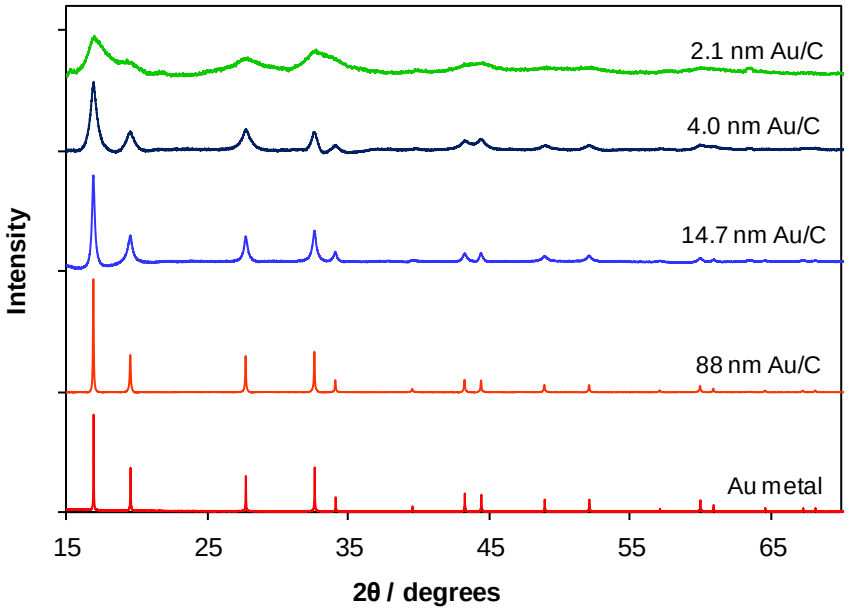


***Figure 35. XRD patterns of some Au/C catalysts at an X-ray wavelength of 0.689 Å. Intensities of gold metal, 88 nm Au/C, 14.7 nm Au/C and 4.0 nm Au/C have been scaled down by factors of 5, 20, 3 and 2, respectively.***

TEM micrographs (Figure 36) showed that each catalyst contained a distribution of gold particle sizes, and some areas with particle agglomeration (e.g. Figure 36c) were observed for most samples. There did not appear to be any particle agglomeration for the catalyst with an average gold particle size of 2.1 nm, but due to the difficulty in imaging these small gold particles, the possibility of some gold agglomeration being present cannot be discounted.

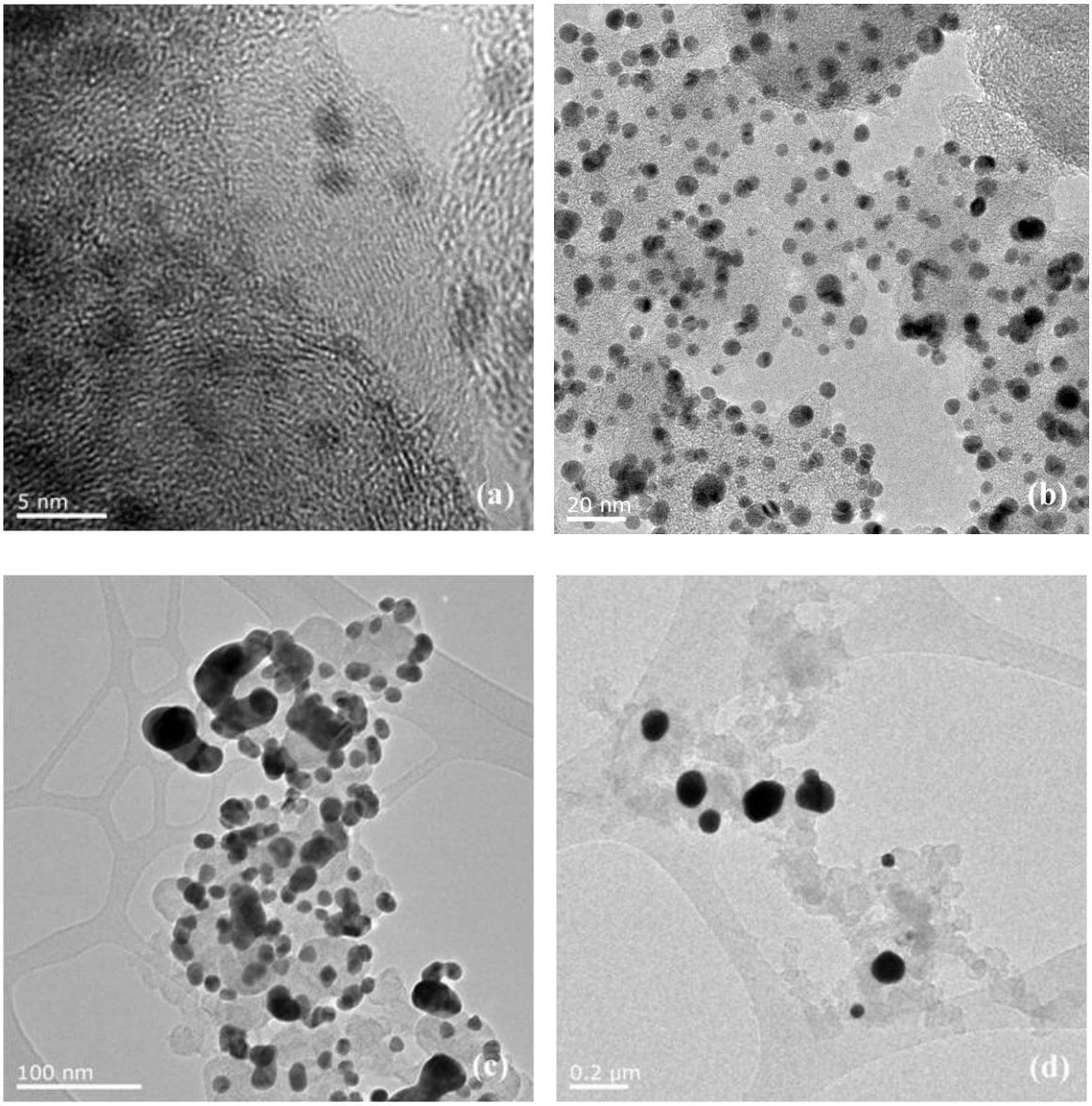


***Figure 36. TEM images of Au/C catalysts with average diameter (a) 2.1 nm, (b) 4.7 nm, (c) 14.7 nm and (d) 120 nm.***

Size-based histograms were generated by measuring only the individual, non-agglomerated gold particles and the gold PSD, $d_{ave}$ and S.A. of each catalyst were also determined from these measurements (Figure 37). The statistical error on the gold surface area was determined by error propagation based on an initial standard error of ± $x$ nm per particle, where $x$ = 0.2 nm for catalysts with gold $d_{ave}$ < 10 nm, and where $x$ = 0.9 nm, 3.6 nm, 13 nm and 6 nm for catalysts with gold $d_{ave}$ 14.7 nm, 43 nm, 88 nm and 120 nm, respectively. The standard error per particle is the estimated uncertainty determined from repeat measurements of a few particles on each catalyst.

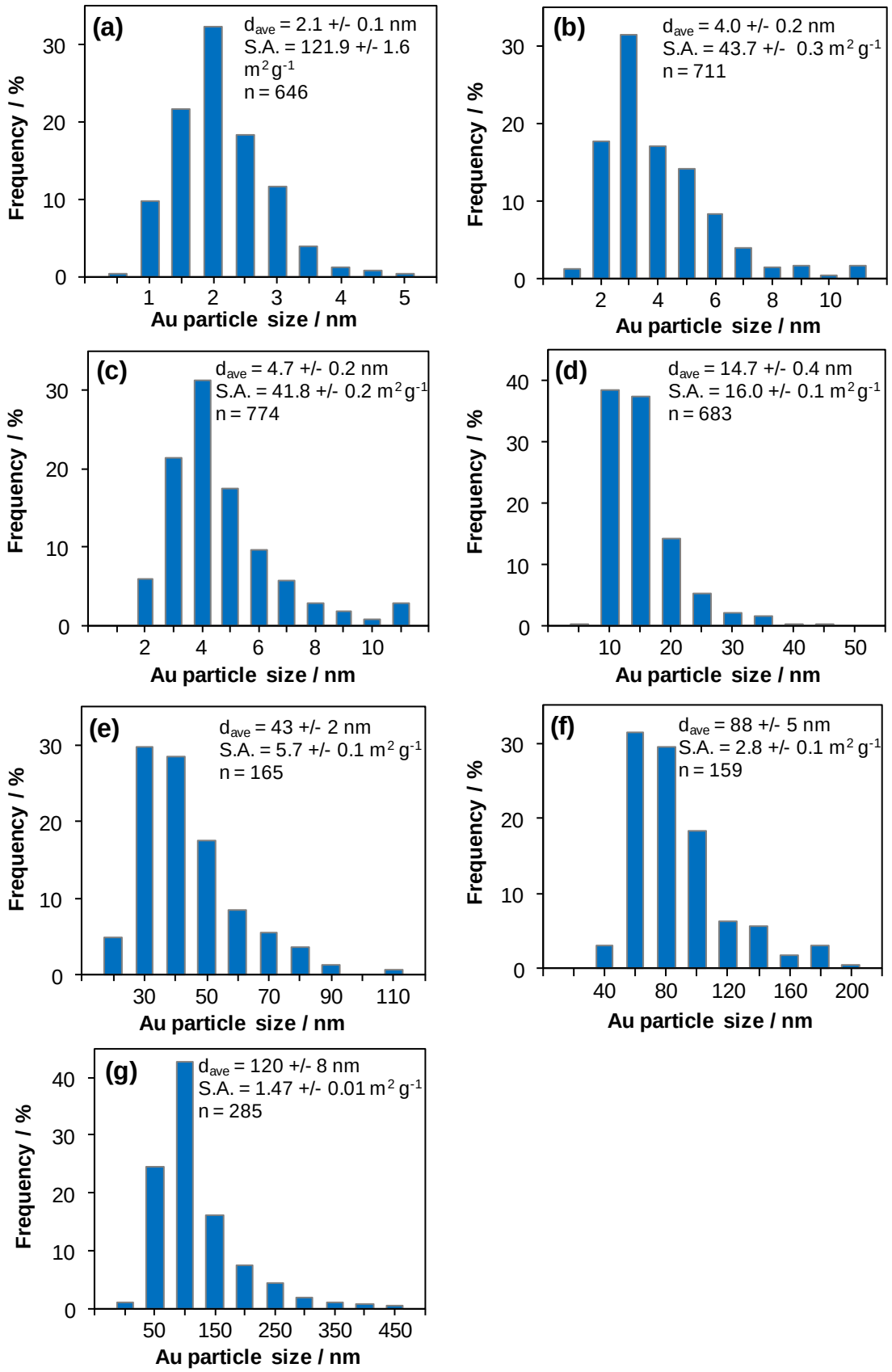


***Figure 37. Gold PSD, $d_{ave}$ and S.A. calculated using TEM data for Au/C catalysts, with average gold diameter (a) 2.1 nm, (b) 4.0 nm (c) 4.7 nm, (d) 14.7 nm, (e) 43 nm, (f) 88 nm and (g) 120 nm.***

In order to easily distinguish between the electrochemical behaviour characteristic of the various particle size regimes, the catalysts have been grouped into three categories based on the TEM measurements, and from here on will be referred to as small (≤ 4.7 nm), medium (14.7 nm) and large (≥ 43 nm) gold particles.

Cyclic voltammetry was used to characterise the gold nanoparticle surface of the catalysts in 1 M KOH solution. It was clear that the gold oxide reduction peak occurred at lower potentials for catalysts with small gold particles and the peak potential approached that of bulk gold for catalysts with medium or large gold particles (Figure 38, Appendix 5.1). This behaviour has also been noted for platinum [151, 152] and palladium [153] catalysts and has been attributed to increasing oxophilicity with decreasing particle size [151].

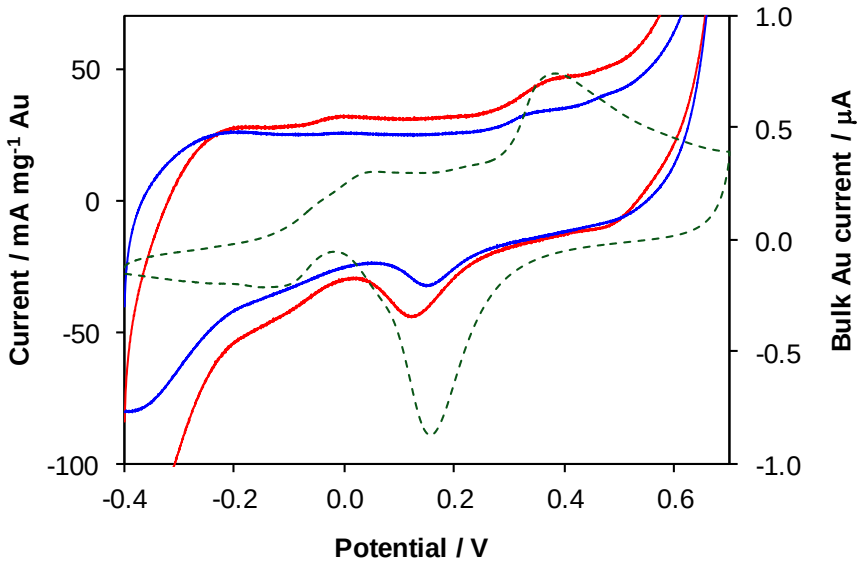


***Figure 38. CVs of 4.7 nm Au/C (red curve), 14.7 nm Au/C (blue curve) and bulk gold (dotted curve) in 1 M KOH at 50 mV $s^{-1}$. Potentials are shown vs. Hg/HgO reference.***

It was also noticed while cycling the 2.1 nm Au/C catalyst in KOH, that the charge associated with the gold oxide reduction decreased and the peak potential shifted by 31 mV to more positive potentials during that time (Appendix 5.1). As the gold oxide reduction charge can be correlated with the electrochemically active surface area, this observation indicates an increase in gold particle size with repeated cycling for the 2.1 nm catalyst. This is believed to be a reasonable assumption, since it has been confirmed with TEM for platinum catalysts that an oxide reduction peak shift to higher potentials after repeated cycling was the result of an increase in particle size [152]. The peak shifts were significantly lower for all the other catalysts and there was no decrease in surface area with repeated cycling, signifying that the catalysts with gold $d_{ave}$ ≥ 4.0 nm were more stable. Based on the electrochemically determined surface area of the 2.1 nm Au/C catalyst in the last cycle in KOH, it is estimated that the average gold particle size of this catalyst grew to be in the region between 4.0 and

4.7 nm, which is supported by similar electrochemical behaviour to the 4.0 and 4.7 nm Au/C catalysts in glycerol (shown later).

The onset of glycerol oxidation was observed to occur at lower potentials over small gold particles (Table 8), indicating that small gold particles were more easily activated than medium or large particles. The small and medium gold particles were also active over a wider range of potentials than the large particles, as evidenced by the higher peak drop-off potentials (Table 8). Peak drop-off potential is defined as the potential at which the anodic current during the forward sweep decreases to half the peak current, and this is indicative of the potential at which glycerol oxidation ceases.

***Table 8. Glycerol oxidation onset potentials and peak drop-off potentials for Au/C catalysts measured from CV in 0.5 M glycerol/1 M KOH. Potentials are reported vs. Hg/HgO reference.***

| $d_{ave}$ / nm | Onset potential / V | Peak drop-off potential / V |
|---|---|---|
| 2.1 | -0.22 | 0.44 |
| 4.0 | -0.22 | 0.51 |
| 4.7 | -0.20 | 0.49 |
| 14.7 | -0.19 | 0.50 |
| 43 | -0.10 | 0.40 |
| 88 | -0.10 | 0.41 |
| 120 | -0.08 | 0.41 |

As previously stated, the drop-off in glycerol oxidation at higher potentials can be attributed to the formation of the gold oxide monolayer, which renders the gold surface inactive [107]. This was observed for the catalysts with both small and medium gold particles (e.g. Figure 39a). However, the catalysts with large gold particles showed early deactivation in glycerol, possibly before formation of the passivating gold oxide monolayer (Figure 39b). As these larger gold particles exhibit a more positive gold oxide reduction potential and by implication a more positive gold oxide formation potential, the lower glycerol drop-off potential may actually be related to poisoning from build-up of glycerol and/or its intermediates on these particles.

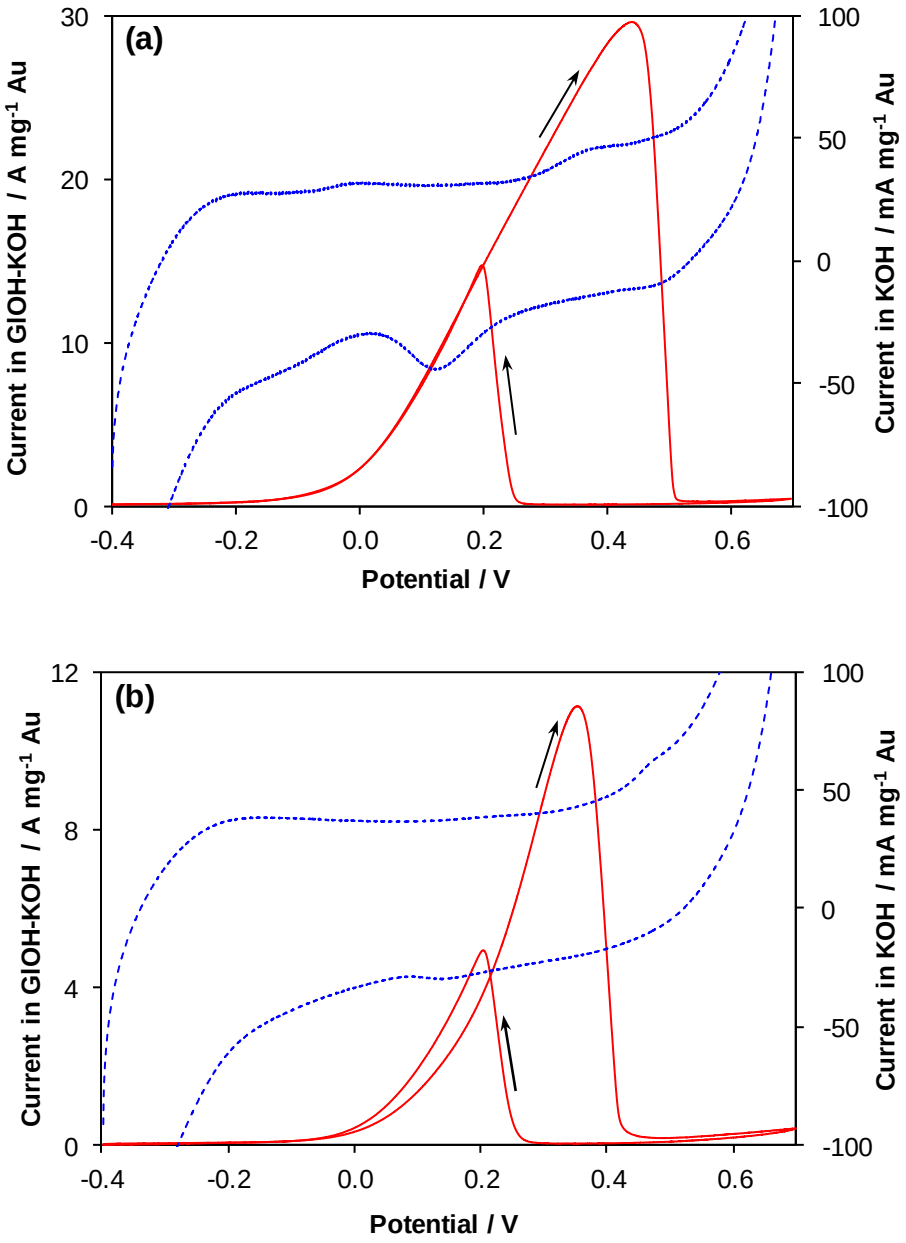


***Figure 39. CVs of (a) 4.7 nm Au/C and (b) 43 nm Au/C catalysts in 0.5 M glycerol/1 M KOH at 10 mV $s^{-1}$ (solid curve) and 1 M KOH at 50 mV $s^{-1}$ (dotted curve). Potentials are shown vs. Hg/HgO reference.***

The reverse oxidation curves of the catalysts which showed early deactivation on the forward sweep in 0.5 M glycerol/1 M KOH also took longer to merge with the forward sweep curves at lower potentials (Figure 39b). This again implies that the gold sites on these catalysts were blocked by glycerol oxidation intermediates, which made freeing of the gold surface more difficult to achieve.

Since the gold loadings varied on the Au/C catalysts, the gold-based mass activities were compared for glycerol oxidation (Figure 40; electrochemical data for all catalysts in Appendix 5.2). A clear activity trend is apparent, with small gold particles demonstrating the highest activities, followed by a general decrease in glycerol oxidation activity with increasing particle size. The small gold particles

were at least twice as active as the large gold particles. This is clearly expected, due to the decrease in active surface area per unit mass of gold as the gold particle size increases.

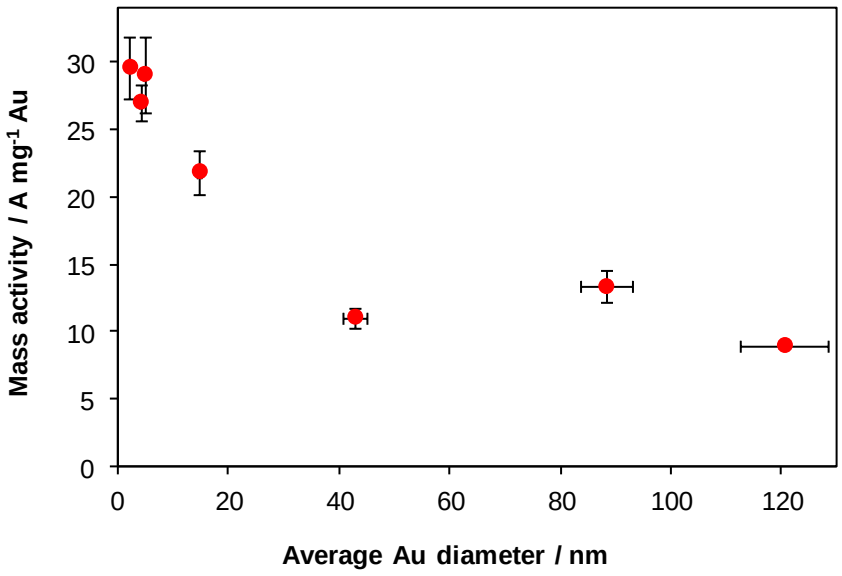


***Figure 40. Effect of gold particle size on mass activities of Au/C catalysts for glycerol oxidation. Peak currents were measured from forward sweep of CV in 0.5 M glycerol/1 M KOH.***

To assess whether the observed differences in mass activity (Figure 40) were due solely to gold surface area, the surface area of each catalyst was determined both electrochemically (EASA) and from TEM measurements, and the calculated specific activities (i.e. free from surface area effects) for each method were compared (Figure 41a). The EASA- and TEM- determined specific activities differed for most of the catalysts, and similar activities were only obtained for the catalyst with the largest (120 nm) gold particles. The EASA/TEM specific activity ratios were then compared for each catalyst (Figure 41b) and were observed to decrease with increasing gold particle size.

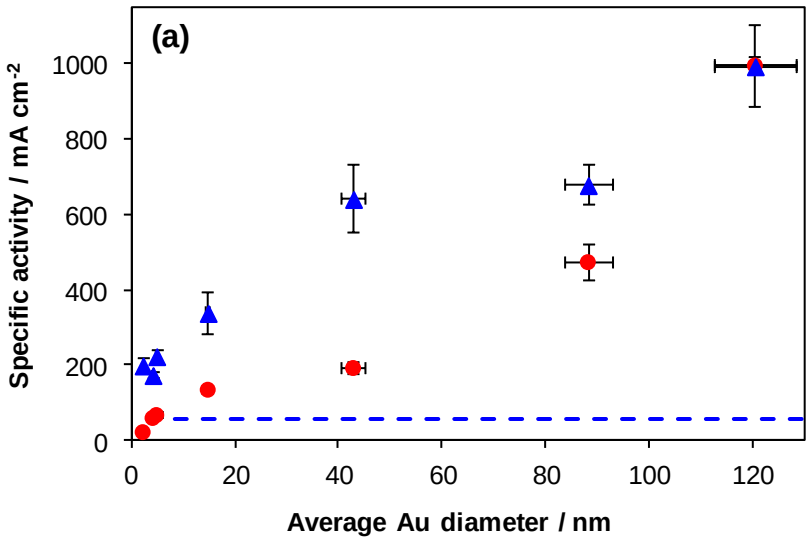

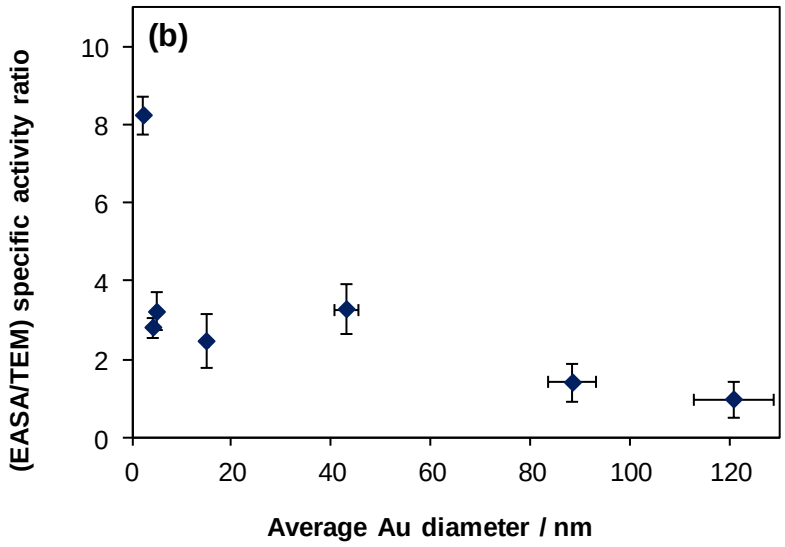


***Figure 41(a). Specific activities of Au/C catalysts for glycerol oxidation determined (▲) electrochemically and (●) from TEM analysis. The dashed line shows the electrochemically determined specific activity for polycrystalline gold, and (b) Ratio of EASA- to TEM- determined specific activities of Au/C catalysts.***

There are a number of possible reasons for this discrepancy – one of which is that agglomerated particles were not taken into account in TEM analysis, leading to higher calculated surface areas than electrochemically determined, and hence lower specific activities. Another reason could be the presence of micropores in the Vulcan XC-72R carbon which have been shown to cause inaccessibility of the nanoparticles which get trapped within, resulting in lower EASA values [128]. Given that pore entrapment would be a bigger problem for small nanoparticles than large ones and especially considering that the discrepancy between the EASA- and TEM- determined specific activities was highest for the 2.1 nm gold catalyst (Figure 41b), this therefore seems a plausible reason. The measure of uncertainty regarding the accuracy of the gold EASA determination [97, 98, 106] also needs to be taken into consideration, which implies that the gold surface areas obtained using this method can never be regarded as exact. However, the EASA-determined specific activities are still believed to be more accurate than TEM-determined activities.

Regardless of the differences in absolute values of the specific activities, a clear trend of increasing specific activity with increasing gold particle size is evident (Figure 41a). It is interesting to note that a similar trend has been observed for supported metal catalysts for other reactions, e.g. Au/C for CO oxidation [119] and Pt/C for methanol oxidation [152] and oxygen reduction [151]. However, Poirier and Stoner [154] have shown that the trend is reversed over thin-film platinum for oxygen reduction, i.e. smaller particles have higher specific activities. The authors have explained the difference in specific activity trends between thin-film and carbon-supported catalysts by mass transfer effects and over-simplifying the complexity of dispersed catalysts by using particle size as a dominant microstructural variable.

It is also noteworthy that this trend differs from that found in heterogeneous gold catalysis, where the turnover frequency for CO oxidation over supported gold catalysts has been shown to increase with decreasing gold particle size [155]. Another important observation is that the Au/C catalysts were found to have significantly higher EASA-based specific activities than bulk gold (Figure 41a), demonstrating the superiority of gold nanoparticles over that of bulk gold, for alcohol electrooxidation.

As with the Au/$x$MnO$_2$/C system (Chapter 4), all nano-gold catalysts had significantly higher $I_f/I_r$ peak ratios than bulk gold (Figure 42). However, unlike the Au/$x$MnO$_2$/C catalysts, the most active catalysts in this study did not necessarily have the highest $I_f/I_r$ peak ratios. Since a low $I_f/I_r$ ratio is supposed to be both an indicator of poor alcohol oxidation in the forward sweep, as well as poor resistance to poisoning by residues [111, 113], this ratio is clearly not always an accurate measure of a catalyst's activity. This is probably because under the dynamic conditions in which CV is run, each catalyst could experience different mass transfer effects, depending on the extent to which glycerol and its intermediates are oxidised, how easily they are released, etc. A similar finding was reported by Ding, *et al.* [156], where their most active catalyst also had the lowest $I_f/I_r$ ratio. The authors concluded that catalytic activity could therefore not be completely evaluated by using only the $I_f/I_r$ ratio.

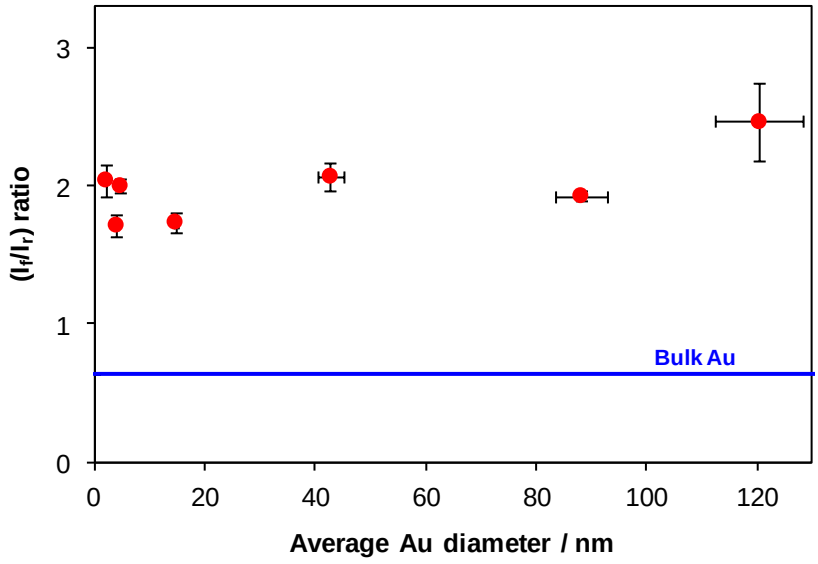


***Figure 42. Forward-to-reverse peak ($I_f/I_r$) ratios of Au/C catalysts in glycerol measured from CV in 0.5 M glycerol/1 M KOH.***

To elucidate the possible role of gold surface orientation on the observed catalyst activities for glycerol oxidation, the surface structure of the Au nanoparticles was investigated by using lead UPD. This is a well-known technique for identifying the exposed gold facets from the positions of their stripping peaks in the lead UPD region [103]. The stripping potentials of lead adsorbed on polycrystalline gold in the UPD region were compared with peak assignments from literature [103, 157], in order to assist with identification of the surface facets of some of the gold colloids (Figure 43, Appendix 5.3).

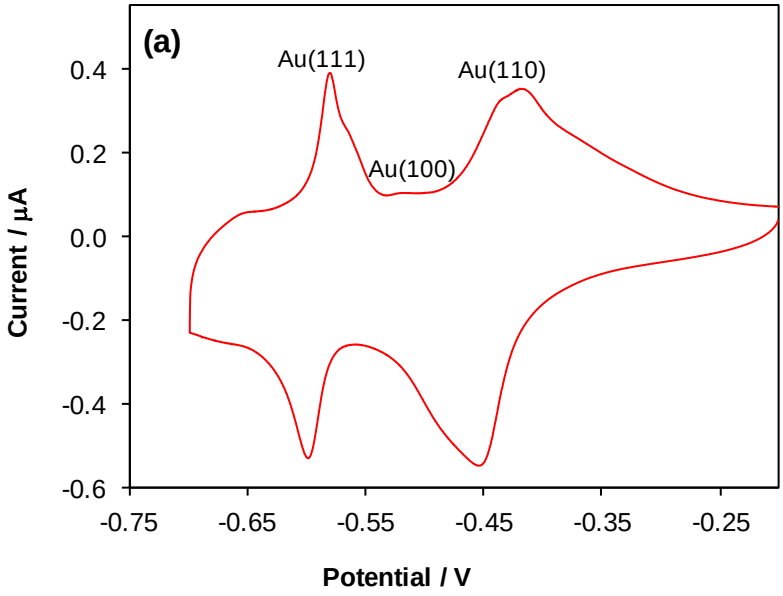
(a)
Au(111)
Au(110)
Au(100)
0.4
0.2
0.0
-0.2
-0.4
-0.6
-0.75
-0.65
-0.55
-0.45
-0.35
-0.25
Current / µA
Potential / V

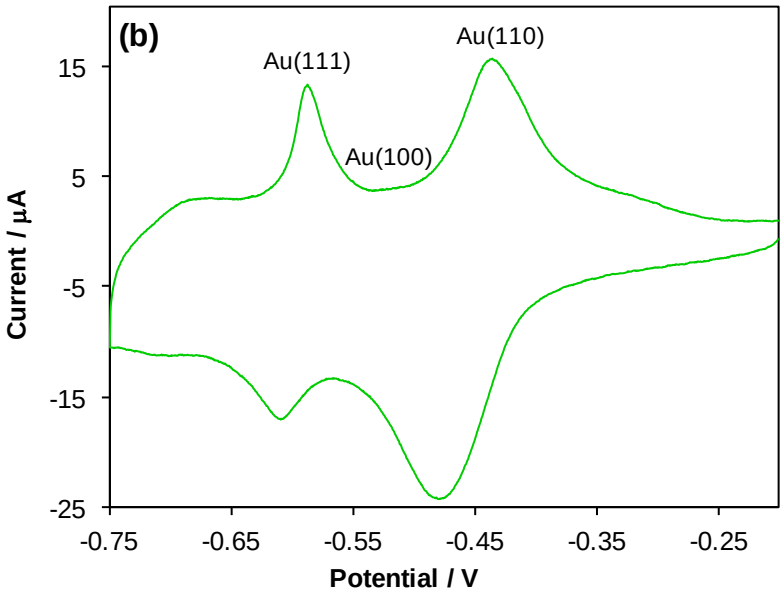
(b)
Au(111)
Au(110)
Au(100)
15
5
-5
-15
-25
-0.75
-0.65
-0.55
-0.45
-0.35
-0.25
Current / µA
Potential / V

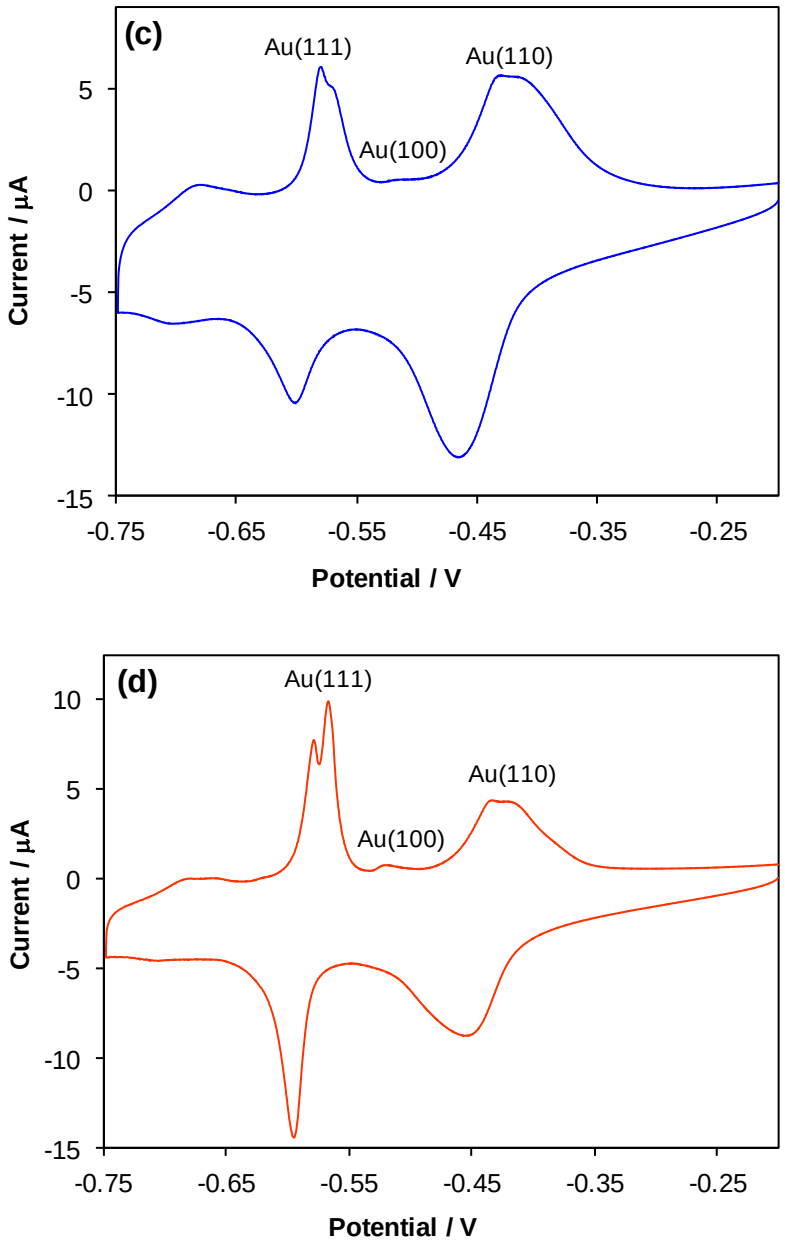


***Figure 43. CV profiles of (a) polycrystalline gold, (b) 3.2 nm Au colloids, (c) 14.7 nm Au colloids and (d) 88 nm Au colloids in 1 mM $Pb(NO_3)_2$/0.1 M NaOH at 50 mV $s^{-1}$. Potentials are referenced vs. SCE.***

Au(111) and Au(110) were the predominant crystal planes on polycrystalline gold as well as on the gold nanoparticles. The Au(100) surface, which was present as only a very small peak in polycrystalline gold, was barely noticeable for the 3.2 nm colloids [114] which were used to synthesise the 4.0 and 4.7 nm catalysts. This can be attributed to ill-defined Au(100) domains on these small particles [103]. With an increase in gold colloid size from medium (14.7 nm) to large (88 nm), the Au(100) peak started to become more prominent – although it was still significantly smaller than the Au(111) and Au(110) peaks. Another noticeable difference between the medium and large gold colloids was the splitting of the Au(111) peak becoming more apparent, accompanied by an increase in Au(111) wide domains [103] at -0.568 V, with increasing colloid size.

The charge under each peak was calculated for each of the colloids and their percentages compared (Table 9, Appendix 5.3). It should be noted that these values are merely indicative of the proportionate values of the lower-index gold facets, since the higher-index facets which cannot be identified with lead UPD, are not taken into account here.

***Table 9. Percentage of surface facets on gold colloids, based on peak charges in the lead UPD region***

| **Au colloid size / nm** | **Peak area / %** | | |
|---|---|---|---|
| | **Au(111)** | **Au(110)** | **Au(100)** |
| 3.2 | 24.2 | 75.7 | 0.1 |
| 14.7 | 28.9 | 70.9 | 0.2 |
| 88 | 47 | 52 | 1 |

Au(110) was found to be the dominant plane on small gold particles, and was observed to decrease in relation to Au(111) with increasing particle size – a trend also recently reported by Wain, *et al*. [157]. The higher concentration of Au(110) on the small gold particles could explain the lower onset potentials for glycerol oxidation over these particles, since the oxidation (and hence activation) of the Au(110) surface has been shown to take place at significantly lower potentials than Au(111) and Au(100) in a basic medium [158]. The increase in specific activity with increasing gold particle size can be attributed to the corresponding increase in Au(111) surface facets. This is supported by the reported order of electrocatalytic activity for glycerol oxidation over gold single crystals, of Au (111) > (100) > (110) [159]. Given the low concentration of Au(100), it seems unlikely that it made any significant contribution to the glycerol oxidation activities of the larger particles.

Potentiostatic measurements were used to assess catalyst stability over time (Figure 44) and as expected, all the catalysts were at least 5 times more active at 0.2 V than at 0 V. At both potentials, the catalysts with the small gold particles had the highest mass activities for the duration of the scan. In addition, these catalysts, along with the catalyst with medium gold particles, had the smallest change in current over the measurement period – i.e. higher $I_{30\ min}/I_{0\ min}$ values (Table 10). For the $I_{0\ min}$ value, the current recorded at 2 s was used instead of at 0 s, in order to minimise the influence of the double layer capacitive charging current. All catalysts had smaller decay rates at 0.2 V than 0 V, indicating better stability at the higher potential.

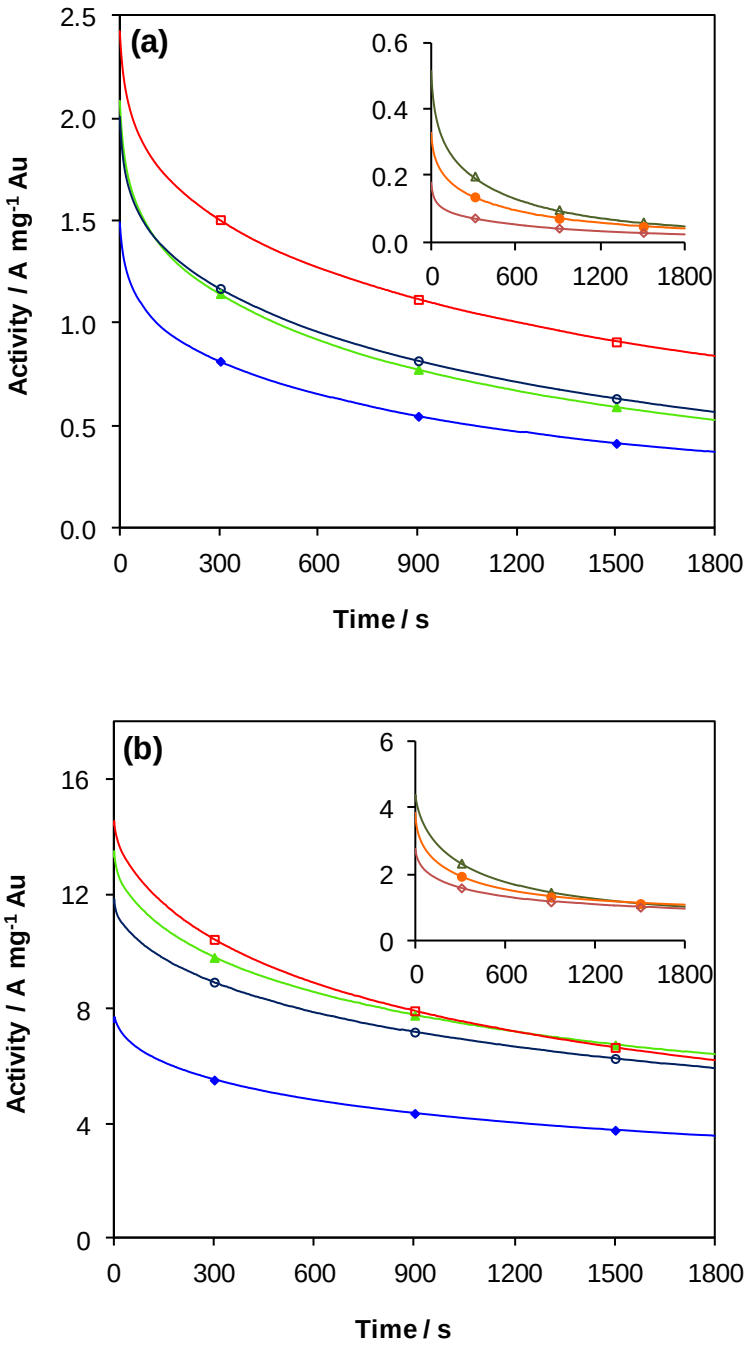


***Figure 44. Potentiostatic measurements of Au/C catalysts with $d_{ave}$ values of (▲)2.1 nm, (○)4.0 nm, (□)4.7 nm, (♦)14.7 nm. Inset shows (△)43 nm, (●)88 nm and (◊)120 nm. Scans were recorded at (a) 0 V and (b) 0.2 V (vs. Hg/HgO) for 30 min.***

***Table 10. Glycerol oxidation current ratios ($I_{30\ min}/I_{0\ min}$) of Au/C catalysts from potentiostatic measurements at 0 V and 0.2 V (vs. Hg/HgO) in 0.5 M glycerol/1 M KOH.***

| $d_{ave}$ / nm | Current ratio ($I_{30\ min}/I_{0\ min}$) | |
|---|---|---|
| | **0 V** | **0.2 V** |
| 2.1 | 0.26 | 0.48 |
| 4.0 | 0.29 | 0.50 |
| 4.7 | 0.35 | 0.43 |
| 14.7 | 0.25 | 0.48 |
| 43 | 0.10 | 0.24 |
| 88 | 0.12 | 0.28 |
| 120 | 0.13 | 0.34 |

While the catalysts with large gold particles had the highest intrinsic activities for glycerol oxidation, they were also the most unstable, with the largest decreases in current during potentiostatic measurements (Table 10). The lower stability of the catalysts with large gold particles (which is supported by the early decline in glycerol oxidation currents observed from CV - Figure 39b) could be due to poisoning of the larger proportion of Au(111) facets by glycerol oxidation intermediates. Another possible reason is that because of the low gold surface area on these catalysts, there are insufficient gold sites available for the oxidation of adsorbed intermediates. A much smaller contribution to the lower stability could also come from the increase in the Au(100) domain with increasing particle size, as Yin, *et al*. [160] demonstrated that Pt-Pd alloy (100) nanocubes were less stable than (111)-facet-enclosed nanotetrahedrons and even Pt/C after repetitive cycling in methanol.

In Chapter 4, it was speculated that the lower stability of the $MnO_2$-containing catalysts during potentiostatic measurements at 0 V could be due to poisoning of either mixed-valence $MnO_2$ or the smaller gold particles on those catalysts. In order to further investigate this, the current ratios (at 0 and 0.2 V) of the active catalysts from the $MnO_2$ investigation (i.e. catalysts containing ≤ 9 % $MnO_2$), along with those from this study, were plotted against the gold $d_{ave}$ values (Figure 45).

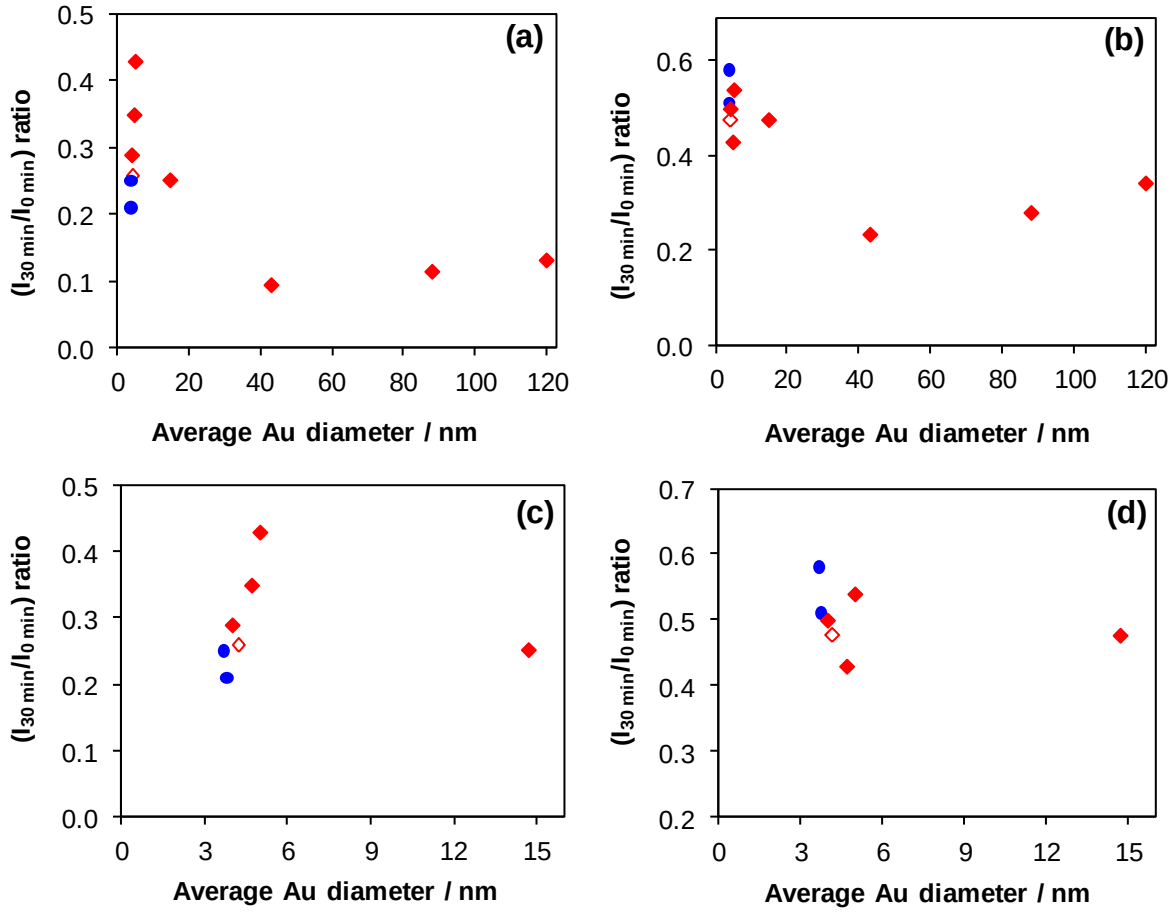


***Figure 45. Current ratios from potentiostatic scans as a function of gold $d_{ave}$ for (♦) Au/C catalysts and (●) Au/$MnO_2$/C catalysts at (a) 0 V and (b) 0.2 V (vs. Hg/HgO). Enlarged views of the current ratios of catalysts with $d_{ave}$ ≤ 14.7 nm at 0 V and 0.2 V are shown in (c) and (d), respectively. Due to growth of gold particles on the 2.1 nm Au/C catalyst, the data point was plotted at the estimated (from measured EASA) gold $d_{ave}$ value of 4.2 nm and is designated as (◊).***

At 0 V (Figure 45a and c), there appears to be a clear correlation between gold particle size and catalyst stability, with an increase in the current ratio up to 5.0 nm and then a rapid decrease with further increase in gold particle size. At 0.2 V (Figure 45 b and d), even excluding the $MnO_2$ catalysts which improve the stability at the higher potential (discussed in Chapter 4), there is no such clear trend within the region of small gold particles.

However, in assessing these results, there are a few cautionary factors which have to be taken into consideration:

- There are no data points between 5.0 nm and 14.7 nm, so if there is a true optimum, it may yet lie in that region,
- The plotted data points are based on only one measurement, which means the range of error is unknown,
- Plotting the CA ratio *vs.* average gold diameter could be seen as an oversimplification of the results, as there is actually a spread of gold particle sizes on each catalyst, and

- Adding the catalysts containing $MnO_2$ – although it makes the trend look stronger – is not ideal, as there are two variables here ($MnO_2$ and gold size) which could be causing the observed poisoning effect.

With that being said, there is a strong indication that very small gold particles may be more easily poisoned at lower potentials, and that there may be an optimum size with respect to catalyst stability within the region of small particles. This should be further investigated, preferably by synthesising and testing small gold catalysts (e.g. 2-10 nm) with a more monodisperse particle size distribution.

Electrochemical impedance spectroscopy (EIS) was used to evaluate the glycerol oxidation kinetics on the Au/C catalysts at 0 V and 0.2 V (Figure 46).

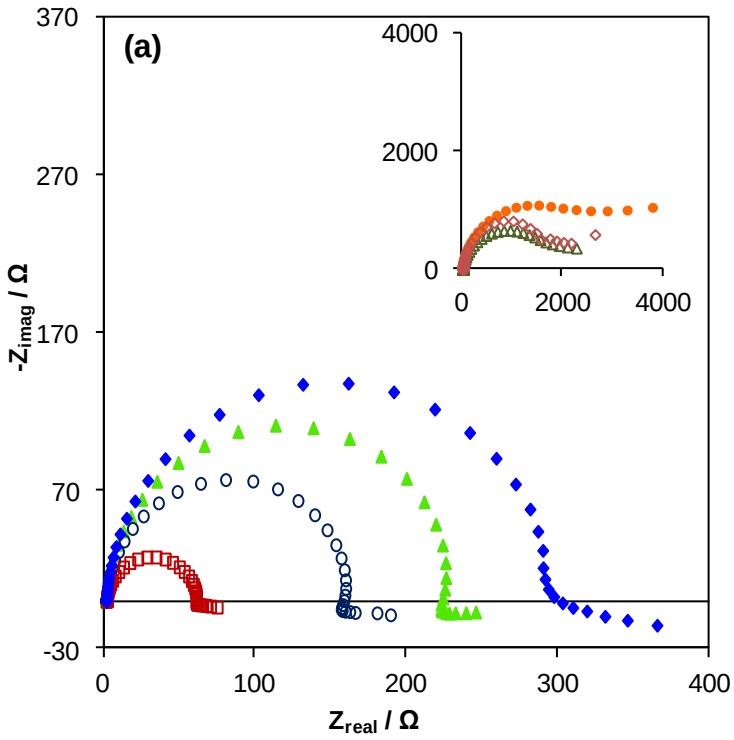

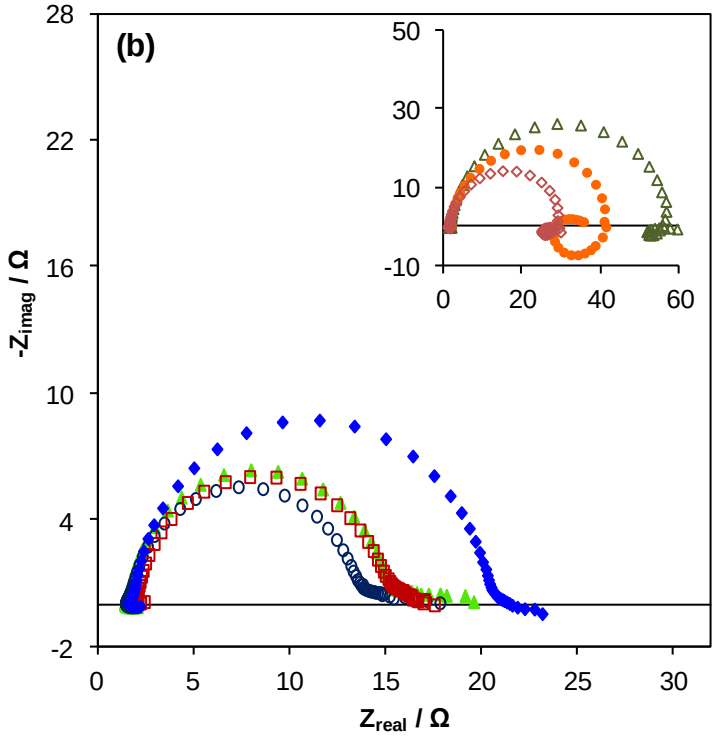


***Figure 46. Nyquist plots of Au/C catalysts with $d_{ave}$ values of (▲)2.1 nm, (○)4.0 nm, (□)4.7 nm, (♦)14.7 nm. Inset shows (△)43 nm, (●)88 nm and (◊)120 nm. Plots were recorded at (a) 0 V and (b) 0.2 V (vs. Hg/HgO).***

Increasing the potential from 0 V to 0.2 V gave decreased $R_{ct}$ for all catalysts, signifying improved glycerol oxidation kinetics at the higher potential. The catalysts with small gold particles had the lowest $R_{ct}$ values at both 0 V and 0.2 V, which is in agreement with the higher mass activities seen in both CV and potentiostatic scans.

At 0 V, the curves of the catalysts with small and medium gold particles moved into another quadrant (+ve $Z_{real}$, +ve $Z_{imag}$ values) at low frequencies. This feature has been attributed to pseudoinductance caused by the oxidation of adsorbed intermediates [142]. The catalysts with large gold particles had significantly larger impedance arcs, indicating slower glycerol oxidation kinetics. This ties in with the lower mass activities obtained in both cyclic voltammetry and potentiostatic measurements for these catalysts.

At 0.2 V, the pseudoinductance feature was not as evident for the catalysts with small gold particles, which could imply that the adsorbed intermediates were removed at the higher potential. Given the significantly lower $R_{ct}$ values for those catalysts, it is possible that glycerol oxidation could occur with relative ease and even proceed further along the oxidation pathway for the catalysts with small gold particles than over those with medium- to large- gold particles. This was tested by investigating the electrooxidation of possible gold-catalysed glycerol oxidation intermediates over some of the catalysts with small, medium or large gold particles – the results of which are reported in Chapter 7. For the catalysts with large gold particles, a low-frequency inductive loop was observed (Figure 46b - inset).

This can be attributed to an increase in $OH_{ad}$ sites at the higher potential, which oxidises the adsorbed intermediates, thereby freeing up the metal sites for further oxidation [161].

To summarise the study into gold particle size, it was found that gold-based mass activities decreased with increasing gold $d_{ave}$ and small gold particles were at least twice as active as the large gold particles. In addition, small gold particles were activated earlier, resulting in lower onset potentials – which is likely due to the predominance of Au(110) facets on those particles. Catalysts with large gold particles had the highest specific activities, which was attributed to the increase in Au(111) with increasing gold particle size. However these catalysts were also more easily poisoned, showing early peak drop-offs during CV, and were less stable during potentiostatic measurements. This could be due to the higher fraction of Au(111) or the lower gold surface area. There is also an indication from potentiostatic measurements that very small gold particles may be more easily poisoned at lower potentials and the “optimum” size with respect to catalyst stability could lie somewhere in the region of 5 nm. Importantly for fuel cell applications, conditions such as high mass activity, lower overpotentials and higher stability can all be met by small gold particles with predominantly Au(110) facets.

# 6 EFFECT OF GOLD LOADING

## 6.1 Introduction

Preparation of gold catalysts with varying gold loadings was initially attempted for the investigation into particle size (Chapter 5), where it was expected that the average gold diameter would increase with increasing gold loading. However, as already discussed, this did not occur. There were some interesting findings relating to gold loading and diffusion, however, and this is detailed in this chapter. This was also a subject of interest as studies into electrocatalysts are carried out using catalysts with high metal loadings (≥ 20 wt %), while heterogeneous catalysis utilises much less gold; e.g. studies into the heterogeneously-catalysed oxidation of glycerol have been carried out using only 1 wt % gold [162, 163].

## 6.2 Experimental

The preparation of the average 3.2 nm gold colloids using a modified version of the method of Martin, *et al.* [114] and the method of deposition onto the carbon support are detailed in Chapter 4. In order to vary the gold loadings, the gold concentration was kept the same for each preparation and only the amount of carbon support was varied.

The characterisation and electrochemistry techniques used in this section have been detailed in Chapter 4.

## 6.3 Results and discussion

Analysis by TEM showed that all the catalysts had areas of well-dispersed gold particles with a distribution of particle sizes, as well as areas with gold agglomeration. Selected TEM micrographs of the lower-loaded (1 - 12.5 %) gold catalysts are shown in Figure 47. Images of the 15 and 20 % Au/C catalysts were shown in Chapter 5, representing the 4.7 nm and 4.0 nm Au/C catalysts, respectively.

The particle size histograms (Figure 48) were generated by measuring only the individual, non-agglomerated particles. The gold PSD, number-weighted gold $d_{ave}$ and S.A. of each catalyst were determined from TEM measurements. The statistical error on the gold surface area was determined by error propagation based on an initial standard error of ± 0.2 nm per measured particle. The PSDs of the 15 and 20 % Au/C catalysts were shown in Chapter 5. As stated previously, there did not appear to be any trend relating gold loading with the average particle size distribution obtained from TEM analysis, and most catalysts had similar $d_{ave}$ values of around 4.6 – 4.8 (± 0.2) nm (Figure 49).

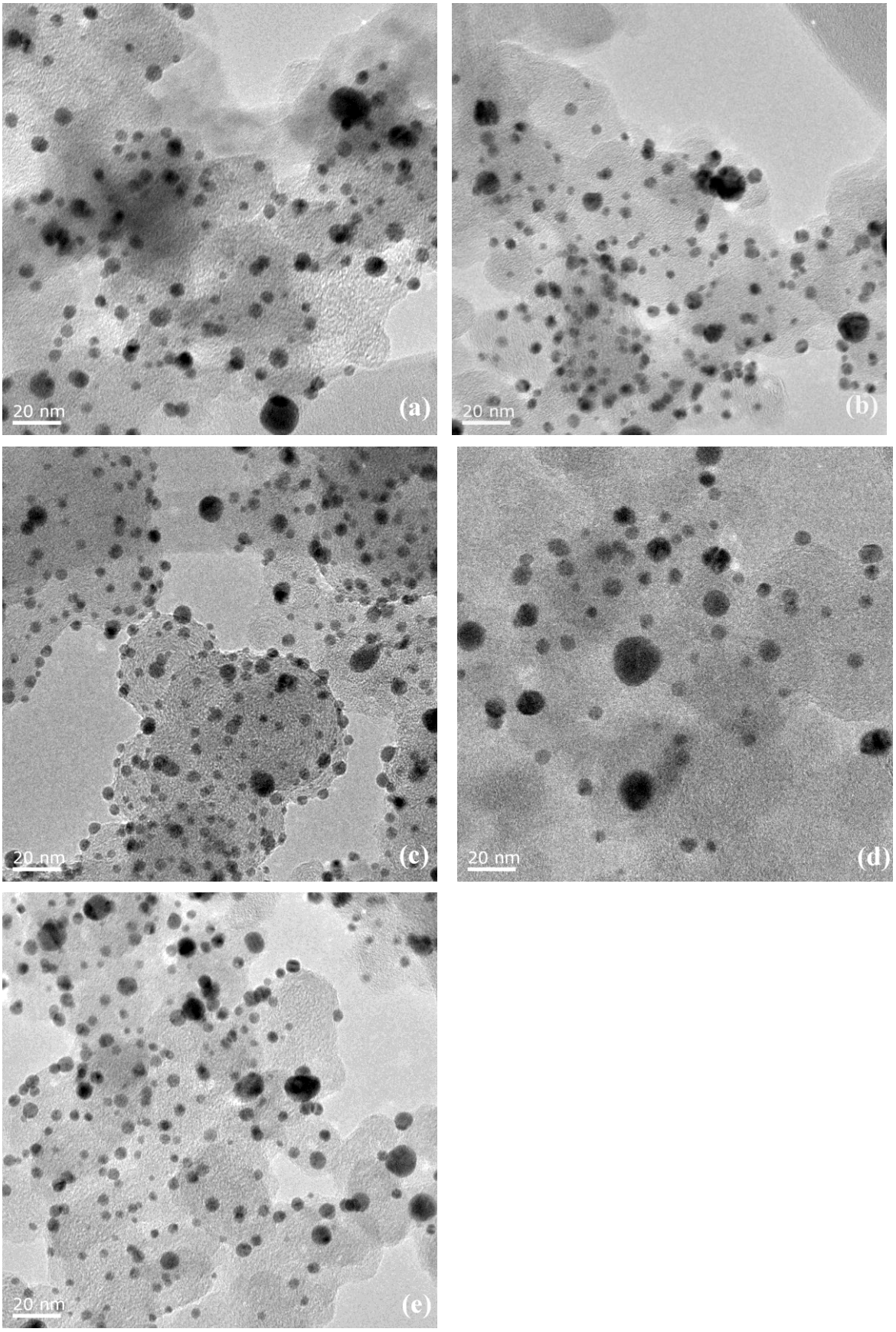


***Figure 47. TEM micrographs of xAu/C catalysts, where x = (a) 1 %, (b) 5 %, (c) 7.5 %, (d) 10 % and (e) 12.5 %.***

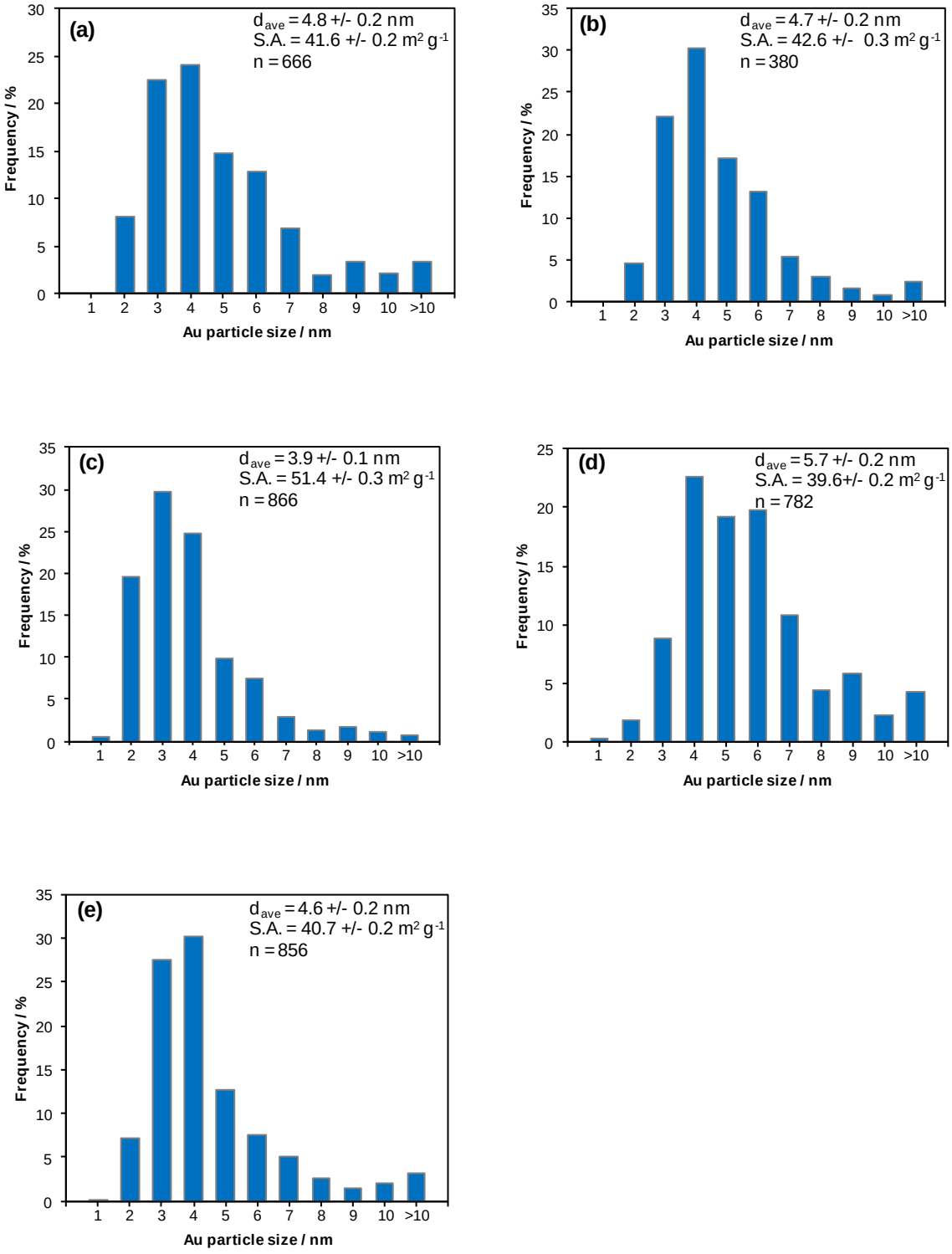


***Figure 48. Gold PSD, $d_{ave}$ and S.A. calculated using TEM data of xAu/C catalysts, where x = (a) 1 %, (b) 5 %, (c) 7.5 %, (d) 10 % and (e) 12.5 %.***

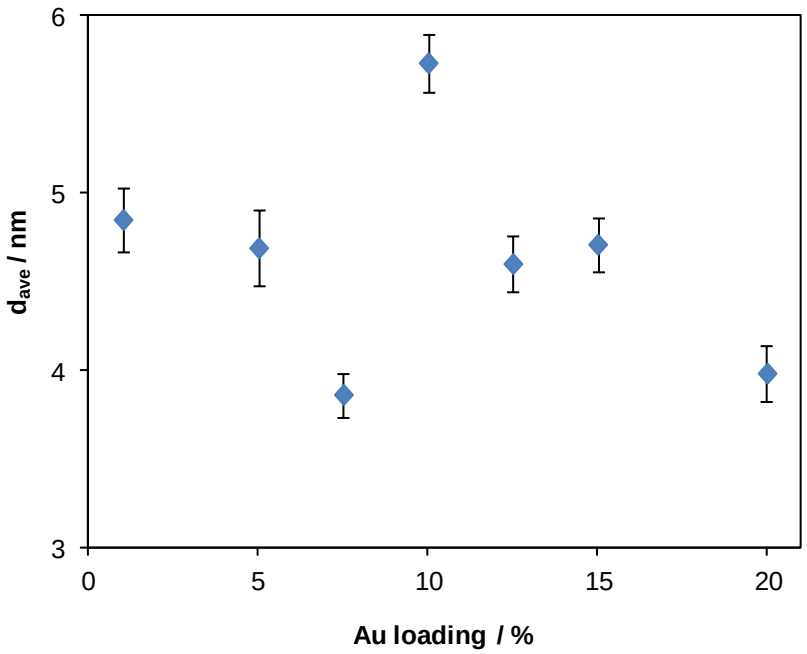


***Figure 49. $d_{ave}$ calculated from TEM analysis for Au/C catalysts with varying gold loadings.***

The average charge under the gold oxide reduction peak was calculated and plotted as a function of the gold loading (Figure 50a; data in Appendix 6.1). An almost-linear trend of increasing charge (and by implication, increasing gold surface area) with increasing gold loading is apparent. The deviations from linearity are most evident for those catalysts which had statistically significant differences in $d_{ave}$ values, *viz.* the catalysts with 7.5, 10 and 20 % gold loadings (Figure 49). In order to correct for these differences, the gold oxide reduction charges were plotted against the mass-normalised surface area determined from TEM measurements (Figure 50b; data in Appendix 6.1). A clear linear trend is apparent ($r^2$ = 0.985), which strongly suggests that a similar proportion of the gold surface is exposed to the KOH electrolyte on all the catalysts. This result also serves to confirm the relative accuracy of the TEM-determined surface areas of the gold catalysts. However, there is still a discrepancy between TEM- and EASA- determined surface areas (shown later in terms of specific activities), which indicates that possibly not all of the catalyst layer is active. It has been considered that this could be due to the bottom of the catalyst layer not being fully wetted – although it was deemed unlikely, as large gold particles with an identical bottom layer (i.e. the Vulcan carbon support) showed good correlations between EASA and TEM surface areas (Chapter 5). The EASA-TEM discrepancy is discussed in more detail later on in this chapter.

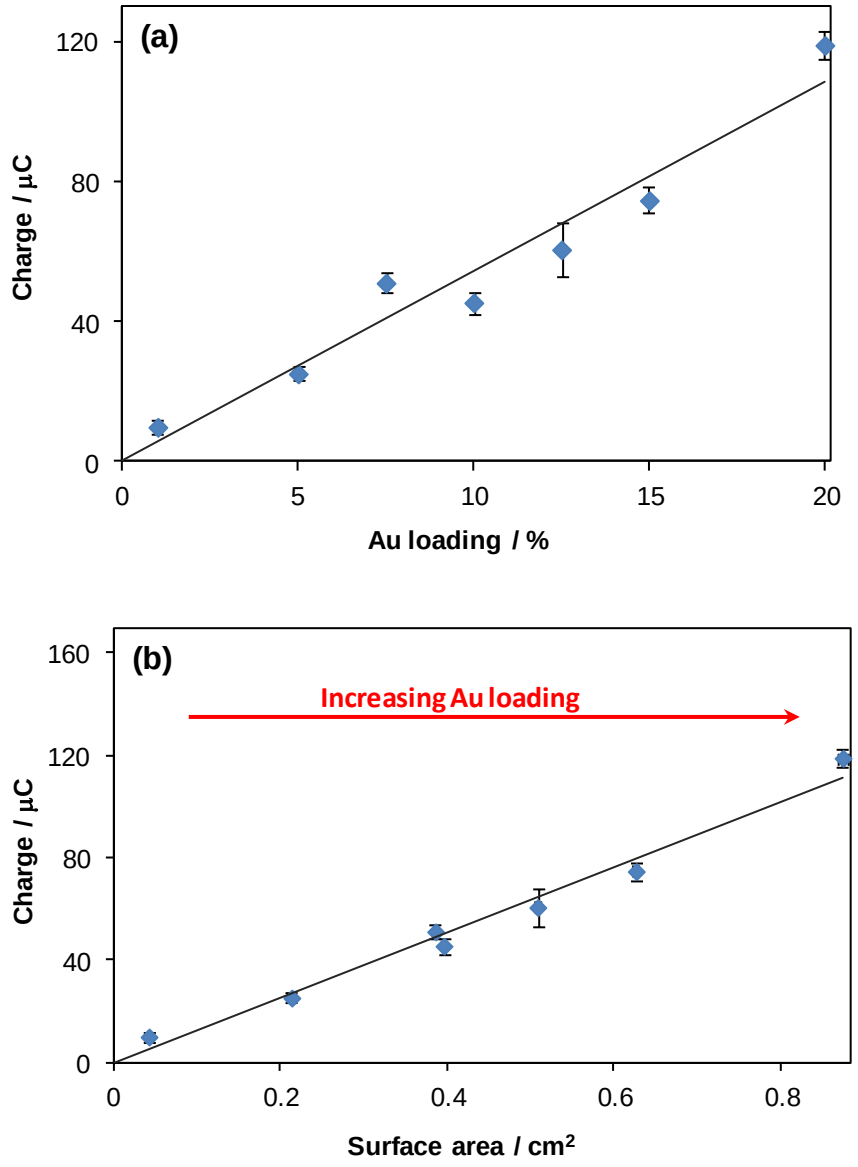


***Figure 50. Correlation between gold oxide reduction charge and (a) gold loading, (b) TEM-determined surface area.***

From CV in 0.5 M glycerol/1 M KOH, it was clear that the catalysts with lower (≤12.5 %) gold loadings deactivated earlier, possibly even before monolayer oxide formation (Figure 51, Table 11). This indicates that there is insufficient gold surface area on catalysts with lower gold loadings to resist poisoning. This is possibly a result of the higher proportion of glycerol relative to gold on these catalysts – resulting in a build-up of glycerol and/or its intermediates on the gold surface or within the catalytic layer. An important observation to note here is that this result correlates well with the study into the effect of gold particle size (Chapter 5), where large gold particles (with lower surface areas) also showed early deactivation in glycerol. The implications of this are discussed later.

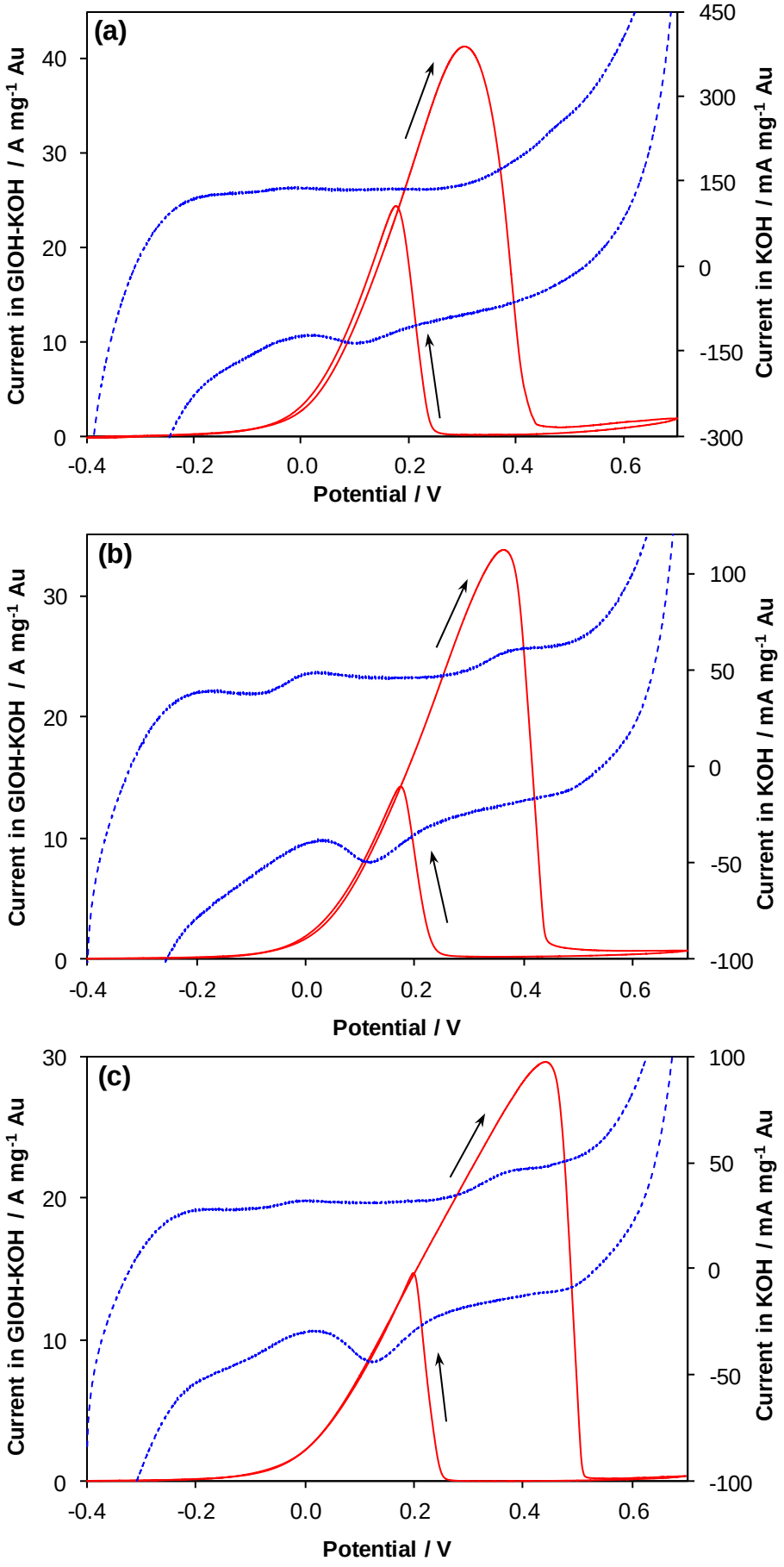
(a)
Current in GlOH-KOH / A mg-1 Au
Current in KOH / mA mg-1 Au
Potential / V
(b)
Current in GlOH-KOH / A mg-1 Au
Current in KOH / mA mg-1 Au
Potential / V
(c)
Current in GlOH-KOH / A mg-1 Au
Current in KOH / mA mg-1 Au
Potential / V

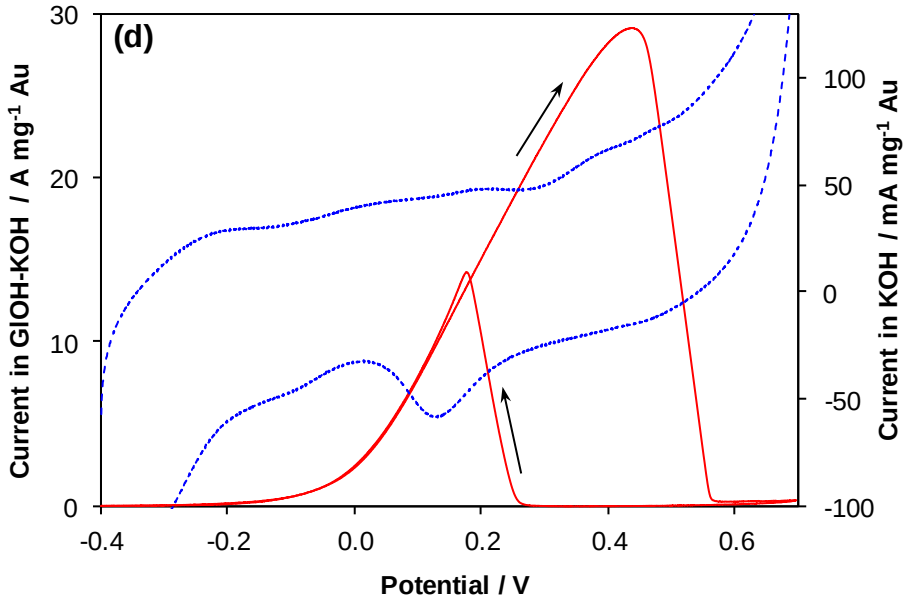


***Figure 51. CVs of xAu/C catalysts in 0.5 M glycerol/1 M KOH at 10 mV $s^{-1}$ (red solid curve) and 1 M KOH at 50 mV $s^{-1}$ (blue dotted curve), where x = (a) 5 %, (b) 10 %, (c) 15 % and (d) 20 %.***

A comparison of the onset potentials and peak drop-off potentials (Table 11) showed that the catalysts containing ≤ 12.5 % gold were active over a smaller range of potentials than the catalysts with ≥ 15 % gold loadings. The onset potentials for the 1-10 % gold-loaded catalysts were at least 20 mV higher than for the other catalysts, which is likely due to slight mass transfer effects in the 0.5 M glycerol/1 M KOH solution at low potentials. However, it should be noted that the onset potential for glycerol oxidation over the catalysts with ≤ 10 % gold still occurs at least 60 mV earlier than over large (≥ 43 nm) gold particles (i.e. the effect of having small particles outweighs the effect of having low loadings). This again confirms the ability of Au(110) to induce earlier glycerol oxidation on the small gold particles (discussed in Chapter 5).

***Table 11. Glycerol oxidation onset potentials and peak drop-off potentials for Au/C catalysts, measured from CV in 0.5 M glycerol/1 M KOH. Potentials are reported vs. Hg/HgO reference.***

| Au loading / % | Onset potential / V | Peak drop-off potential / V |
|---|---|---|
| 1 | -0.16 | 0.31 |
| 5 | -0.17 | 0.38 |
| 7.5 | -0.18 | 0.41 |
| 10 | -0.17 | 0.41 |
| 12.5 | -0.20 | 0.43 |
| 15 | -0.20 | 0.49 |
| 20 | -0.22 | 0.51 |

The linear relationship ($r^2$ = 0.984) between gold loading and catalyst mass activity (Figure 52a; data in Appendix 6.2 and 6.3) for the catalysts with gold loadings from 5 to 20 %, implies equivalent utilisation of the gold surface on each catalyst. It was therefore expected that these catalysts would have similar gold mass- and area- normalised activities – which is confirmed in Figure 52b and Figure 53 for the catalysts with 5-20 % gold loadings, with most of the catalysts demonstrating similar activities (within statistical error). Only the catalyst with the lowest (1 %) gold loading was significantly less active, and considering that this catalyst fitted the linear charge/surface area trend in 1 M KOH (Figure 50b), the deviation from linearity in the 0.5 M glycerol/1 M KOH solution can only be attributed to significant mass transfer limitations in glycerol for the 1 % Au/C catalyst.

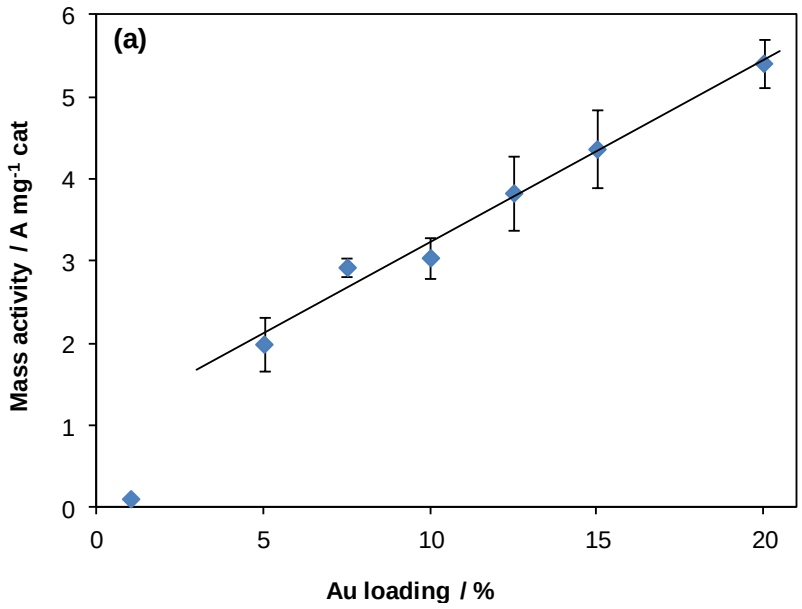

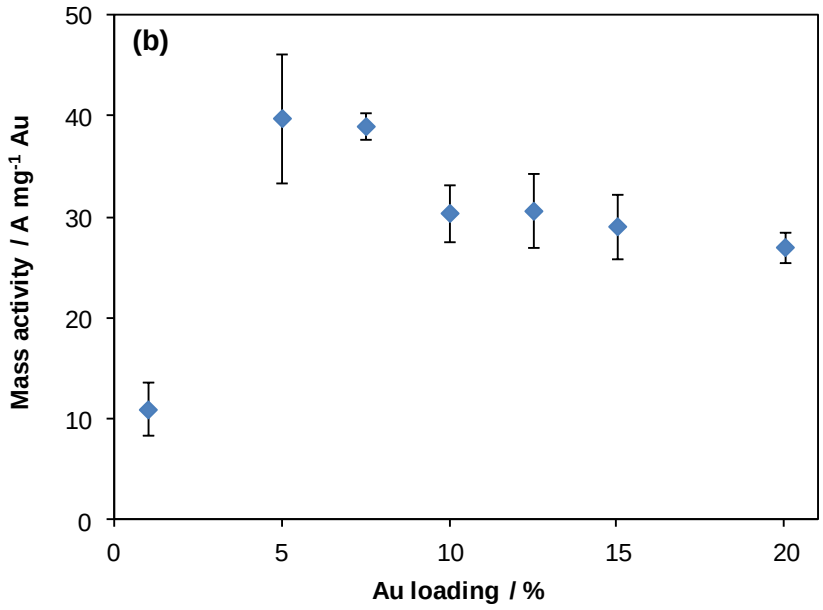


***Figure 52. Effect of gold loading on (a) catalyst-based- and (b) gold-based- mass activity. Activities are calculated from peak currents measured from forward sweep of CV on 0.5 M glycerol/1 M KOH.***

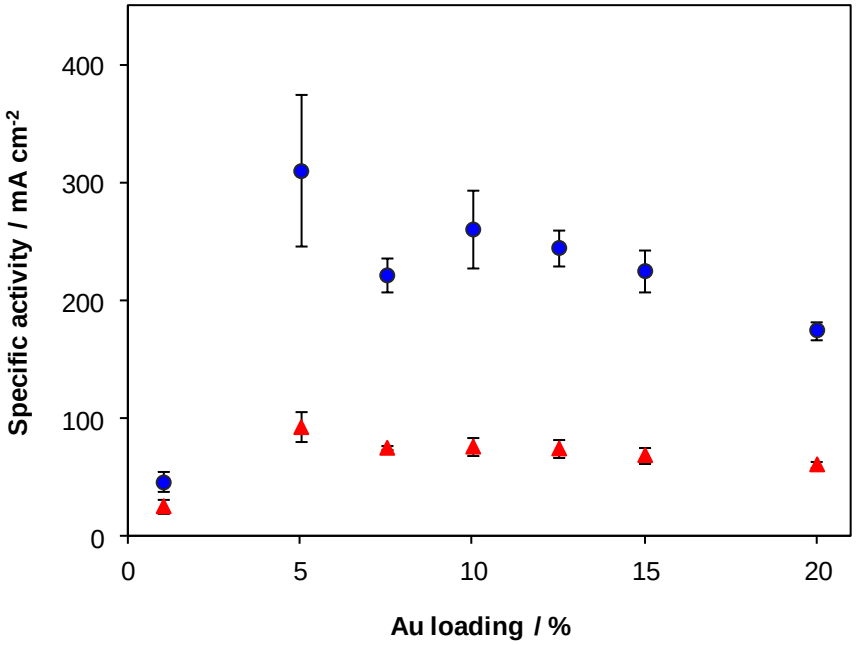


***Figure 53. Specific activities of Au/C catalysts for glycerol oxidation determined (●) electrochemically and (▲) from TEM analysis. Activities are calculated from peak currents measured from forward sweep of CV in 0.5 M glycerol/1 M KOH.***

While it was previously speculated (Chapter 5) that the discrepancies between EASA- and TEM-determined activities (Figure 53) had partly to do with agglomerated particles not being taken into account in TEM analysis – leading to higher gold surface areas and therefore lower TEM-based specific activities – the linear correlation between electrochemically-determined gold surface charge and TEM-determined gold surface area (Figure 50b) implies that there is generally an even

distribution and utilisation of gold on the carbon surface and that there are probably other reasons contributing more greatly to this deviation.

For the catalysts made with 3.2 nm colloids, the measured EASA values are approximately 30 % of the S.A. values determined with TEM. Interestingly, this discrepancy was also found in literature, with EASA values of 27 % for 3.5 nm gold [78] and 20 % for 7.4 nm gold [35], relative to TEM S.A. (calculated from the $d_{ave}$ values given in those papers). It is also noteworthy that EASA ratios of 36 % (from hydrogen desorption peak) and 33 % (from oxide reduction peak) were calculated from EASA and TEM data for 2.4 nm platinum and 3.4 nm palladium, respectively [78] – indicating that this discrepancy is not unique to gold. From the EASA ratio for platinum, it can also be ruled out that the discrepancy exists because the oxide reduction technique is less accurate than the hydrogen desorption technique for EASA determination.

As discussed in Chapter 3, the gold EASA was calculated using the $Q_{theoretical}$ value for Au(100). However, lead profiling has shown that the 3.2 nm colloids that were used to make most of the "small" gold catalysts – including all of the catalysts reported in this chapter – contained almost 76 % Au (110) facets and only 0.1 % Au(100) facets (Chapter 5). It was therefore decided to re-calculate the EASA based on the proportions of Au(110), (111) and (100) found from lead profiling, using the respective $Q_{theoretical}$ values of 272, 444 and 384 µC $cm^{-2}$ (supporting information in [118]). This was done for the 20 % Au/C catalyst, and was found to increase the EASA from 34 % to 44 % of the TEM S.A. (Appendix 6.4), due to Au(110) having a much lower $Q_{theoretical}$ value. However, while this improved the EASA, it is still far from the TEM-derived value, and is therefore a minor contribution to the discrepancy.

Since it was shown in Chapter 5 that the EASA value approaches the TEM surface area value with increasing gold particle size, it is possible that a large proportion of the metal sites on the small gold catalysts are not available for oxygen/$OH^-$ adsorption and resulting activation. After consideration of the possible factors, it is now believed that there are three factors which either individually or jointly, are the major contributors to the EASA/TEM discrepancy.

Firstly, it is possible that the small gold particles may be more deeply embedded in the Vulcan carbon support, making those particles less accessible to the electrolyte. Then, it has very recently been demonstrated on commercial Pt/C catalysts that ultrasonication of a catalyst dispersion for long periods of time resulted in decreased EASA, which was believed to be caused by detachment, dissolution and/or agglomeration of the platinum nanoparticles [164]. It was also noted in this paper that the measured EASA (platinum $d_{ave}$ 3.0 and 3.9 nm) was at least 90% of the TEM-determined surface area. Since the commercial catalysts were also prepared on Vulcan carbon, it is possible that some sort of pre- or post-treatment is applied to the carbon support during preparation of the commercial catalysts, in order to maximise the exposure of the platinum nanoparticles. Based on the two possible factors outlined above, it would therefore be interesting to explore this further by comparing pre- and post- treatments (for example, heat-treatment before or after catalyst deposition) with no treatment, on the EASA of small gold particles supported on Vulcan carbon. It would also be

useful to investigate other carbon supports, such as MWCNTs. The effect of ultrasonication time could also be investigated for all catalysts.

The final possible contributing factor to the lower EASA on small gold particles could be that the smaller gold domains have different oxygen adsorption properties. Of course, by this type of reasoning, it could also be speculated that on the small gold particles, not all the gold surface available for oxygen adsorption and desorption are utilised in oxidation of the much larger glycerol molecule (due to possible size and steric effects) – but insight into the glycerol adsorption and oxidation mechanism on gold in a basic medium will probably require theoretical modelling studies, and a search of the literature has so far not revealed any such studies relating to this specific system. It is, however, known from electrochemical studies of glycerol oxidation over 3.5 nm Au/C in KOH, that very high KOH concentrations cause higher onset potentials and lower peak currents, due to adsorbed $OH^-$ blocking sites and preventing glycerol adsorption [117]. This is therefore an indication that both glycerol and $OH^-$ get adsorbed directly onto the gold surface. But while it cannot be said with any certainty at this point that all of the gold sites available to oxygen are actively involved in glycerol oxidation, it can at least be stated that for the catalysts with ≥ 5 % gold loadings, all of the gold sites available to glycerol are equally active.

Potentiostatic measurements showed the usual trend of higher glycerol oxidation activity (Figure 54), and higher stability over time (Table 12) at 0.2 V than at 0 V. At both potentials, the catalysts with the higher gold loadings (≥ 12.5 %) had the smallest current decay rates over time – again indicating the greater susceptibility of the catalysts with low gold loadings to poisoning by glycerol oxidation products.

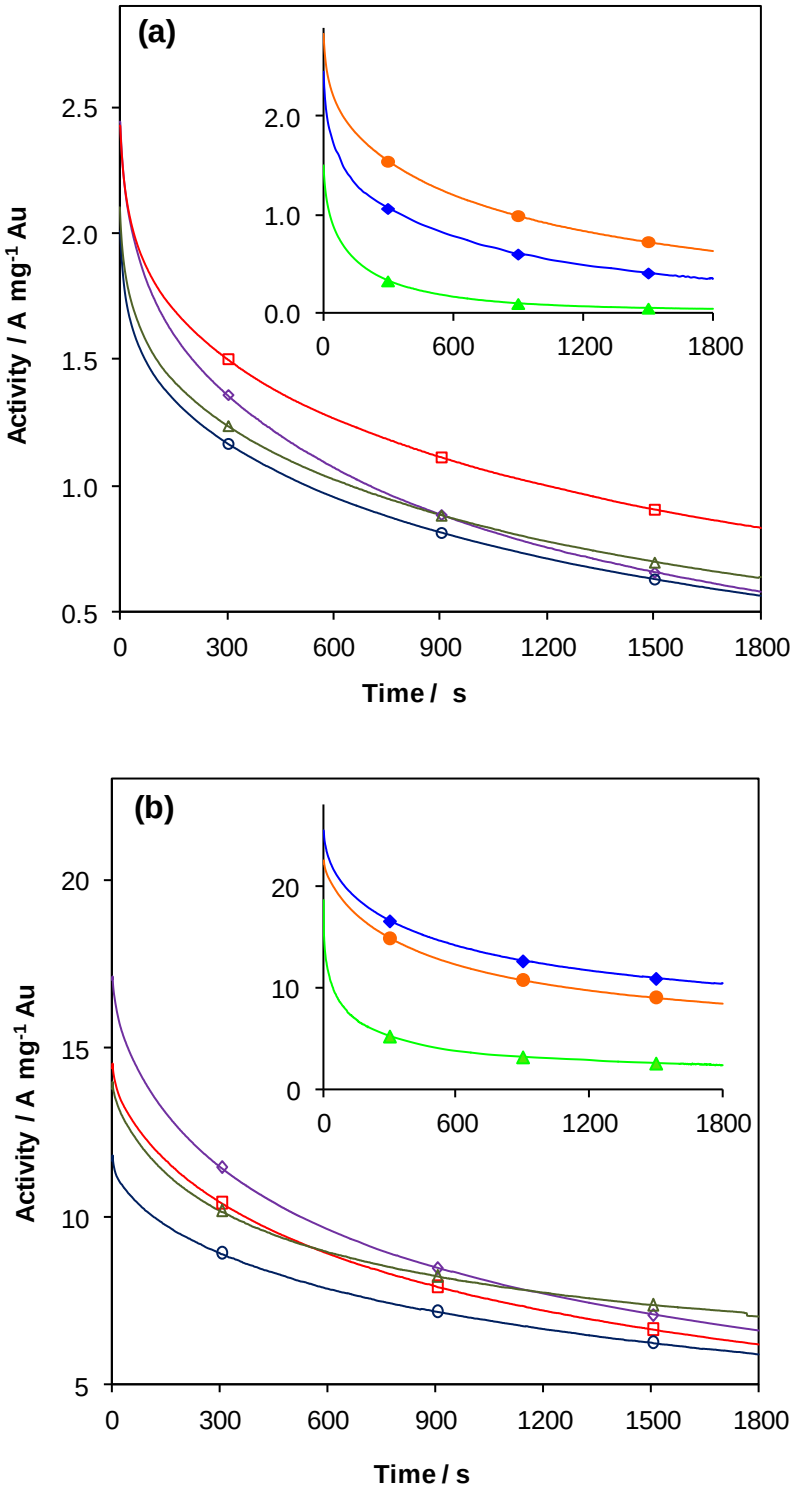


***Figure 54. Potentiostatic measurements of xAu/C catalysts, where x = (◊)10 %, (Δ)12.5 %, (□)15 %, (○)20 %. Inset shows (▲)1 %, (♦)5 %, (●)7.5 %. Scans were recorded at (a) 0 V and (b) 0.2 V (vs. Hg/HgO) in 0.5 M glycerol/1 M KOH for 30 min.***

***Table 12. Glycerol oxidation current ratios ($I_{30\ min}/I_{0\ min}$) of Au/C catalysts from potentiostatic measurements at 0 V and 0.2 V (vs. Hg/HgO) in 0.5 M glycerol/1 M KOH.***

| Au loading / % | Current ratio ($I_{30\ min}/I_{0\ min}$) | |
|---|---|---|
| | 0 V | 0.2 V |
| 1 | 0.02 | 0.15 |
| 5 | 0.14 | 0.41 |
| 7.5 | 0.23 | 0.38 |
| 10 | 0.24 | 0.38 |
| 12.5 | 0.31 | 0.50 |
| 15 | 0.35 | 0.43 |
| 20 | 0.29 | 0.50 |

In Chapter 5, it was speculated that the cause of the early deactivation during CV in 0.5 M glycerol/1 M KOH and the higher rate of current decay over time during potentiostatic measurements was due to the larger proportion of Au(111) on the large gold particles. However, since similar behaviour was also observed over catalysts with small gold particles (with significantly more Au(110) facets) and lower gold loadings, this implies that the limited gold surface area on the catalysts with large particles may be the major contributor to the observed behaviour, rather than the Au(111) facets. To get more clarity on this would require the synthesis and testing of catalysts containing small (e.g. 5 nm) gold particles enclosed by (111) facets. This can possibly be achieved by following a similar approach to Yin, *et al*. [160], who compared the activities of monodisperse < 10 nm Pt-Pd nanotetrahedrons enclosed by (111) facets with nanocubes enclosed by (100) facets for methanol electrooxidation.

Nyquist plots at 0 and 0.2 V (Figure 55) showed improved glycerol oxidation kinetics at the higher potential, as indicated by the smaller $R_{ct}$ values. The catalysts could be separated into three distinct types of impedance behaviour according to their gold loadings.

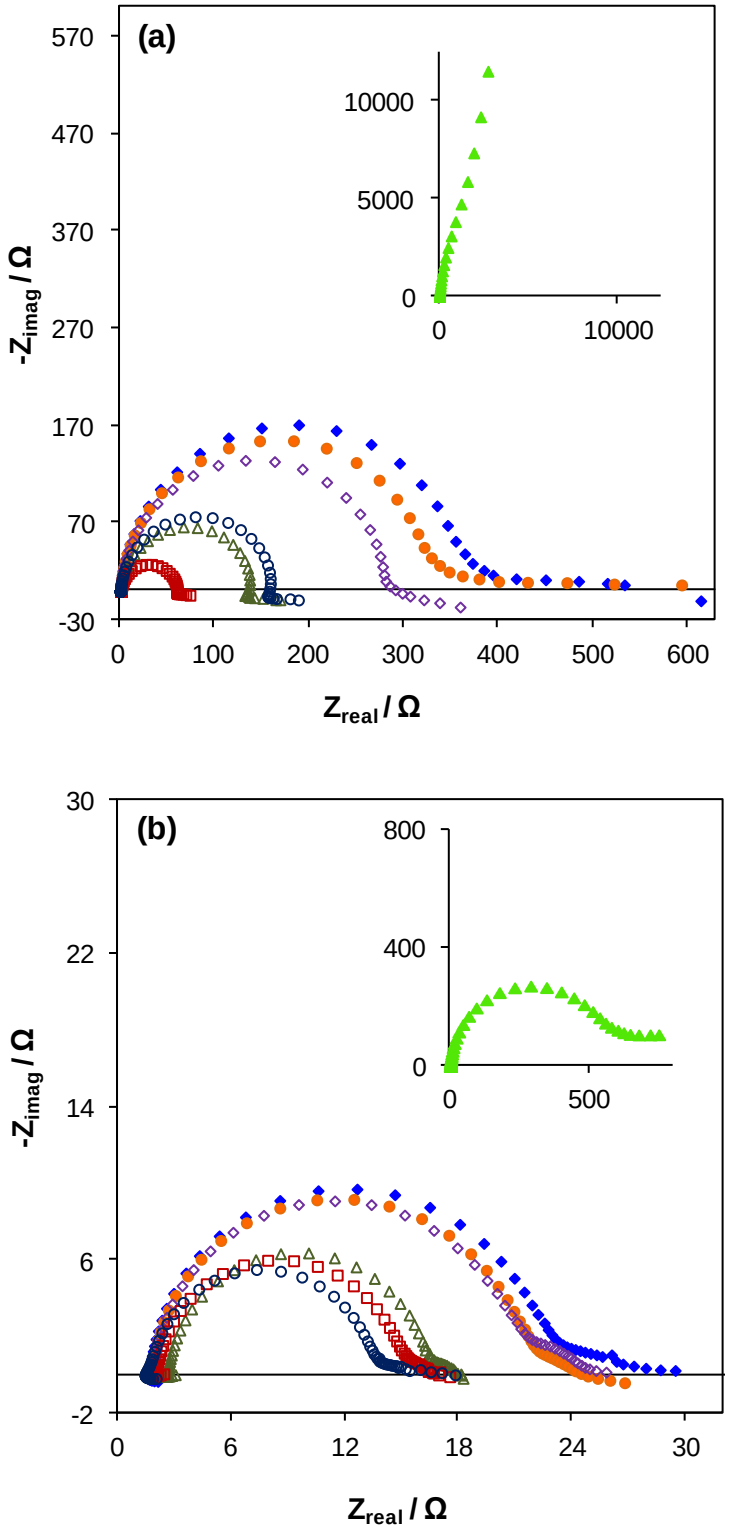


***Figure 55. Nyquist plots of xAu/C catalysts, where x = (♦)5 %, (●)7.5 %, (◊)10 %, (△)12.5 %, (□)15 %, (○)20 %. Inset shows EIS for (▲)1 % Au/C. Plots were recorded at (a) 0V and (b) 0.2 V (vs. Hg/HgO) in 0.5 M glycerol/1 M KOH.***

The 12.5-20 % gold-loaded catalysts had the lowest $R_{ct}$ values at both potentials, indicating the fastest glycerol oxidation kinetics (hence the highest catalyst mass activities), and all three catalysts demonstrated pseudoinductance caused by oxidation of adsorbed intermediates at low frequencies [142]. The pseudoinductance feature was less obvious at 0.2 V for these catalysts, which (as discussed in Chapter 5) is believed to be due to further oxidation, resulting in less adsorbed intermediates at the higher potential.

The catalysts with 5-10 % gold loadings had the next highest $R_{ct}$ values, as demonstrated by their larger impedance arcs. At 0 V, only the 10 % Au/C catalyst demonstrated clear pseudoinductance features at low frequencies, while at 0.2 V, this feature was present on 7.5 % Au/C, indicating that as the gold loadings decreased, higher overpotentials were required for oxidation of adsorbed intermediates.

In accordance with the deviations in activity trends from CV, the 1 % Au/C catalyst demonstrated significantly different impedance behaviour to the other catalysts. At 0V, the impedance profile for the 1 % Au/C catalyst did not show any features relating to charge transfer, but instead displayed significant diffusion limitations [165]. The semi-circle indicating charge transfer was only seen at the higher potential of 0.2 V, with $R_{ct}$ values at least 20 times higher than for the other catalysts, and even at the higher potential there was no oxidation of adsorbed intermediates, as evidenced by the absence of an inductive feature. This can also be seen in the significantly lower current ratios of the 1 % Au/C catalyst at both potentials (Table 12), indicating severe poisoning of this catalyst.

Finally, the dependence of glycerol oxidation peak current on the square root of scan rate was investigated for the 1, 10 and 20 % Au/C catalysts and compared with polycrystalline gold. Scan rates of 1 - 200 mV $s^{-1}$ were applied. A linear relationship, indicating a diffusion-controlled process [48, 166] was observed for all catalysts (Figure 56, Appendix 6.5). However, while polycrystalline gold displayed a good linear trend over the entire range of scan rates, significant deviations from linearity were evident over all Au/C catalysts at the lowest scan rate of 1 mV $s^{-1}$. This could indicate poisoning of active sites on the carbon-supported catalysts due to slow diffusion of glycerol oxidation intermediates away from the electrode at the slower scan rate.

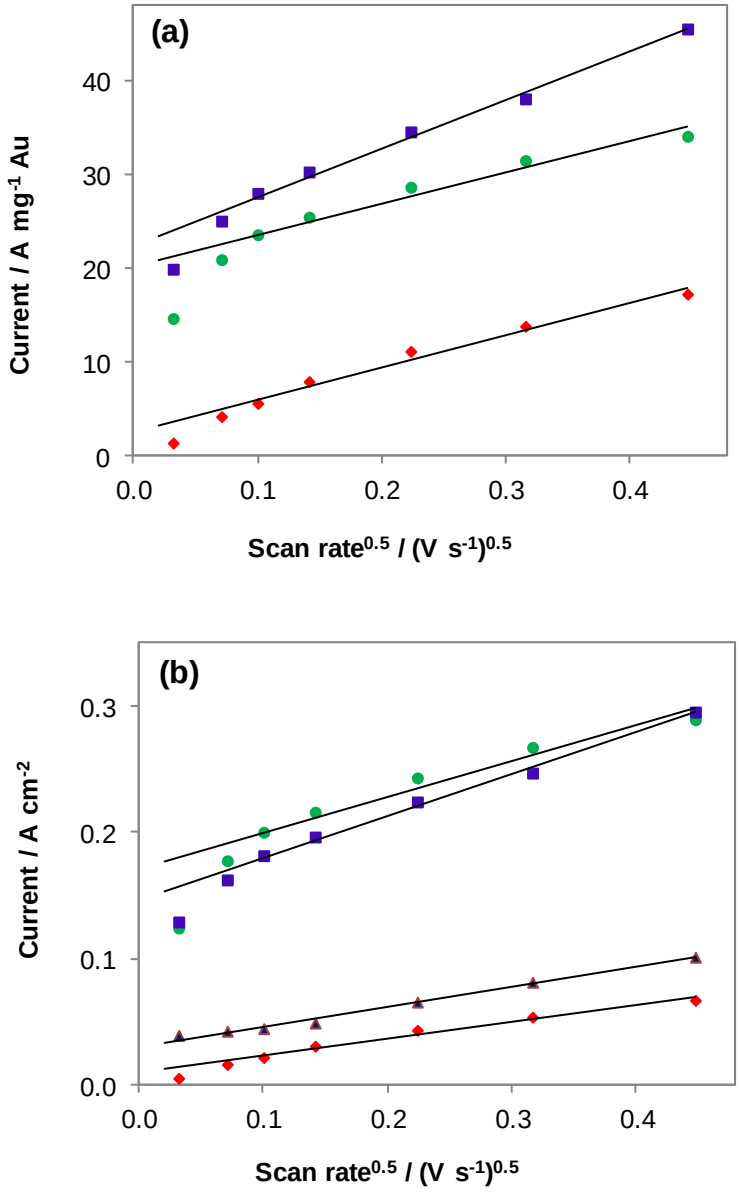


***Figure 56. Dependence of peak current represented as (a) mass activity and (b) specific activity on scan rate of xAu/C catalysts, where x = (♦) 1 %, (●)10 %,(■) 20 %. Also shown in (b) is (▲) bulk gold. Peak currents were measured from forward sweep of CV.***

The peak potential was observed to shift with scan rate, which indicated that this is an irreversible system [167]. The Randles-Sevcik equation for a diffusion-controlled, irreversible system at 25°C is

$$I_p = (2.99 \times 10^5)\alpha^{1/2} n^{3/2} A D^{1/2} C v^{1/2} \qquad (11)$$

where $I_p$ = peak current (A), α = transfer coefficient, $n$ = number of electrons transferred, $A$ = area ($cm^2$), $D$ = diffusion coefficient ($cm^2\ s^{-1}$), $C$ = bulk solution concentration (mol $cm^{-3}$) and $v$ = scan rate ($V\ s^{-1}$).

Strictly speaking, irreversible in this sense refers to redox systems with sluggish kinetics. The glycerol oxidation reaction is itself an irreversible chemical reaction, in that the products do not get reduced back to glycerol. The Randles-Sevcik equation and the conclusions drawn from it (see below) have therefore been used here merely to give an indication of the differing electrochemical behaviour of the catalysts with varying gold loadings.

Since the gold surface area on each catalyst is different, the slopes of the trendlines (fitted for scan rates of 5 - 200 mV $s^{-1}$) for the specific activity/scan rate relationship (Figure 56b) are given in Table 13.

***Table 13. Calculated slopes from linear fit trendline for specific activity/scan rate plots***

| Catalyst | Slope / F $cm^{-2}$ | $r^2$ |
|---|---|---|
| 1 % Au/C | 0.134 | 0.980 |
| 10 % Au/C | 0.287 | 0.955 |
| 20 % Au/C | 0.336 | 0.992 |
| Bulk gold | 0.163 | 0.995 |

From the Randles-Sevcik equation for irreversible systems, it is clear that in a plot of specific activity *vs*. scan rate, the change in slope can be attributed to either α, *n* or *D*, or a combination of the three (since *C* is constant). Assuming α is constant in this instance, then for the carbon-supported gold catalysts, the increase in slope with increasing gold loading implies easier diffusion of glycerol to the active gold sites (higher *D*) and/or further oxidation of glycerol (higher *n*) with increased gold loading. The 1 % Au/C catalyst had a lower slope than even bulk gold, which – considering that 1 % Au/C had a higher gold EASA (0.03 $cm^2$) than bulk gold (0.006 $cm^2$) – is an indication of the role that the carbon support plays in the diffusion of glycerol to the active sites, particularly at low gold loadings (as there will be a longer effective path length for glycerol to travel through the carbon layer before reaching the gold site).

Assuming glycerol is oxidised to formate in an alkaline medium, which is a likely reaction over gold according to Kwon, *et al*. [41], then the reaction would generate 8 electrons according to

$$C_3H_5(OH)_3 + 11\ OH^- \rightarrow 3CHOO^- + 8\ H_2O + 8\ e^- \quad (\mathbf{12})$$

Since α is a reciprocal of the Tafel slope, *b*, with the equation taking the form [165]

$$\alpha = (2.3RT/F)*(1/b) \quad (\mathbf{13})$$

then using the Tafel slope value of 134 mV/dec reported by Zhang, *et al*. [78] for glycerol oxidation over a 35 % Au/C catalyst at 25°C in 0.5 M glycerol/1 M KOH solution, yields an α value of 0.44. This value was then used in calculating *D* for the 20 % Au/C system. A value of 2.2 x $10^{-8}$ $cm^2$ $s^{-1}$ was

obtained, which seems reasonable considering that *D* values of 6.5 x $10^{-5}$ [168] and 5.2 x $10^{-8}$ $cm^2$ $s^{-1}$ [169] have been reported in alkaline media for methanol and ethanol oxidation, respectively.

From an overview of the electrochemical results, it can therefore be concluded that while catalysts with gold loadings between 5-20 % demonstrated equal utilisation of the gold surface, gold loadings of ≥ 12.5 % would be most appropriate in a fuel cell set-up, due to the lower onset potentials, higher glycerol oxidation kinetics and higher stabilities. Although the 12.5 % Au/C catalyst demonstrated early deactivation along with its lower-loaded counterparts in CV, the peak drop-off occurred at much higher overpotentials than would be feasible for a fuel cell – while at lower overpotentials, this catalyst proved to be as stable as the catalysts with higher gold loadings. Ultimately, the amount of gold needed would depend on the required power output of the fuel cell.

# 7 GOLD PARTICLE SIZE EFFECT ON GLYCEROL OXIDATION INTERMEDIATES

## 7.1 Introduction

One of the more meticulous studies into the glycerol oxidation mechanism is that carried out by Kwon, *et al*. [41], in which gold- and platinum- catalysed glycerol electrooxidation pathways were established for alkaline, neutral and acidic media. The oxidation pathway in an alkaline medium (shown in Scheme 2 of Chapter 2) is of relevance here, and the glycerol oxidation pathway specific to gold is shown in Figure 57. According to this mechanism, glycerol gets oxidised directly to glyceric acid over gold, since glyceraldehyde is an unstable intermediate at the higher overpotentials at which gold is active. Then glyceric acid is oxidised to approximately equal quantities of the final oxidation products, glycolic acid and formic acid. Kwon, *et al*. did not believe that any further oxidation was possible over gold.

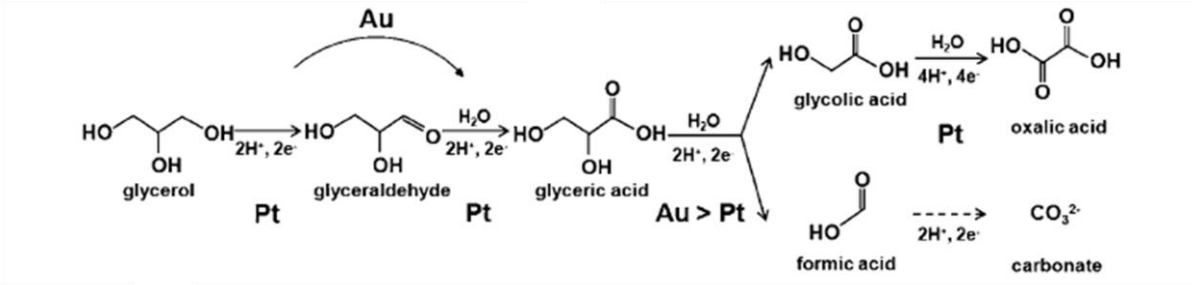


***Figure 57. Glycerol oxidation mechanism in alkaline medium over polycrystalline gold (taken from Kwon, et al. [41]).***

The different impedance profiles obtained over the carbon-supported catalysts with small, medium and large gold particles (Chapter 5) indicated the possibility that glycerol oxidation could proceed further along the oxidation pathway for the catalysts with small gold particles than over the other catalysts. This was therefore tested by carrying out a cursory investigation into the oxidation of all the possible gold-catalysed glycerol oxidation products listed in Figure 57. One catalyst from each of the size regimes (*viz*. 4.7 nm, 14.7 nm and 88 nm Au/C) was chosen for testing. Potentiodynamic scans were first carried out on the polycrystalline gold electrode, in order to identify the potential region in which oxidation peaks (if any) would occur.

## 7.2 Experimental

Glycolic acid (98 %) and calcium DL-glycerate dihydrate were sourced from Alfa Aesar. Potassium formate (99 %) and DL-glyceraldehyde (≥ 90 %) were sourced from Sigma-Aldrich. Glycolic acid and potassium formate were made up to concentrations of 0.5 M in 1 M KOH. However, due to the small

quantities of glyceraldehyde and glycerate salts obtained from the suppliers, these salts were made up to lower solution concentrations of 10 mM in 1 M KOH.

The same electrochemical testing procedure was followed for the glycerol oxidation products as for glycerol (detailed in Chapter 4). For repeatability measurements, each catalyst was deposited and tested on 2 electrodes.

## 7.3 Results and discussion

The glycerol oxidation mechanism over gold (Figure 57) shows the protonated species of the oxidation intermediates, presumably due to Kwon, *et al*. [41] acidifying the solutions in order to stabilise them before analysis with HPLC. The salts are referred to here in their deprotonated form (i.e. glycerate, glycolate and formate), since they were tested in an identical alkaline environment to that in which glycerol oxidation studies were carried out.

### 7.3.1 Glyceraldehyde

Although Kwon, *et al*. [41] showed that glyceraldehyde degrades within minutes in an alkaline medium and furthermore, that glycerol oxidation over gold skips the glyceraldehyde intermediate step, this compound was still included purely out of interest.

An extended oxidation profile was seen to occur over the small and medium gold particles (Figure 58) as well as over bulk gold (Appendix 7.1), which is likely due to the combined oxidation of glyceraldehyde and its various base-catalysed degradation products – which were shown in a deaerated alkaline medium to consist of mostly lactic acid, as well as dihydroxyacetone, fructose and dimers such as sorbitol [41]. At the highest oxidation peak (~ 0.15 V), the catalyst with small gold particles was twice as active on a mass basis as the catalyst with medium gold. For these catalysts, the reverse oxidation peak was higher than the forward oxidation peak – indicating significant poisoning by the glyceraldehyde oxidation and/or degradation products. By comparison with glycerol oxidation, a higher reverse peak has only ever been observed over bulk gold (Chapter 2). The catalyst with large gold particles was fairly inactive, with barely noticeable oxidation peaks.

It is interesting to note that all catalysts demonstrated a much smaller ionic double layer capacitance in 10 mM glyceraldehyde/1 M KOH than in 1 M KOH (Appendix 7.1), which is attributed to the adsorption of neutral organic compounds on the electrode surface [165]. This was also evident for the other compounds tested – as will be seen later.

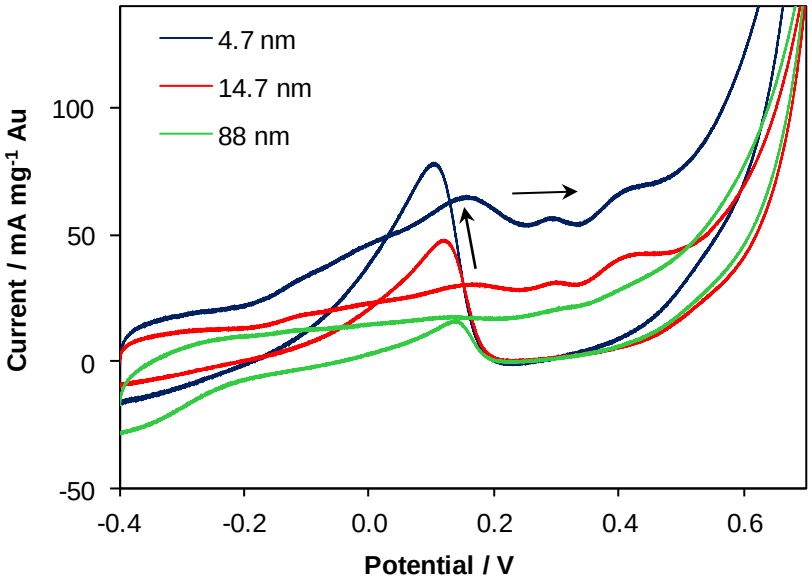


***Figure 58. CVs of Au/C catalysts in 10 mM glyceraldehyde/ 1 M KOH at 10 mV $s^{-1}$. Potentials are shown vs. Hg/HgO reference.***

### 7.3.2 Glycerate

Glycerate oxidation CVs over Au/C catalysts were similar in appearance to glycerol oxidation curves, with a single sharp forward peak and smaller reverse peak (Figure 59b-d). A second oxidation peak at higher potentials was observed over bulk gold, which was present at a more anodic potential than the monolayer oxide peak (Figure 59a). Since the formation of the gold oxide monolayer is known to cause deactivation of the gold electrode, the second peak would not be expected to arise from further oxidation of glycerate or its products. It is therefore more likely that the second peak is the gold monolayer oxide peak shifted to higher potentials in the presence of glycerate. However, without carrying out an in-situ analysis of the reaction over bulk gold, the origin of the second peak cannot be identified for certain. It also cannot be stated with any certainty that this peak was absent on the carbon-supported gold catalysts, as it could be masked by oxidation of the glassy carbon surface at those potentials.

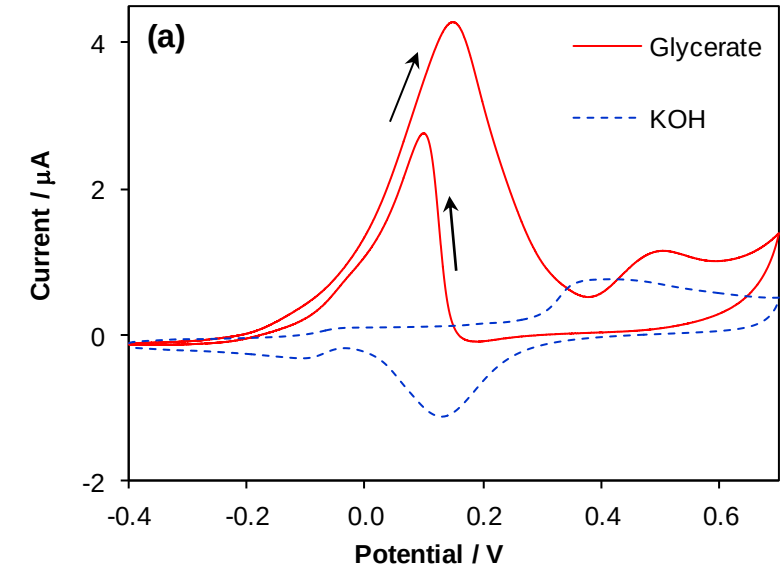
(a)
Glycerate
KOH
Current / µA
Potential / V
4
2
0
-2
-0.4
-0.2
0.0
0.2
0.4
0.6

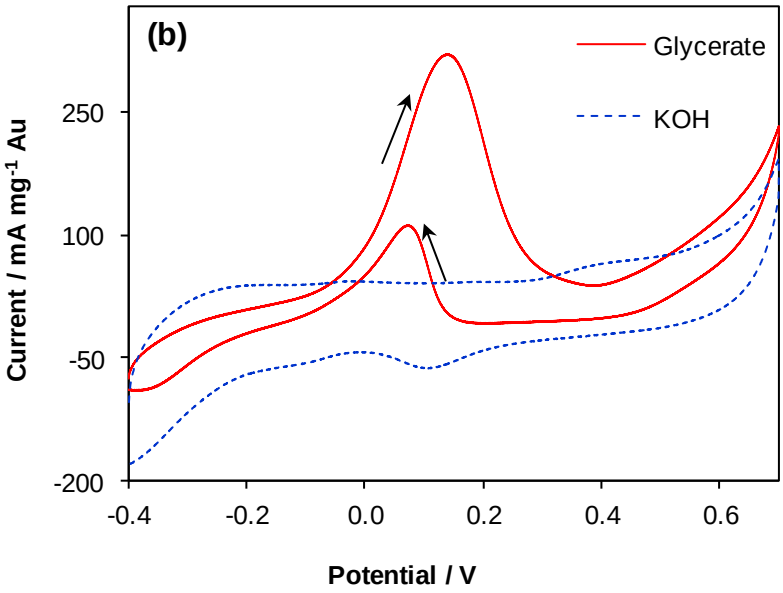
(b)
Glycerate
KOH
Current / mA mg-1 Au
Potential / V
250
100
-50
-200
-0.4
-0.2
0.0
0.2
0.4
0.6

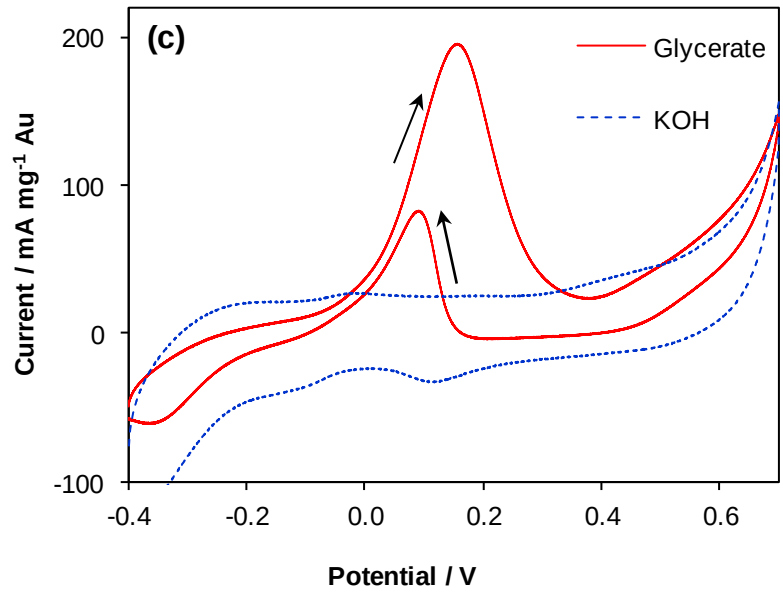
(c)
Glycerate
KOH
Current / mA mg-1 Au
Potential / V
200
100
0
-100
-0.4
-0.2
0.0
0.2
0.4
0.6

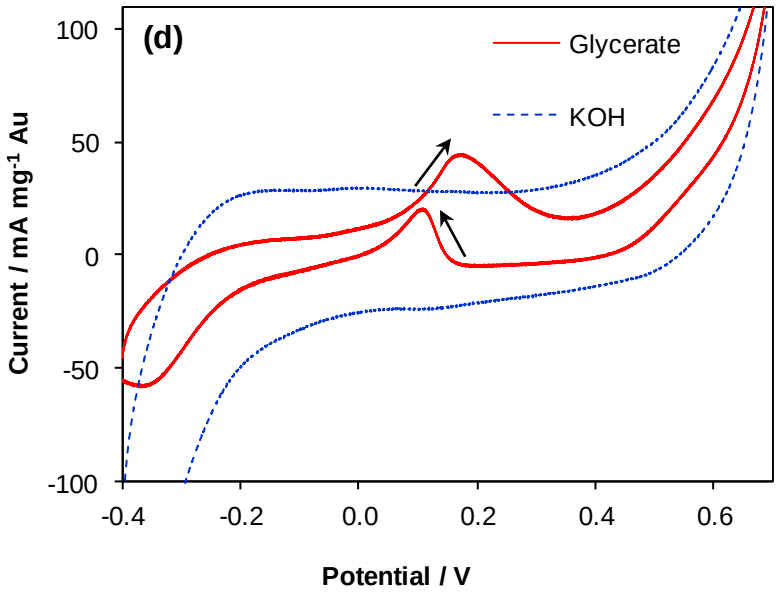


***Figure 59. CVs of (a) bulk Au, (b) 4.7 nm Au/C, (c) 14.7 nm Au/C and (d) 88 nm Au/C catalysts in 10 mM glycerate/1 M KOH at 10 mV $s^{-1}$ (solid curve) and 1 M KOH at 50 mV $s^{-1}$ (dotted curve). Potentials are shown vs. Hg/HgO reference.***

The gold mass- and specific- activity trends (Figure 60; data in Appendix 7.2) were the same for the oxidation of glycerate as for glycerol – with mass-based activity decreasing and specific activity increasing, with increasing gold particle size. As with glycerol, all carbon-supported catalysts had a higher specific activity than bulk gold. Besides the significantly higher mass activity of the small gold particles, it was also noted that the 4.7 nm Au/C catalyst had lower onset- and peak- potentials than the other catalysts in 10 mM glycerate/1 M KOH solution (Table 14) – confirming the easier glycerate oxidation kinetics over the small gold particles. All catalysts had similar peak drop-off potentials.

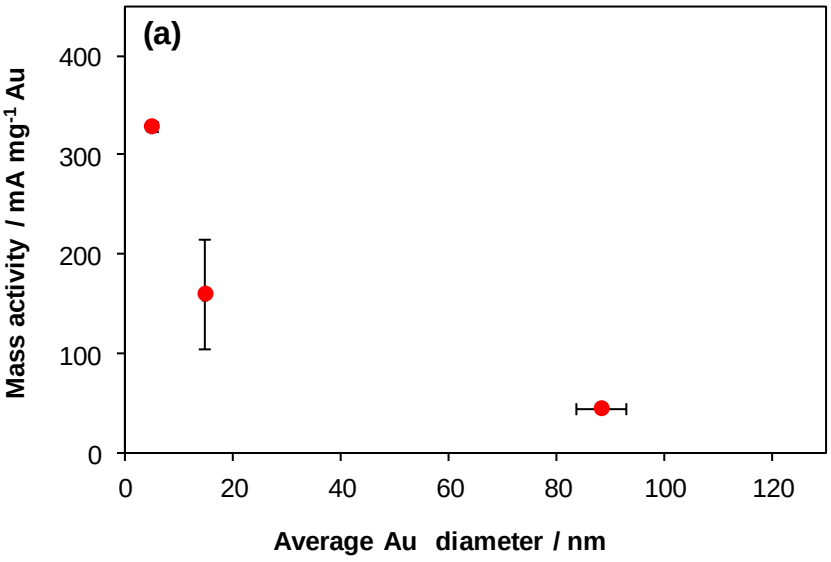

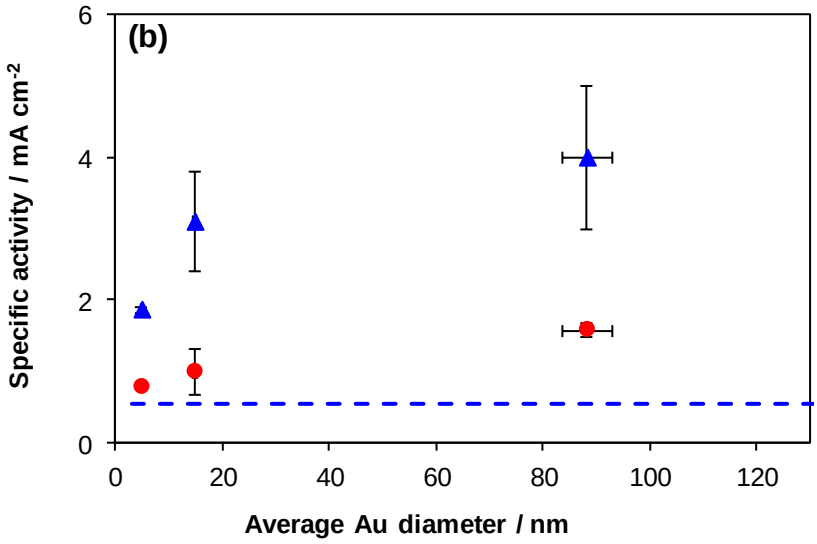


***Figure 60. Effect of gold particle size on (a) mass activities and (b) specific activities of Au/C catalysts for glycerol oxidation determined (▲) electrochemically and (●) from TEM analysis. The dashed line shows the electrochemically determined specific activity for polycrystalline gold. Peak currents were measured from forward sweep of CV in 10 mM glycerate/1 M KOH.***

***Table 14. Glycerate oxidation onset, forward peak and drop-off potentials for Au/C catalysts measured from CV in 10 mM glycerate/1 M KOH. Potentials are reported vs. Hg/HgO reference.***

| Au $d_{ave}$ / nm | Onset potential / V | Forward peak potential / V | Peak drop-off potential / V |
|---|---|---|---|
| 4.7 | -0.12 | 0.14 | 0.23 |
| 14.7 | -0.06 | 0.16 | 0.23 |
| 88 | -0.04 | 0.17 | 0.24 |

In this instance, glycerol and glycerate oxidation currents cannot be compared because of the significantly different concentrations, but this is something that could be explored in future research – although ideally, in-situ analysis should be conducted, so that glycerol oxidation products can be identified and correlated with oxidation potential.

### 7.3.3 Glycolate

From a comparison of bulk gold in 0.5 M glycolate/1 M KOH and 1 M KOH solutions, a broad peak centred at ~ 0.21 V (shown by arrow in Figure 61a), was the only feature not present over bulk gold in 1 M KOH, and was therefore attributed to possible glycolate oxidation. This was confirmed over the catalyst with small gold particles (Figure 61b), where a more well-defined oxidation peak was observed at an average potential of 0.20 V. For the catalyst with medium gold particles, a slight, broad peak centred at a higher potential (~ 0.25 V) was seen (Figure 61c), while a glycolate oxidation peak was barely evident for the catalyst with large gold (Figure 61d). This difference can be seen

more clearly in a comparison of the CVs of the three carbon-supported catalysts in glycolate (Figure 62).

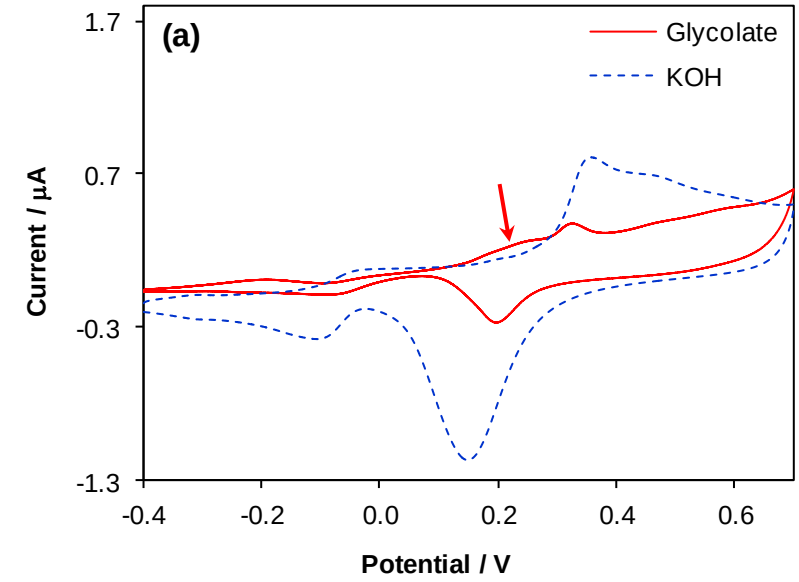


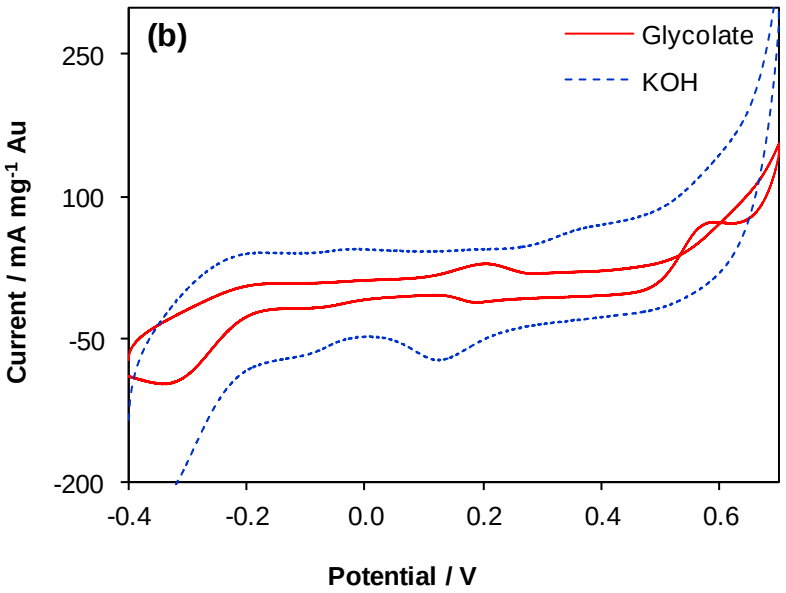

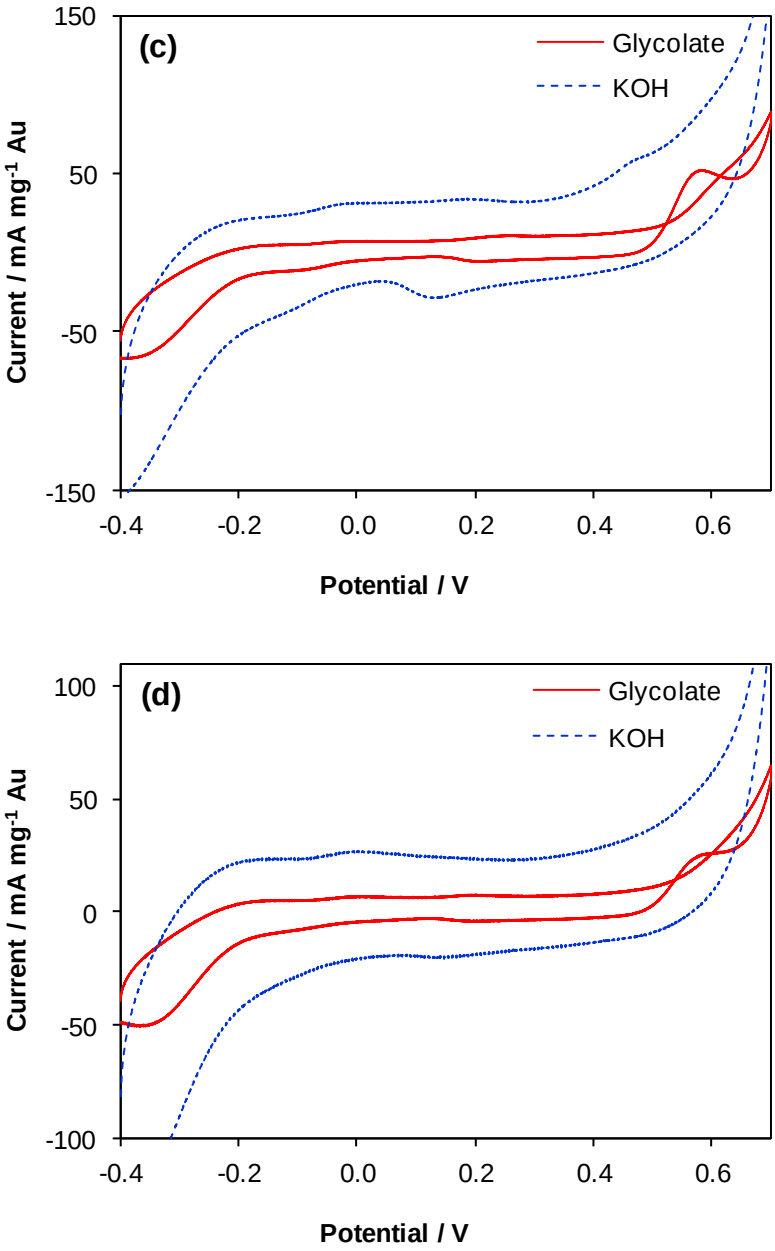


***Figure 61. CVs of (a) bulk Au, (b) 4.7 nm Au/C, (c) 14.7 nm Au/C and (d) 88 nm Au/C catalysts in 0.5 M glycolate/1 M KOH at 10 mV $s^{-1}$ (solid curve) and 1 M KOH at 50 mV $s^{-1}$ (dotted curve). Potentials are shown vs. Hg/HgO reference.***

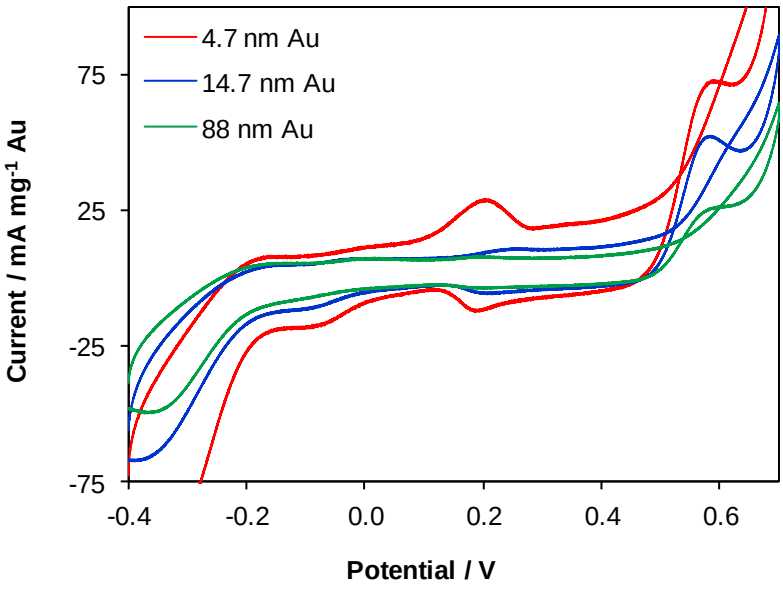


***Figure 62. CVs of Au/C catalysts in 0.5 M glycolate/1 M KOH at 10 mV $s^{-1}$. Potentials are shown vs. Hg/HgO reference.***

A strange feature was also noticed for the carbon-supported gold catalysts in glycolate – which was an oxidation peak occurring on the reverse sweep at 0.58 V. Since this was not observed on bulk gold, it is assumed to be caused by oxidation of glycolate and/or its oxidation product(s) which must have been adsorbed on carbon.

From an overall comparison of the results, it is clear from Figure 61a, that Kwon, *et al*. [41] were correct in stating that glycolate is one of the end products of glycerol oxidation over bulk gold, as oxidation of glycolate is quite limited. However, it is also clear from Figure 61b that small gold particles actually have the potential advantage (however minute), of extending the oxidation of glycerol beyond that of glycolate.

### 7.3.4 Formate

There were no formate oxidation peaks present on either bulk gold or any of the Au/C catalysts – indicating, in agreement with Kwon, *et al*. [41], that this single-carbon glycerol oxidation intermediate cannot be oxidised further over gold. The CV profiles of the gold catalysts in formate are shown in Appendix 7.3.

# 8 CONCLUSIONS AND RECOMMENDATIONS

Some significant findings were made during this study into gold-based catalysts for glycerol electrooxidation. It was first demonstrated that the pre-deposition of $MnO_2$ onto carbon stabilised the gold nanoparticles, resulting in smaller, more uniform gold deposition than on carbon alone. Catalysts with $MnO_2$/C contents of 5 and 9 wt % gave promising results, with lower onset and peak potentials, the highest mass activities (35-37 A $mg^{-1}$ Au) and comparable $I_f/I_r$ ratios to Au/C. It is speculated that this is partly due to $MnO_2$ preventing gold agglomeration, thereby creating a larger gold surface area for reaction. In addition, $MnO_2$ may act as an active co-catalyst, especially at higher potentials, by means of oxygen spillover onto gold. Stability and impedance studies showed that $MnO_2$-modified catalysts were less stable at a low potential (0 V) than Au/C. This was believed to be caused by blocking of mixed-valence manganese oxide sites or poisoning of the smaller gold particles on these catalysts. However, at a higher potential of 0.2 V, Au/5 % $MnO_2$/C demonstrated the best mass activity and stability. All catalysts were more active than the platinum- and palladium- based catalysts reported in literature – with the best-performing catalyst on a mass activity basis (Au/9 % $MnO_2$/C) being at least 12 times more active and the most active catalyst on a specific activity basis (Au/C) being at least 27 times more active. This has clearly demonstrated the superiority of gold catalysts for glycerol electrooxidation, as well as the advantage of incorporating $MnO_2$ as a co-catalyst, in order to lower the overpotential for the activation of gold.

Investigations into the effect of gold particle size on glycerol electrooxidation showed that Au/C catalysts containing small gold particles had the highest mass activities and were at least twice as active as the catalysts with large gold particles. However, very small (2.1 nm) gold particles were not stable and are estimated to have grown by at least 2 nm with repetitive cycling in KOH. The catalysts containing small gold particles also demonstrated lower glycerol oxidation onset potentials (at least 100 mV earlier than the catalysts with large gold particles), corresponding to their activation at lower potentials. The lower onset potentials could be due to the predominance of Au(110) facets on the small gold particles. Impedance studies also indicated that glycerol oxidation may proceed further over small gold particles. In addition to their lower mass activities, the large gold catalysts were also more easily poisoned – possibly due to a higher fraction of Au(111) or the lower gold surface area – showing an early decline in glycerol oxidation currents, in the region where gold should still be active. While the mass activity trend favoured small gold particles (due to the influence of particle size on specific surface area), the larger gold particles were found to have a higher specific electrocatalytic activity (i.e. free from surface area effects) for glycerol oxidation. This could be attributed mainly to the contribution of the Au(111) plane. However, the catalysts with large gold particles were also the most unstable, showing the biggest decreases in current during potentiostatic measurements. In support of the speculation in the study into Au/$MnO_2$/C catalysts, it also appeared from this study that very small gold particles may be more easily poisoned at lower potentials and that an optimum particle size may exist for catalyst stability – possibly in the region of 5 nm. From a practical fuel cell application point of view, factors such as high mass activity, low overpotentials and high stability are most relevant, and

these conditions can all be met by the catalysts containing small gold particles defined by predominantly Au(110) facets. The value of this study lies in being able to use this information to selectively design catalysts in such a way as to maximise fuel cell performance.

Comparisons of Au/C catalysts with gold loadings varying from 1-20 wt % showed a linear increase in gold oxide reduction charge with increasing surface area in KOH – indicating equivalent surface exposure to KOH for all the catalysts. However, the electrochemically determined surface areas were less than half of the TEM-determined areas, indicating that on small gold nanoparticles, not all of the gold surface area is electrochemically accessible. In glycerol, severe mass transfer effects were evident for the 1 % Au/C catalyst, leading to much lower activities than the catalysts with higher (≥5 %) gold loadings. In addition, the low gold surface area on this catalyst meant that there were insufficient gold sites to oxidise adsorbed intermediates, resulting in rapid poisoning of this catalyst. On the other hand, the catalysts with 5-20 % gold loadings were much more active and demonstrated a linear relationship between catalyst activity and gold loading. This implied comparable gold utilisation on these catalysts, which was confirmed by similar mass- and specific- activities. However, only the catalysts with higher gold loadings (15-20 %) did not deactivate early during CV, indicating that a larger gold surface area is necessary to resist poisoning at high potentials. On the basis of low onset potentials, high mass activity, and stability at low overpotentials, a minimum gold loading of 12.5 % appears to be necessary for a supported gold catalyst with small gold nanoparticles; although even higher loadings may be preferable for a higher power output in a fuel cell. The increase in current with an increase in gold loading can be attributed to further oxidation of glycerol and/or increased diffusion of glycerol to active gold sites on the catalysts with high gold loadings.

For investigations into the oxidation of possible gold-catalysed glycerol oxidation intermediates, the higher oxidation currents as well as the lower potential at which glycerate and glycolate oxidation occurred on the 4.7 nm Au/C catalyst, supports the assumption made that glycerol oxidation could proceed further along the oxidation pathway for catalysts with small gold particles than over medium and large gold particles. The oxidation of glycolate over small gold particles also indicates that unlike bulk gold, glycolate is not necessarily a final product in the glycerol oxidation pathway over small gold nanoparticles. However, the further oxidation of formate over gold does not appear to be possible.

Of relevance to fuel cell catalyst screening in general, optimisation of the electrochemical cell design and the testing methodology were also described at the start. This was a vital component of the study and helped to ensure that accurate, repeatable and reproducible results were obtained. There is also total confidence that the optimisation testwork ensured the maximum possible activity was obtained from the catalyst as-is. However, significant discrepancies between electrochemically determined- and TEM-determined surface areas means that there is still some work to be done in order to make certain that the catalyst itself is prepared in such a way as ensure that most of the gold sites are likely to be exposed to the electrolyte solution before deposition onto the electrode for testing.

It is therefore recommended that investigations be carried out into ways in which to maximise the exposure of the gold surface on these catalysts, such as pre- and post- heat treatment of the

catalysts or exploring other carbon-based supports, such as MWCNTs. It also needs to be investigated whether the ultrasonication procedures could be contributing to the lower EASA by causing loss/agglomeration of gold nanoparticles.

Other recommendations for future work include investigations into the “optimum” gold particle size for catalyst stability – preferably by comparing monodisperse gold catalysts with sizes ranging from 3-10 nm. In-situ analysis of glycerol oxidation products, which can be correlated to the oxidation potential, would also yield valuable information on the glycerol oxidation mechanism over the different-sized gold particles as well as over shape-controlled particles. It would also be useful to determine whether glycerol can be selectively oxidised to certain valuable chemicals over gold nanoparticles of different shapes. For this reason, investigations into the synthesis and deposition onto carbon of small (< 10 nm) shape-controlled gold nanoparticles are highly recommended.

Ultimately, the true test is how these catalysts will perform in a direct glycerol fuel cell and it is hoped that some of the development work outlined in this thesis will be useful for the synthesis of high-performance gold-based fuel cell catalysts in the future.

# REFERENCES

[1] A. Serov, C. Kwak, Recent achievements in direct ethylene glycol fuel cells (DEGFC), Appl. Catal., B 97 (2010) 1.

[2] C. Bianchini, P.K. Shen, Palladium-Based Electrocatalysts for Alcohol Oxidation in Half Cells and in Direct Alcohol Fuel Cells, Chem. Rev. 109 (2009) 4183.

[3] V.S. Bagotzky, N.V. Osetrova, A.M. Skundin, Fuel Cells: State-of-the-Art and Major Scientific and Engineering Problems, Russ. J. Electrochem. 39 (2003) 919.

[4] K. Matsuoka, Y. Iriyama, T. Abe, M. Matsuoka, Z. Ogumi, Alkaline direct alcohol fuel cells using an anion exchange membrane, J. Power Sources 150 (2005) 27.

[5] D.T. Johnson, K.A. Taconi, The glycerin glut: Options for the value-added conversion of crude glycerol resulting from biodiesel production, Environ. Prog. 26 (2007) 338.

[6] J.O. Metzger, U. Biermann, Sustainable Development and Renewable Feedstocks for Chemical Industry, in: J.J. Bozell, M.K. Patel (Eds.) Feedstocks for the Future, vol. 921, American Chemical Society, 2006, pp. 13.

[7] A.T. Marshall, R.G. Haverkamp, Production of hydrogen by the electrochemical reforming of glycerol-water solutions in a PEM electrolysis cell, Int. J. Hydrogen Energ. 33 (2008) 4649.

[8] J.-h. Zhang, Y.-j. Liang, N. Li, Z.-y. Li, C.-w. Xu, S.P. Jiang, A remarkable activity of glycerol electrooxidation on gold in alkaline medium, Electrochim. Acta 59 (2012) 156.

[9] J. Schnaidt, M. Heinen, D. Denot, Z. Jusys, R. Jürgen Behm, Electrooxidation of glycerol studied by combined in situ IR spectroscopy and online mass spectrometry under continuous flow conditions, J. Electroanal. Chem. 661 (2011) 250.

[10] A. Nirmala Grace, K. Pandian, Pt, Pt-Pd and Pt-Pd/Ru nanoparticles entrapped polyaniline electrodes - A potent electrocatalyst towards the oxidation of glycerol, Electrochem. Commun. 8 (2006) 1340.

[11] E. Antolini, E.R. Gonzalez, Alkaline direct alcohol fuel cells, J. Power Sources 195 (2010) 3431.

[12] C. Fu, H. Zhou, D. Xie, L. Sun, Y. Yin, J. Chen, Y. Kuang, Electrodeposition of gold nanoparticles from ionic liquid microemulsion, Colloid & Polymer Science 288 (2010) 1097.

[13] B.K. Jena, C.R. Raj, Synthesis of Flower-like Gold Nanoparticles and Their Electrocatalytic Activity Towards the Oxidation of Methanol and the Reduction of Oxygen, Langmuir 23 (2007) 4064.

[14] D. Padayachee, V. Golovko, A.T. Marshall, The effect of $MnO_2$ loading on the glycerol electrooxidation activity of Au/$MnO_2$/C catalysts, Electrochim. Acta 98 (2013) 208.

[15] D. Padayachee, V. Golovko, B. Ingham, A.T. Marshall, Influence of particle size on the electrocatalytic oxidation of glycerol over carbon-supported gold nanoparticles, Electrochim. Acta 120 (2014) 398.

[16] V.S. Bagotsky, Fuel Cells: Problems and Solutions, John Wiley & Sons, Inc., Hoboken, New Jersey, 2009.

[17] S.P.S. Badwal, K. Foger, Solid oxide electrolyte fuel cell review, Ceram. Int. 22 (1996) 257.

[18] J.M. Léger, C. Coutanceau, C. Lamy, Electrocatalysis for the Direct Alcohol Fuel Cell, in: M.T.M. Koper (Ed.) Fuel Cell Catalysis: A Surface Science Approach, John Wiley & Sons, Inc., Hoboken, NJ, USA, 2008, pp. 343.

[19] R. O' Hayre, S.-W. Cha, W.G. Colella, F.B. Prinz, Fuel Cell Fundamentals, John Wiley & Sons, Inc., New York, 2009.

[20] K. Scott, A.K. Shukla, Polymer electrolyte membrane fuel cells: Principles and advances, Reviews in Environmental Science and Biotechnology 3 (2004) 273.

[21] J. Wu, X.Z. Yuan, J.J. Martin, H. Wang, J. Zhang, J. Shen, S. Wu, W. Merida, A review of PEM fuel cell durability: Degradation mechanisms and mitigation strategies, J. Power Sources 184 (2008) 104.

[22] L. Qingfeng, H.A. Hjuler, N.J. Bjerrum, Phosphoric acid doped polybenzimidazole membranes: Physiochemical characterization and fuel cell applications, J. Appl. Electrochem. 31 (2001) 773.

[23] J.R. Varcoe, R.C.T. Slade, Prospects for Alkaline Anion-Exchange Membranes in Low Temperature Fuel Cells, in, WILEY-VCH Verlag, 2005, pp. 187.

[24] F. Bidault, D.J.L. Brett, P.H. Middleton, N.P. Brandon, Review of gas diffusion cathodes for alkaline fuel cells, J. Power Sources 187 (2009) 39.

[25] A. Kirubakaran, S. Jain, R.K. Nema, A review on fuel cell technologies and power electronic interface, Renew. Sust. Energ. Rev. 13 (2009) 2430.

[26] J. Larminie, A. Dicks, (Eds), Fuel Cell Systems Explained, J. Wiley, 2002.

[27] L. Demarconnay, S. Brimaud, C. Coutanceau, J.M. Léger, Ethylene glycol electrooxidation in alkaline medium at multi-metallic Pt based catalysts, J. Electroanal. Chem. 601 (2007) 169.

[28] R. Lan, X. Xu, S. Tao, J.T.S. Irvine, A fuel cell operating between room temperature and 250 °C based on a new phosphoric acid based composite electrolyte, J. Power Sources 195 (2010) 6983.

[29] N. Sammes, R. Bove, K. Stahl, Phosphoric acid fuel cells: Fundamentals and applications, Curr. Opin. Solid State Mater. Sci. 8 (2004) 372.

[30] A.L. Dicks, Molten carbonate fuel cells, Curr. Opin. Solid State Mater. Sci. 8 (2004) 379.

[31] S.C. Singhal, Solid oxide fuel cells, Electrochem. Soc. Interface 16 (2007) 41.

[32] E.D. Wachsman, S.C. Singhal, Solid oxide fuel cell commercialization, research, and challenges, Electrochem. Soc. Interface 18 (2009) 38.

[33] C. Lamy, A. Lima, V. LeRhun, F. Delime, C. Coutanceau, J.-M. Léger, Recent advances in the development of direct alcohol fuel cells (DAFC), J. Power Sources 105 (2002) 283.

[34] A. Lima, C. Coutanceau, J.M. Léger, C. Lamy, Investigation of Ternary Catalysts for Methanol Electrooxidation, J. Appl. Electrochem. 31 (2001) 379.

[35] M. Simões, S. Baranton, C. Coutanceau, Electro-oxidation of glycerol at Pd based nano-catalysts for an application in alkaline fuel cells for chemicals and energy cogeneration, Appl. Catal., B 93 (2010) 354.

[36] E.V. Spinacé, M. Linardi, A.O. Neto, Co-catalytic effect of nickel in the electro-oxidation of ethanol on binary Pt-Sn electrocatalysts, Electrochem. Commun. 7 (2005) 365.

[37] E. Antolini, Catalysts for direct ethanol fuel cells, J. Power Sources 170 (2007) 1.

[38] J.B. Xu, T.S. Zhao, Y.S. Li, W.W. Yang, Synthesis and characterization of the Au-modified Pd cathode catalyst for alkaline direct ethanol fuel cells, Int. J. Hydrogen Energ. 35 (2010) 9693.

[39] A. Ilie, M. Simoes, S. Baranton, C. Coutanceau, S. Martemianov, Influence of operational parameters and of catalytic materials on electrical performance of Direct Glycerol Solid Alkaline Membrane Fuel Cells, J. Power Sources 196 (2011) 4965.

[40] S. Song, V. Maragou, P. Tsiakaras, How Far Are Direct Alcohol Fuel Cells From Our Energy Future?, J. Fuel Cell Sci. Technol. 4 (2007) 203.

[41] Y. Kwon, K.J.P. Schouten, M.T.M. Koper, Mechanism of the Catalytic Oxidation of Glycerol on Polycrystalline Gold and Platinum Electrodes, ChemCatChem 3 (2011) 1176.

[42] Z. Zhang, L. Xin, J. Qi, D.J. Chadderdon, K. Sun, K.M. Warsko, W. Li, Selective electro-oxidation of glycerol to tartronate or mesoxalate on Au nanoparticle catalyst via electrode potential tuning in anion-exchange membrane electro-catalytic flow reactor, Appl. Catal., B 147 (2014) 871.

[43] S. Kalcheva, P. Iotov, Comparative mechanistic studies on the oxidation of aromatic and aliphatic hydroxyl derivatives in an alkaline medium at preanodized Pt, Au and Pt/Au electrodes in presence of redox mediators, Turk. J. Chem. 23 (1999) 369.

[44] H. Liu, C. Song, L. Zhang, J. Zhang, H. Wang, D.P. Wilkinson, A review of anode catalysis in the direct methanol fuel cell, J. Power Sources 155 (2006) 95.

[45] C. Coutanceau, S. Brimaud, C. Lamy, J.M. Léger, L. Dubau, S. Rousseau, F. Vigier, Review of different methods for developing nanoelectrocatalysts for the oxidation of organic compounds, Electrochim. Acta 53 (2008) 6865.

[46] G. Yildiz, F. Kadirgan, Synergistic effect in the electrocatalytic oxidation of glycerol on platinum-palladium alloy electrodes, Anal. Chim. 84 (1994) 455.

[47] F. Kadirgan, S. Beyhan, T. Atilan, Preparation and characterization of nano-sized Pt-Pd/C catalysts and comparison of their electro-activity toward methanol and ethanol oxidation, Int. J. Hydrogen Energ. 34 (2009) 4312.

[48] V. Bambagioni, C. Bianchini, A. Marchionni, J. Filippi, F. Vizza, J. Teddy, P. Serp, M. Zhiani, Pd and Pt-Ru anode electrocatalysts supported on multi-walled carbon nanotubes and their use in passive and active direct alcohol fuel cells with an anion-exchange membrane (alcohol = methanol, ethanol, glycerol), J. Power Sources 190 (2009) 241.

[49] T. Saida, N. Ogiwara, Y. Takasu, W. Sugimoto, Titanium Oxide Nanosheet Modified PtRu/C Electrocatalyst for Direct Methanol Fuel Cell Anodes, J. Phys. Chem. C 114 (2010) 13390.

[50] S. Basri, S.K. Kamarudin, W.R.W. Daud, Z. Yaakub, Nanocatalyst for direct methanol fuel cell (DMFC), Int. J. Hydrogen Energ. 35 (2010) 7957.

[51] D.R. Rolison, P.L. Hagans, K.E. Swider, J.W. Long, Role of Hydrous Ruthenium Oxide in Pt-Ru Direct Methanol Fuel Cell Anode Electrocatalysts: The Importance of Mixed Electron/Proton Conductivity, Langmuir 15 (1999) 774.

[52] J.W. Long, R.M. Stroud, K.E. Swider-Lyons, D.R. Rolison, How To Make Electrocatalysts More Active for Direct Methanol Oxidation - Avoid PtRu Bimetallic Alloys!, J. Phys. Chem. B 104 (2000) 9772.

[53] Y. Shimazaki, S. Hayasaka, T. Koyama, D. Nagao, Y. Kobayashi, M. Konno, A durable PtRu/C catalyst with a thin protective layer for direct methanol fuel cells, J. Colloid Interface Sci. 351 (2010) 580.

[54] C. Zhou, F. Peng, H. Wang, H. Yu, C. Peng, J. Yang, Development of stable PtRu catalyst coated with manganese dioxide for electrocatalytic oxidation of methanol, Electrochem. Commun. 12 (2010) 1210.

[55] N. Tsiouvaras, M.V. Martínez-Huerta, O. Paschos, U. Stimming, J.L.G. Fierro, M.A. Peña, PtRuMo/C catalysts for direct methanol fuel cells: Effect of the pretreatment on the structural characteristics and methanol electrooxidation, Int. J. Hydrogen Energ. 35 (2010) 11478.

[56] S. Takenaka, H. Matsumori, K. Nakagawa, H. Matsune, E. Tanabe, M. Kishida, Improvement in the Durability of Pt Electrocatalysts by Coverage with Silica Layers, J. Phys. Chem. C 111 (2007) 15133.

[57] L. Kuai, S. Wang, B. Geng, Gold-platinum yolk-shell structure: a facile galvanic displacement synthesis and highly active electrocatalytic properties for methanol oxidation with super CO-tolerance, Chem. Commun. 47 (2011) 6093.

[58] R. Wang, H. Wang, B. Wei, W. Wang, Z. Lei, Carbon supported Pt-shell modified PdCo-core with electrocatalyst for methanol oxidation, Int. J. Hydrogen Energ. 35 (2010) 10081.

[59] C. Xu, L. Cheng, P. Shen, Y. Liu, Methanol and ethanol electrooxidation on Pt and Pd supported on carbon microspheres in alkaline media, Electrochem. Commun. 9 (2007) 997.

[60] S.T. Nguyen, H.M. Law, H.T. Nguyen, N. Kristian, S. Wang, S.H. Chan, X. Wang, Enhancement effect of Ag for Pd/C towards the ethanol electro-oxidation in alkaline media, Appl. Catal., B 91 (2009) 507.

[61] S.T. Nguyen, D.S. Ling Tan, J.-M. Lee, S.H. Chan, J.Y. Wang, X. Wang, Tb promoted Pd/C catalysts for the electrooxidation of ethanol in alkaline media, Int. J. Hydrogen Energ. 36 (2011) 9645.

[62] M.M.O. Thotiyl, T.R. Kumar, S. Sampath, Pd Supported on Titanium Nitride for Efficient Ethanol Oxidation, J. Phys. Chem. C 114 (2010) 17934.

[63] Z. Zhang, L. Xin, K. Sun, W. Li, Pd–Ni electrocatalysts for efficient ethanol oxidation reaction in alkaline electrolyte, Int. J. Hydrogen Energ. 36 (2011) 12686.

[64] C. Xu, Z. Tian, P. Shen, S.P. Jiang, Oxide ($CeO_2$, NiO, $Co_3O_4$ and $Mn_3O_4$)-promoted Pd/C electrocatalysts for alcohol electrooxidation in alkaline media, Electrochim. Acta 53 (2008) 2610.

[65] F. Hu, F. Ding, S. Song, P.K. Shen, Pd electrocatalyst supported on carbonized $TiO_2$ nanotube for ethanol oxidation, J. Power Sources 163 (2006) 415.

[66] M. Mougenot, A. Caillard, M. Simoes, S. Baranton, C. Coutanceau, P. Brault, PdAu/C catalysts prepared by plasma sputtering for the electro-oxidation of glycerol, Appl. Catal., B 107 (2011) 372.

[67] M. Simões, S. Baranton, C. Coutanceau, Enhancement of catalytic properties for glycerol electrooxidation on Pt and Pd nanoparticles induced by Bi surface modification, Appl. Catal., B 110 (2011) 40.

[68] L. Su, W. Jia, A. Schempf, Y. Lei, Palladium/titanium dioxide nanofibers for glycerol electrooxidation in alkaline medium, Electrochem. Commun. 11 (2009) 2199.

[69] Z. Wang, F. Hu, P.K. Shen, Carbonized porous anodic alumina as electrocatalyst support for alcohol oxidation, Electrochem. Commun. 8 (2006) 1764.

[70] C. Xu, P.K. Shen, Novel Pt/$CeO_2$/C catalysts for electrooxidation of alcohols in alkaline media, Chem. Commun. (2004) 2238.

[71] S. Lee, H.J. Kim, S.M. Choi, M.H. Seo, W.B. Kim, The promotional effect of Ni on bimetallic PtNi/C catalysts for glycerol electrooxidation, Appl. Catal., A 429–430 (2012) 39.

[72] A. Kahyaoglu, B. Beden, C. Lamy, in: Electrochim. Acta 29 (1984), 1489, cited in Alonso, *et al*., Z. phys. Chemie 271 (1990), p. 800.

[73] X. Li, J. Liu, Q. Huang, W. Vogel, D.L. Akins, H. Yang, Effect of heat treatment on stability of gold particle modified carbon supported Pt-Ru anode catalysts for a direct methanol fuel cell, Electrochim. Acta 56 (2010) 278.

[74] E.C. Venancio, W.T. Napporn, A.J. Motheo, Electro-oxidation of glycerol on platinum dispersed in polyaniline matrices, Electrochim. Acta 47 (2002) 1495.

[75] M.L. Avramov-Ivic, J.M. Leger, C. Lamy, V.D. Jovic, S.D. Petrovic, The electro-oxidation of glycerol on the gold(100)-oriented single-crystal surface and poly crystalline surface in 0.1 M NaOH, J. Electroanal. Chem. 308 (1991) 309.

[76] Y.W. Lee, M. Kim, Y. Kim, S.W. Kang, J.-H. Lee, S.W. Han, Synthesis and Electrocatalytic Activity of Au-Pd Alloy Nanodendrites for Ethanol Oxidation, J. Phys. Chem. C 114 (2010) 7689.

[77] C. Xu, Z. Tian, Z. Chen, S.P. Jiang, Pd/C promoted by Au for 2-propanol electrooxidation in alkaline media, Electrochem. Commun. 10 (2008) 246.

[78] Z. Zhang, L. Xin, J. Qi, D.J. Chadderdon, W. Li, Supported Pt, Pd and Au nanoparticle anode catalysts for anion-exchange membrane fuel cells with glycerol and crude glycerol fuels, Appl. Catal., B 136–137 (2013) 29.

[79] I. Danaee, M. Jafarian, F. Forouzandeh, F. Gobal, M.G. Mahjani, Electrocatalytic oxidation of methanol on Ni and NiCu alloy modified glassy carbon electrode, Int. J. Hydrogen Energ. 33 (2008) 4367.

[80] D. Das, P. Samaddar, P. Sen, K. Das, Oxidation of some aliphatic polyols on anodically deposited MnO2, J. Appl. Electrochem. 38 (2008) 743.

[81] M.-W. Xu, G.-Y. Gao, W.-J. Zhou, K.-F. Zhang, H.-L. Li, Novel Pd/[beta]-MnO2 nanotubes composites as catalysts for methanol oxidation in alkaline solution, J. Power Sources 175 (2008) 217.

[82] S. Tang, G. Sun, J. Qi, S. Sun, J. Guo, Q. Xin, G.M. Haarberg, Review of New Carbon Materials as Catalyst Supports in Direct Alcohol Fuel Cells, Chin. J. Catal. 31 (2010) 12.

[83] J. Thepkaew, S. Therdthianwong, A. Therdthianwong, Effect of pre-treatment approach of a carbon support on activity of PtSn/C electrocatalysts for direct ethanol fuel cells, J. Appl. Electrochem. 41 (2011) 435.

[84] A. Halder, S. Sharma, M.S. Hegde, N. Ravishankar, Controlled Attachment of Ultrafine Platinum Nanoparticles on Functionalized Carbon Nanotubes with High Electrocatalytic Activity for Methanol Oxidation, J. Phys. Chem. C 113 (2009) 1466.

[85] L. Zhang, F. Li, Helical nanocoiled and microcoiled carbon fibers as effective catalyst supports for electrooxidation of methanol, Electrochim. Acta 55 (2010) 6695.

[86] Z. Yan, Z. Hu, C. Chen, H. Meng, P.K. Shen, H. Ji, Y. Meng, Hollow carbon hemispheres supported palladium electrocatalyst at improved performance for alcohol oxidation, J. Power Sources 195 (2010) 7146.

[87] H.J. Kim, S.M. Choi, M.H. Seo, S. Green, G.W. Huber, W.B. Kim, Efficient electrooxidation of biomass-derived glycerol over a graphene-supported PtRu electrocatalyst, Electrochem. Commun. 13 (2011) 890.

[88] L. Xing, J. Jia, Y. Wang, B. Zhang, S. Dong, Pt modified TiO2 nanotubes electrode: Preparation and electrocatalytic application for methanol oxidation, Int. J. Hydrogen Energ. 35 (2010) 12169.

[89] S. Guerin, B.E. Hayden, D. Pletcher, M.E. Rendall, J.-P. Suchsland, L.J. Williams, Combinatorial Approach to the Study of Particle Size Effects in Electrocatalysis: Synthesis of Supported Gold Nanoparticles, J. Comb. Chem. 8 (2006) 791.

[90] B.E. Hayden, D. Pletcher, J.-P. Suchsland, Enhanced Activity for Electrocatalytic Oxidation of Carbon Monoxide on Titania-Supported Gold Nanoparticles, Angew. Chem. Int. Ed. 46 (2007) 3530.

[91] M. Avramov-Ivic, Adsorption of glycerol on platinum in alkaline medium: effect of the electrode structure J. Electroanal. Chem. 351 (1993) 285.

[92] A. Marchionni, M. Bevilacqua, C. Bianchini, Y.-X. Chen, J. Filippi, P. Fornasiero, A. Lavacchi, H. Miller, L. Wang, F. Vizza, Electrooxidation of Ethylene Glycol and Glycerol on Pd-(Ni-Zn)/C Anodes in Direct Alcohol Fuel Cells, ChemSusChem 6 (2013) 518.

[93] C.A. Martins, M.J. Giz, G.A. Camara, Generation of carbon dioxide from glycerol: Evidences of massive production on polycrystalline platinum, Electrochim. Acta 56 (2011) 4549.

[94] Y. Kwon, M.T.M. Koper, Combining Voltammetry with HPLC: Application to Electro-Oxidation of Glycerol, Anal. Chem. 82 (2010) 5420.

[95] L. Roquet, E.M. Belgsir, J.M. Léger, C. Lamy, Kinetics and mechanisms of the electrocatalytic oxidation of glycerol as investigated by chromatographic analysis of the reaction products: Potential and pH effects, Electrochim. Acta 39 (1994) 2387.

[96] D.Z. Jeffery, G.A. Camara, The formation of carbon dioxide during glycerol electrooxidation in alkaline media: First spectroscopic evidences, Electrochem. Commun. 12 (2010) 1129.

[97] S. Trasatti, O.A. Petrii, Real surface area measurements in electrochemistry, Pure Appl. Chem. 63 (1991) 711.

[98] R. Woods, Chemisorption at electrodes, in: A.J. Bard (Ed.) Electroanalytical Chemistry: a Series of Advances, vol. 9, Marcel Dekker, New York, 1976, pp. 1.

[99] C. Batchelor-McAuley, G.G. Wildgoose, R.G. Compton, The contrasting behaviour of polycrystalline bulk gold and gold nanoparticle modified electrodes towards the underpotential deposition of thallium, New J. Chem. 32 (2008) 941.

[100] S.G. Hickey, D.J. Riley, Underpotential deposition of copper on electrodes modified with colloidal gold, Electrochem. Commun. 1 (1999) 116.

[101] J. Zhao, Liniu, S. Dong, Technique for Determination of Gold Electrode Area and its Application of Characterization in Self-Assembling Process, Molecular Crystals and Liquid Crystals Science and Technology. Section A. Molecular Crystals and Liquid Crystals 337 (1999) 265.

[102] M.O. Finot, G.D. Braybrook, M.T. McDermott, Characterization of electrochemically deposited gold nanocrystals on glassy carbon electrodes, J. Electroanal. Chem. 466 (1999) 234.

[103] J. Hernández, J. Solla-Gullón, E. Herrero, Gold nanoparticles synthesized in a water-in-oil microemulsion: electrochemical characterization and effect of the surface structure on the oxygen reduction reaction, J. Electroanal. Chem. 574 (2004) 185.

[104] Z. Jusys, T.J. Schmidt, L. Dubau, K. Lasch, L. Jörissen, J. Garche, R.J. Behm, Activity of PtRuMeOx (Me = W, Mo or V) catalysts towards methanol oxidation and their characterization, J. Power Sources 105 (2002) 297.

[105] L.-I. Fang, Q. Tao, M.-F. Li, L.-W. Liao, D. Chen, Y.-X. Chen, Determination of the real surface area of palladium electrode, Chin. J. Chem. Phys. 23 (2010) 543.

[106] L.D. Burke, P.F. Nugent, The Electrochemistry of Gold: I The Redox Behaviour of the Metal in Aqueous Media Gold Bull. 30 (1997) 43.

[107] L.D. Burke, P.F. Nugent, The Electrochemistry of Gold: II The Electrocatalytic Behaviour of the Metal in Aqueous Media, Gold Bull. 31 (1998) 39.

[108] C. Alonso, J. Gonzalez-Velsasco, Oxidation electrocatalytic of glycerol on gold in alkaline medium, Z. Phys. Chemie 271 (1990) 799.

[109] E. Verlato, S. Cattarin, N. Comisso, A. Gambirasi, M. Musiani, L. Vázquez-Gómez, Preparation of Pd-Modified Ni Foam Electrodes and Their Use as Anodes for the Oxidation of Alcohols in Basic Media, Electrocatal. 3 (2012) 48.

[110] M. Zhiani, H. Rostami, S. Majidi, K. Karami, Bis (dibenzylidene acetone) palladium (0) catalyst for glycerol oxidation in half cell and in alkaline direct glycerol fuel cell, Int. J. Hydrogen Energ. 38 (2013) 5435.

[111] H. Li, D. Kang, H. Wang, R. Wang, Carbon-supported Pt-RuCo nanoparticles with low-noble-metal content and superior catalysis for ethanol oxidization, Int. J. Electrochem. Sci. 2 (2011) 1058

[112] Y. Zhao, S. Nie, H. Wang, J. Tian, Z. Ning, X. Li, Direct synthesis of palladium nanoparticles on Mn3O4 modified multi-walled carbon nanotubes: A highly active catalyst for methanol electro-oxidation in alkaline media, J. Power Sources 218 (2012) 320.

[113] S. Sharma, A. Ganguly, P. Papakonstantinou, X. Miao, M. Li, J.L. Hutchison, M. Delichatsios, S. Ukleja, Rapid Microwave Synthesis of CO Tolerant Reduced Graphene Oxide-Supported Platinum Electrocatalysts for Oxidation of Methanol, J. Phys. Chem. C 114 (2010) 19459.

[114] M.N. Martin, J.I. Basham, P. Chando, S.-K. Eah, Charged Gold Nanoparticles in Non-Polar Solvents: 10-min Synthesis and 2D Self-Assembly, Langmuir 26 (2010) 7410.

[115] Z. Borkowska, A. Tymosiak-Zielinska, G. Shul, Electrooxidation of methanol on polycrystalline and single crystal gold electrodes, Electrochim. Acta 49 (2004) 1209.

[116] J.C. Hoogvliet, M. Dijksma, B. Kamp, W.P. van Bennekom, Electrochemical Pretreatment of Polycrystalline Gold Electrodes To Produce a Reproducible Surface Roughness for Self-Assembly: A Study in Phosphate Buffer pH 7.4, Anal. Chem. 72 (2000) 2016.

[117] Z. Zhang, L. Xin, W. Li, Supported gold nanoparticles as anode catalyst for anion-exchange membrane-direct glycerol fuel cell (AEM-DGFC), Int. J. Hydrogen Energ. 37 (2012) 9393.

[118] J. Wang, J. Gong, Y. Xiong, J. Yang, Y. Gao, Y. Liu, X. Lu, Z. Tang, Shape-dependent electrocatalytic activity of monodispersed gold nanocrystals toward glucose oxidation, Chem. Commun. 47 (2011) 6894.

[119] B.E. Hayden, D. Pletcher, M.E. Rendall, J.-P. Suchsland, CO Oxidation on Gold in Acidic Environments: Particle Size and Substrate Effects, J. Phys. Chem. C 111 (2007) 17044.

[120] A. Santasalo-Aarnio, S. Tuomi, K. Jalkanen, K. Kontturi, T. Kallio, The correlation of electrochemical and fuel cell results for alcohol oxidation in acidic and alkaline media, Electrochim. Acta 87 (2013) 730.

[121] Y.S. Li, T.S. Zhao, Z.X. Liang, Effect of polymer binders in anode catalyst layer on performance of alkaline direct ethanol fuel cells, J. Power Sources 190 (2009) 223.

[122] M.S. McGovern, E.C. Garnett, C. Rice, R.I. Masel, A. Wieckowski, Effects of Nafion as a binding agent for unsupported nanoparticle catalysts, J. Power Sources 115 (2003) 35.

[123] J.A. Lopez-Sanchez, N. Dimitratos, C. Hammond, G.L. Brett, L. Kesavan, S. White, P. Miedziak, R. Tiruvalam, R.L. Jenkins, A.F. Carley, D. Knight, C.J. Kiely, G.J. Hutchings, Facile removal of stabilizer-ligands from supported gold nanoparticles, Nat. Chem. 3 (2011) 551.

[124] M.S. El-Deab, Electrocatalytic oxidation of methanol at $\gamma$-MnOOH nanorods modified Pt electrodes, Int. J. Electrochem. Sci. 4 (2009) 1329.

[125] F. Teng, S. Santhanagopalan, D.D. Meng, Microstructure control of $MnO_2$/CNT hybrids under in-situ hydrothermal conditions, Solid State Sci. 12 (2010) 1677.

[126] A.E. Fischer, K.A. Pettigrew, D.R. Rolison, R.M. Stroud, J.W. Long, Incorporation of Homogeneous, Nanoscale $MnO_2$ within Ultraporous Carbon Structures via Self-Limiting Electroless Deposition: Implications for Electrochemical Capacitors, Nano Lett. 7 (2007) 281.

[127] Z. Ma, C. Liang, S.H. Overbury, S. Dai, Gold nanoparticles on electroless-deposition-derived $MnO_x$/C: Synthesis, characterization, and catalytic CO oxidation, J. Catal. 252 (2007) 119.

[128] V. Raghuveer, A. Manthiram, Mesoporous Carbon with Larger Pore Diameter as an Electrocatalyst Support for Methanol Oxidation, Electrochem. Solid-State Lett. 7 (2004) A336.

[129] D. Padayachee, Manganese- oxide based gold catalysts for low temperature CO conversion, Chemistry, University of the Witwatersrand, Johannesburg, MSc thesis, 2003.

[130] H. Tamura, N. Katayama, R. Furuichi, Modeling of Ion-Exchange Reactions on Metal Oxides with the Frumkin Isotherm. 1. Acid−Base and Charge Characteristics of $MnO_2$, $TiO_2$, $Fe_3O_4$, and $Al_2O_3$ Surfaces and Adsorption Affinity of Alkali Metal Ions, Environ. Sci. Technol. 30 (1996) 1198.

[131] X. Dong, W. Shen, J. Gu, L. Xiong, Y. Zhu, H. Li, J. Shi, A structure of $MnO_2$ embedded in CMK-3 framework developed by a redox method, Microporous Mesoporous Mater. 91 (2006) 120.

[132] M.P. Casaletto, A. Longo, A. Martorana, A. Prestianni, A.M. Venezia, XPS study of supported gold catalysts: the role of $Au^0$ and $Au^{+\delta}$ species as active sites, Surf. Interface Anal. 38 (2006) 215.

[133] P. Ascarelli, M. Cini, G. Missoni, N. Nistico, X.P.S. line broadening in small metal particles, J. Phys. Colloques 38 (1977) C2.

[134] H. Darmstadt, C. Roy, S. Kaliaguine, S.J. Choi, R. Ryoo, Surface chemistry of ordered mesoporous carbons, Carbon 40 (2002) 2673.

[135] S.M. Senthil Kumar, J. Soler Herrero, S. Irusta, K. Scott, The effect of pretreatment of Vulcan XC-72R carbon on morphology and electrochemical oxygen reduction kinetics of supported Pd nano-particle in acidic electrolyte, J. Electroanal. Chem. 647 (2010) 211.

[136] J.-H. Zhou, Z.-J. Sui, J. Zhu, P. Li, D. Chen, Y.-C. Dai, W.-K. Yuan, Characterization of surface oxygen complexes on carbon nanofibers by TPD, XPS and FT-IR, Carbon 45 (2007) 785.

[137] B.L. Wu, D. Lincot, J. Vedel, L.T. Yu, Voltammetric and electrogravimetric study of manganese dioxide thin film electrodes. Part 1. Electrodeposited films, J. Electroanal. Chem. 420 (1997) 159.

[138] M. Morita, C. Iwakura, H. Tamura, The anodic characteristics of manganese dioxide electrodes prepared by thermal decomposition of manganese nitrate, Electrochim. Acta 22 (1977) 325.

[139] M.S. El-Deab, M.I. Awad, A.M. Mohammad, T. Ohsaka, Enhanced water electrolysis: Electrocatalytic generation of oxygen gas at manganese oxide nanorods modified electrodes, Electrochem. Commun. 9 (2007) 2082.

[140] S. Sen Gupta, J. Datta, Electrode kinetics of ethanol oxidation on novel CuNi alloy supported catalysts synthesized from PTFE suspension, J. Power Sources 145 (2005) 124.

[141] H.T. Zheng, Y. Li, S. Chen, P.K. Shen, Effect of support on the activity of Pd electrocatalyst for ethanol oxidation, J. Power Sources 163 (2006) 371.

[142] W. Chen, J. Kim, S. Sun, S. Chen, Composition Effects of FePt Alloy Nanoparticles on the Electro-Oxidation of Formic Acid, Langmuir 23 (2007) 11303.

[143] C. Xu, R. Zeng, P.K. Shen, Z. Wei, Synergistic effect of $CeO_2$ modified Pt/C catalysts on the alcohols oxidation, Electrochim. Acta 51 (2005) 1031.

[144] P.K. Shen, C. Xu, Alcohol oxidation on nanocrystalline oxide Pd/C promoted electrocatalysts, Electrochem. Commun. 8 (2006) 184.

[145] R. Awasthi, Anindita, R.N. Singh, Synthesis and Characterization of Nano Structured Pd-Ni and Pd-Ni-C Composites Towards Electrooxidation of Alcohols, The Open Catalysis Journal 3 (2010) 70.

[146] D.G. Duff, A. Baiker, P.P. Edwards, A new hydrosol of gold clusters. 1. Formation and particle size variation, Langmuir 9 (1993) 2301.

[147] J. Kimling, M. Maier, B. Okenve, V. Kotaidis, H. Ballot, A. Plech, Turkevich Method for Gold Nanoparticle Synthesis Revisited, J. Phys. Chem. B 110 (2006) 15700.

[148] A. Orlov, D. Jefferson, N. Macleod, R. Lambert, Photocatalytic Properties of TiO2 Modified with Gold Nanoparticles in the Degradation of 4-Chlorophenol in Aqueous Solution, Catal. Lett. 92 (2004) 41.

[149] P.S. Haider, Potential of gold-based catalysts for catalytic oxidation with oxygen, Chemical Engineering and Industrial Chemistry, ETH, Zürich, Dr.sc. thesis, 2009.

[150] J.-D. Grunwaldt, C. Kiener, C. Wögerbauer, A. Baiker, Preparation of Supported Gold Catalysts for Low-Temperature CO Oxidation via “Size-Controlled” Gold Colloids, J. Catal. 181 (1999) 223.

[151] K.J.J. Mayrhofer, B.B. Blizanac, M. Arenz, V.R. Stamenkovic, P.N. Ross, N.M. Markovic, The Impact of Geometric and Surface Electronic Properties of Pt-Catalysts on the Particle Size Effect in Electrocatalysis, J. Phys. Chem. B 109 (2005) 14433.

[152] T. Frelink, W. Visscher, J.A.R. van Veen, Particle size effect of carbon-supported platinum catalysts for the electrooxidation of methanol, J. Electroanal. Chem. 382 (1995) 65.

[153] X.-M. Wang, Y.-Y. Xia, Synthesis, characterization and catalytic activity of an ultrafine Pd/C catalyst for formic acid electrooxidation, Electrochim. Acta 54 (2009) 7525.

[154] J.A. Poirier, G.E. Stoner, Microstructural effects on electrocatalytic oxygen reduction activity of nano-grained thin-film platinum in acid media, J. Electrochem. Soc. 141 (1994) 425.

[155] M. Haruta, Gold as a novel catalyst in the 21st century: Preparation, working mechanism and applications, Gold Bull. 37 (2004) 27.

[156] K. Ding, Y. Wang, H. Yang, C. Zheng, YanliCao, H. Wei, Y. Wang, Z. Guo, Electrocatalytic activity of multi-walled carbon nanotubes-supported PtxPdy catalysts prepared by a pyrolysis process toward ethanol oxidation reaction, Electrochim. Acta 100 (2013) 147.

[157] A.J. Wain, Imaging size effects on the electrocatalytic activity of gold nanoparticles using scanning electrochemical microscopy, Electrochim. Acta 92 (2013) 383.

[158] J. Hernández, J. Solla-Gullón, E. Herrero, A. Aldaz, J.M. Feliu, Methanol oxidation on gold nanoparticles in alkaline media: Unusual electrocatalytic activity, Electrochim. Acta 52 (2006) 1662.

[159] A. Hamelin, Y. Ho, S.C. Chang, X. Gao, M.J. Weaver, Surface crystallographic dependence of voltammetric oxidation of polyhydric alcohols and related systems at monocrystalline gold-acidic aqueous interfaces, Langmuir 8 (1992) 975.

[160] A.-X. Yin, X.-Q. Min, Y.-W. Zhang, C.-H. Yan, Shape-Selective Synthesis and Facet-Dependent Enhanced Electrocatalytic Activity and Durability of Monodisperse Sub-10 nm Pt−Pd Tetrahedrons and Cubes, J. Am. Chem. Soc 133 (2011) 3816.

[161] G. Wu, B.-Q. Xu, Carbon nanotube supported Pt electrodes for methanol oxidation: A comparison between multi- and single-walled carbon nanotubes, J. Power Sources 174 (2007) 148.

[162] I. Sobczak, K. Jagodzinska, M. Ziolek, Glycerol oxidation on gold catalysts supported on group five metal oxides - A comparative study with other metal oxides and carbon based catalysts, Catal. Today 158 (2010) 121.

[163] S. Carrettin, P. McMorn, P. Johnston, K. Griffin, G.J. Hutchings, Selective oxidation of glycerol to glyceric acid using a gold catalyst in aqueous sodium hydroxide, Chem. Commun. (2002) 696.

[164] B.G. Pollet, J.T.E. Goh, The Importance of Ultrasonic Parameters in the Preparation of Fuel Cell Catalyst Inks, Electrochim. Acta (2013) http://dx.doi.org/10.1016/j.electacta.2013.09.160.

[165] E. Gileadi, Electrode kinetics for chemists, chemical engineers, and materials scientists, VCH Publishers Inc., New York, 1993.

[166] B. Liu, J.H. Chen, C.H. Xiao, K.Z. Cui, L. Yang, H.L. Pang, Y.F. Kuang, Preparation of Pt/MgO/CNT Hybrid Catalysts and Their Electrocatalytic Properties for Ethanol Electrooxidation, Energ. Fuel. 21 (2007) 1365.

[167] J. Wang, Analytical Electrochemistry, 2nd ed., Wiley-VCH, New York, 2001.

[168] H. Wang, M. Zhang, F. Cheng, C. Xu, Pt Supported on Ti for Methanol Electrooxidation by Magnetron Sputter Method, Int. J. Electrochem. Sci. 3 (2008) 946.

[169] A.S. Adekunle, O.S. Oluwafemi, V. Ncapayi, R.E. Sadiku, J.T. Agee, S.O. Ojo, S.P. Songca, Ethanol sensor based on platinum-MWCNT-NiO nanoparticles platform electrode, Int. J. Electrochem. Sci. 7 (2012) 2695.

# APPENDICES

Note: Each Appendix is numbered according the respective chapter. There are no appendices to Chapters 1 and 2, and the numbering in this section therefore begins at Appendix 3 – corresponding to Chapter 3.

# APPENDIX 3

## Appendix 3.1 Typical glycerol oxidation CVs of 19 % Au/C catalyst in different electrochemical cell designs

**EC 1 with titanium discs**

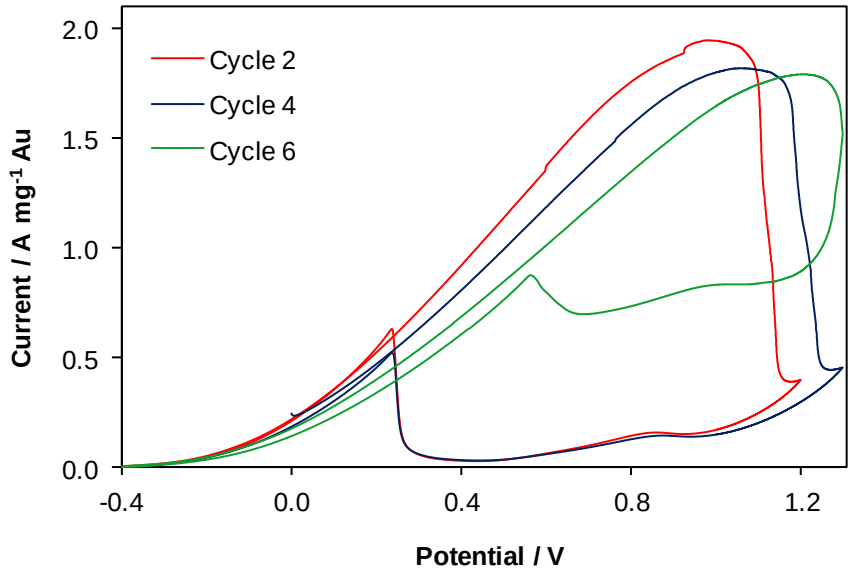


**EC 2 with GCEs**

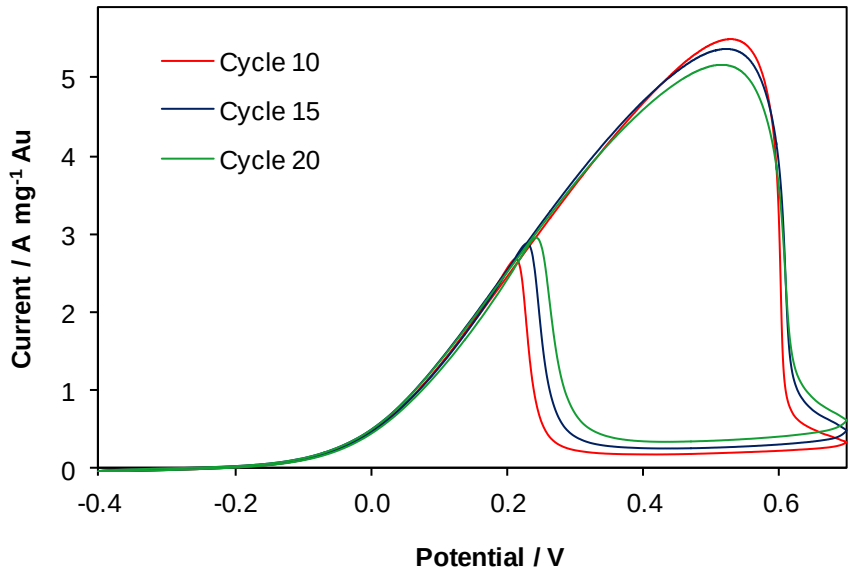

**EC 3 with GCPs**

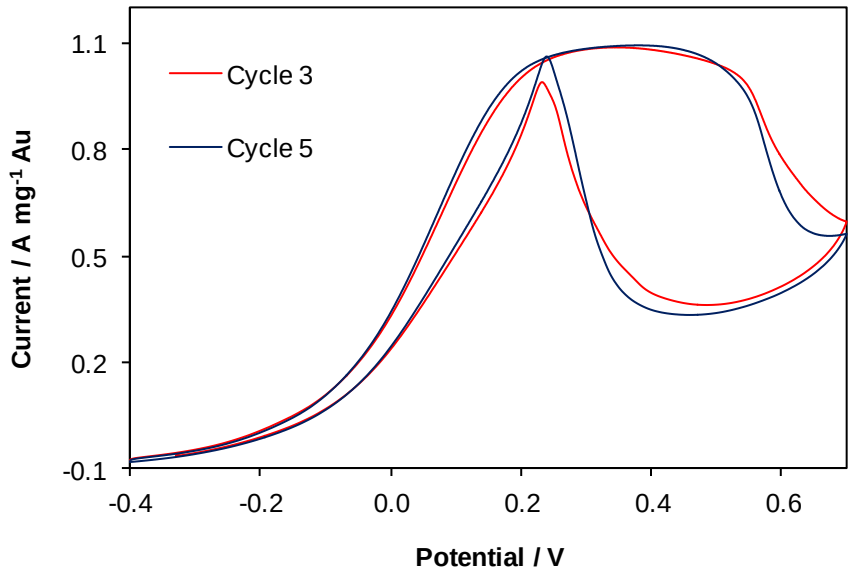


**EC 4 (Optimised electrochemical cell) with GCPs**

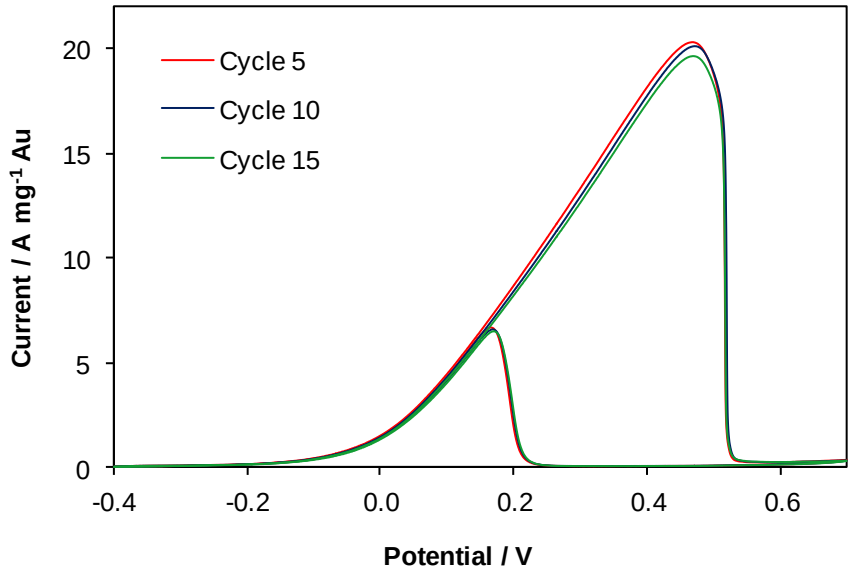


All CVs carried out in 0.5 M glycerol/1 M KOH at 50 mV $s^{-1}$. No pre-soak or strip cycles. No post-IR correction. Potentials are shown *vs*. Hg/ HgO reference.

| EC no. | Electrode | Ru | Ave current (3 nm Au/C cat) | | | |
|---|---|---|---|---|---|---|
| | | | A/mg Au | Error | mA/cm$^2$ | Error |
| EC1 | Ti discs# | 13.6 - 19.6 | 2 | | 17 | |
| EC2 | GCEs | 11 - 22 | 5 | 2 | 42 | 18 |
| EC3 | GCPs* | 57 | 0.6 | | 101 | |
| EC4 | GCPs | 1.0 - 2.2 | 20 | 3 | 237 | 31 |

**No error values for Ti discs and GCPs with o-ring, since replicability was not possible**

**50 mV/s, no pre-soak, no post-IR correction**

| | | |
|---|---|---|
| * Taken from GCP C results on 06/10/2011: | Current | 20 mA |
| | EASA | 0.198 cm^2 |
| | Au exposed | 0.029 mg |
| # Taken from Ti disc C results on 19/07/2011: | Current | 35.38 mA |
| | EASA | 2.045 cm^2 |
| | Au exposed | 0.018 mg |

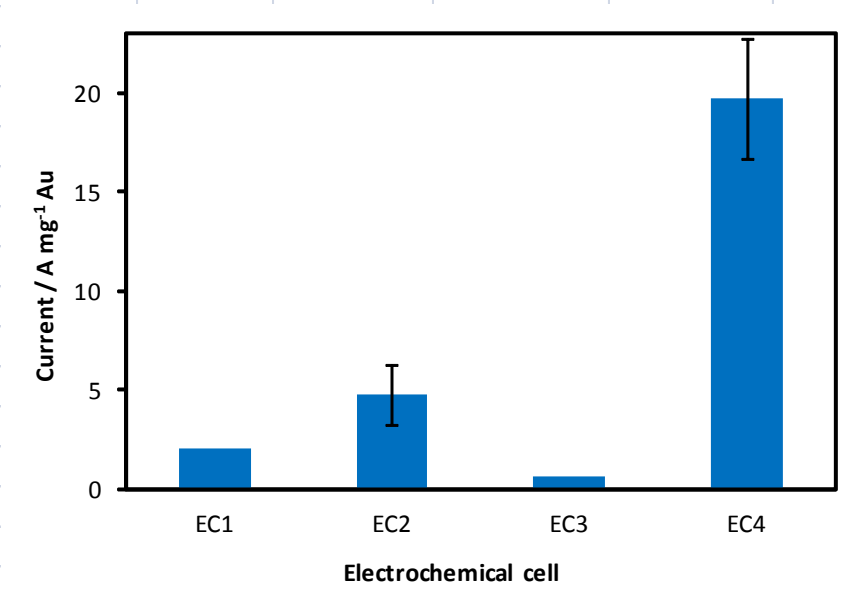

## Appendix 3.2 Calculation of Hg/HgO reference potential

**In 1 M KOH**:

0 V *vs*. RHE at pH 14 = 0 – (14*0.0595) = -0.833 V

*vs*. AgAgCl/satd KCl = -0.833 – 0.197 = -1.03 V

Measured open circuit potential Hg/HgO *vs*. AgAgCl/satd KCl ref. electrode = -77 mV

Therefore Hg/HgO *vs*. RHE at pH 14 = **+0.95 V**

## Appendix 3.3 CV of polycrystalline gold electrode in 1 M $H_2SO_4$

**Potentials *vs.* SCE; scan rate 50 mV/s**

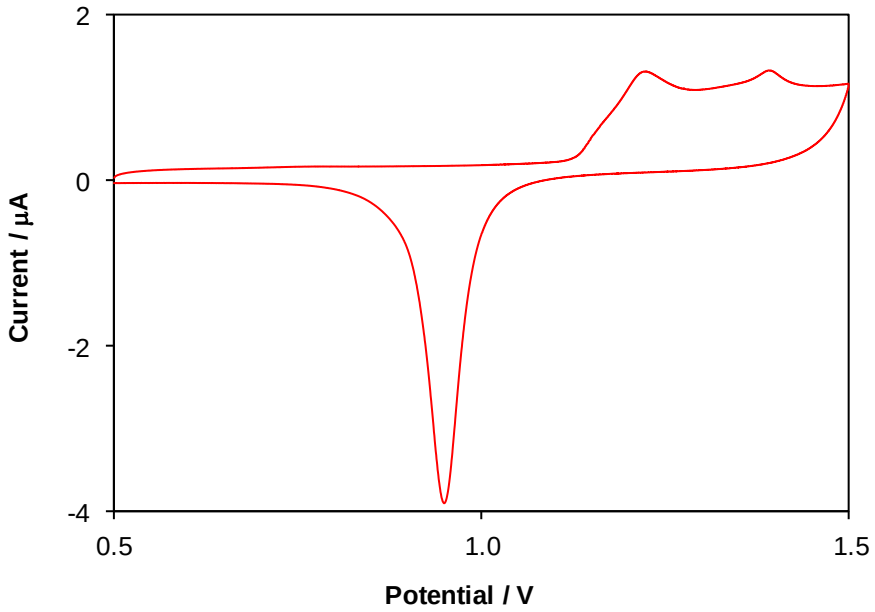

## Appendix 3.4 Integrated peaks for EASA determination of polycrystalline gold

**Integration of gold oxide reduction peak in 1 M KOH. Potentials *vs.* Hg/HgO; scan rate 50 mV $s^{-1}$**

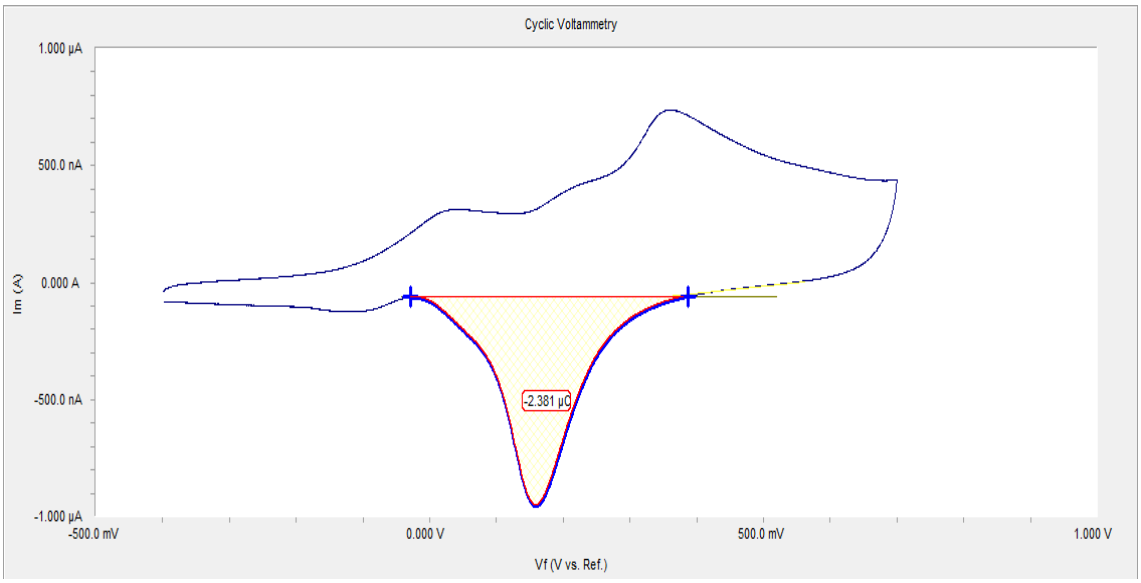


**Integration of copper UPD stripping peak in 3 mM $CuSO_4$/0.1 M $H_2SO_4$. Potentials *vs.* SCE; Electrode scanned at 50 mV $s^{-1}$ to cathodic limit of -0.2 V.**

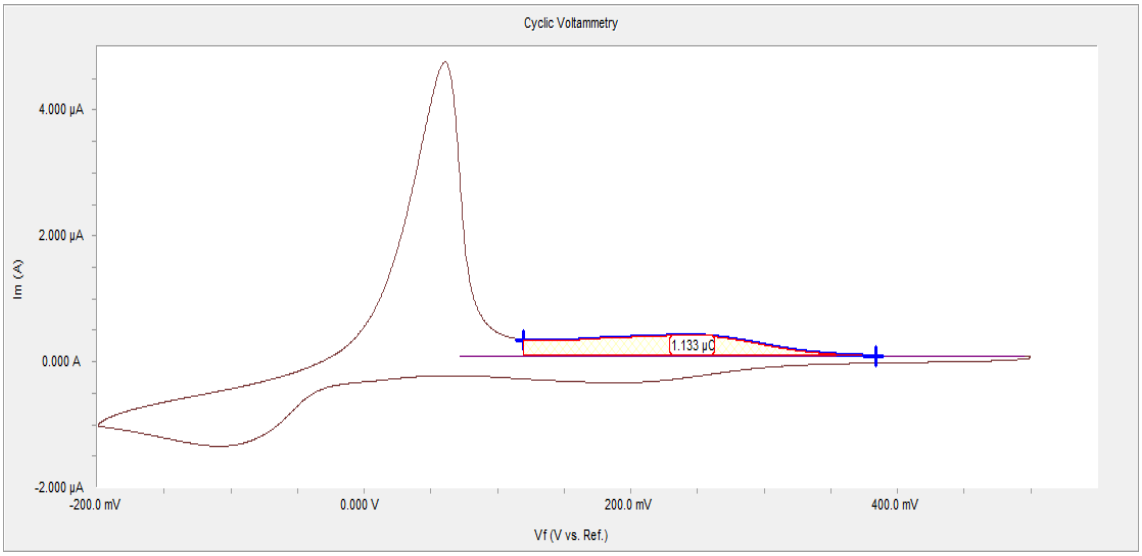

**Integration of copper UPD stripping peak in 3 mM $CuSO_4$/0.1 M $H_2SO_4$. Potentials *vs.* SCE; Electrode scanned at 50 mV $s^{-1}$ to cathodic limit of 0 V.**

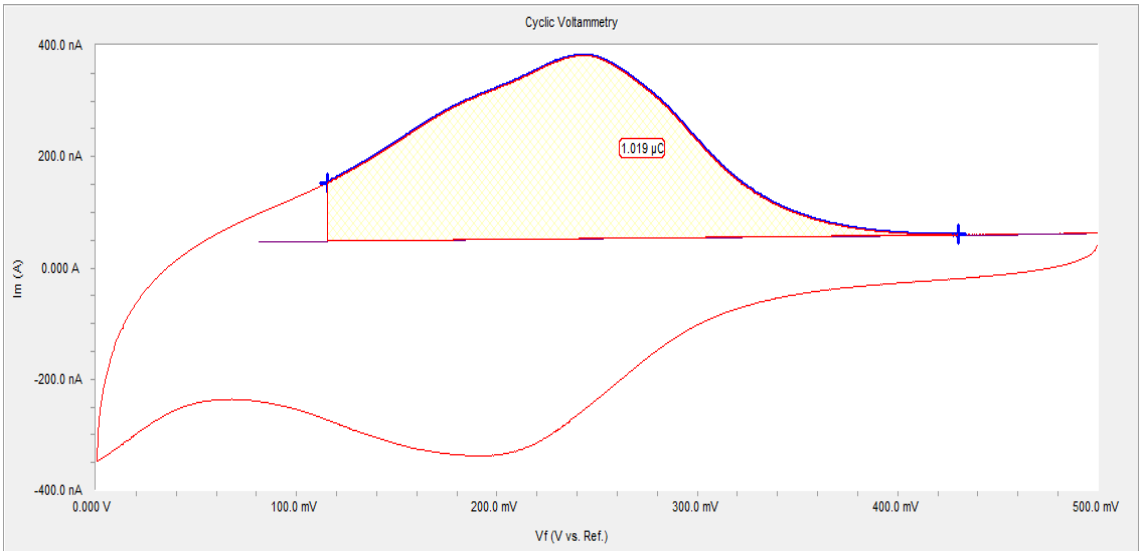

## Appendix 3.5 CV of clean glassy carbon plate in 3 mM $CuSO_4$/0.1 M $H_2SO_4$

**Scan rate 50 mV $s^{-1}$; potentials *vs.* SCE**

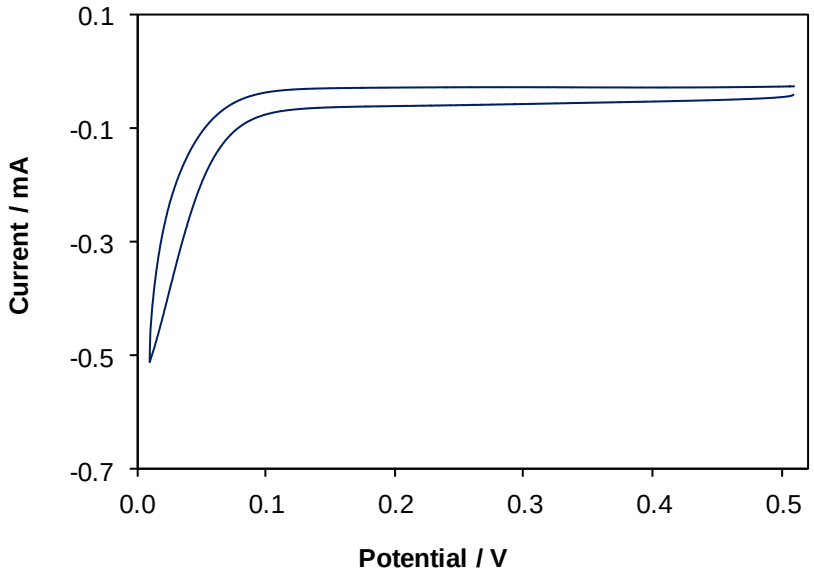

## Appendix 3.6 Integrated peaks for EASA determination of 4.0 nm Au/C catalyst (20 % gold loading) using copper UPD in 3 mM $CuSO_4$/0.1 M $H_2SO_4$

**Using straight line at higher potentials as baseline**

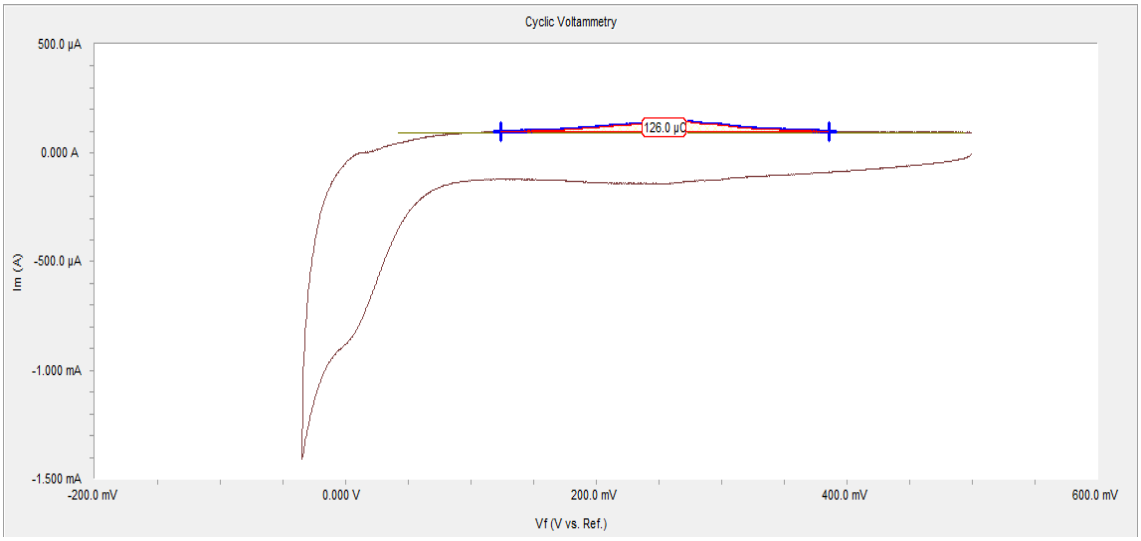


**Using CV in 0.1 M $H_2SO_4$ as baseline**

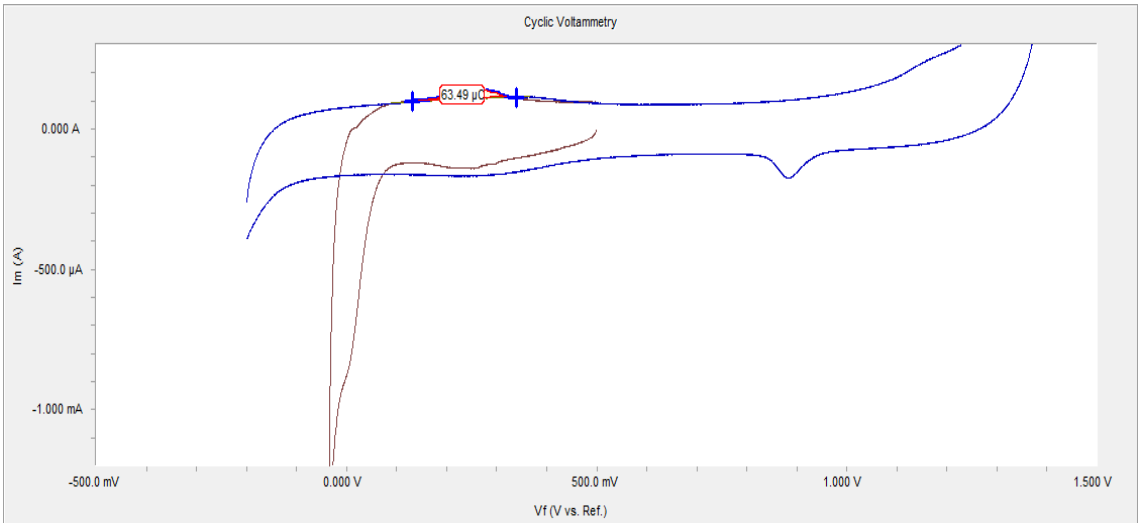

## Appendix 3.7 Comparison of gold oxide reduction and copper UPD for EASA determination of 4.0 nm Au/C catalyst (20 % gold loading)

**EASA determined from cycle 5 of CV at 50 mV $s^{-1}$**

Catalyst in 1 M KOH. Ref potentials vs Hg/HgO

| Catalyst | GCP | Catalyst conc., mg/ml | Integrated peak charge, µC # | Monolayer charge, µC/cm² | Metal surface area, cm² | Cat mass, mg | Metal loading, % | Metal mass, mg | EASA, cm²/mg metal | EASA, m²/g metal |
|---|---|---|---|---|---|---|---|---|---|---|
| DP20%Au_C with 1 and 2 mg/ml cat concs | 6 | 1.0 | 127.5 | 386 | 0.330 | 0.01 | 20 | 0.002 | 165.2 | 16.52 |
| | 8 | 1.0 | 124.6 | 386 | 0.323 | 0.01 | 20 | 0.002 | 161.4 | 16.14 |
| | 5 | 1.0 | 113.3 | 386 | 0.294 | 0.01 | 20 | 0.002 | 146.8 | 14.68 |
| | 6 | 2.0 | 262.9 | 386 | 0.681 | 0.02 | 20 | 0.004 | 170.3 | 17.03 |
| | 8 | 2.0 | 242.8 | 386 | 0.629 | 0.02 | 20 | 0.004 | 157.3 | 15.73 |
| | | | | | | | | AVE | | 16.0 |
| | | | | | | | | STD DEVP | | 0.8 |
| | | | | | | | | CONFIDENCE | | 0.7 |

Catalyst in 0.1 M H2SO4 after glycerol oxidation. Ref potentials vs Calomel 4 in sat'd KCl

| GCP | Integrated peak charge, µC | Monolayer charge, µC/cm² | Metal surface area, cm² | Cat mass, mg | Metal loading, % | Metal mass, mg | EASA, cm²/mg metal | EASA, m²/g metal |
|---|---|---|---|---|---|---|---|---|
| 6 | 121.6 | 386 | 0.315 | 0.01 | 20 | 0.0020 | 157.5 | 15.75 |
| 8 | 114.7 | 386 | 0.297 | 0.01 | 20 | 0.0020 | 148.6 | 14.86 |
| 5 | 53.1 | 386 | 0.138 | 0.01 | 20 | 0.0020 | 68.8 | 6.88 |
| 6 | 169.8 | 386 | 0.440 | 0.02 | 20 | 0.0040 | 110.0 | 11.00 |
| 8 | 147.4 | 386 | 0.382 | 0.02 | 20 | 0.0040 | 95.5 | 9.55 |
| | | | | | | AVE | | 12 |
| | | | | | | STD DEVP | | 3 |
| | | | | | | CONFIDENCE | | 3 |

Cu UPD - 3 mM CuSO4 in 0.1 M H2SO4. Ref potentials vs Calomel 4 in sat'd KCl

| GCP | Integrated peak charge, µC | Monolayer charge, µC/cm² | Metal surface area, cm² | Cat mass, mg | Metal loading, % | Metal mass, mg | EASA, cm²/mg metal | EASA, m²/g metal |
|---|---|---|---|---|---|---|---|---|
| 6 | 127.0 | 430 | 0.295 | 0.01 | 20 | 0.0020 | 147.7 | 14.77 |
| 8 | 122.4 | 430 | 0.285 | 0.01 | 20 | 0.0020 | 142.3 | 14.23 |
| 5 | 106.3 | 430 | 0.247 | 0.01 | 20 | 0.0020 | 123.6 | 12.36 |
| 6 | 271.2 | 430 | 0.631 | 0.02 | 20 | 0.0040 | 157.7 | 15.77 |
| 8 | 255.5 | 430 | 0.594 | 0.02 | 20 | 0.0040 | 148.5 | 14.85 |
| | | | | | | AVE | | 14 |
| | | | | | | STD DEVP | | 1 |
| | | | | | | CONFIDENCE | | 1 |

- Procedure before EASA determination in 1 M KOH: CA at -0.2 V for 10 min, followed by 5 strip cycles from -0.9 to 0.8 V (*vs*. Hg/HgO).

- Procedure before EASA determination in 0.1 M $H_2SO_4$: CA at -0.2 V for 5 min.

- Integration of copper UPD stripping peak carried out using the straight section of the curve in 3 mM $CuSO_4$ /0.1 M $H_2SO_4$ as a baseline

# Appendix 3.8 Effect of stripping conditions on EASA of 19 % Au/C catalyst and precursor gold colloids

**Tested on 19 and 21 March 2012**

| Catalyst | GCP | Ligand strip condition | 1 M KOH | | | | | | | | |
|---|---|---|---|---|---|---|---|---|---|---|---|
| | | | Ru (Ω) * | Integrated peak charge, µC # | Monolayer charge, µC/cm² | Metal surface area, cm² | Cat mass, mg | Metal loading, % | Metal mass, mg | EASA, cm²/mg metal | EASA, m²/g metal |
| **5.0 nm Au/C** on 7 GCPs; 1 mg/ml cat + 10% Nafion in 4:1 IPA/H2O mix. Deposited and tested on GCPS on 19 Mar 2012 | 1 | No strip | 1.7 | 40.9 | 386 | 0.106 | 0.01 | 19.3 | 0.00193 | 54.9 | 5.49 |
| | 2 | 5 cycles from **-0.9 → 0.8 V** in 1 M KOH | 2.0 | 69.1 | 386 | 0.179 | 0.01 | 19.3 | 0.00193 | 92.7 | 9.27 |
| | 4 | | 1.3 | 69.0 | 386 | 0.179 | 0.01 | 19.3 | 0.00193 | 92.6 | 9.26 |
| | 5 | 10 cycles from **-0.9 → 0.8 V** in 1 M KOH | 1.3 | 62.4 | 386 | 0.162 | 0.01 | 19.3 | 0.00193 | 83.8 | 8.38 |
| | 6 | | 1.3 | 65.8 | 386 | 0.170 | 0.01 | 19.3 | 0.00193 | 88.3 | 8.83 |
| | 7 | 15 cycles from **-0.9 → 0.8 V** in 1 M KOH | 1.3 | 70.2 | 386 | 0.182 | 0.01 | 19.3 | 0.00193 | 94.2 | 9.42 |
| | 8 | | 1.4 | 65.3 | 386 | 0.169 | 0.01 | 19.3 | 0.00193 | 87.6 | 8.76 |

| | | | Ru (Ω) * | Integrated peak charge, µC # | Monolayer charge, µC/cm² | Metal surface area, cm² | Cat mass, mg | Metal loading, % | Metal mass, mg | EASA, cm²/mg metal | EASA, m²/g metal |
|---|---|---|---|---|---|---|---|---|---|---|---|
| **5.0 nm Au/C** on 7 GCPs; 1 mg/ml cat + 10% Nafion in 4:1 IPA/H2O mix. Deposited and tested on GCPS on 21 Mar 2012 | 1 | No strip | 1.4 | 38.7 | 386 | 0.100 | 0.01 | 19.3 | 0.00193 | 52.0 | 5.20 |
| | 2 | 5 cycles from **-0.9 → 0.8 V** in 1 M KOH | 1.4 | 76.1 | 386 | 0.197 | 0.01 | 19.3 | 0.00193 | 102.2 | 10.22 |
| | 4 | | 1.3 | 70.2 | 386 | 0.182 | 0.01 | 19.3 | 0.00193 | 94.2 | 9.42 |
| | 5 | 10 cycles from **-0.9 → 0.8 V** in 1 M KOH | 1.3 | 65.7 | 386 | 0.170 | 0.01 | 19.3 | 0.00193 | 88.2 | 8.82 |
| | 6 | | 1.4 | 69.3 | 386 | 0.180 | 0.01 | 19.3 | 0.00193 | 93.0 | 9.30 |
| | 7 | 15 cycles from **-0.9 → 0.8 V** in 1 M KOH | 1.2 | 65.2 | 386 | 0.169 | 0.01 | 19.3 | 0.00193 | 87.5 | 8.75 |
| | 8 | | 1.6 | 69.3 | 386 | 0.180 | 0.01 | 19.3 | 0.00193 | 93.0 | 9.30 |

*** Applied PF correction 0.5 Ω**

**#From run 5 of CV at 50 mV/s in 1 M KOH, after strip cycling**

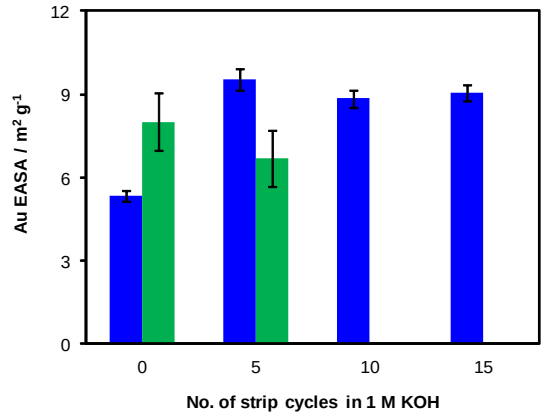


**Au/C catalyst**

| No. of strip cycles | Ave charge, µC | Std devp | 95 % confid. | Ave EASA, m²/g | Std dev | 95 % confid. |
|---|---|---|---|---|---|---|
| 0 | 40 | 1 | 2 | 5.3 | 0.1 | 0.2 |
| 5 | 71 | 3 | 3 | 9.5 | 0.4 | 0.4 |
| 10 | 66 | 2 | 2 | 8.8 | 0.3 | 0.3 |
| 15 | 67 | 2 | 2 | 9.1 | 0.3 | 0.3 |

**Colloids**

| No. strip cycles | Ave EASA, m²/g | Std devp | Conf |
|---|---|---|---|
| 0 | 8 | 0.8 | 1.0 |
| 5 | 7 | 0.7 | 1.0 |

## Appendix 3.9 Effect of soaking time on EASA of 19 % Au/C catalyst

| | No. of GCPs tested | CA period at -0.2 V | Ave charge, µC | Std devp | 95 % confid. | Ave EASA, $m^2/g$ | Std devp | 95 % confid. |
|---|---|---|---|---|---|---|---|---|
| **Soaking without stripping 22/03/2012** | 1 | 10 | 73 | | | 9.5 | | |
| **Taken from 19&21/03/2012** | 4 | 0 | 71 | 3 | 3 | 9.5 | 0.4 | 0.4 |
| **Taken from 30/03/2012** | 4 | 10 | 139 | 11 | 11 | 18 | 1 | 1 |
| **Taken from 05/04/2012** | 2 | 30 | 127 | 2 | 2 | 17 | 0.2 | 0.3 |
| | 1 | 60 | 126 | | | 17 | | |

Soaking followed by 5 strip cycles from -0.9 to 0.8 V before EASA determination

No error bar for 60 min soak and 10 min soak w/out stripping - only tested 1 electrode

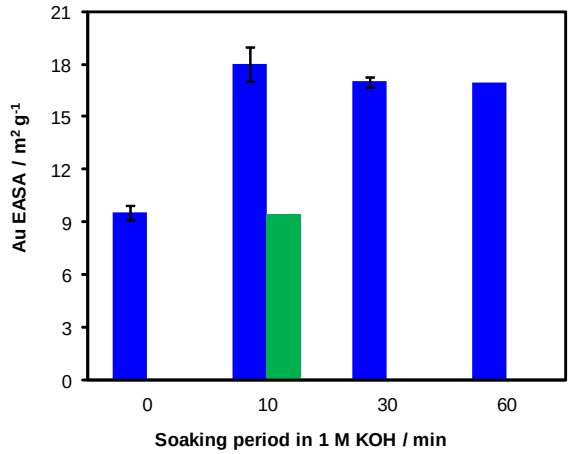


Blue columns: Soaking for set amount of time, followed by 5 strip cycles.

Green column: Soaking for 10 min only. No strip cycles.

## Appendix 3.10 Effect of soaking and electrochemical stripping on glycerol oxidation activity of 19 % Au/C catalyst

| Electrochemical treatment conditions | Symbol on x-axis | No. of GCPs tested | GlOH oxidation current | | | |
|---|---|---|---|---|---|---|
| | | | mA/cm$^2$ | Error, 95 % conf. | A/mg Au | Error, 95 % conf. |
| **No soak or strip** | **A** | 6 | 389 | 24 | 22 | 2 |
| **No soak; 5 strip cycles** | **B** | 4 | 255 | 57 | 24 | 5 |
| **10 min soak + 5 strip cycles** | **C** | 4 | 128 | 11 | 24 | 1 |

Soak conditions: CA at -0.2 V vs Hg/HgO for 10 min in 1 M KOH and 0.5 M GlOH/KOH
Strip conditions: 5 cycles from -0.9 V to 0.8 V at 50 mV/s in 1 M KOH
Scan rate in KOH and GlOH: 50 mV/s

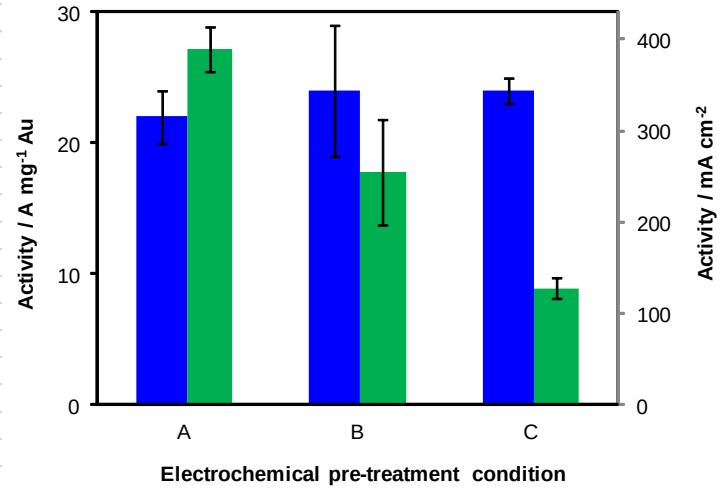


Blue columns: Mass activity, A mg$^{-1}$ Au

Green columns: Specific activity from EASA, mA cm$^{-2}$

# APPENDIX 4

## Appendix 4.1 O 1s and C 1s peak fits from XPS for Au/C and Au/23$MnO_2$/C catalysts

**Au/C**

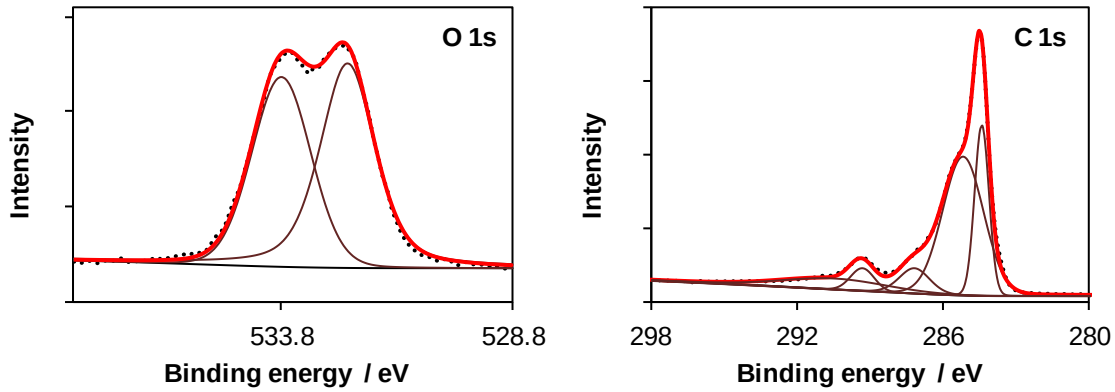


**Au/23$MnO_2$/C**

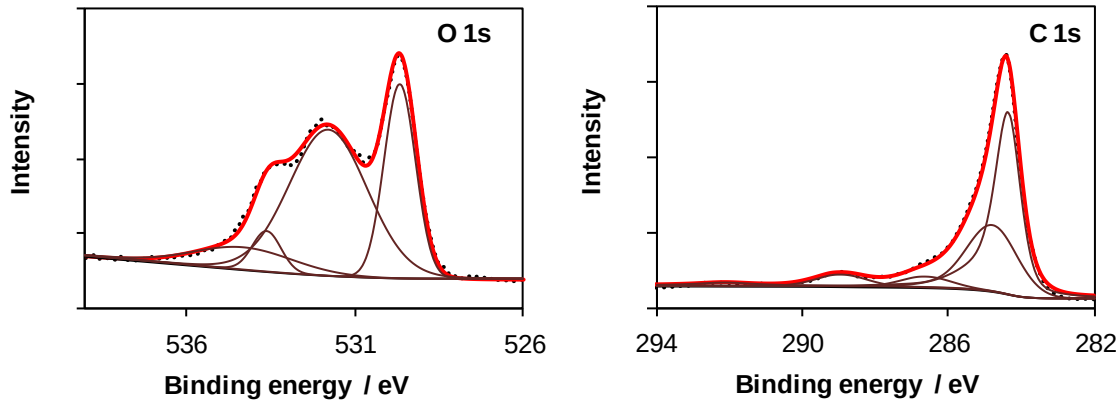

## Appendix 4.2 O 1s and C 1s peak assignments from XPS for Au/$x$MnO$_2$/C catalysts

**O 1s spectra**

| Catalyst | Binding energy, eV | | | | |
|---|---|---|---|---|---|
| | O-Mn | O=C | O-C | Ads $H_2O$ | O=C-O |
| Au/C | | | 532.5 | 533.8 | |
| Au/5MnO$_2$/C | 529.43 | 531.36 | 532.99 | 534.20 | |
| Au/9MnO$_2$/C | 529.59 | 532.06 | | 533.76 | |
| Au/16MnO$_2$/C | 529.58 | 530.96 | 532.37 | | 535.41 |
| Au/23MnO$_2$/C | 529.65 | 531.77 | 533.60 | 534.29 | |

| | | | | | |
|---|---|---|---|---|---|
| 529.6 | 531.3 | 533.1 | 534.2 | | Ref: Dong, *et al*., Microporous Mesoporous Mater. 91 (2006) 120. |
| | 531.6-532.2 | 533 | | | Ref: Senthil Kumar, et al., J. Electroanal. Chem. 647 (2010) 211. |
| | 532.3-532.8 | 533.1-533.8 | | 534.3-535.4 | Ref: Zhou, *et al*., Carbon 45 (2007) 785. |
| | 531.1 | 532.8 | 535.1 | | Ref: Darmstadt, *et al*., Carbon 40 (2002) 2673. |

**C 1s spectra**

| Catalyst | Binding energy, eV | | | | | |
|---|---|---|---|---|---|---|
| | C-C, C-H | C-C, C-H | C-O | C=O | O=C-O | Π→Π* |
| Au/C | 284.43 | 285.20 | | 287.20 | 289.34 | 290.48 |
| Au/5MnO$_2$/C | 284.29 | 284.67 | 286.07 | | 290.03 | |
| Au/9MnO$_2$/C | 284.41 | 284.71 | 286.54 | | 288.98 | 290.85 |
| Au/16MnO$_2$/C | 284.3 | 285.46 | 285.85 | | 290.02 | |
| Au/23MnO$_2$/C | 284.38 | 284.81 | 286.62 | | 288.93 | 292.10 |

| | | | | | | |
|---|---|---|---|---|---|---|
| 284.4 | 285.9 | 287.4 | 288.9 | 290.4; 294.4 | Ref: Darmstadt, *et al*., Carbon 40 (2002) 2673. |
| 284.2 | 285 | | | | Ref: Senthil Kumar, et al., J. Electroanal. Chem. 647 (2010) 211. |
| 284.6 | 286-286.3 | 287.3-287.6 | 290.5-291.2 | | Ref: Zhou, *et al*., Carbon 45 (2007) 785. |

## Appendix 4.3 SEM-EDS spot and area analysis of $x$MnO$_2$/C supports

| Spot/Area | % $MnO_2$/C | | | |
|---|---|---|---|---|
| | 5 | 9 | 16 | 23 |
| 1 | 1 | 5 | 8.8 | 10.5 |
| 2 | 1.1 | 4.8 | 8.2 | 9.9 |
| 3 | 0.6 | 4.7 | 8.5 | 9.6 |
| 4 | 1.1 | 4.4 | 7.6 | 10 |
| 5 | 0.6 | 5.4 | 7.7 | 10.6 |
| **Ave wt % Mn** | 0.9 | 4.9 | 8.2 | 10.1 |
| **Std dev** | 0.3 | 0.4 | 0.5 | 0.4 |
| **Calculated ave wt % $MnO_2$** | **1** | **8** | **13** | **16** |

Note: The % $MnO_2$ values determined by EDS are lower than the values determined using AAS, due to the EDS beam picking up the background carbon tape as well, resulting in lower % Mn values than actual.

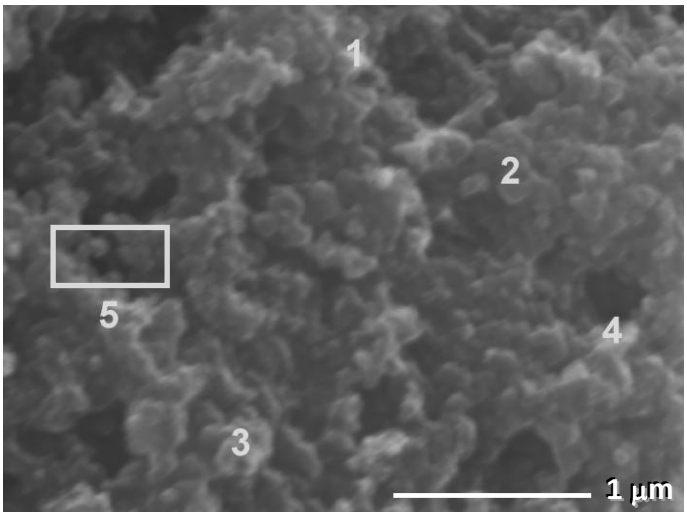


**5 % $MnO_2$/C support**

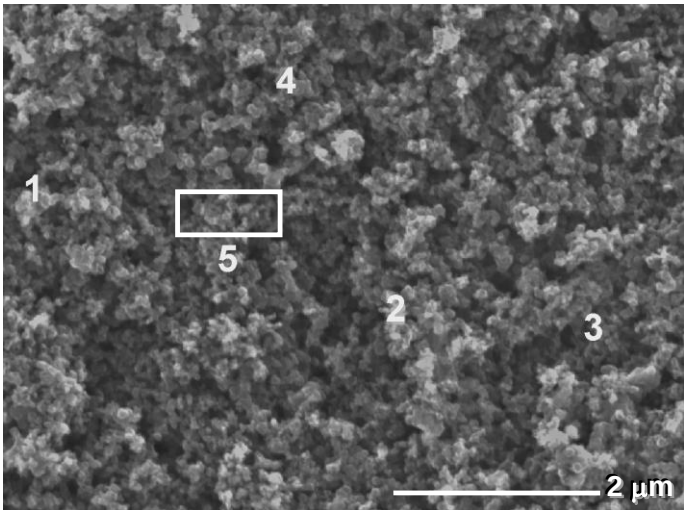


**9 % $MnO_2$/C support**

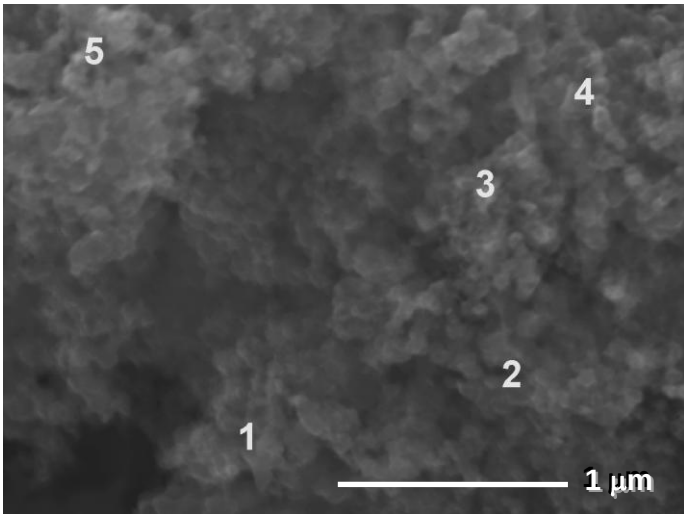


**16 % $MnO_2$/C support**

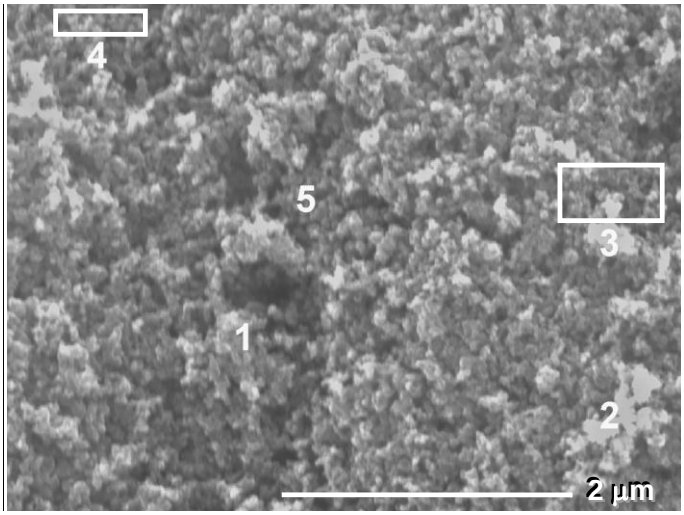


**23 % $MnO_2$/C support**

**Appendix 4.4 CVs of Vulcan carbon and $x$MnO$_2$/C supports in glycerol (0.5 M GlOH/1M KOH)**

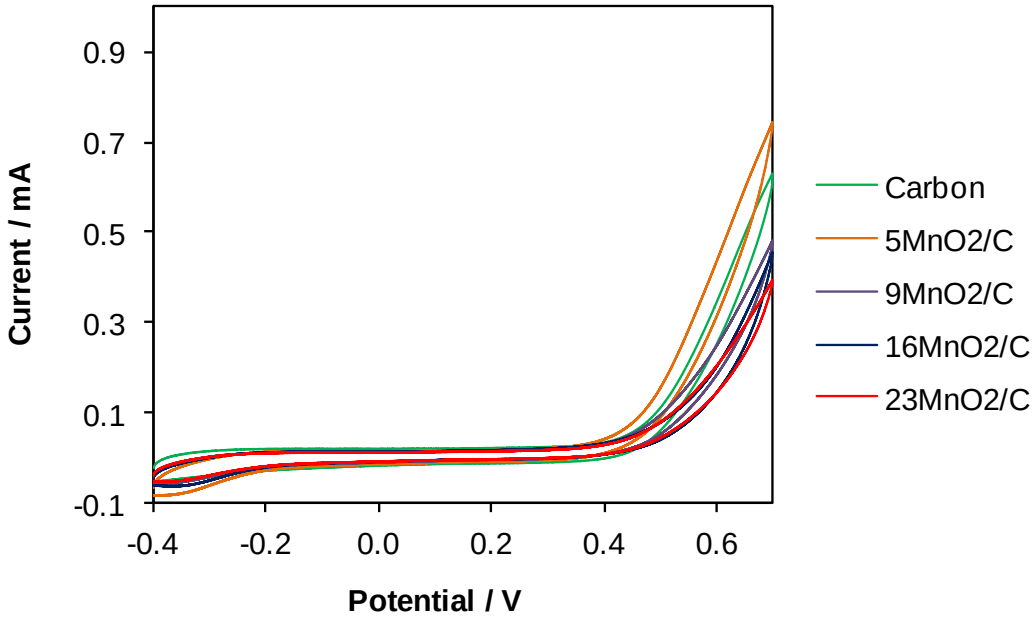

## Appendix 4.5 Electrochemistry data for Au/$x$MnO$_2$/C catalysts

## Au/C

| Catalyst | Sample no. | 1 M KOH** | | | | | | | | | Glycerol oxidation (0.5 M) in 1 M KOH** | | | | | | | |
|---|---|---|---|---|---|---|---|---|---|---|---|---|---|---|---|---|---|---|
| | | | | | | | | | | | | | | | Highest peak | | | |
| | | Ru (Ω) * | Integrated peak charge, μC # | Monolayer charge, μC/cm$^2$ | Metal surface area, cm$^2$ | Cat mass, mg | Metal loading, % | Metal mass, mg | EASA, cm$^2$/mg metal | EASA, m$^2$/g metal | Ru (Ω)* | Scan rate, mV/s | Number of cycles | Number of highest peak | Current, mA | Current, mA.cm$^{-2}$ | A.mg$^{-1}$ cat | A.mg$^{-1}$ Au |
| **Au/C** on GCPs; 1 mg/ml cat + 10% Nafion in 4:1 IPA/H2O mix. Deposited and tested on GCPS on 21May2012 | 1 | 1.7 | 128.9 | 386 | 0.334 | 0.01 | 20 | 0.002 | 167.0 | 16.70 | 1.6 | 10 | 5 | 4 | 47.3 | 141.6 | 4.729 | 23.6 |
| | 2 | 1.2 | 147.6 | 386 | 0.382 | 0.01 | 20 | 0.002 | 191.2 | 19.12 | 1.5 | 10 | 5 | 4 | 51.2 | 133.9 | 5.122 | 25.6 |
| | 3 | 1.4 | 154.5 | 386 | 0.400 | 0.01 | 20 | 0.002 | 200.1 | 20.01 | 1.7 | 10 | 5 | 4 | 53.1 | 132.6 | 5.306 | 26.5 |
| | 4 | 1.1 | 118.5 | 386 | 0.307 | 0.01 | 20 | 0.002 | 153.5 | 15.35 | 2.0 | 10 | 5 | 4 | 50.1 | 163.1 | 5.007 | 25.0 |
| | 5 | 1.2 | 150.6 | 386 | 0.390 | 0.01 | 20 | 0.002 | 195.1 | 19.51 | 1.9 | 10 | 5 | 4 | 51.6 | 132.2 | 5.157 | 25.8 |
| | **AVE** | 140.020 | | | 0.363 | | | | | | | | | **AVE** | 51 | 141 | 5.1 | 25.3 |
| | **STD DEVP** | 13.90 | | | 0.04 | | ** CA for 10 min at -0.2 V in both KOH and glycerol, before CV scans | | | | | | | **STD DEVP** | 2 | 12 | 0.2 | 1.0 |
| | **CONFIDENCE** | 12.182 | | | 0.032 | | | | | | | | | **CONFIDENCE** | 2 | 10 | 0.2 | 0.8 |

#From run 5 of CV at 50 mV/s in 1 M KOH, after CA and strip cycling from -0.9 → 0.8 V for 5 cycles

* Applied PF correction 0.5 Ω

| Electrode | Forward/Reverse | |
|---|---|---|
| | Max. I | Curve no. |
| GCP 1 | 1.7 | 4 |
| GCP 4 | 1.7 | 4 |
| GCP 5 | 1.8 | 4 |
| GCP 6 | 1.9 | 4 |
| GCP 8 | 1.9 | 4 |
| **AVE** | 1.80 | |
| **STD DEVP** | 0.07 | |
| **CONFIDENCE** | 0.06 | |

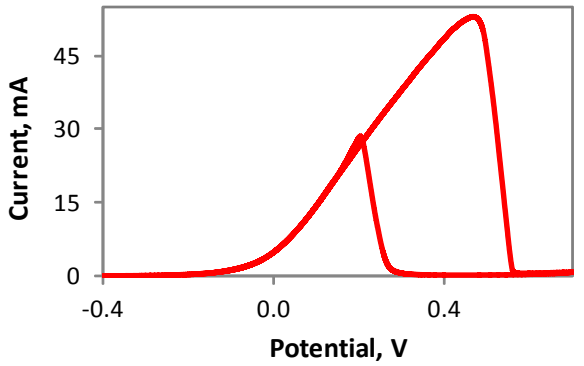


Catalyst samples 1-5 were deposited on GCPs 1, 4, 5, 6 and 8,respectively

## Au/5$MnO_2$/C

| Catalyst | Sample no. | 1 M KOH** | | | | | | | | Glycerol oxidation (0.5 M) in 1 M KOH** | | | | | | | |
|---|---|---|---|---|---|---|---|---|---|---|---|---|---|---|---|---|---|
| | | | | | | | | | | | | | Highest peak | | | | |
| | | Ru (Ω) * | Integrated peak charge, μC # | Monolayer charge, μC/cm² | Metal surface area, cm² | Cat mass, mg | Metal loading, % | Metal mass, mg | EASA, cm²/mg metal | EASA, m²/g metal | Ru (Ω)* | Scan rate, mV/s | Number of cycles | Number of highest peak | Current, mA | Current, mA.cm⁻² | A.mg⁻¹ cat | A.mg⁻¹ Au |
| Au/5$MnO_2$/C on GCPs; 1 mg/ml cat + 10% Nafion in 4:1 IPA/H2O mix. Deposited and tested on GCPS on 03May2012 | 1 | 1.3 | 44.4 | 386 | 0.115 | 0.01 | 14.2 | 0.00142 | 80.9 | 8.09 | 1.5 | 10 | 5 | 4 | 49.4 | 429.8 | 4.941 | 34.8 |
| | 2 | 1.3 | 37.3 | 386 | 0.097 | 0.01 | 14.2 | 0.00142 | 68.1 | 6.81 | 1.7 | 10 | 5 | 4 | 43.4 | 448.9 | 4.341 | 30.6 |
| | 3 | 1.3 | 38.0 | 386 | 0.098 | 0.01 | 14.2 | 0.00142 | 69.4 | 6.94 | 1.5 | 10 | 5 | 4 | 48.8 | 495.0 | 4.876 | 34.3 |
| | 4 | 1.4 | 47.9 | 386 | 0.124 | 0.01 | 14.2 | 0.00142 | 87.4 | 8.74 | 1.5 | 10 | 5 | 4 | 50.5 | 406.9 | 5.051 | 35.6 |
| | 5 | 1.2 | 38.2 | 386 | 0.099 | 0.01 | 14.2 | 0.00142 | 69.6 | 6.96 | 1.6 | 10 | 5 | 4 | 57.3 | 579.6 | 5.728 | 40.3 |
| | | | | | | | | | | | | | | AVE | 50 | | 5.0 | 35 |
| | | * Applied PF correction 0.5 Ω | | | | | ** CA for 10 min at -0.2 V in both KOH and glycerol, before CV scans | | | | | | | STD DEVP | 4 | | 0.4 | 3 |
| | | | | | | | | | | | | | | CONFIDENCE | 4 | | 0.4 | 3 |

#From run 5 of CV at 50 mV/s in 1 M KOH, after CA and strip cycling from -0.9 → 0.8 V for 5 cycles

| Electrode | Forward/Reverse | |
|---|---|---|
| | Max. I | Curve no. |
| GCP 1 | 1.7 | 4 |
| GCP 4 | 1.7 | 4 |
| GCP 5 | 1.7 | 4 |
| GCP 6 | 1.8 | 4 |
| GCP 8 | 1.8 | 4 |
| AVE | 1.74 | |
| STD DEVP | 0.05 | |
| CONFIDENCE | 0.05 | |

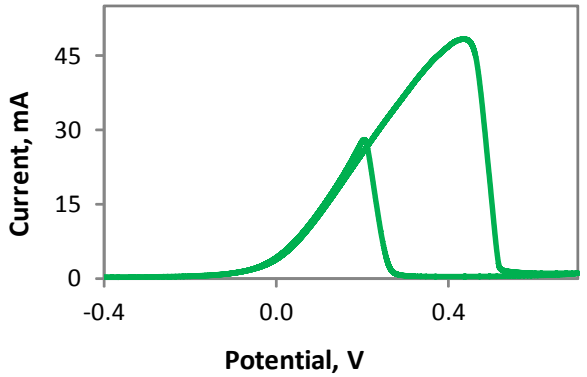


Catalyst samples 1-5 were deposited on GCPs 1, 4, 5, 6 and 8,respectively

## Au/9$MnO_2$/C

| Catalyst | Sample no. | 1 M KOH** | | | | | | | | Glycerol oxidation (0.5 M) in 1 M KOH** | | | | | | | |
|---|---|---|---|---|---|---|---|---|---|---|---|---|---|---|---|---|---|
| | | | | | | | | | | | | | | Highest peak | | | |
| | | Ru (Ω) * | Integrated peak charge, μC # | Monolayer charge, μC/cm² | Metal surface area, cm² | Cat mass, mg | Metal loading, % | Metal mass, mg | EASA, cm²/mg metal | EASA, m²/g metal | Ru (Ω)* | Scan rate, mV/s | Number of cycles | Number of highest peak | Current, mA | Current, mA.cm⁻² | A.mg⁻¹ cat | A.mg⁻¹ Au |
| Au/9$MnO_2$/C on GCPs; 1 mg/ml cat + 10% Nafion in 4:1 IPA/H2O mix. Deposited and tested on GCPS on 07May2012 | 1 | 2.7 | 22.2 | 386 | 0.058 | 0.01 | 12.7 | 0.00127 | 45.3 | 4.53 | 1.9 | 10 | 5 | 2 | 50.0 | 870.1 | 5.004 | 39.4 |
| | 2 | 1.9 | 24.0 | 386 | 0.062 | 0.01 | 12.7 | 0.00127 | 48.9 | 4.89 | 2.4 | 10 | 5 | 2 | 40.6 | 652.9 | 4.056 | 31.9 |
| | 3 | 1.7 | 23.2 | 386 | 0.060 | 0.01 | 12.7 | 0.00127 | 47.4 | 4.74 | 1.9 | 10 | 5 | 2 | 41.1 | 682.7 | 4.107 | 32.3 |
| | 4 | 1.5 | 24.3 | 386 | 0.063 | 0.01 | 12.7 | 0.00127 | 49.6 | 4.96 | 2.3 | 10 | 5 | 2 | 43.6 | 692.5 | 4.363 | 34.4 |
| | 5 | 2.0 | 29.2 | 386 | 0.076 | 0.01 | 12.7 | 0.00127 | 59.5 | 5.95 | 1.7 | 10 | 5 | 2 | 56.8 | 751.5 | 5.675 | 44.7 |
| | | | | | | | | | | | | | | AVE | 46 | | 4.6 | 37 |
| | | * Applied PF correction 0.5 Ω | | | | | ** CA for 10 min at -0.2 V in both KOH and glycerol, before CV scans | | | | | | | STD DEVP | 6 | | 0.6 | 5 |
| | | | | | | | | | | | | | | CONFIDENCE | 5 | | 0.5 | 4 |

#From run 5 of CV at 50 mV/s in 1 M KOH, after CA and strip cycling from -0.9 → 0.8 V for 5 cycles

| Electrode | Forward/Reverse | |
|---|---|---|
| | Max. I | Curve no. |
| GCP 1 | 1.7 | 2 |
| GCP 4 | 1.6 | 2 |
| GCP 5 | 1.6 | 2 |
| GCP 6 | 1.7 | 2 |
| GCP 8 | 1.8 | 2 |
| AVE | 1.69 | |
| STD DEVP | 0.09 | |
| CONFIDENCE | 0.08 | |

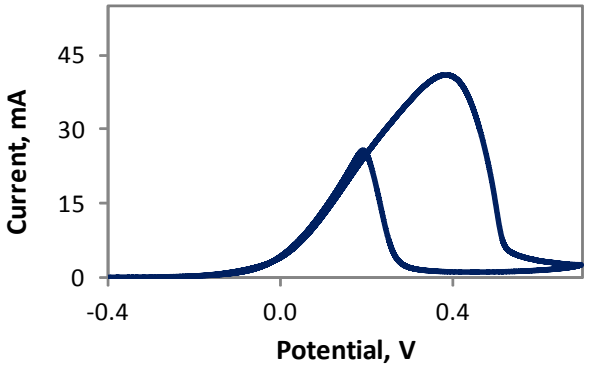


Catalyst samples 1-5 were deposited on GCPs 1, 4, 5, 6 and 8,respectively

## Au/16$MnO_2$/C

| Catalyst | Sample no. | Ru (Ω) * | 1 M KOH** | | | | | | | | Glycerol oxidation (0.5 M) in 1 M KOH** | | | | | | | |
|---|---|---|---|---|---|---|---|---|---|---|---|---|---|---|---|---|---|---|
| | | | Integrated peak charge, μC # | Monolayer charge, μC/cm² | Metal surface area, cm² | Cat mass, mg | Metal loading, % | Metal mass, mg | EASA, cm²/mg metal | EASA, m²/g metal | Ru (Ω)* | Scan rate, mV/s | Number of cycles | Number of highest peak | Highest peak Current, mA | Highest peak Current, mA.cm⁻² | A.mg⁻¹ cat | A.mg⁻¹ Au |
| Au/16$MnO_2$/C on GCPs; 1 mg/ml cat + 10% Nafion in 4:1 IPA/H2O mix. Deposited and tested on GCPS on 09May2012 | 1 | 1.2 | CND | 386 | #VALUE! | 0.01 | 13.2 | 0.00132 | #VALUE! | #VALUE! | 1.6 | 10 | 5 | 2 | 33.1 | #VALUE! | 3.313 | 25.1 |
| | 2 | 1.4 | CND | 386 | #VALUE! | 0.01 | 13.2 | 0.00132 | #VALUE! | #VALUE! | 1.6 | 10 | 5 | 2 | 23.2 | #VALUE! | 2.318 | 17.6 |
| | 3 | 1.4 | CND | 386 | #VALUE! | 0.01 | 13.2 | 0.00132 | #VALUE! | #VALUE! | 1.5 | 10 | 5 | 3 | 21.8 | #VALUE! | 2.182 | 16.5 |
| | 4 | 1.3 | CND | 386 | #VALUE! | 0.01 | 13.2 | 0.00132 | #VALUE! | #VALUE! | 1.5 | 10 | 5 | 2 | 28.7 | #VALUE! | 2.873 | 21.8 |
| | 5 | 1.3 | CND | 386 | #VALUE! | 0.01 | 13.2 | 0.00132 | #VALUE! | #VALUE! | 1.4 | 10 | 5 | 3 | 22.8 | #VALUE! | 2.282 | 17.3 |
| | | | | | | | | | | | | | | AVE | 26 | | 2.6 | 20 |
| CND = could not determine | | * Applied PF correction 0.5 Ω | | | | | ** CA for 10 min at -0.2 V in both KOH and glycerol, before CV scans | | | | | | | STD DEVP | 4 | | 0.4 | 3 |
| | | | | | | | | | | | | | | CONFIDENCE | 4 | | 0.4 | 3 |

#From run 5 of CV at 50 mV/s in 1 M KOH, after CA and strip cycling from -0.9 → 0.8 V for 5 cycles

| Electrode | Forward/Reverse Max. I | Curve no. |
|---|---|---|
| GCP 1 | 1.4 | 2 |
| GCP 4 | 1.4 | 2 |
| GCP 5 | 1.4 | 3 |
| GCP 6 | 1.4 | 2 |
| GCP 8 | 1.4 | 3 |
| AVE | 1.39 | |
| STD DEVP | 0.02 | |
| CONFIDENCE | 0.02 | |

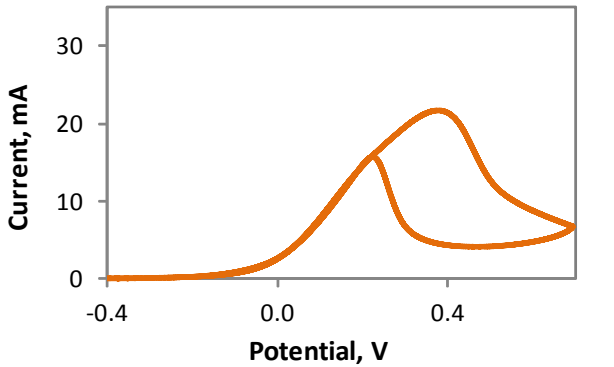


Catalyst samples 1-5 were deposited on GCPs 1, 4, 5, 6 and 8,respectively

## Au/23$MnO_2$/C

| Catalyst | Sample no. | Ru (Ω) * | 1 M KOH** | | | | | | | | Glycerol oxidation (0.5 M) in 1 M KOH** | | | | | | | |
|---|---|---|---|---|---|---|---|---|---|---|---|---|---|---|---|---|---|---|
| | | | Integrated peak charge, μC # | Monolayer charge, μC/cm² | Metal surface area, cm² | Cat mass, mg | Metal loading, % | Metal mass, mg | EASA, cm²/mg metal | EASA, m²/g metal | Ru (Ω)* | Scan rate, mV/s | Number of cycles | Number of highest peak | Highest peak Current, mA | Highest peak Current, mA.cm⁻² | A.mg⁻¹ cat | A.mg⁻¹ Au |
| Au/23$MnO_2$/C on GCPs; 1 mg/ml cat + 10% Nafion in 4:1 IPA/H2O mix. Deposited and tested on GCPS on 08May2012 | 1 | 1.6 | CND | 386 | #VALUE! | 0.01 | 7.9 | 0.00079 | #VALUE! | #VALUE! | 3.5 | 10 | 5 | 5 | 11.3 | #VALUE! | 1.1 | 14 |
| | 2 | 1.5 | CND | 386 | #VALUE! | 0.01 | 7.9 | 0.00079 | #VALUE! | #VALUE! | 3.1 | 10 | 6 | 4 | 9.2 | #VALUE! | 0.9 | 12 |
| | 3 | 1.8 | CND | 386 | #VALUE! | 0.01 | 7.9 | 0.00079 | #VALUE! | #VALUE! | 1.7 | 10 | 5 | 4 | 7.8 | #VALUE! | 0.8 | 10 |
| | 4 | 2.7 | CND | 386 | #VALUE! | 0.01 | 7.9 | 0.00079 | #VALUE! | #VALUE! | 3.4 | 10 | 5 | 4 | 8.5 | #VALUE! | 0.8 | 11 |
| | 5 | 3.0 | CND | 386 | #VALUE! | 0.01 | 7.9 | 0.00079 | #VALUE! | #VALUE! | 2.1 | 10 | 5 | 3 | 10.1 | #VALUE! | 1.0 | 13 |
| | | | | | | | | | | | | | | AVE | 9 | | 0.9 | 12 |
| CND = could not determine | | * Applied PF correction 0.5 Ω | | | | | ** CA for 10 min at -0.2 V in both KOH and glycerol, before CV scans | | | | | | | STD DEVP | 1 | | 0.1 | 2 |
| | | | | | | | | | | | | | | CONFIDENCE | 1 | | 0.1 | 1 |

#From run 5 of CV at 50 mV/s in 1 M KOH, after CA and strip cycling from -0.9 → 0.8 V for 5 cycles

| Electrode | Forward/Reverse Max. I | Curve no. |
|---|---|---|
| GCP 1 | 1.4 | 5 |
| GCP 4 | 1.3 | 4 |
| GCP 5 | 1.3 | 4 |
| GCP 6 | 1.3 | 4 |
| GCP 8 | 1.3 | 3 |
| AVE | 1.33 | |
| STD DEVP | 0.02 | |
| CONFIDENCE | 0.02 | |

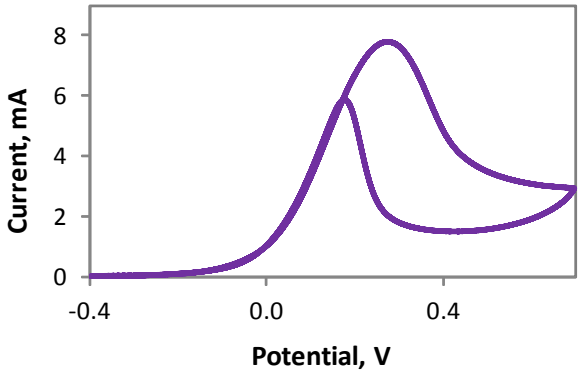


Catalyst samples 1-5 were deposited on GCPs 1, 4, 5, 6 and 8,respectively

## Appendix 4.6 Glycerol oxidation curves for Au/*x*$MnO_2$/C catalysts

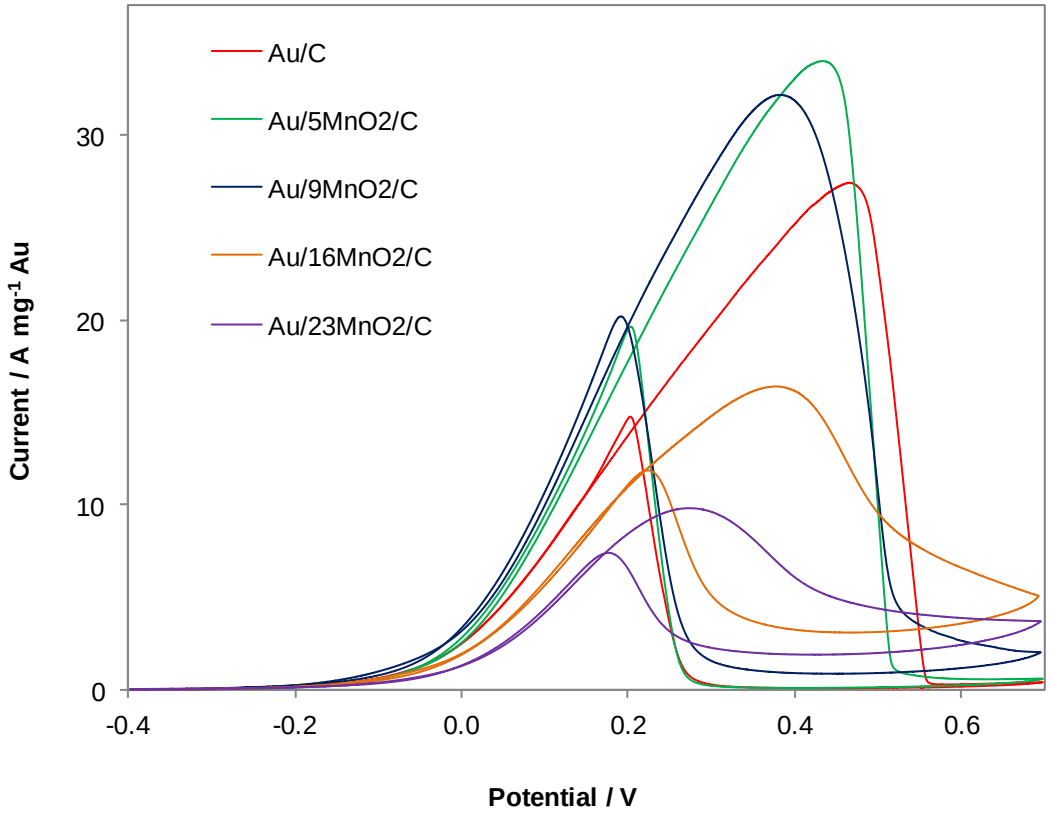

# APPENDIX 5

## Appendix 5.1 Gold oxide reduction peak comparisons

**Gold oxide reduction peak positions of Au/C catalysts in 1 M KOH**

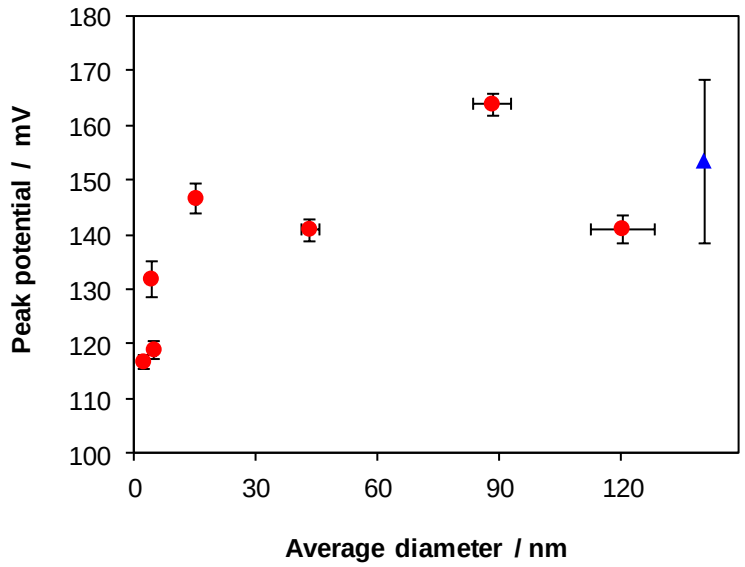


●: Au/C catalysts

▲: polycrystalline/bulk gold

Data shown in Table below.

**Comparisons of gold oxide reduction peak shifts on Au/C catalysts during cycling in 1 M KOH**

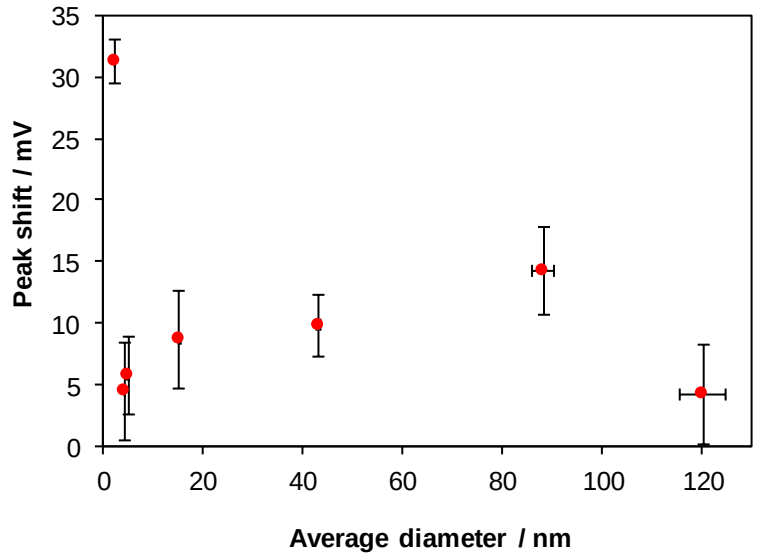


***Peak shift comparisons of all catalysts (gold $d_{ave}$ 2.1 – 120 nm)***

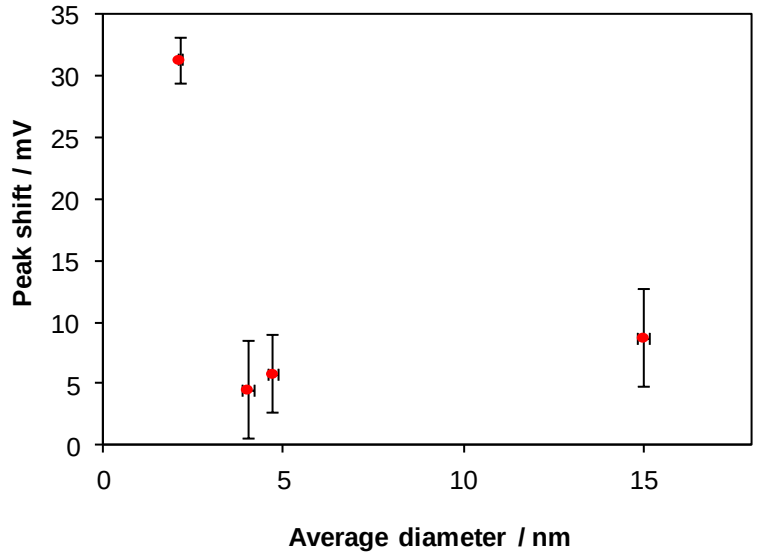


***Enlarged view of peak shifts of catalysts with small and medium gold ($d_{ave}$ 2.1 – 14.7 nm)***

Data shown in Table below.

## Gold oxide reduction peak data

| Catalyst | Au particle size, nm | | | Ave EASA, | Std error | Position of AuO reduction peak in 1 M KOH STRIP cycle 2, mV | | | | | | | | Position of AuO reduction peak in 1 M KOH, mV | | | | | | | | | Peak position | |
|---|---|---|---|---|---|---|---|---|---|---|---|---|---|---|---|---|---|---|---|---|---|---|---|---|
| | Ave | Median | Mode | $m^2/g$ | (95 % conf) | GCP1/2 | GCP4 | GCP5 | GCP6 | GCP8 | Ave | Std dev | Conf. | Cycle no. | GCP1/2 | GCP4 | GCP5 | GCP6 | GCP8 | Ave | Std dev | Conf. | Diff. | Error |
| **Au_THPC3** | **2.1** | 2.0 | 1.7 | **14.8** | 0.9 | 86.65 | 85.12 | 85.17 | 87.18 | 83.18 | **85** | **2** | 1 | 5* | 115.1 | 117.1 | 115.6 | 118.1 | 118.1 | **117** | **1** | 1 | 31 | 2 |
| **DP20%Au_C** | **4.0** | 3.4 | 3.1 | **15.4** | 0.5 | 123.2 | 127.2 | 128.8 | 130.2 | 127.7 | **127** | **3** | 2 | 5# | 126.7 | 130.8 | 135.3 | 131.2 | 135.8 | **132** | **4** | 3 | 5 | 4 |
| **15 % Au/C** | **4.7** | 4.2 | 4.2 | **12.9** | 0.6 | 112.7 | 116.7 | 116.1 | 110.2 | 110.2 | **113** | **3** | 3 | 2 | 119 | 119 | 122 | 117.5 | 117.5 | **119** | **2** | 2 | 6 | 3 |
| **Au_cit1** | **15** | 13 | 12 | **6.6** | 0.9 | 135.3 | 136.3 | 135.3 | 141.2 | 141.7 | **138** | **3** | 3 | 2 | 141.3 | 146.7 | 149.7 | 148.2 | 147.7 | **147** | **3** | 3 | 9 | 4 |
| **Au_cit4** | **43** | 39 | 35 | **1.8** | 0.3 | 130.2 | 132.7 | 128.7 | 131.7 | 132.8 | **131** | **2** | 2 | 2 | 137.7 | 143.6 | 140.7 | 142.7 | 140.7 | **141** | **2** | 2 | 10 | 3 |
| **Au_cit3** | **88** | 82 | 82 | **2.0** | 0.2 | 148.7 | 144.7 | 150.2 | 150.7 | 154.2 | **150** | **3** | 3 | 2 | 164.2 | 163.2 | 160.7 | 166.7 | 165.2 | **164** | **2** | 2 | 14 | 4 |
| **Au_THPC1** | **120** | 100 | 96 | **0.9** | 0.1 | 132.7 | 136.7 | 134.2 | 140.6 | 140.2 | **137** | **4** | 3 | 2 | 139.2 | 142.6 | 137.7 | 145.2 | 141.2 | **141** | **3** | 3 | 4 | 4 |
| **Bulk Au** | | | | | | | | | | | | | | | | | | | | **154** | **15** | 15 | | |

*Peak shifts & decreases with each sweep.

#Slight decrease in peak with each cycle, with negligible change in EASA but no further shifting.

| **Bulk Au** | |
|---|---|
| **Date** | **AuO red peak position, mV** |
| 09/12/2011 | 146.1 |
| 18/12/2012 | 171.7 |
| 18/12/2012 | 159.6 |
| 23/07/2013 | 137 |
| **Ave** | 154 |
| **Std dev** | 15 |
| **Conf.** | 15 |

## Appendix 5.2 Electrochemistry data for Au/C catalysts

## 2.1 nm Au/C

| Catalyst | Sample no. | Ru (Ω) * | 1 M KOH** | | | | | | | | Glycerol oxidation (0.5 M) in 1 M KOH** | | | | | | | |
|---|---|---|---|---|---|---|---|---|---|---|---|---|---|---|---|---|---|---|
| | | | | | | | | | | | | | | Highest peak | | | | |
| | | | Integrated peak charge, μC # | Monolayer charge, μC/cm² | Metal surface area, cm² | Cat mass, mg | Metal loading, % | Metal mass, mg | EASA, cm²/mg metal | EASA, m²/g metal | Ru (Ω) | Scan rate, mV/s | Number of cycles | Number of highest peak | Current, mA | Current, mA.cm⁻² | A.mg⁻¹ cat | A.mg⁻¹ Au |
| Au_THPC3: 2.1 nm Au/C on GCPs; 1 mg/ml cat + 10% Nafion in 4:1 IPA/H2O mix. Deposited and tested on GCPS on 27Mar2013 | 1 | 2.7 | 83.8 | 386 | 0.217 | 0.01 | 15.3 | 0.0015 | 142.0 | 14.20 | 3.7 | 10 | 6 | 4 | 50.5 | 232.7 | 5.054 | 33.0 |
| | 2 | 2.5 | 93.6 | 386 | 0.243 | 0.01 | 15.3 | 0.0015 | 158.5 | 15.85 | 2.2 | 10 | 5 | 3 | 40.6 | 167.4 | 4.061 | 26.5 |
| | 3 | 2.1 | 78.0 | 386 | 0.202 | 0.01 | 15.3 | 0.0015 | 132.1 | 13.21 | 2.2 | 10 | 5 | 3 | 41.7 | 206.6 | 4.174 | 27.3 |
| | 4 | 2.1 | 91.8 | 386 | 0.238 | 0.01 | 15.3 | 0.0015 | 155.4 | 15.54 | 2.4 | 10 | 5 | 3 | 49.1 | 206.5 | 4.908 | 32.1 |
| | 5 | 2.0 | 90.2 | 386 | 0.234 | 0.01 | 15.3 | 0.0015 | 152.7 | 15.27 | 2.1 | 10 | 5 | 3 | 44.8 | 191.5 | 4.475 | 29.2 |
| | | | | AVE | 0.227 | | | | AVE | 14.8 | | | | AVE | 45.3 | 201 | 4.5 | 29.6 |
| | * Applied PF correction 0.5 Ω | | | STD DEVP | 0.01 | | | | STD DEVP | 1.0 | | | | STD DEVP | 3.92 | 21.4 | 0.39 | 2.6 |
| | | | | CONFIDENCE | 0.013 | | | | CONFIDENCE | 0.9 | | | | CONFIDENCE | 3.43 | 18.72 | 0.34 | 2.2 |

** CA for 10 min at -0.2 V in both KOH and glycerol, before CV scans

#From run 5 of CV at 50 mV/s in 1 M KOH, after CA and strip cycling from -0.9 → 0.8 V for 5 cycles

Catalyst samples 1-5 were deposited on GCPs 2, 4, 5, 6 and 8, respectively

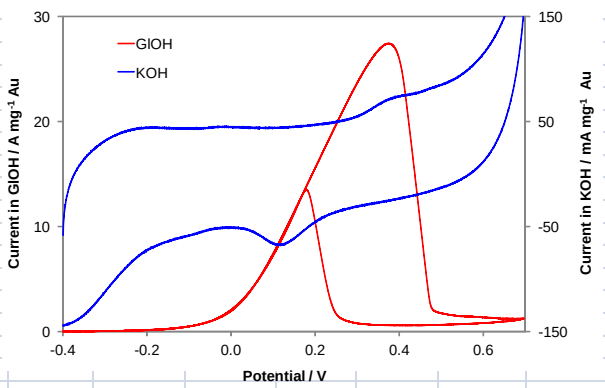

## 4.0 nm Au/C

| Catalyst | Sample no. | Ru (Ω) * | 1 M KOH** Integrated peak charge, μC # | Monolayer charge, μC/cm² | Metal surface area, cm² | Cat mass, mg | Metal loading, % | Metal mass, mg | EASA, cm²/mg metal | EASA, m²/g metal | Glycerol oxidation (0.5 M) in 1 M KOH** Ru (Ω) | Scan rate, mV/s | Number of cycles | Number of highest peak | Highest peak Current, mA | Highest peak Current, mA.cm⁻² | A.mg⁻¹ cat | A.mg⁻¹ Au |
|---|---|---|---|---|---|---|---|---|---|---|---|---|---|---|---|---|---|---|
| DP20Au_C:4.0 nm Au/C on GCPs; 1 mg/ml cat + 10% Nafion in 4:1 IPA/H2O mix. Deposited and tested on GCPS on 04Mar2013 | 1 | 1.2 | 119.9 | 386 | 0.311 | 0.01 | 20 | 0.002 | 155.3 | 15.53 | 2.1 | 10 | 6 | 4 | 58.5 | 188.3 | 5.8 | 29.2 |
| | 2 | 1.7 | 123.8 | 386 | 0.321 | 0.01 | 20 | 0.002 | 160.4 | 16.04 | 1.9 | 10 | 6 | 3 | 56.4 | 175.7 | 5.6 | 28.2 |
| | 3 | 1.9 | 111.4 | 386 | 0.289 | 0.01 | 20 | 0.002 | 144.3 | 14.43 | 1.8 | 10 | 5 | 3 | 50.9 | 176.2 | 5.1 | 25.4 |
| | 4 | 1.9 | 122.4 | 386 | 0.317 | 0.01 | 20 | 0.002 | 158.5 | 15.85 | 2.1 | 10 | 5 | 3 | 51.0 | 160.9 | 5.1 | 25.5 |
| | 5 | 3.1 | 117.4 | 386 | 0.304 | 0.01 | 20 | 0.002 | 152.1 | 15.21 | 1.8 | 10 | 5 | 3 | 53.7 | 176.7 | 5.4 | 26.9 |
| | | | 119 | AVE | 0.308 | | | | AVE | 15.4 | | | | AVE | 54.1 | 176 | 5.4 | 27.0 |
| * Applied PF correction 0.5 Ω | | | 4 | STD DEVP | 0.01 | | | | STD DEVP | 0.6 | | | | STD DEVP | 2.98 | 8.7 | 0.30 | 1.5 |
| | | | 4 | CONFIDENCE | 0.01 | | | | CONFIDENCE | 0.5 | | | | CONFIDENCE | 2.61 | 7.61 | 0.26 | 1.3 |

** CA for 10 min at -0.2 V in both KOH and glycerol, before CV scans

#From run 5 of CV at 50 mV/s in 1 M KOH, after CA and strip cycling from -0.9 → 0.8 V for 5 cycles

Catalyst samples 1-5 were deposited on GCPs 2, 4, 5, 6 and 8, respectively

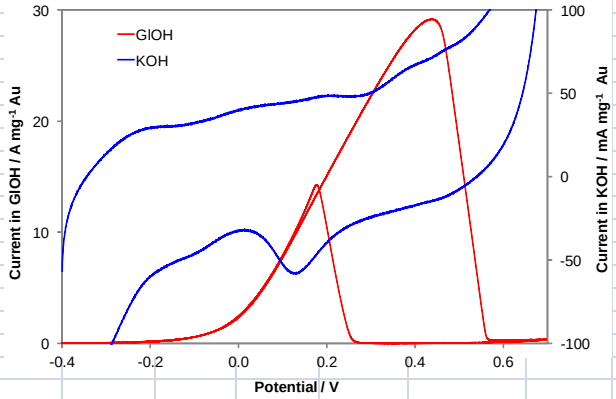

## 4.7 nm Au/C

| Catalyst | Sample no. | Ru (Ω) * | 1 M KOH** | | | | | | | | Glycerol oxidation (0.5 M) in 1 M KOH** | | | | | | | |
|---|---|---|---|---|---|---|---|---|---|---|---|---|---|---|---|---|---|---|
| | | | | | | | | | | | | | | | Highest peak | | | |
| | | | Integrated peak charge, μC # | Monolayer charge, μC/cm² | Metal surface area, cm² | Cat mass, mg | Metal loading, % | Metal mass, mg | EASA, cm²/mg metal | EASA, m²/g metal | Ru (Ω) | Scan rate, mV/s | Number of cycles | Number of highest peak | Current, mA | Current, mA.cm⁻² | A.mg⁻¹ cat | A.mg⁻¹ Au |
| **15 % Au: 4.7 nm Au/C** on GCPs; 1 mg/ml cat + 10% Nafion in 4:1 IPA/H2O mix. Deposited and tested on GCPS on 04July2012 | **1** | 1.4 | 72.6 | 386 | 0.188 | 0.01 | 15 | 0.0015 | 125.4 | 12.54 | 2.0 | 10 | 5 | 5 | 37.4 | 199.1 | 3.74 | 25.0 |
| | **2** | 1.2 | 79.7 | 386 | 0.206 | 0.01 | 15 | 0.0015 | 137.6 | 13.76 | 1.5 | 10 | 5 | 4 | 43.1 | 208.9 | 4.31 | 28.7 |
| | **3** | 1.3 | 73.9 | 386 | 0.191 | 0.01 | 15 | 0.0015 | 127.6 | 12.76 | 1.4 | 10 | 5 | 4 | 44.6 | 232.9 | 4.46 | 29.7 |
| | **4** | 2.0 | 78.9 | 386 | 0.204 | 0.01 | 15 | 0.0015 | 136.3 | 13.63 | 1.5 | 10 | 5 | 4 | 51.8 | 253.5 | 5.18 | 34.6 |
| | **5** | 1.5 | 68.2 | 386 | 0.177 | 0.01 | 15 | 0.0015 | 117.9 | 11.79 | 1.6 | 10 | 5 | 4 | 41.4 | 234.0 | 4.14 | 27.6 |
| | | | 75 | **AVE** | 0.19 | | | | **AVE** | 12.9 | | | | **AVE** | 43.7 | 226 | 4.4 | 29 |
| *** Applied PF correction 0.5 Ω** | | | 4 | **STD DEVP** | 0.01 | | | | **STD DEVP** | 0.7 | | | | **STD DEVP** | 4.73 | 19 | 0.5 | 3 |
| | | | 4 | **CONFIDENCE** | 0.01 | | | | **CONFIDENCE** | 0.6 | | | | **CONFIDENCE** | 4.15 | 17 | 0.4 | 3 |

** CA for 10 min at -0.2 V in both KOH and glycerol, before CV scans

#From run 2 of CV at 50 mV/s in 1 M KOH, after CA and strip cycling from -0.9 → 0.8 V for 5 cycles

Catalyst samples 1-5 were deposited on GCPs 2, 4, 5, 6 and 8, respectively

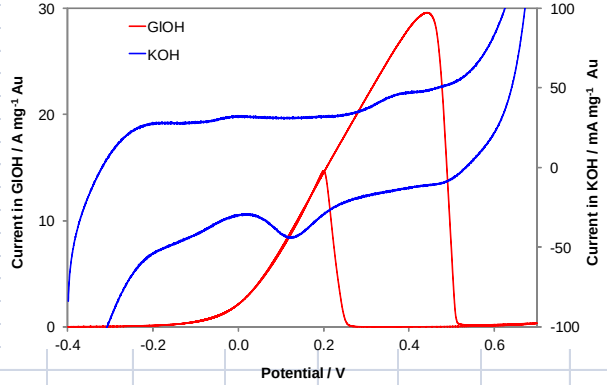

## 14.7 nm Au/C

| Catalyst | Sample no. | Ru (Ω) * | 1 M KOH** | | | | | | | | Glycerol oxidation (0.5 M) in 1 M KOH** | | | | | | | |
|---|---|---|---|---|---|---|---|---|---|---|---|---|---|---|---|---|---|---|
| | | | | | | | | | | | | | | Highest peak | | | | |
| | | | Integrated peak charge, μC # | Monolayer charge, μC/cm² | Metal surface area, cm² | Cat mass, mg | Metal loading, % | Metal mass, mg | EASA, cm²/mg metal | EASA, m²/g metal | Ru (Ω) | Scan rate, mV/s | Number of cycles | Number of highest peak | Current, mA | Current, mA.cm⁻² | A.mg⁻¹ cat | A.mg⁻¹ Au |
| Au_Cit 1: 14.7 nm Au/C on GCPs; 1 mg/ml cat + 10% Nafion in 4:1 IPA/H2O mix. Deposited and tested on GCPS on 03Dec2012 | 1 | 3.1 | 41.1 | 386 | 0.107 | 0.01 | 20 | 0.002 | 53.3 | 5.33 | 1.6 | 10 | 5 | 5 | 47.4 | 445.0 | 4.7 | 23.7 |
| | 2 | 3.4 | 45.3 | 386 | 0.117 | 0.01 | 20 | 0.002 | 58.7 | 5.87 | 2.1 | 10 | 5 | 5 | 36.9 | 314.5 | 3.7 | 18.5 |
| | 3 | 2.1 | 55.3 | 386 | 0.143 | 0.01 | 20 | 0.002 | 71.7 | 7.17 | 1.2 | 10 | 5 | 4 | 44.4 | 309.4 | 4.4 | 22.2 |
| | 4 | 2.7 | 48.8 | 386 | 0.126 | 0.01 | 20 | 0.002 | 63.2 | 6.32 | 1.7 | 10 | 5 | 4 | 46.6 | 368.2 | 4.7 | 23.3 |
| | 5 | 2.1 | 63.9 | 386 | 0.165 | 0.01 | 20 | 0.002 | 82.7 | 8.27 | 1.4 | 10 | 5 | 5 | 43.7 | 263.8 | 4.4 | 21.8 |
| | | | | | 0.13 | | | | AVE | 6.6 | | | | AVE | 44 | 340 | 4.4 | 22 |
| | | * Applied PF correction 0.5 Ω | | | 0.02 | | | | STD DEVP | 1.0 | | | | STD DEVP | 4 | 62 | 0.4 | 2 |
| | | | | | 0.02 | | | | CONFIDENCE | 0.9 | | | | CONFIDENCE | 3 | 54 | 0.3 | 2 |

** CA for 10 min at -0.2 V in both KOH and glycerol, before CV scans

#From run 2 of CV at 50 mV/s in 1 M KOH, after CA and strip cycling from -0.9 → 0.8 V for 5 cycles

Catalyst samples 1-5 were deposited on GCPs 2, 4, 5, 6 and 8, respectively

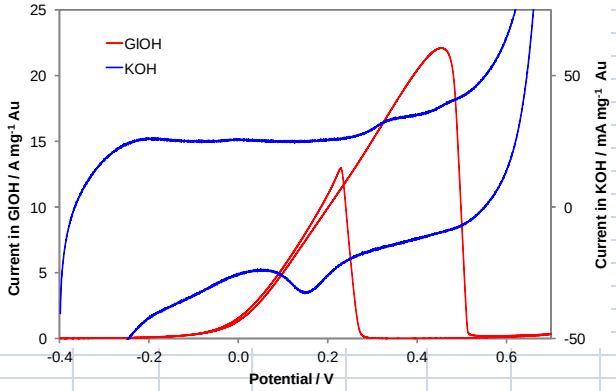

## 43 nm Au/C

| Catalyst | Sample no. | 1 M KOH** | | | | | | | | Glycerol oxidation (0.5 M) in 1 M KOH** | | | | | | | |
|---|---|---|---|---|---|---|---|---|---|---|---|---|---|---|---|---|---|
| | | | | | | | | | | | | | | Highest peak | | | |
| | | Ru (Ω) * | Integrated peak charge, μC # | Monolayer charge, μC/cm² | Metal surface area, cm² | Cat mass, mg | Metal loading, % | Metal mass, mg | EASA, cm²/mg metal | EASA, m²/g metal | Ru (Ω) | Scan rate, mV/s | Number of cycles | Number of highest peak | Current, mA | Current, mA.cm⁻² | A.mg⁻¹ cat | A.mg⁻¹ Au |
| **Au_Cit 4: 43 nm Au/C** on GCPs; 1 mg/ml cat + 10% Nafion in 4:1 IPA/H2O mix. Deposited and tested on GCPS on 12Dec2012 | **1** | 4.1 | 11.0 | 386 | 0.028 | 0.01 | 20 | 0.002 | 14.2 | 1.42 | 2.4 | 10 | 5 | 5 | 22.4 | 790.3 | 2.2 | 11.2 |
| | **2** | 1.7 | 12.9 | 386 | 0.033 | 0.01 | 20 | 0.002 | 16.7 | 1.67 | 1.9 | 10 | 5 | 5 | 21.6 | 647.0 | 2.2 | 10.8 |
| | **3** | 1.8 | 14.5 | 386 | 0.038 | 0.01 | 20 | 0.002 | 18.8 | 1.88 | 1.8 | 10 | 6 | 6 | 19.6 | 521.7 | 2.0 | 9.8 |
| | **4** | 1.8 | 17.9 | 386 | 0.046 | 0.01 | 20 | 0.002 | 23.2 | 2.32 | 2.1 | 10 | 6 | 5 | 25.0 | 539.1 | 2.5 | 12.5 |
| | **5** | 1.7 | 12.0 | 386 | 0.031 | 0.01 | 20 | 0.002 | 15.5 | 1.55 | 3.3 | 10 | 6 | 5 | 22.1 | 713.9 | 2.2 | 11.1 |
| | | | | | 0.04 | | | | **AVE** | 1.8 | | | | **AVE** | 22.2 | 642 | 2.2 | 11 |
| | | *** Applied PF correction 0.5 Ω** | | | 0.01 | | | | **STD DEVP** | 0.3 | | | | **STD DEVP** | 1.74 | 102.2 | 0.17 | 0.9 |
| | | | | | 0.01 | | | | **CONFIDENCE** | 0.3 | | | | **CONFIDENCE** | 1.53 | 89.61 | 0.15 | 0.8 |

** CA for 10 min at -0.2 V in both KOH and glycerol, before CV scans

#From run 2 of CV at 50 mV/s in 1 M KOH, after CA and strip cycling from -0.9 → 0.8 V for 5 cycles

Catalyst samples 1-5 were deposited on GCPs 1, 4, 5, 6 and 8, respectively

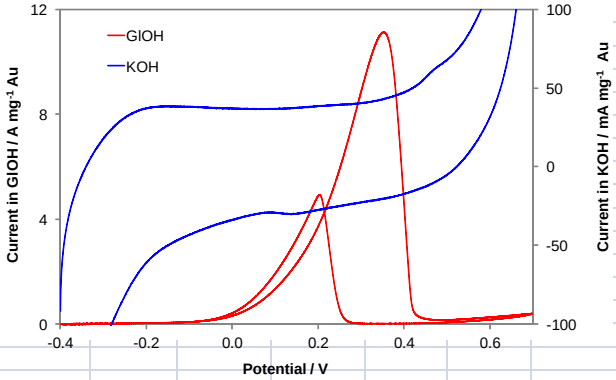

## 88 nm Au/C

| Catalyst | Sample no. | Ru (Ω) * | 1 M KOH** Integrated peak charge, μC # | Monolayer charge, μC/cm² | Metal surface area, cm² | Cat mass, mg | Metal loading, % | Metal mass, mg | EASA, cm²/mg metal | EASA, m²/g metal | Glycerol oxidation (0.5 M) in 1 M KOH** Ru (Ω) | Scan rate, mV/s | Number of cycles | Number of highest peak | Highest peak Current, mA | Current, mA.cm⁻² | A.mg⁻¹ cat | A.mg⁻¹ Au |
|---|---|---|---|---|---|---|---|---|---|---|---|---|---|---|---|---|---|---|
| **Au_Cit 3: 88 nm Au_C** on GCPs; 1 mg/ml cat + 10% Nafion in 4:1 IPA/H2O mix. Deposited and tested on GCPS on 05Dec2012 | **1** | 1.7 | 14.9 | 386 | 0.039 | 0.01 | 20 | 0.002 | 19.3 | 1.93 | 1.9 | 10 | 5 | 5 | 30.6 | 790.4 | 3.1 | 15.3 |
| | **2** | 1.6 | 18.3 | 386 | 0.047 | 0.01 | 20 | 0.002 | 23.7 | 2.37 | 1.8 | 10 | 7 | 5 | 29.2 | 616.1 | 2.9 | 14.6 |
| | **3** | 1.5 | 14.1 | 386 | 0.037 | 0.01 | 20 | 0.002 | 18.3 | 1.83 | 2.1 | 10 | 6 | 5 | 24.9 | 680.0 | 2.5 | 12.5 |
| | **4** | 1.7 | 15.0 | 386 | 0.039 | 0.01 | 20 | 0.002 | 19.4 | 1.94 | 1.7 | 10 | 7 | 6 | 24.8 | 640.2 | 2.5 | 12.4 |
| | **5** | 1.6 | 13.9 | 386 | 0.036 | 0.01 | 20 | 0.002 | 17.9 | 1.79 | 1.9 | 10 | 7 | 4 | 24.0 | 669.4 | 2.4 | 12.0 |
| | | | | **AVE** | 0.039 | | | | **AVE** | 2.0 | | | | **AVE** | 27 | 679 | 2.7 | 13 |
| | *** Applied PF correction 0.5 Ω** | | | **STD DEVP** | 0.004 | | | | **STD DEVP** | 0.2 | | | | **STD DEVP** | 3 | 60 | 0.3 | 1 |
| | | | | **CONFIDENCE** | 0.004 | | | | **CONFIDENCE** | 0.2 | | | | **CONFIDENCE** | 2 | 53 | 0.2 | 1 |

** CA for 10 min at -0.2 V in both KOH and glycerol, before CV scans

#From run 2 of CV at 50 mV/s in 1 M KOH, after CA and strip cycling from -0.9 → 0.8 V for 5 cycles

Catalyst samples 1-5 were deposited on GCPs 1, 4, 5, 6 and 8, respectively

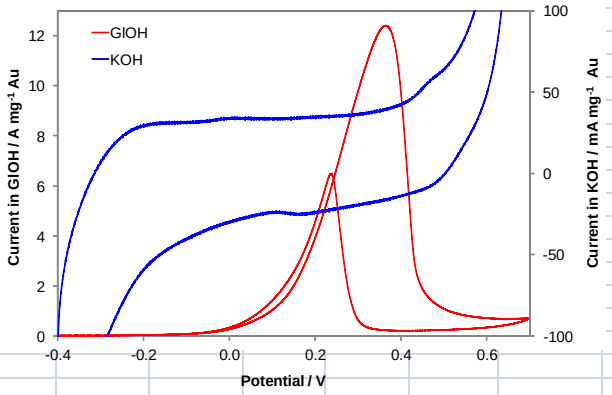

# 120 nm Au/C

| Catalyst | Sample no. | Ru (Ω) * | 1 M KOH** | | | | | | | | Glycerol oxidation (0.5 M) in 1 M KOH** | | | | | | | |
|---|---|---|---|---|---|---|---|---|---|---|---|---|---|---|---|---|---|---|
| | | | | | | | | | | | | | | | Highest peak | | | |
| | | | Integrated peak charge, μC # | Monolayer charge, μC/cm² | Metal surface area, cm² | Cat mass, mg | Metal loading, % | Metal mass, mg | EASA, cm²/mg metal | EASA, m²/g metal | Ru (Ω) | Scan rate, mV/s | Number of cycles | Number of highest peak | Current, mA | Current, mA.cm⁻² | A.mg⁻¹ cat | A.mg⁻¹ Au |
| Au_THPC1: 120 nm Au/C on GCPs; 1 mg/ml cat + 10% Nafion in 4:1 IPA/H2O mix. Deposited and tested on GCPS on 25Mar2013 | 1 | 0.9 | 9.2 | 386 | 0.024 | 0.01 | 32.6 | 0.0033 | 7.3 | 0.73 | 1.6 | 10 | 5 | 4 | 28.5 | 1200.0 | 2.849 | 8.7 |
| | 2 | 1.5 | 11.1 | 386 | 0.029 | 0.01 | 32.6 | 0.0033 | 8.8 | 0.88 | 1.6 | 10 | 5 | 5 | 29.3 | 1022.1 | 2.934 | 9.0 |
| | 3 | 0.9 | 12.5 | 386 | 0.032 | 0.01 | 32.6 | 0.0033 | 9.9 | 0.99 | 1.7 | 10 | 5 | 4 | 29.3 | 906.0 | 2.934 | 9.0 |
| | 4 | 0.9 | 14.1 | 386 | 0.036 | 0.01 | 32.6 | 0.0033 | 11.2 | 1.12 | 1.7 | 10 | 5 | 4 | 30.4 | 833.8 | 3.035 | 9.3 |
| | 5 | 0.9 | 11.0 | 386 | 0.028 | 0.01 | 32.6 | 0.0033 | 8.7 | 0.87 | 1.7 | 10 | 5 | 4 | 28.8 | 1009.9 | 2.878 | 8.8 |
| | | | | AVE | 0.030 | | | | AVE | 0.9 | | | | AVE | 29.3 | 994 | 2.93 | 9.0 |
| | * Applied PF correction 0.5 Ω | | | STD DEVP | 0.004 | | | | STD DEVP | 0.1 | | | | STD DEVP | 0.6 | 124 | 0.06 | 0.2 |
| | | | | CONFIDENCE | 0.004 | | | | CONFIDENCE | 0.1 | | | | CONFIDENCE | 0.6 | 109 | 0.06 | 0.2 |

** CA for 10 min at -0.2 V in both KOH and glycerol, before CV scans

#From run 2 of CV at 50 mV/s in 1 M KOH, after CA and strip cycling from -0.9 → 0.8 V for 5 cycles

Catalyst samples 1-5 were deposited on GCPs 2, 4, 5, 6 and 8, respectively

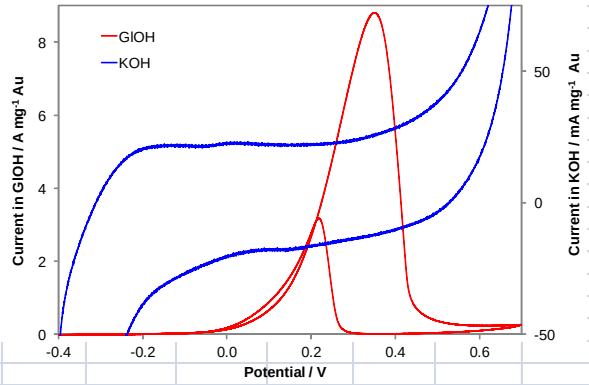

## Appendix 5.3 Lead profiling of gold colloids

| Source | Peak potentials, V | | | | | | |
|---|---|---|---|---|---|---|---|
| | (111) narrow domains | (111) wide domains | (100) | (110) | Diff (100) and (111) wide | Diff (100) and (110) | Diff (111) and (110) |
| Hernandez2004JElectroanalChem, potentials *vs* . RHE | 0.415 | 0.435 | 0.475 | 0.560 | 0.04 | 0.09 | 0.13 |
| Hernandez potentials *vs* . SCE | -0.580 | -0.560 | -0.520 | -0.435 | | | |
| Bulk Au (*vs* . SCE) - my results | -0.580 | -0.567 | -0.522 | -0.420 | 0.04 | 0.10 | 0.15 |
| Difference Hernandez & my results | | 1.00 | 1.00 | 0.98 | | | |
| Wain2013ElectrochimActa | | -0.540 | -0.470 | -0.390 | 0.07 | 0.08 | 0.15 |
| Difference Wain & mine | | 0.03 | 0.05 | 0.03 | | | |
| Wang2012Analyst (vs SCE) | | -0.580 | | -0.380 | | | 0.20 |
| | | | | | | | |
| Colloids | | | | | | | |
| Bulk Au | -0.580 | -0.567 | -0.522 | -0.420 | 0.04 | 0.10 | 0.15 |
| 3 nm colloids | -0.587 | | | -0.436 | | | 0.15 |
| 14.7 nm colloids | -0.581 | -0.573 | -0.523 | -0.424 | 0.05 | 0.10 | 0.15 |
| 88 nm colloids | -0.580 | -0.568 | -0.521 | -0.429 | 0.05 | 0.09 | 0.14 |

| | Peak area, µC | | | Total | % Area | | |
|---|---|---|---|---|---|---|---|
| | Au(111) | Au(100) | Au(110) | Area | Au (111) | Au (100) | Au (110) |
| (a) Bulk Au | 0.23 | 0.019 | 0.66 | 0.91 | 25.3 | 2.1 | 72.6 |
| (b) 3.2 nm | 6.2 | 0.016 | 19 | 25.6 | 24.2 | 0.1 | 75.7 |
| (c) 15 nm | 4.1 | 0.032 | 9.9 | 14.0 | 28.9 | 0.2 | 70.9 |
| (d) 88 nm | 5.3 | 0.13 | 6.0 | 11.4 | 47 | 1 | 52 |

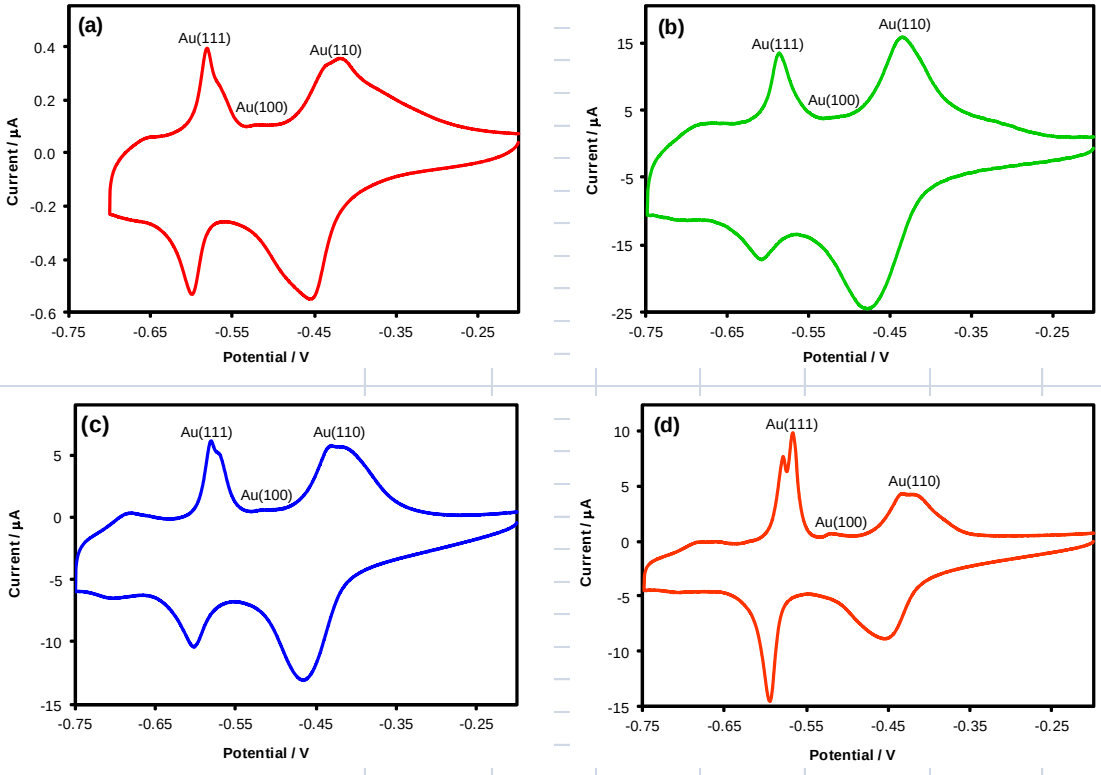

# APPENDIX 6

## Appendix 6.1 Data for plots of gold oxide reduction charge *vs*. (a) Au loading and (b) TEM-determined surface area

| % Au/C | $d_{ave}$ , nm | Ave AuO red charge in KOH, μC | Error | Surface area from TEM, $cm^2$ | Error |
|---|---|---|---|---|---|
| 0 | 0 | 0 | 0 | 0 | 0 |
| 1 | 4.8 | 10 | 2 | 0.0416 | 0.0002 |
| 5 | 4.7 | 25 | 2 | 0.213 | 0.002 |
| 7.5 | 3.9 | 51 | 3 | 0.386 | 0.002 |
| 10 | 5.7 | 45 | 3 | 0.396 | 0.002 |
| 12.5 | 4.6 | 61 | 8 | 0.508 | 0.003 |
| 15 | 4.7 | 75 | 4 | 0.626 | 0.003 |
| 20 | 4.0 | 119 | 4 | 0.874 | 0.006 |

## Appendix 6.2 Activity comparisons for *x* % Au/C catalysts

| % Au/C | No. of particles measured | Diameter, nm | | | Coefficient of variation, % | Specific SA from TEM, $m^2/g$ | Error | Mass Au, mg | Surface area from TEM, $cm^2$ | Surface area from EASA, $cm^2$ | Error | Ave current, mA | Error | Specific activity TEM, $mA/cm^2$ | Error | $mA/cm^2$ from EASA | Error |
|---|---|---|---|---|---|---|---|---|---|---|---|---|---|---|---|---|---|
| | | Mean | Median | Mode | | | | | | | | | | | | | |
| 1 | 666 | 4.8 | 4.4 | 2.8 | 48.5 | 41.6 | 0.2 | 0.0001 | 0.04 | 0.026 | 0.005 | 1.1 | 0.2 | 26 | 6 | 47 | 8 |
| 5 | 380 | 4.7 | 4.2 | 4.2 | 46.2 | 42.6 | 0.3 | 0.0005 | 0.21 | 0.065 | 0.005 | 20 | 3 | 93 | 13 | 310 | 64 |
| 7.5 | 866 | 3.9 | 3.5 | 3.6 | 48.8 | 51.4 | 0.3 | 0.00075 | 0.39 | 0.13 | 0.01 | 29 | 1 | 76 | 2 | 222 | 14 |
| 10 | 782 | 5.7 | 5.2 | 5.2 | 40.6 | 39.6 | 0.2 | 0.001 | 0.40 | 0.118 | 0.008 | 30 | 3 | 77 | 7 | 261 | 34 |
| 12.5 | 856 | 4.6 | 3.9 | 3.4 | 51.2 | 40.7 | 0.2 | 0.00125 | 0.51 | 0.16 | 0.02 | 38 | 4 | 75 | 8 | 245 | 15 |
| 15 | 774 | 4.7 | 4.2 | 4.2 | 46.9 | 41.8 | 0.2 | 0.0015 | 0.63 | 0.19 | 0.01 | 44 | 4 | 70 | 7 | 226 | 17 |
| 20 | 711 | 4.0 | 3.4 | 3.1 | 54.4 | 43.7 | 0.3 | 0.002 | 0.87 | 0.31 | 0.01 | 54 | 3 | 62 | 3 | 176 | 8 |

## Appendix 6.3 Electrochemistry data for *x* % Au/C catalysts

NB: Electrochemistry data for 15 and 20 % Au/C catalysts are shown in Appendix 5.2 for 4.7 and 4.0 nm Au/C catalysts, respectively.

## 1 % Au/C

| Catalyst | Sample no. | Ru (Ω) * | 1 M KOH** | | | | | | | | Glycerol oxidation (0.5 M) in 1 M KOH** | | | | | | | |
|---|---|---|---|---|---|---|---|---|---|---|---|---|---|---|---|---|---|---|
| | | | | | | | | | | | | | | | Highest peak | | | |
| | | | Integrated peak charge, µC # | Monolayer charge, µC/cm$^2$ | Metal surface area, cm$^2$ | Cat mass, mg | Metal loading, % | Metal mass, mg | EASA, cm$^2$/mg metal | EASA, m$^2$/g metal | Ru (Ω) | Scan rate, mV/s | Number of cycles | Number of highest peak | Current, mA | Current, mA.cm$^{-2}$ | A.mg$^{-1}$ cat | A.mg$^{-1}$ Au |
| **1 % Au/C** on GCPs; 1 mg/ml cat + 10% Nafion in 4:1 IPA/H2O mix. Deposited and tested on GCPS on 02July2012 | **1** | 1.6 | 6.2 | 386 | 0.016 | 0.01 | 1 | 0.0001 | 159.7 | 15.97 | 1.7 | 10 | 5 | 3 | 0.7 | 46.5 | 0.07 | 7.4 |
| | **2** | 1.4 | 12.3 | 386 | 0.032 | 0.01 | 1 | 0.0001 | 318.9 | 31.89 | 1.5 | 10 | 5 | 5 | 1.0 | 32.0 | 0.10 | 10.2 |
| | **3** | 1.4 | 11.3 | 386 | 0.029 | 0.01 | 1 | 0.0001 | 293.5 | 29.35 | 1.6 | 10 | 5 | 3 | 1.0 | 33.2 | 0.10 | 9.7 |
| | **4** | 1.4 | 8.9 | 386 | 0.023 | 0.01 | 1 | 0.0001 | 230.3 | 23.03 | 1.8 | 10 | 6 | 6 | 1.2 | 52.9 | 0.12 | 12.2 |
| | **5** | 1.4 | 11.0 | 386 | 0.028 | 0.01 | 1 | 0.0001 | 283.9 | 28.39 | 1.5 | 10 | 7 | 6 | 1.5 | 53.8 | 0.15 | 15.3 |
| | | | 10 | **AVE** | 0.026 | | | | | | | | | **AVE** | 1.1 | 44 | 0.11 | 11 |
| *** Applied PF correction 0.5 Ω** | | | 2 | **STD DEVP** | 0.01 | | ** CA for 10 min at -0.2 V in both KOH and glycerol, before CV scans | | | | | | | **STD DEVP** | 0.3 | 9 | 0.03 | 3 |
| | | | 2 | **CONFIDENCE** | 0.005 | | | | | | | | | **CONFIDENCE** | 0.2 | 8 | 0.02 | 2 |

#From run 2 of CV at 50 mV/s in 1 M KOH, after CA and strip cycling from -0.9 → 0.8 V for 5 cycles

Catalyst samples 1-5 were deposited on GCPs 1, 4, 5, 6 and 8, respectively

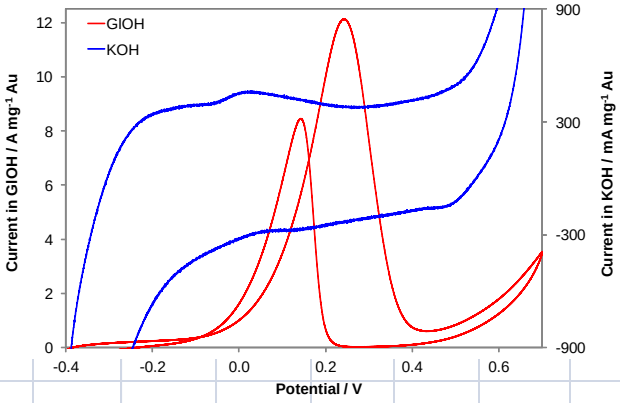

## 5 % Au/C

| Catalyst | Sample no. | 1 M KOH** | | | | | | | | | Glycerol oxidation (0.5 M) in 1 M KOH** | | | | | | | |
|---|---|---|---|---|---|---|---|---|---|---|---|---|---|---|---|---|---|---|
| | | | | | | | | | | | | | | | Highest peak | | | |
| | | Ru (Ω) * | Integrated peak charge, μC # | Monolayer charge, μC/cm² | Metal surface area, cm² | Cat mass, mg | Metal loading, % | Metal mass, mg | EASA, cm²/mg metal | EASA, m²/g metal | Ru (Ω) | Scan rate, mV/s | Number of cycles | Number of highest peak | Current, mA | Current, mA.cm⁻² | A.mg⁻¹ cat | A.mg⁻¹ Au |
| **5 % Au/C** on GCPs; 1 mg/ml cat + 10% Nafion in 4:1 IPA/H2O mix. Deposited and tested on GCPS on 03July2013 | **1** | 2.6 | 26.4 | 386 | 0.068 | 0.01 | 5 | 0.0005 | 136.7 | 13.67 | 2.4 | 10 | 7 | 5 | 17.7 | 259.1 | 1.8 | 35.4 |
| | **2** | 2.6 | 25.1 | 386 | 0.065 | 0.01 | 5 | 0.0005 | 130.3 | 13.03 | 2.2 | 10 | 5 | 5 | 15.7 | 240.4 | 1.6 | 31.3 |
| | **3** | 2.1 | 21.9 | 386 | 0.057 | 0.01 | 5 | 0.0005 | 113.7 | 11.37 | 1.5 | 10 | 5 | 5 | 25.1 | 441.4 | 2.5 | 50.2 |
| | **4** | 1.9 | 28.5 | 386 | 0.074 | 0.01 | 5 | 0.0005 | 147.6 | 14.76 | 2.1 | 10 | 6 | 6 | 20.2 | 274.3 | 2.0 | 40.5 |
| | **5** | 2.0 | 23.9 | 386 | 0.062 | 0.01 | 5 | 0.0005 | 123.9 | 12.39 | 2.3 | 10 | 6 | 6 | 20.9 | 336.8 | 2.1 | 41.7 |
| | | | 25 | **AVE** | 0.065 | | | | | | | | | **AVE** | 20 | 310 | 2.0 | 40 |
| *** Applied PF correction 0.5 Ω** | | | 2 | **STD DEVP** | 0.01 | | ** CA for 10 min at -0.2 V in both KOH and glycerol, before CV scans | | | | | | | **STD DEVP** | 3 | 73 | 0.3 | 6 |
| | | | 2 | **CONFIDENCE** | 0.005 | | | | | | | | | **CONFIDENCE** | 3 | 64 | 0.3 | 6 |

#From run 2 of CV at 50 mV/s in 1 M KOH, after CA and strip cycling from -0.9 → 0.8 V for 5 cycles

Catalyst samples 1-5 were deposited on GCPs 2, 4, 5, 6 and 8, respectively

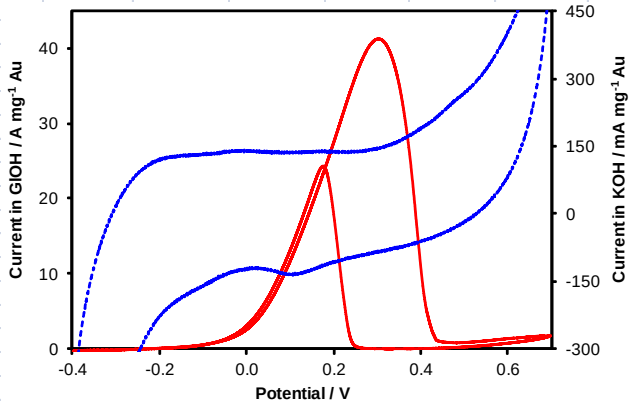

## 7.5 % Au/C

| Catalyst | Sample no. | Ru (Ω) * | 1 M KOH** Integrated peak charge, µC # | Monolayer charge, µC/cm² | Metal surface area, cm² | Cat mass, mg | Metal loading, % | Metal mass, mg | EASA, cm²/mg metal | EASA, m²/g metal | Glycerol oxidation (0.5 M) in 1 M KOH** Ru (Ω) | Scan rate, mV/s | Number of cycles | Number of highest peak | Highest peak Current, mA | Current, mA.cm⁻² | A.mg⁻¹ cat | A.mg⁻¹ Au |
|---|---|---|---|---|---|---|---|---|---|---|---|---|---|---|---|---|---|---|
| **7.5 % Au/C** on GCPs; 1 mg/ml cat + 10% Nafion in 4:1 IPA/H2O mix. Deposited and tested on GCPS on 12Sept2012 | **1** | 1.5 | 55.7 | 386 | 0.144 | 0.01 | 7.5 | 0.00075 | 192.3 | 19.23 | 2.0 | 10 | 5 | 5 | 28.1 | 194.6 | 2.8 | 37.4 |
| | **2** | 1.6 | 48.5 | 386 | 0.126 | 0.01 | 7.5 | 0.00075 | 167.4 | 16.74 | 2.0 | 10 | 5 | 4 | 30.5 | 242.5 | 3.0 | 40.6 |
| | **3** | 1.7 | 49.5 | 386 | 0.128 | 0.01 | 7.5 | 0.00075 | 170.9 | 17.09 | 2.0 | 10 | 5 | 3 | 28.9 | 225.1 | 2.9 | 38.5 |
| | **4** | 1.4 | 47.9 | 386 | 0.124 | 0.01 | 7.5 | 0.00075 | 165.3 | 16.53 | 1.5 | 10 | 5 | 4 | 28.4 | 229.2 | 2.8 | 37.9 |
| | **5** | 1.2 | 53.9 | 386 | 0.140 | 0.01 | 7.5 | 0.00075 | 186.2 | 18.62 | 2.0 | 10 | 5 | 4 | 30.6 | 218.9 | 3.1 | 40.7 |
| | | | 51 | **AVE** | 0.132 | | | | | | | | | **AVE** | 29.3 | 222 | 2.93 | 39 |
| *** Applied PF correction 0.5 Ω** | | | 3 | **STD DEVP** | 0.01 | | ** CA for 10 min at -0.2 V in both KOH and glycerol, before CV scans | | | | | | | **STD DEVP** | 1.0 | 16 | 0.10 | 1 |
| | | | 3 | **CONFIDENCE** | 0.007 | | | | | | | | | **CONFIDENCE** | 0.9 | 14 | 0.09 | 1 |

#From run 2 of CV at 50 mV/s in 1 M KOH, after CA and strip cycling from -0.9 → 0.8 V for 5 cycles

Catalyst samples 1-5 were deposited on GCPs 1, 4, 5, 6 and 8, respectively

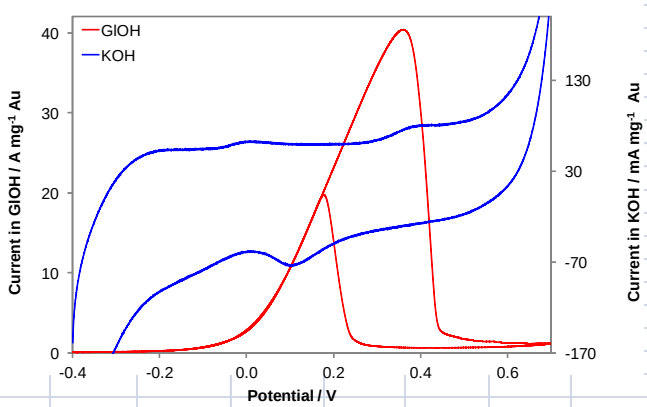

## 10 % Au/C

| Catalyst | Sample no. | Ru (Ω) * | 1 M KOH** | | | | | | | | Glycerol oxidation (0.5 M) in 1 M KOH** | | | | | | | |
|---|---|---|---|---|---|---|---|---|---|---|---|---|---|---|---|---|---|---|
| | | | | | | | | | | | | | | | Highest peak | | | |
| | | | Integrated peak charge, μC # | Monolayer charge, μC/cm² | Metal surface area, cm² | Cat mass, mg | Metal loading, % | Metal mass, mg | EASA, cm²/mg metal | EASA, m²/g metal | Ru (Ω) | Scan rate, mV/s | Number of cycles | Number of highest peak | Current, mA | Current, mA.cm⁻² | A.mg⁻¹ cat | A.mg⁻¹ Au |
| **10 % Au/C** on GCPs; 1 mg/ml cat + 10% Nafion in 4:1 IPA/H2O mix. Deposited and tested on GCPS on 27June2012 | **1** | 1.2 | 50.5 | 386 | 0.131 | 0.01 | 10 | 0.001 | 130.9 | 13.09 | 1.8 | 10 | 5 | 5 | 29.0 | 221.5 | 2.9 | 29.0 |
| | **2** | 1.6 | 41.0 | 386 | 0.106 | 0.01 | 10 | 0.001 | 106.2 | 10.62 | 1.8 | 10 | 6 | 5 | 31.2 | 293.5 | 3.1 | 31.2 |
| | **3** | 1.4 | 45.1 | 386 | 0.117 | 0.01 | 10 | 0.001 | 116.8 | 11.68 | 2 | 10 | 6 | 5 | 33.9 | 290.4 | 3.4 | 33.9 |
| | **4** | 1.2 | 48.2 | 386 | 0.125 | 0.01 | 10 | 0.001 | 124.8 | 12.48 | 2.0 | 10 | 6 | 5 | 25.9 | 207.3 | 2.6 | 25.9 |
| | **5** | 1.2 | 42.6 | 386 | 0.110 | 0.01 | 10 | 0.001 | 110.3 | 11.03 | 1.8 | 10 | 6 | 5 | 32.2 | 292.1 | 3.2 | 32.2 |
| | | | 45 | **AVE** | 0.118 | | | | **AVE** | 11.8 | | | | **AVE** | 30 | 261 | 3.0 | 30 |
| *** Applied PF correction 0.5 Ω** | | | 4 | **STD DEVP** | 0.01 | | | | **STD DEVP** | 0.9 | | | | **STD DEVP** | 3 | 38 | 0.3 | 3 |
| | | | 3 | **ONFIDENCE** | 0.008 | | | | **CONFIDENCE** | 0.8 | | | | **CONFIDENCE** | 2 | 34 | 0.2 | 2 |

** CA for 10 min at -0.2 V in both KOH and glycerol, before CV scans

#From run 2 of CV at 50 mV/s in 1 M KOH, after CA and strip cycling from -0.9 → 0.8 V for 5 cycles

Catalyst samples 1-5 were deposited on GCPs 1, 4, 5, 6 and 8, respectively

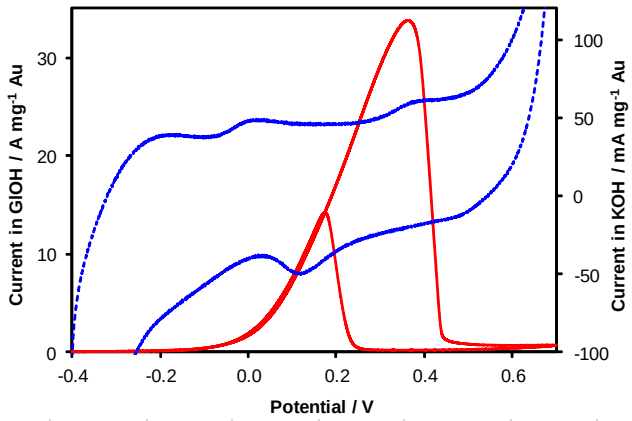

## 12.5 % Au/C

| Catalyst | Sample no. | Ru (Ω) * | 1 M KOH** Integrated peak charge, μC # | Monolayer charge, μC/cm² | Metal surface area, cm² | Cat mass, mg | Metal loading, % | Metal mass, mg | EASA, cm²/mg metal | EASA, m²/g metal | Glycerol oxidation (0.5 M) in 1 M KOH** Ru (Ω) | Scan rate, mV/s | Number of cycles | Highest peak: Number of highest peak | Current, mA | Current, mA.cm⁻² | A.mg⁻¹ cat | A.mg⁻¹ Au |
|---|---|---|---|---|---|---|---|---|---|---|---|---|---|---|---|---|---|---|
| **12.5 % Au/C** on GCPs; 1 mg/ml cat + 10% Nafion in 4:1 IPA/H2O mix. Deposited and tested on GCPS on 10Sept2012 | 1 | 1.2 | 50.3 | 386 | 0.130 | 0.01 | 12.5 | 0.00125 | 104.3 | 10.43 | 1.3 | 10 | 5 | 5 | 36.1 | 276.8 | 3.6 | 28.9 |
| | 2 | 1.7 | 53.3 | 386 | 0.138 | 0.01 | 12.5 | 0.00125 | 110.5 | 11.05 | 1.3 | 10 | 5 | 4 | 31.5 | 227.6 | 3.1 | 25.2 |
| | 3 | 1.7 | 62.1 | 386 | 0.161 | 0.01 | 12.5 | 0.00125 | 128.8 | 12.88 | 1.9 | 10 | 5 | 4 | 40.2 | 249.7 | 4.0 | 32.2 |
| | 4 | 1.8 | 62.2 | 386 | 0.161 | 0.01 | 12.5 | 0.00125 | 128.9 | 12.89 | 1.2 | 10 | 5 | 4 | 38.7 | 239.9 | 3.9 | 30.9 |
| | 5 | 1.7 | 75.0 | 386 | 0.194 | 0.01 | 12.5 | 0.00125 | 155.5 | 15.55 | 1.9 | 10 | 5 | 4 | 45.2 | 232.4 | 4.5 | 36.1 |
| | | | 61 | **AVE** | 0.157 | | | | | | | | | **AVE** | 38 | 245 | 3.8 | 31 |
| *** Applied PF correction 0.5 Ω** | | | 9 | **STD DEVP** | 0.02 | | ** CA for 10 min at -0.2 V in both KOH and glycerol, before CV scans | | | | | | | **STD DEVP** | 5 | 17 | 0.5 | 4 |
| | | | 8 | **CONFIDENCE** | 0.020 | | | | | | | | | **CONFIDENCE** | 4 | 15 | 0.4 | 3 |

#From run 2 of CV at 50 mV/s in 1 M KOH, after CA and strip cycling from -0.9 → 0.8 V for 5 cycles

Catalyst samples 1-5 were deposited on GCPs 1, 4, 5, 6 and 8, respectively

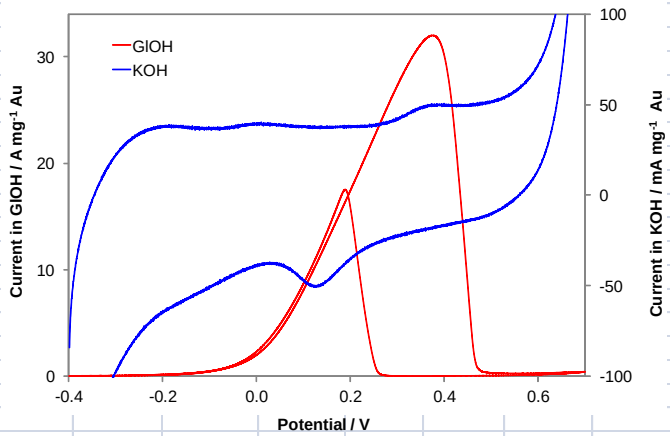

**Appendix 6.4 Re-calculation of EASA for 20% Au/C catalyst using percentages of gold facets obtained for precursor gold colloids with lead profiling**

| Au facet | * Monolayer charge, μC/cm$^2$ | #3.2 nm colloids % Au facet | 20 % Au/C ave total charge, μC | Ave charge facets, μC | EASA facets, cm$^2$ | |
|---|---|---|---|---|---|---|
| **(110)** | 272 | 75.7 | 119 | 90.1 | 0.3 | |
| **(100)** | 384 | 0.1 | 119 | 0.1 | 0.0003 | |
| **(111)** | 444 | 24.2 | 119 | 28.8 | 0.06 | |
| | | | | **Total EASA** | 0.40 | cm$^2$ |
| | | | | **% of TEM** | **44** | |
| TEM S.A. | 0.9 | cm$^2$ | | | | |
| EASA using Au(100) value | 0.31 | cm$^2$ | | | | |
| **% of TEM** | **34** | | | | | |

*Wang, *et al* ., Chem. Commun. 47 (2011) 6894

# From Pb UPD

## Appendix 6.5 Peak current *vs*. scan rate data

| Scan rate V $s^{-1}$ | Sqrt scan rate $(V\ s^{-1})^{0.5}$ | 1 % Au/C | | | 10 % Au/C | | | 20 % Au/C | | | Bulk Au | |
|---|---|---|---|---|---|---|---|---|---|---|---|---|
| | | Peak current | | Max peak no. | Peak current | | Max peak no. | Peak current | | Max peak no. | Peak current | Max. peak no. |
| | | mA | A $mg^{-1}$ Au | | mA | A $mg^{-1}$ Au | | mA | A $mg^{-1}$ Au | | mA | |
| 0.001 | 0.03 | 0.13 | 1.3 | 5 | 14.7 | 15 | 2 | 39.8 | 20 | 1 | 0.253 | 2 |
| 0.005 | 0.07 | 0.42 | 4.2 | 3 | 20.9 | 21 | 3 | 50.1 | 25 | 1 | 0.275 | 2 |
| 0.01 | 0.10 | 0.56 | 5.6 | 5 | 23.6 | 24 | 2 | 56.1 | 28 | 2 | 0.288 | 3 |
| 0.02 | 0.14 | 0.79 | 7.9 | 3 | 25.5 | 25 | 2 | 60.6 | 30 | 2 | 0.316 | 2 |
| 0.05 | 0.22 | 1.11 | 11 | 3 | 28.7 | 29 | 2 | 69.2 | 35 | 3 | 0.424 | 3 |
| 0.1 | 0.3 | 1.38 | 14 | 3 | 31.5 | 32 | 2 | 76.2 | 38 | 3 | 0.525 | 3 |
| 0.2 | 0.4 | 1.73 | 17 | 4 | 34.1 | 34 | 3 | 91.2 | 46 | 1 | 0.653 | 3 |

| Au | µC | $cm^2$ |
|---|---|---|
| 1% | 9.9 | 0.03 |
| 10% | 45 | 0.12 |
| 20% | 119 | 0.31 |
| Bulk | 2.5 | 0.006 |

| Scan rate V $s^{-1}$ | Sqrt scan rate $(V\ s^{-1})^{0.5}$ | 1 % Au/C | | | 10 % Au/C | | | 20 % Au/C | | | Bulk Au | | |
|---|---|---|---|---|---|---|---|---|---|---|---|---|---|
| | | Peak current | | Max peak no. | Peak current | | Max peak no. | Peak current | | Max peak no. | Peak current | | Max. peak no. |
| | | mA | A $cm^{-2}$ | | mA | A $cm^{-2}$ | | mA | A $cm^{-2}$ | | mA | A $cm^{-2}$ | |
| 0.001 | 0.03 | 0.13 | 0.005 | 5 | 14.7 | 0.124 | 2 | 39.8 | 0.129 | 1 | 0.253 | 0.039 | 2 |
| 0.005 | 0.07 | 0.42 | 0.016 | 3 | 20.9 | 0.178 | 3 | 50.1 | 0.163 | 1 | 0.275 | 0.043 | 2 |
| 0.01 | 0.10 | 0.56 | 0.022 | 5 | 23.6 | 0.200 | 2 | 56.1 | 0.182 | 2 | 0.288 | 0.045 | 3 |
| 0.02 | 0.14 | 0.79 | 0.031 | 3 | 25.5 | 0.216 | 2 | 60.6 | 0.197 | 2 | 0.316 | 0.049 | 2 |
| 0.05 | 0.22 | 1.11 | 0.043 | 3 | 28.7 | 0.243 | 2 | 69.2 | 0.224 | 3 | 0.424 | 0.066 | 3 |
| 0.1 | 0.3 | 1.38 | 0.054 | 3 | 31.5 | 0.268 | 2 | 76.2 | 0.247 | 3 | 0.525 | 0.081 | 3 |
| 0.2 | 0.4 | 1.73 | 0.067 | 4 | 34.1 | 0.290 | 3 | 91.2 | 0.296 | 1 | 0.653 | 0.101 | 3 |

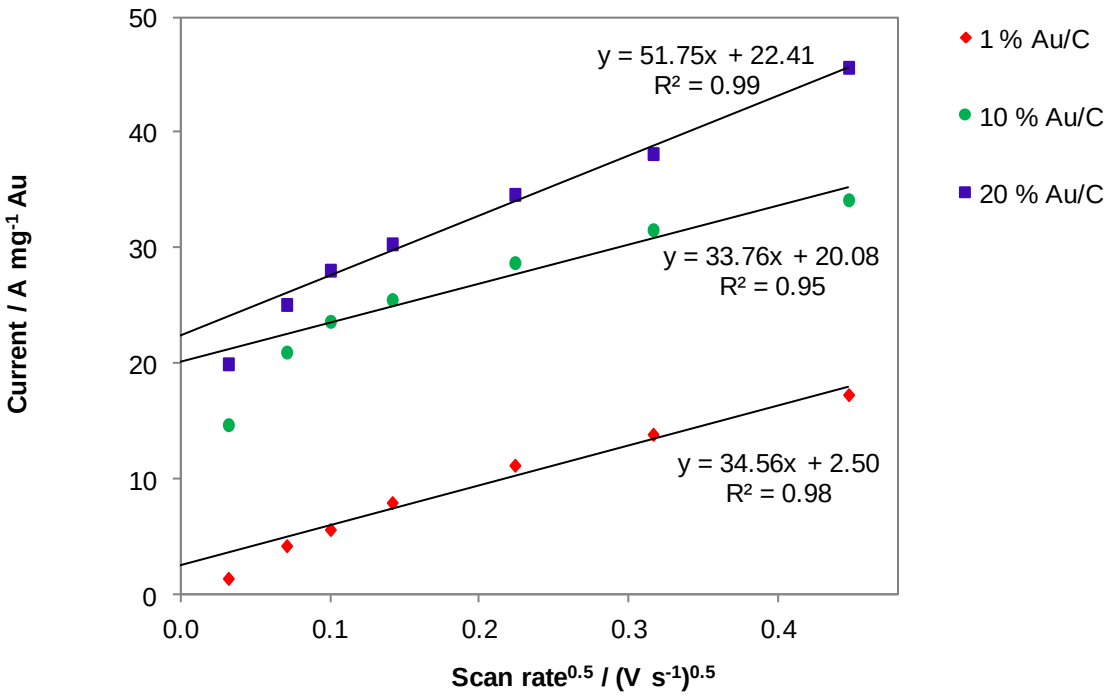

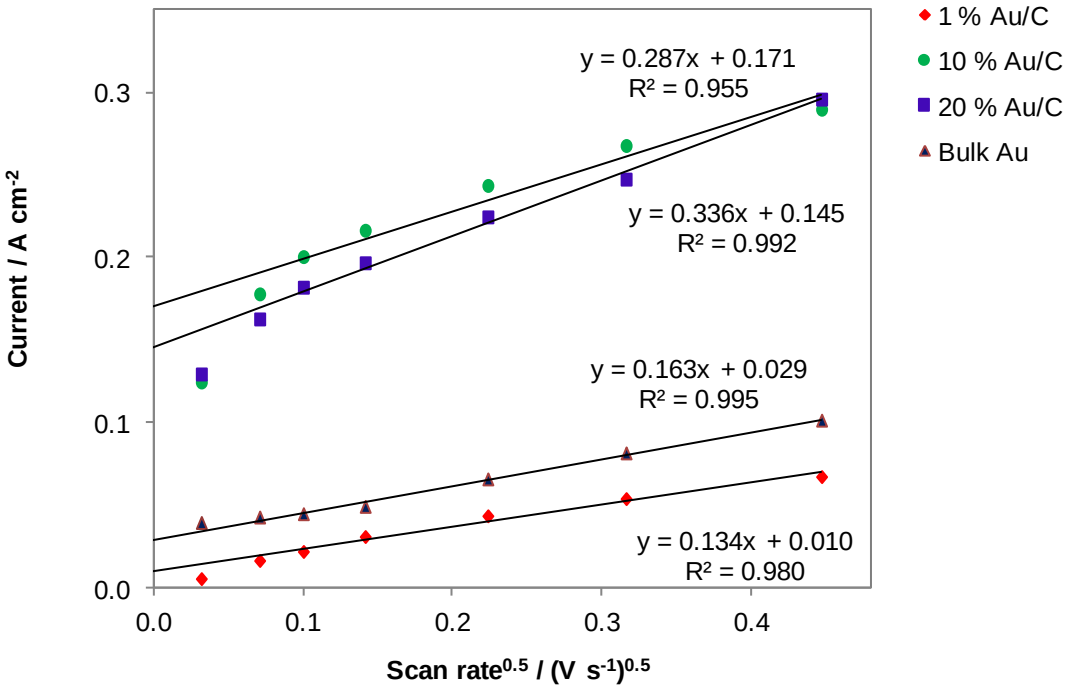
y = 0.287x + 0.171
R² = 0.955
y = 0.336x + 0.145
R² = 0.992
y = 0.163x + 0.029
R² = 0.995
y = 0.134x + 0.010
R² = 0.980
1 % Au/C
10 % Au/C
20 % Au/C
Bulk Au
Current / A cm-2
Scan rate0.5 / (V s-1)0.5
0.0
0.1
0.2
0.3
0.4

# APPENDIX 7

## Appendix 7.1 CVs of gold catalysts in 10 mM glyceraldehyde/1 M KOH and 1 M KOH

**Bulk gold**

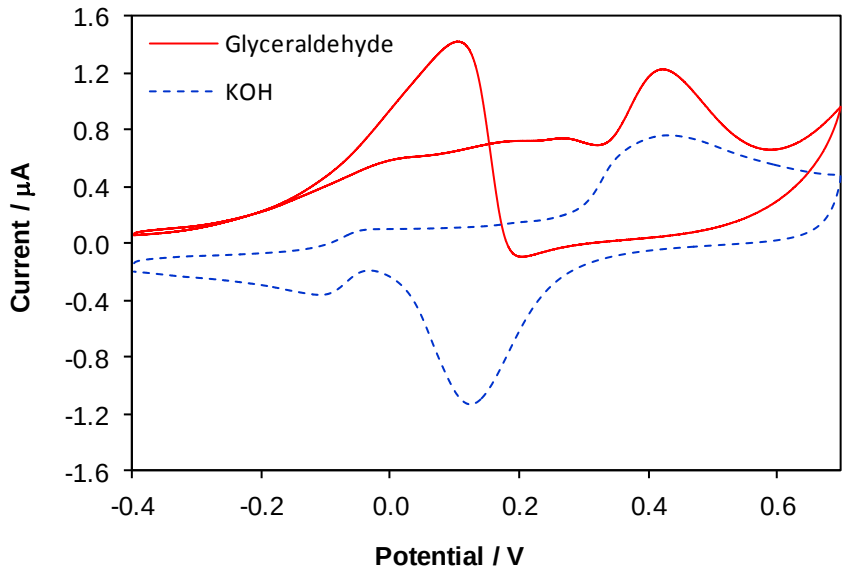


**4.7 nm Au/C**

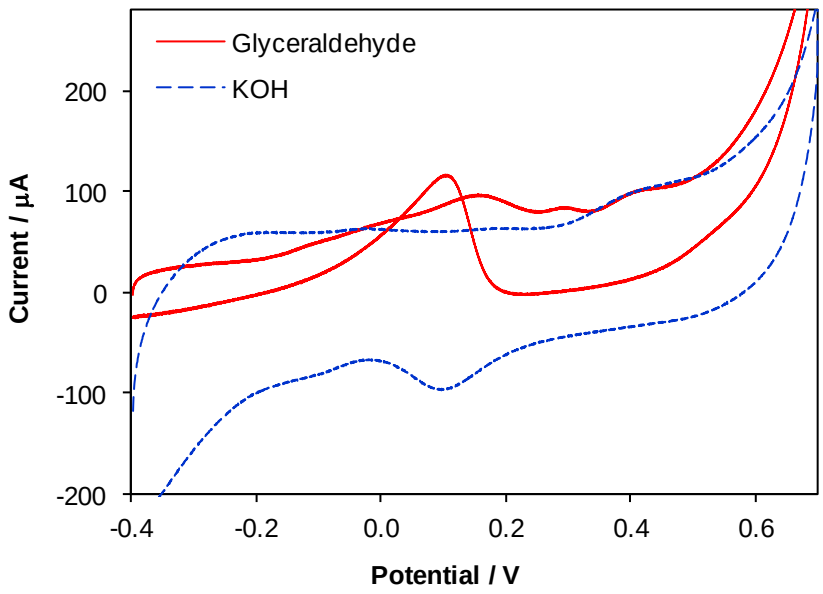

**14.7 nm Au/C**

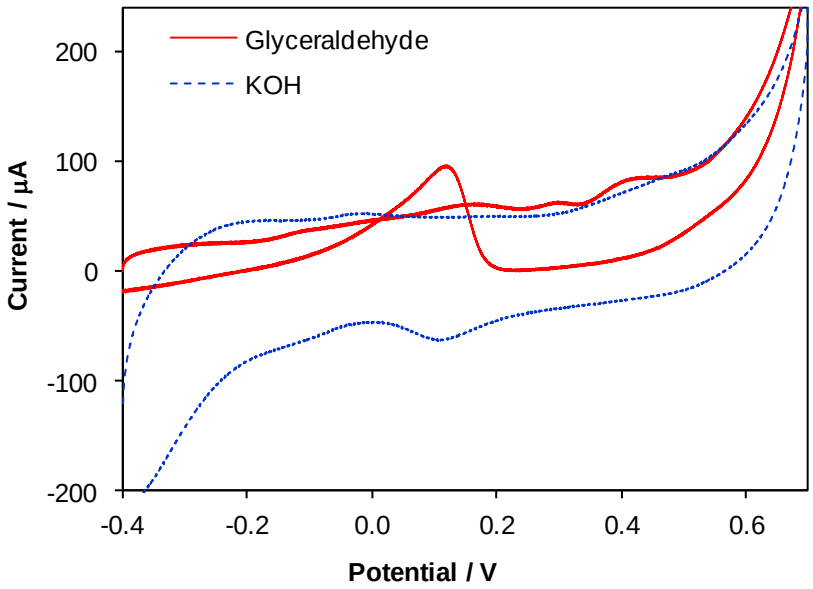


**88 nm Au/C**

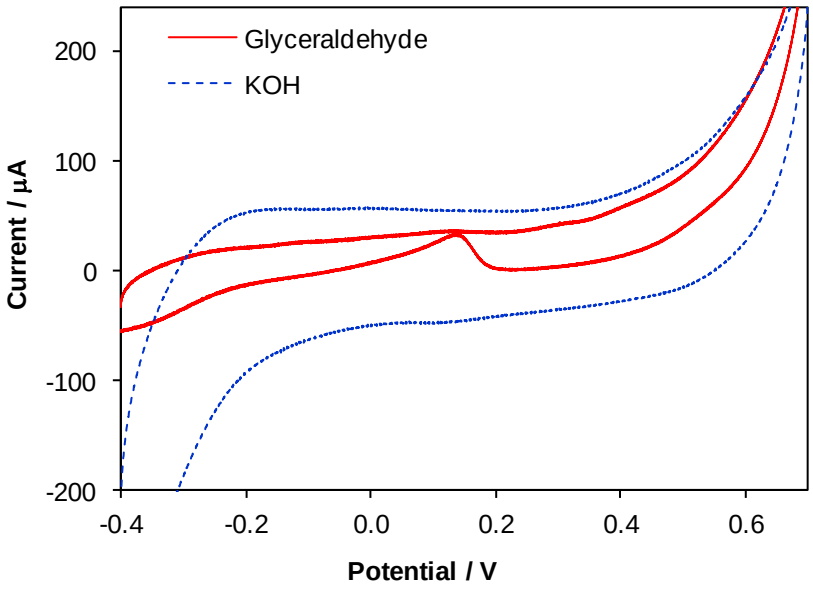

## Appendix 7.2 Electrochemistry data for gold catalysts in 10 mM glycerate/1 M KOH

### Raw data

| Catalyst | Sample no. | GCP | Ru (Ω) * | 1 M KOH** | | | | | | | | Glycerate oxidation** | | | | | | | |
|---|---|---|---|---|---|---|---|---|---|---|---|---|---|---|---|---|---|---|---|
| | | | | | | | | | | | | | | | Highest peak | | | | |
| | | | | Integrated peak charge, μC # | Monolayer charge, μC/cm² | Metal surface area, cm² | Cat mass, mg | Metal loading, % | Metal mass, mg | EASA, cm²/mg metal | EASA, m²/g metal | Ru (Ω) | Scan rate, mV/s | Number of cycles | Number of highest peak | Current, mA | Current, mA.cm⁻² | Current, mA.mg⁻¹ Au | Current, mA.mg⁻¹ cat |
| Bulk Au | | | 59.9 | 3.1 | 386 | 0.008 | | | | | | 59.9 | 10 | 5 | 5 | 4.3E-03 | 0.54 | | |
| 15% Au/C (4.7 nm) | 1 | 1 | 2.4 | 101.0 | 386 | 0.262 | 0.01 | 15 | 0.0015 | 174.4 | 17.44 | 3.1 | 10 | 5 | 5 | 0.50 | 1.9 | 332 | 49.84 |
| | 2 | 5 | 2.3 | 102.2 | 386 | 0.265 | 0.01 | 15 | 0.0015 | 176.5 | 17.65 | 2.9 | 10 | 5 | 5 | 0.49 | 1.8 | 325 | 48.71 |
| Au_cit1 (14.7 nm) | 1 | 2 | 1.8 | 36.5 | 386 | 0.095 | 0.01 | 20 | 0.002 | 47.3 | 4.73 | 2.2 | 10 | 5 | 5 | 0.24 | 2.5 | 120 | 24.00 |
| | 2 | 6 | 1.9 | 43.2 | 386 | 0.112 | 0.01 | 20 | 0.002 | 56.0 | 5.60 | 2.2 | 10 | 7 | 7 | 0.40 | 3.6 | 200 | 40.00 |
| Au_cit3 (88 nm) | 1 | 4 | 3.0 | 7.7 | 386 | 0.020 | 0.01 | 20 | 0.002 | 10.0 | 1.00 | 2.3 | 10 | 6 | 6 | 0.087 | 4.3 | 43 | 8.66 |
| | 2 | 8 | 1.9 | 12.4 | 386 | 0.032 | 0.01 | 20 | 0.002 | 16.1 | 1.61 | 1.9 | 10 | 7 | 6 | 0.092 | 2.9 | 46 | 9.18 |

* Applied PF correction 0.5 Ω for supported Au and 90 % of Ru for bulk Au

Roughness factor 4.1

** CA for 10 min at -0.2 V in both KOH and glycerate, before CV

#From run 2 of CV at 50 mV/s in 1 M KOH, after CA and strip cycling from -0.9 → 0.8 V for 5 cycles

### Average values

| Catalyst | Current, mA | | | Current, mA.cm⁻² | | | Current, mA.mg⁻¹ Au | | |
|---|---|---|---|---|---|---|---|---|---|
| | Ave | Std dev | Conf | Ave | Std dev | Conf | Ave | Std dev | Conf |
| 15% Au/C (4.7 nm) | 0.49 | 0.01 | 0.01 | 1.87 | 0.03 | 0.05 | 329 | 4 | 5 |
| Au_cit1 (14.7 nm) | 0.3 | 0.08 | 0.1 | 3.1 | 0.5 | 0.7 | 160 | 40 | 55 |
| Au_cit3 (88 nm) | 0.089 | 0.003 | 0.004 | 4 | 0.7 | 1 | 45 | 1 | 2 |

## Appendix 7.3 CVs of gold catalysts in 0.5 M formate/1 M KOH and 1 M KOH

**Bulk gold**

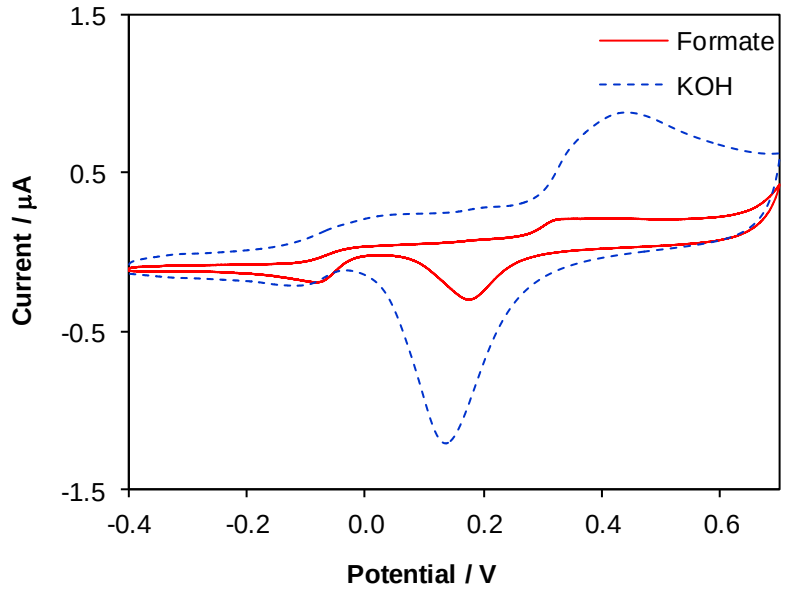


**4.7 nm Au/C**

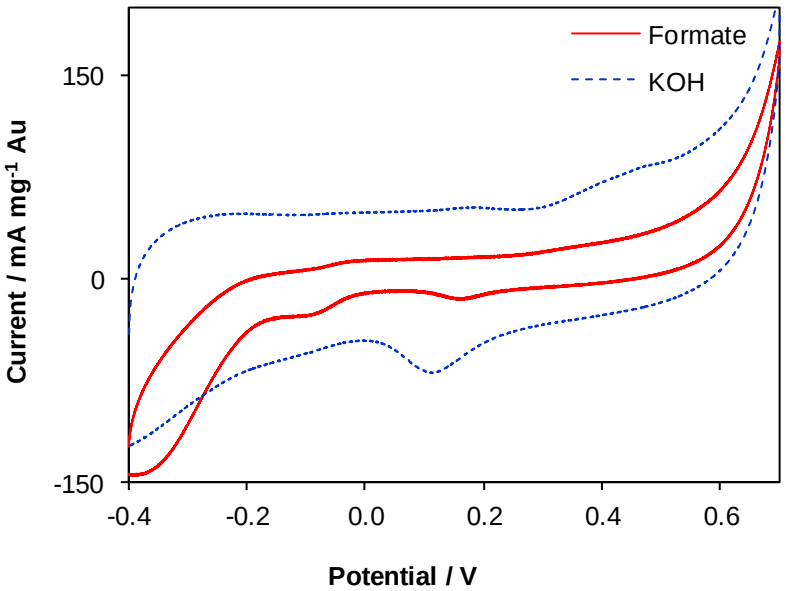

**14.7 nm Au/C**

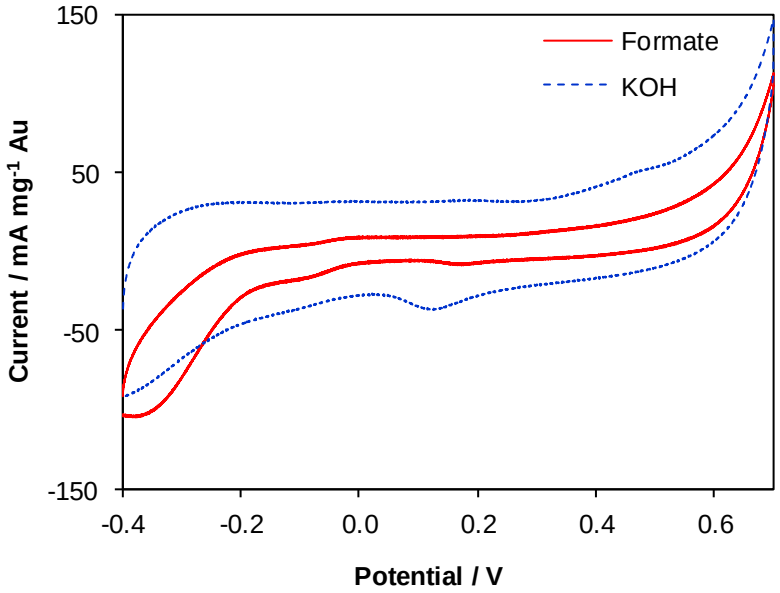


**88 nm Au/C**